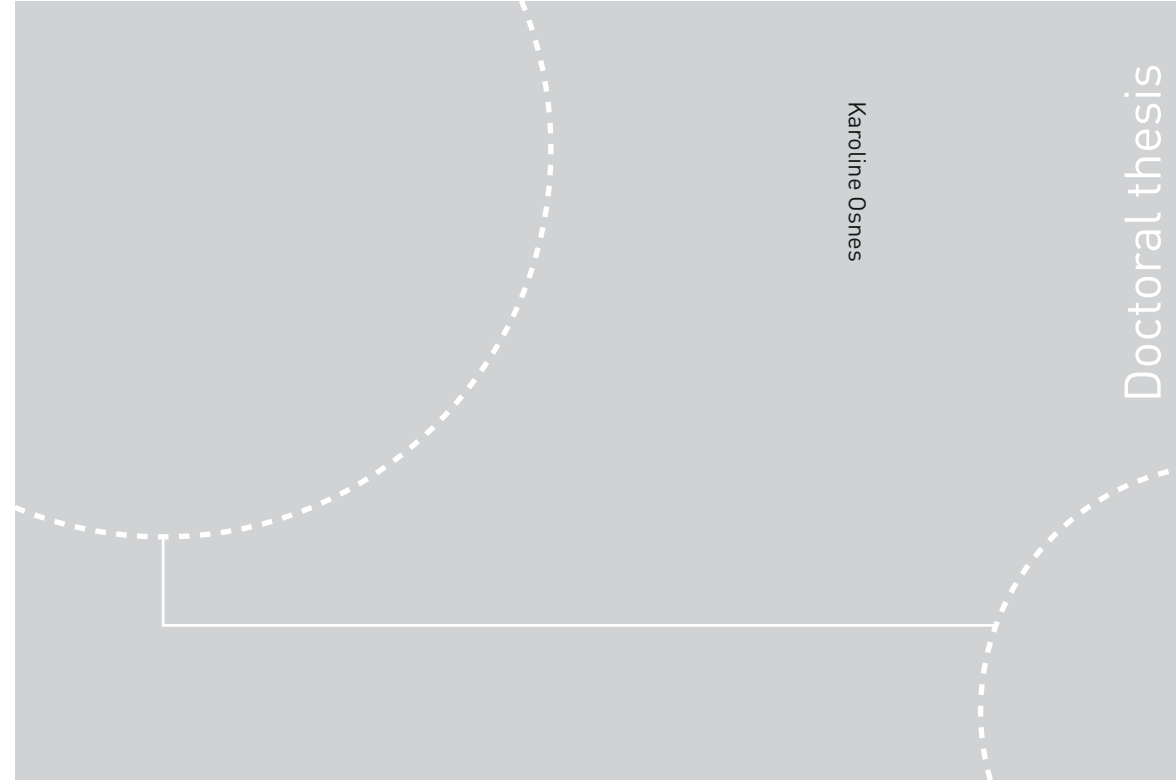


ISBN 978-82-326-4204-5 (printed ver.)
ISBN 978-82-326-4205-2 (electronic ver.)
ISSN 1503-8181



Doctoral theses at NTNU, 2019:304

Karoline Osnes

Monolithic and laminated glass under extreme loading: Experiments, modelling and simulations

Doctoral theses at NTNU, 2019:304

NTNU
Norwegian University of Science and Technology
Thesis for the Degree of
Philosophiae Doctor
Faculty of Engineering
Department of Structural Engineering

 **NTNU**
Norwegian University of
Science and Technology

 **NTNU**
Norwegian University of
Science and Technology

 NTNU

Karoline Osnes

Monolithic and laminated glass under extreme loading: Experiments, modelling and simulations

Thesis for the Degree of Philosophiae Doctor

Trondheim, November 2019

Norwegian University of Science and Technology
Faculty of Engineering
Department of Structural Engineering



Norwegian University of
Science and Technology

NTNU

Norwegian University of Science and Technology

Thesis for the Degree of Philosophiae Doctor

Faculty of Engineering

Department of Structural Engineering

© Karoline Osnes

ISBN 978-82-326-4204-5 (printed ver.)

ISBN 978-82-326-4205-2 (electronic ver.)

ISSN 1503-8181

Doctoral theses at NTNU, 2019:304

Printed by NTNU Grafisk senter

Preface

This thesis is submitted in partial fulfilment of the requirements for the degree of Philosophiae Doctor in Structural Engineering at the Norwegian University of Science and Technology (NTNU). The work has been conducted at the Structural Impact Laboratory (SIMLab) at the Department of Structural Engineering, NTNU. Funding was provided by the Centre for Advanced Structural Analysis (CASA), Centre for Research-based Innovation (CRI) at NTNU. The work was supervised by Professor Tore Børvik and Professor Odd Sture Hopperstad. The thesis consists of four journal articles, referred to as Parts 1 to 4. Parts 1 to 3 have been published in international peer-reviewed journals, while Part 4 is submitted for possible publication in an international peer-reviewed journal. A synopsis binds the four individual parts together. The first author has been responsible for the experimental work, the numerical modelling and simulations, and the preparation of the manuscripts.

Karoline Osnes
Trondheim, Norway
October 18, 2019

Abstract

Design of glass components has become more challenging over the past few decades, owing to the increased use of glass as a structural material. When a structure is required to withstand extreme loading, such as blast or impact, the design process becomes all the more difficult. The work of this thesis aims to facilitate more predictive glass design, and focuses on the development of numerical tools that can predict the structural capacity of glass components under various loading conditions. Glass components designed against extreme loading are often made from laminated glass, i.e., a sandwich structure including a polymeric interlayer. Thus, the work of this thesis also considers laminated glass, as well as regular monolithic (non-laminated) glass. Glass is a brittle material that fails in a sudden manner, and has a highly stochastic fracture behaviour. Fracture initiation in monolithic glass typically induces complete failure, but laminated glass is able to maintain some structural integrity also after glass fracture due to properties of the polymeric interlayer. Thus, the numerical work is divided into two parts. The first part aims to predict the fracture initiation of glass, with special emphasis on the probabilistic fracture strength of glass components. In the second part, we investigate the possibility of describing the post-fracture behaviour in finite element (FE) simulations. In an effort to validate the numerical tools, we perform an extensive experimental study using different setups and loading rates, including various geometries of the glass specimens. In this study, the glass and polymer material is limited to annealed soda-lime-silica float glass and polyvinyl butyral (PVB), respectively.

The thesis consists of four individual parts in the form of journal articles, in addition to a synopsis. The synopsis includes the motivation and background of the thesis, the objectives and scope, along with a summary of the four parts, and an overall conclusion and suggestions for further work. Part 1 of the thesis presents a strength prediction model (SPM), which aims to predict the probabilistic fracture strength of glass under various loading conditions. The SPM is based on the notion of microscopic surface flaws, in which fracture in glass typically initiates. Three different experimental test series were performed for validation of the SPM, including quasi-static four point bending tests, quasi-static pressure tests and blast-pressure tests on monolithic glass. The blast-pressure tests were performed in the SIMLab Shock Tube Facility. The experiments demonstrated the stochastic fracture behaviour of glass by means of a varying fracture strength and position of fracture initiation. In addition, the fracture strength proved to be dependent on the experimental setup and the geometry of the glass specimens. The SPM was able to recreate many of the trends from the four-point bending tests, and managed to reproduce the fracture behaviour of the pressure tests reasonably well. However, further studies on loading rate dependency on the fracture strength were deemed necessary. Part 2 presents an experimental study on the response of laminated glass exposed to fragment impact before blast loading. The blast pressure was produced in the SIMLab Shock Tube Facility, while fragment impact was mimicked by 7.62 mm armour-piercing bullets or drilled holes. Blast tests on laminated glass

excluding fragment impact were also performed as a reference. It was found that the safety and structural integrity of the laminated glass against blast loading are significantly reduced if the glass is damaged by fragments beforehand. Part 3 presents a numerical study on the post-fracture behaviour of blast-loaded monolithic and laminated glass using non-linear explicit FE simulations. The simulations applied novel numerical techniques, such as higher-order elements and node splitting. The simulations were compared to blast experiments conducted in the SIMLab Shock Tube Facility. The experiments on laminated glass demonstrated a progressive failure response, which depends on the fracture initiation in the glass. The simulations of both monolithic and laminated were in good agreement with the blast tests, revealing the potential of the employed numerical techniques. Part 4 deals with the probabilistic fracture strength of glass through an experimental and numerical study. In the numerical part, we propose an extension of the SPM, in which the loading-rate dependency of the fracture strength of glass is considered. To validate the rate-dependent SPM, we performed an extensive experimental study including quasi-static punch tests and low-velocity impact tests on monolithic and laminated glass. The experimental work demonstrated again the stochastic fracture behaviour of glass by a variation in fracture load and position of fracture initiation. The predictions obtained with the rate-dependent SPM were in general in good agreement with the experiments, and provided a realistic rate enhancement of the fracture strength.

Acknowledgements

First of all, I would like to express my sincere gratitude to my supervisors Professor Tore Børvik and Professor Odd Sture Hopperstad for great support and guidance. The time and effort you put into this work have been invaluable to me.

This thesis would not be the same without the support of my friends and colleagues at SIMLab. Your contributions in discussions and your willingness to help are much appreciated. Special thanks goes to PhD Candidate Ole Vestrum for countless discussions and invaluable help with Python, Dr. Jens Kristian Holmen for guidance with the IMPETUS Afea Solver and for the contributions as a co-author, Dr. Joakim Johnsen for discussions regarding polymer modelling, Associate Professor Vegard Aune for providing helpful insights regarding testing in the SIMLab Shock Tube Facility, PhD Candidates Bjørn Håkon Frodal and John Fredrick Berntsen for many discussions and help with the course work during the first semesters, and PhD Candidate Susanne Thomesen for great support during the final stages of the PhD. I would also like to thank Professor Magnus Langseth for the support, and for encouraging me to start at SIMLab. Also, thanks to all of you, the four years I spent working on this thesis have been anything but boring.

The experimental studies in this thesis could not be completed without the assistance from Mr. Trond Auestad, Mr. Tore Wisth and Mr. Tore André Christensen in the laboratory. Your help is deeply appreciated. I would also like to thank Dr. Egil Fagerholt for help with the digital image correlation analyses, and Dr. Octavian Knoll for the guidance and support during my internship at BMW. I would also like to express my gratitude to Dr. Lars Olovsson for the assistance and discussions regarding finite element simulations in the IMPETUS Afea Solver. I also received great assistance with the experimental studies from nine master students, to which I am very grateful. I would also like to acknowledge Modum Glassindustri for providing the glass specimens for use in the experimental studies.

The funding for this work was provided by the Centre for Advanced Structural Analysis (CASA), Centre for Research-based Innovation (CRI) at the Norwegian University of Science and Technology (NTNU). The support is highly acknowledged.

I am deeply grateful to Petter, for the encouragement and understanding, and for always knowing how to cheer me up when needed. I also wish to thank my twin sister Henriette for the support and for being my best friend. Lastly, I would like to express my deep and sincere gratitude to the rest of my friends and family, who have provided me with moral and emotional support in my life. Most of all, I would like to thank my mother for the time we had together. This thesis is dedicated to you.

Contents

Synopsis:

1 Introduction	1
2 Objectives and scope	6
3 Summary	7
3.1 Part 1	7
3.2 Part 2	8
3.3 Part 3	9
3.4 Part 4	11
4 Concluding remarks	13
5 Suggestions for further work	14
References	15

Articles:

Part 1:

Osnes, K., Børvik, T., Hopperstad, O.S. (2018). *Testing and modelling of annealed float glass under quasi-static and dynamic loading*. Engineering Fracture Mechanics 201, 107-129.

Part 2:

Osnes, K., Dey, S., Hopperstad, O.S., Børvik, T. (2019). *On the dynamic response of laminated glass exposed to impact before blast loading*. Experimental Mechanics 59, 1033-1046.

Part 3:

Osnes, K., Holmen, J.K., Hopperstad, O.S., Børvik, T. (2019). *Fracture and fragmentation of blast-loaded laminated glass: an experimental and numerical study*. International Journal of Impact Engineering 132, 103334.

Part 4:

Osnes, K., Hopperstad, O.S., Børvik, T. (2019). *Rate dependent failure of monolithic and laminated glass: an experimental and numerical study*. Submitted for possible journal publication.

Synopsis

1 Introduction

In recent years, the demand for high transparency in buildings and structures has increased significantly. As a result, the applications of glass as a building material have advanced from simple windows to full facade claddings and load-bearing components [1, 2]. This development complicates the design of glass components, and leads to a growing demand for models that can predict the structural capacity of glass under various loading conditions. When a structure is expected to withstand extreme loading scenarios, such as blast or impact, the structural design gets considerably more challenging. In the event of an urban explosion, glass failure imposes a significant threat to people nearby, with glass fragments from windows and facades being responsible for 80% of the suffered injuries [3]. From a structural design perspective, the most common approach for reducing this threat is to use laminated window glass instead of windows consisting of regular monolithic glass. Laminated glass consists of two or more plates of monolithic glass bonded together by a polymeric interlayer, typically polyvinyl butyral (PVB) [4]. If the glass fractures, the fragments are retained on the polymeric interlayer, thus preventing large hazardous fragments to be ejected and travel at high velocities. When a flexible polymer is used, such as PVB, the interlayer may contribute to absorbing parts of the blast energy, which reduces the impact transmitted to the window supports [5]. Note that special consideration needs to be taken regarding the design of the window supports to avoid pull-out failure [6].

The most common glass type for structural purposes is soda-lime-silica float glass, which typically has the chemical composition shown in Table 1 [7]. Float glass refers to glass made by the float process, which involves heating the components to 1500°C before pouring molten glass material on a liquid tin bath. The liquid tin ensures that the glass solidifies in a controlled manner with a uniform thickness [4]. The temperature of the glass is then slowly lowered until the glass has hardened and the internal stresses have been relieved. When the glass is cooled, it turns into an amorphous (non-crystalline) solid [7].

Table 1: Chemical composition of soda-lime-silica glass [7].

Component	Silica sand	Lime	Soda	Magnesia	Alumina	Others
Chemical notation	SiO ₂	CaO	Na ₂ O	MgO	Al ₂ O ₃	–
Mass percentage (%)	69-74	5-14	10-16	0-6	0-3	0-5

The production of laminated glass involves a number of different stages. First, the glass plates are cut into the required sizes, and assembled with the interlayer(s) between them. Then, the layers

are placed on a nip roller where they are compressed and heated to approximately 70°C to form the initial bond and to remove excess air between them. Finally, the laminate is transported to an autoclave, where it is subjected to cycles of heat up to 140°C and pressures up to approximately 800 kPa [4].

While laminated glass is requested in blast-protective design, it is also used to increase the resistance of load-bearing glass components, or to reduce the damage of glass towards other types of extreme loading, such as impact loading. The employed polymer material depends on the application of the glass component. There are also other means of increasing the load-bearing capacity, e.g., by thermal strengthening of the glass. Depending on the level of heat treatment, glass can be categorised as either heat-strengthened or fully-tempered [7]. Regular glass that has not been heat treated is referred to as annealed glass. The heat treatment involves heating the glass to temperatures around 620-675°C followed by rapid cooling, which produces compressive stresses near the surface. Fully-tempered glass is cooled more rapidly than heat-strengthened glass, and includes therefore larger compressive stresses. As a result, fully-tempered glass has a higher fracture strength, and creates smaller fragments when broken due to more strain energy stored in the glass [8].

Glass is a brittle material and has a linear elastic behaviour to the point of fracture. The theoretical fracture strength of glass is estimated to be between 15 GPa and 21 GPa [9]. However, experiments on glass demonstrate that glass fails at much lower stresses. The large disagreement between the theoretical and the practical fracture strength was explained by, e.g., Griffith [10] to be caused by microscopic flaws on the surface. Fracture in glass typically initiates in these flaws due to an amplification of the stresses around them, which causes the flaws to grow in an unstable manner [11]. Generally, the flaws only grow if they are exposed to mode I loading, i.e., loading that causes the flaws to open. As a consequence, fracture in glass typically occurs under tensile loading [8], and the tensile strength of glass is therefore much lower than its compressive strength. The increased fracture strength of heat-strengthened and fully-tempered glass is explained by this phenomenon. Upon tensile loading, the inherent compressive stresses in the glass surface must first be exceeded by the applied tensile stresses before the flaws can grow, causing the heat-treated glass to withstand larger loads than annealed glass.

To relate the applied stresses in a material and the amplified stresses around a flaw, Irwin [12] introduced the stress intensity factor K . For a surface flaw under mode I loading, the relationship between the applied normal stress σ and the mode I stress intensity factor K_I can be calculated as [11]

$$K_I = Y\sigma\sqrt{\pi a} \quad (1)$$

where Y is a geometrical factor dependent on the flaw shape, and a is the depth of the surface flaw. To determine the onset of unstable fracture, we compare the stress intensity factor with a critical value, referred to as the fracture toughness K_{IC} . Thus, the applied fracture stress σ_f may be expressed as

$$\sigma_f = \frac{K_{IC}}{Y\sqrt{\pi a}} \quad (2)$$

The fracture toughness of glass is considerably lower than for, e.g., metals, and has been reported to be about $0.75 \text{ MPa}\sqrt{\text{m}}$ for quasi-static loading and room temperature [13]. Additionally, due to the lack of plastic flow in glass, fracture will grow fast with limited chance of crack arrest [14]. From Equation (2), it is evident that the fracture strength of glass is not only dependent on the applied stresses, but also the properties of the surface flaws. Because the sizes and density of the surface flaws can vary significantly between glass plates, the fracture strength of glass is highly probabilistic. The presence of flaws also causes the fracture strength to be dependent on the loading condition and the geometry of the glass plate. For example, glass plates loaded in a biaxial stress state have a lower probabilistic fracture strength than glass plates loaded in a uniaxial state, due to the increased probability of maximising the stresses normal to the flaws. Furthermore, an increased surface area of glass decreases the probabilistic fracture strength because of the increased likelihood of finding a critical surface flaw.

Traditionally, the probabilistic fracture strength of glass is described by a two-parameter Weibull distribution [15]. The distribution adopts two surface strength parameters m and k , which require calibration from experimental data. However, some researchers [16, 17] have found that the parameters for glass are dependent on the geometry and loading conditions, and that they should not be treated as material constants. This finding suggests that the probability distribution must be obtained through other means. In a recent work by Yankelevsky [18], the probabilistic fracture strength of glass is obtained by a model based on the notion of microscopic surface flaws in glass. The model aims to predict the glass strength without the need for material tests or using a pre-determined distribution of the fracture strength. A similar approach was also proposed by Nurhuda et al. [17], and Kinsella and Persson [19]. A further development of the model by Yankelevsky was proposed by Osnes et al. [20], which employs stress histories obtained from finite element (FE) simulations to predict the fracture strength of glass under various loading.

As previously mentioned, fracture in glass is associated with sudden and unstable growth of surface flaws. However, these flaws may also grow slowly and steadily under tensile loading that produces stress intensities below K_{IC} [21]. The flaws can therefore grow slowly into a critical size before unstable fracture occurs. The phenomenon is known as delayed failure, stress corrosion cracking or static fatigue, and is driven by a chemical reaction (stress corrosion) between the flaw tip and water vapour in the ambient atmosphere [22]. Stress corrosion cracking is thus responsible for causing a loading-rate dependency on the fracture strength of glass. Consequently, if the flaws are able to grow over a long period of time, stress corrosion cracking can reduce the fracture strength significantly under long-term loading. Based on this phenomenon, Charles [23] proposed a relationship between the fracture strength and the time to fracture for glass under quasi-static tensile loading, and found that it also applied for dynamic loading [24]. Later, Ritter [25] and Chandan et al. [26] both demonstrated that the fracture strength and the loading rate could be related through the relationship developed by Charles. Ritter performed experiments with displacement rates up to 50 mm/min, while Chandan et al. used stress rates from 10^{-1} MPa/s to 10^7 MPa/s . More recent experimental studies have also demonstrated the loading-rate dependency of fracture in glass in tension [27, 28, 29], but also in compression [29, 30, 31].

Experimental studies on the behaviour of window glass under blast and impact loading have been

reported by several authors in the open literature. These studies include impact loaded automobile glazing [32, 33, 34, 35], laminated window glass [6, 36, 37], and monolithic window glass [38, 39, 30]. In terms of blast loading, experimental studies have been performed by using either explosives [6, 40, 41, 42] or shock tubes [20, 43, 44, 45, 46]. A shock tube may be used to generate pressure-time histories similar to that from far-field blast events, and allows for blast experiments in a laboratory environment [47]. In the event of an explosion, the blast pressure is often accompanied by fragments, which may impact a structure before being exposed to the blast pressure. This scenario was studied experimentally for laminated glass by Osnes et al. [48], where it was found that the structural integrity was significantly reduced if the glass was perforated by fragments before being blast loaded.

In the aforementioned experimental studies on laminated glass, there were two recurring observations. Firstly, glass fracture influences a great deal of the total response, and secondly, laminated glass has a progressive failure process. Pelfrene et al. [45] described this failure process for blast-loaded laminated glass by dividing it into four different phases, visualised in Figure 1. It can also describe the failure process for impact events if the fracture response is not highly localised, such as in ballistic impact.

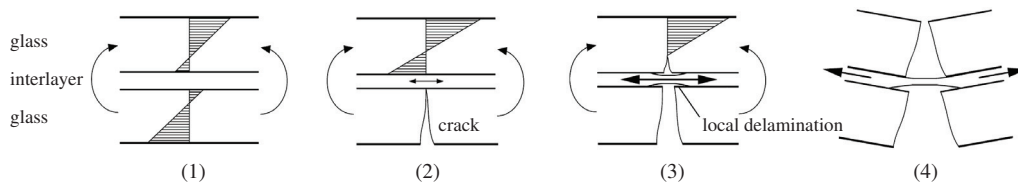


Figure 1: Progressive failure process of laminated glass [45].

The first phase of the failure process is the pre-fracture response. The glass plates have a linear elastic response and the interlayer transfers shear forces between the glass plates (1). Then, the first glass plate fractures, which requires the interlayer to transfer tensile forces perpendicular to the cracks (2). Then, the second glass plate fractures, and delamination occurs locally between the glass and the interlayer. When the cracks are narrow, the glass plate is still able to transfer compressive forces (3). Eventually, excessive stretching occurs in the interlayer, and depending on the failure strain of the interlayer and the adhesion between the layers, the interlayer might tear (4). If the adhesion is too strong, the interlayer will stretch over a small area, creating large strains that can lead to instant tearing [45]. However, a weak adhesion level might lead to a large amount of detaching glass fragments from the interlayer. As illustrated by Figure 1, the post-fracture behaviour of laminated glass is complex. It is also dependent on many different factors, including the applied loading rate [49, 50, 51, 52], the composition of the laminate [53], the polymer type [53, 54], the adhesive properties between the glass and polymer [55], and the ambient temperature [54, 56].

Design of glass solutions required to withstand extreme loading is frequently determined through prototype testing [3]. Unfortunately, such prototype tests are time consuming and expensive to perform. Requirements and test methods for glass solutions under blast loading are addressed in

several standards. See, e.g., standard EN 13541 [57] for testing of structural laminated glass, and standards EN 13123 [58, 59] and EN 13124 [60, 61] for testing of windows, doors and shutters through range tests or shock tube tests. Because of the stochastic fracture behaviour of glass, a large number of tests may be necessary to properly determine the structural capacity of the prototype. An approach that can be used to minimise the need for experimental testing is FE simulations. Naturally, there is a need for validated numerical models that are able to recreate the mechanical behaviour, both in terms of initial glass fracture and the post-fracture response. A number of researchers have applied FE simulations in an effort to recreate the behaviour of laminated glass exposed to blast loading. Among them, Hooper et al. [41] developed a shell element model where the stiffness of the glass plates was set to zero when fracture occurred. The technique gave comparable results with experiments. Larcher et al. [40] investigated the applications and limitations of different types of FE models, including a solid element model, a layered shell element model, a combined shell and solid element model, and a smeared shell element model. It was found that the smeared shell element model could only be used for small displacements, and that the behaviour of the polymer was not sufficiently described by the layered shell element model. Furthermore, the solid element model gave the most accurate results, but shell elements could also be used for the glass if the crack direction is assumed to be orthogonal. Zhang et al. [6] simulated entire window systems, and found that the boundary conditions governed much of the mechanical behaviour. Consequently, special considerations need to be taken regarding modelling of the supports. In the study by Pelfrene et al. [45], special attention was paid to the simulation of delamination between the glass and the PVB. The authors were able to recreate many aspects of the post-fracture behaviour observed in experiments; however, the method used for describing delamination caused instability in the simulations. Note that the glass failure was modelled as deterministic in the aforementioned numerical works.

Element erosion is traditionally used in FE simulations to describe fracture, and involves deletion of elements when reaching a predefined failure criterion. This technique has its shortcomings in simulations of fracture and fragmentation of monolithic and laminated glass. When element erosion is used, a crack of the same size as an element will appear, which requires a highly refined glass mesh to properly describe crack propagation. In the numerical study by Pelfrene et al. [45], the authors demonstrated that when element erosion is applied, very small elements are necessary to accurately describe delamination and subsequent stretching of the interlayer. Furthermore, element erosion also faces difficulties in simulation of free-flying glass fragments. Node splitting is an alternative technique for describing fracture in FE simulations, and can be used to avoid some of the obstacles associated with element erosion. Instead of deleting elements upon failure, elements are separated at the borders, which permits the use of larger elements than if element erosion is applied. In addition, the technique enables a description of fracture and fragmentation without loss of mass or momentum. It should be noted that node splitting still creates mesh sensitivity, as with element erosion, since crack propagation needs to follow the element borders [62]. The node-splitting technique was investigated in a numerical study on blast-loaded monolithic and laminated glass by Osnes et al. [46] using the nonlinear explicit FE code IMPETUS Afea Solver [63]. The applied numerical methods demonstrated a large potential for use in simulations of the post-fracture behaviour of monolithic and laminated

glass. Nevertheless, there is still a need for further investigation of the numerical tools at hand to ensure better predictions of the mechanical behaviour of both monolithic and laminated glass. In addition, more well-documented experimental studies should be performed in order to validate the numerical methods. If (or perhaps when) such models are available, they can be used as a design tool for optimising glass solutions, not only against blast loading, but also other extreme load cases, such as impact or a combination of the two.

2 Objectives and scope

One of the main objectives of this thesis was to develop numerical models for predicting failure of glass components exposed to various loading conditions and loading rates. Due to the brittle nature of glass, and its low resistance to crack propagation, failure of glass components is often associated with initiation of unstable fracture. Thus, we aimed to develop a model for predicting fracture initiation in glass, which could be used to obtain the probabilistic fracture strength distribution for glass components as a function of the geometry, boundary condition and loading situation. In regards to laminated glass, fracture in the glass does not necessarily lead to complete failure due to the additional capacity offered by the polymeric interlayer. For this reason, effort was made to recreate the post-fracture behaviour of laminated glass in finite element (FE) simulations. Due to the limitations of traditional numerical techniques in FE simulations of glass failure, we investigated the use of novel numerical techniques, such as node splitting and higher order elements. An essential part of the work of this thesis dealt with experiments on monolithic and laminated glass. Thus, another main objective of the work was to establish a comprehensive database of experiments for studying the failure process of glass specimens under various loading conditions, and for use in validation of numerical models.

The experimental and numerical work was limited to studies on annealed soda-lime-silica float glass. Thus, heat-treated glass, such as fully-tempered and heat-strengthened glass, was not considered in the work of this thesis. In addition, we only studied the response of monolithic and single-layered laminated glass with a polyvinyl butyral (PVB) interlayer. The experiments were also limited to window glass exposed to transverse loading, thereby excluding load-bearing components with a relatively large thickness compared to the remaining dimensions, e.g., beams and columns. The influence of the window frame design was also not studied, and to eliminate pull-out failure in the experiments, we employed a fastening system with a relatively large bite depth.

A major part of the experimental work consisted of blast experiments on monolithic and laminated glass. However, we also conducted experiments on glass specimens under impact loading, and quasi-static loading using various areal dimensions, thicknesses and loading conditions. Ballistic impact tests were also performed as a part of a study that investigated the combined effect of fragment and pressure loading in a blast event. Instead of using explosives in the blast experiments, we employed a shock tube that produces pressure loading similar to that of far-field explosions. In blast scenarios, the pressure profile generally consists of a positive and a negative pressure phase. However, in our blast experiments, the negative phase was negligible.

Although ballistic impact was studied experimentally, the response was not considered in any numerical study, and is left for further work. The proposed strength prediction model was devised under the assumption of crack growth of microscopic surface flaws under tension. Failure in glass under ballistic impact is generally controlled by other mechanisms, and the proposed model is therefore not applicable. The numerical studies using FE simulations were limited to studies on monolithic and laminated glass under blast loading, and did not consider the probabilistic fracture strength of glass. Possible fluid-structure interaction (FSI) effects were also not considered in this study.

3 Summary

The works in this PhD thesis have been published in international peer-reviewed journals (Parts 1 to 3) or submitted for possible publication in an international peer-reviewed journal (Part 4). The four journal articles are summarised below.

3.1 Part 1

Osnes, K., Børvik, T., Hopperstad, O.S. (2018). *Testing and modelling of annealed float glass under quasi-static and dynamic loading*. Engineering Fracture Mechanics 201, 107-129.

The first part of the thesis is an experimental and numerical study on the stochastic fracture behaviour of monolithic annealed soda-lime-silica float glass under various loading conditions. The experimental work consisted of quasi-static four-point bending tests using three different specimen geometries of a relatively small size, and uniform quasi-static and dynamic pressure tests on larger glass plates. The dynamic pressure tests involved subjecting the glass specimens to blast loading in the SIMLab Shock Tube Facility [47], while the quasi-static pressure tests employed a slowly increasing water pressure. The blast loading used in the shock tube tests had a maximum overpressure P_{\max} ranging from 51.6 kPa to 73.4 kPa. A custom-made clamping system was used for testing of glass specimens in the shock tube, which ensured proper fastening, while simultaneously limiting the clamping pressure on the glass. To obtain the deformation of the larger glass plates, we employed an optical point-tracking procedure [64] to measure the displacements of 25 discrete points that were painted on the plate. The point-tracking procedure employed images from two synchronised cameras, which were filming the specimens during testing. The procedure was validated against laser measurements. From the experimental study, we observed that the fracture strength of glass varied significantly within the same test setup, and was dependent on both the geometry of the glass specimen and the loading condition. The four-point bending tests also demonstrated that the mean and the variance of the fracture strength increased with a decreasing specimen size. It was also observed a large variation in the point of fracture initiation for all of the test setups.

The experiments were used in an effort to validate a strength prediction model (SPM) for glass. The SPM is an extension of a model proposed by Yankelevsky [18], and includes some additional

features and adjustments. Failure in glass components typically results from crack growth of pre-existing microscopic surface flaws, which results in a highly stochastic fracture behaviour. Thus, the fracture strength of glass must be described by a probability distribution, which will be dependent on the stress state on the glass surface during loading and the properties of the surface flaws. The SPM aims to calculate the probabilistic fracture strength for glass components as a function of the geometry, boundary condition and loading situation. Through a Monte Carlo simulation, the SPM performs virtual experiments on glass components by combining stress histories obtained from a finite element (FE) simulation and information about artificial surface flaws. To identify fracture in the virtual experiments, we make use of the criterion for unstable crack growth in Equation (2). Some assumptions are made about the artificial flaws, such as non-interacting flaws, a Mott's size distribution, and semi-circular flaw shapes. To obtain a converged failure probability distribution, we typically perform 5000 virtual experiments [18]. The probability distribution can be given in terms of the fracture stress, fracture force, fracture displacement or fracture time, in addition to the position of fracture initiation.

The SPM was able to successfully capture the trends observed in the quasi-static four-point bending tests, with an increased fracture strength and variance with a decreasing specimen size. In addition, the fracture forces from the experiments were all found to lie within the corresponding predictions. In regards to the quasi-static pressure tests, the SPM obtained slightly larger fracture strengths than the experiments. This disagreement might be explained by stress corrosion, which is known to increase with the relative humidity [22]. For the shock tube tests, we observed that the fracture times and the position of fracture initiation was within the predictions. However, it was considered necessary to include strain-rate sensitivity of the fracture strength in the model to obtain more accurate predictions for dynamic loading. Strain-rate sensitivity was later considered in the SPM, see Part 4 of the thesis.

3.2 Part 2

Osnes, K., Dey, S., Hopperstad, O.S., Børvik, T. (2019). *On the dynamic response of laminated glass exposed to impact before blast loading*. *Experimental Mechanics* 59, 1033-1046.

In the second part of the thesis, we investigated experimentally the effect of fragment impact before blast loading on laminated glass. Whenever a high explosive detonates, it generates an intense blast wave that expands into the surrounding air. The blast wave is often accompanied by fragments, defined as either primary or secondary fragments. The primary fragments are parts initially contained in the explosive device or parts from the fractured casing, while secondary fragments are nearby objects carried by the blast wave, such as building debris or loose items. The primary fragments typically have a lower mass and higher velocity than the secondary fragments, and travels with a rather constant velocity. When the distance from the detonation increases, the intensity and velocity of the blast wave decrease. Thus, if a structure is positioned some distance from the detonation, fragments might hit the structure before being exposed to blast loading. This study is motivated by this possible scenario.

In the study, impact from fragments was mimicked by three different methods, i.e., a hole made by a diamond drill, and ballistic impact using 7.62 mm armour-piercing bullets with and without the brass jacket. The bullets had similar mass and velocity to typical primary fragments in blast scenarios [65, 66, 67]. The laminated glass specimens used in this study were made from two annealed soda-lime-silica float glass plates connected by a polyvinyl butyral (PVB) interlayer. The pre-damaged specimens were exposed to blast loading in the SIMLab Shock Tube Facility using two different levels of pressure with P_{\max} equal to 215.2 kPa and 254.2 kPa. As a reference, we also performed blast tests on initially undamaged specimens using the same pressure levels. In order to investigate the capacity of the PVB, we conducted two additional tests on undamaged specimens with a successively increased blast pressure having P_{\max} equal to 294.5 kPa and 382.1 kPa. Two synchronised cameras were used to obtain the displacements of the specimens during blast testing.

The damage of the specimens induced by ballistic impact was similar for bullets with and without the brass jacket, namely localised damage at the impact location with cracks forming from this point. Consequently, the behaviour of the specimens under blast loading did not substantially differ for the two methods. Drilling of a hole did not lead to visible damage in the rest of the specimens, and thus, the response under blast loading was different than for the bullet-impacted specimens.

It was found that the mimicked fragment impact increased the damage of the laminated glass specimens during blast loading in various ways. Firstly, the pre-damage caused the glass to break into larger fragments, which appeared to increase the amount and size of detached glass fragments from the PVB. This effect was larger for the bullet-impacted specimens than for the drilled-hole specimens. Secondly, the damage of the PVB was severely increased with the amount of pre-damage in the laminated glass, and the pressure was able to pass freely through the barrier. In addition, a significantly higher pressure was required to rupture the PVB in the initially undamaged specimens compared to the damaged ones. Thus, the structural integrity of the laminated glass against blast loading is significantly reduced if it is pre-damaged by fragment impact. Fragment impact should therefore be considered in the design of blast-protective window solutions.

3.3 Part 3

Osnes, K., Holmen, J.K., Hopperstad, O.S., Børvik, T. (2019). *Fracture and fragmentation of blast-loaded laminated glass: an experimental and numerical study*. International Journal of Impact Engineering 132, 103334.

In the third part of the thesis, we investigated the possibility of recreating the post-fracture behaviour of monolithic and laminated glass using explicit FE simulations. In the simulations, we applied modelling techniques such as higher order elements and node splitting, which are available in the FE code IMPETUS Afea Solver [63]. Node splitting is an alternative to element erosion, and describes fracture and crack propagation by separating elements instead of deleting them [62]. Higher order elements provide additional robustness and can describe bending with only one

element over the thickness. Part 3 of the thesis also includes an experimental study on blast-loaded laminated glass specimens consisting of two annealed soda-lime-silica float glass plates and a PVB interlayer. The laminated glass specimens were exposed to blast loading in the SIMLab Shock Tube Facility, and a total of 15 specimens were tested using five different pressure levels with P_{\max} between 167.8 kPa and 258.9 kPa. Two synchronised cameras were used to obtain the displacements of the specimens by point tracking, and to capture the points of fracture initiation.

The experiments demonstrated the probabilistic fracture strength of glass, since the occurrence of fracture was not consistent within the different pressure levels. In addition, both the time and position of fracture initiation varied for the failed specimens. We also observed that the initiation of fracture influenced a great deal of the total failure response, and that the deformation of the specimens became larger when fracture initiated early and at the mid-point. Failure of the PVB interlayer was not observed in the tests.

A selection of experiments on laminated glass specimens was simulated, and the mechanical behaviour of the simulations was compared to the corresponding experiments. We also performed simulations of experiments on blast-loaded monolithic glass specimens, which were presented in Part 1. In the simulations, the glass was modelled as a linear elastic material with a deterministic failure criterion, i.e., fracture occurs at the point of maximum principal stress for a predetermined value. Since the fracture strength of glass is probabilistic, this is a simplification. However, the main purpose of the numerical study was to investigate the applicability of the employed modelling techniques, and the failure model was therefore deemed acceptable. Furthermore, to model the PVB, we employed a viscoelastic material model, which is motivated by the Bergström-Boyce material model [68]. The material parameters were calibrated to tensile tests performed by Hooper et al. [49] and Del Linz et al. [51]. Adhesion between the glass and the PVB was modelled by merging PVB nodes to the glass surface, while delamination was described by separating these nodes when a failure criterion was reached at the interface. The parameters in the delamination criterion were chosen based on experiments found in the open literature, in combination with an inverse-modelling approach. Finally, we employed a purely Lagrangian approach, and potential fluid-structure interaction effects were thus neglected in the simulations.

The simulations of the blast-loaded monolithic glass specimens were able to describe behaviours such as radial crack propagation from the point of fracture initiation, formation of large glass shards and free-flying fragments. Regarding the laminated glass, the simulations managed to recreate fine cracking of the glass, and separation of glass elements from the PVB interlayer. A parametric study was performed to investigate the sensitivity of the FE simulations with regards to selected parameters. The monolithic glass model was most sensitive to the mesh density and parameters in the glass failure criterion, while the laminated glass model was somewhat sensitive to all of the investigated delamination parameters. A more thorough study of the input parameters and the numerical techniques was deemed necessary to increase the predictability of the numerical models.

3.4 Part 4

Osnes, K., Hopperstad, O.S., Børvik, T. (2019). *Rate dependent failure of monolithic and laminated glass: an experimental and numerical study*. Submitted for possible journal publication.

The fourth, and last, part of the thesis is an experimental and numerical study on the loading rate dependency of the probabilistic fracture strength of glass. In the numerical study, we present an extension of the SPM (see Part 1) in which the rate dependency of glass fracture is considered. To identify fracture in the SPM, we made use of the criterion for unstable crack growth in artificial surface flaws, see Equation (2). As a means to include rate dependency in the SPM, we introduced a strain-rate dependent fracture toughness, denoted the dynamic fracture toughness K_{ID} . The proposed expression for K_{ID} was based on the works by Charles [23, 24] on stress corrosion cracking in glass, and is given as

$$K_{ID} = K_{IC} \left(\frac{\bar{\dot{\epsilon}}}{\dot{\epsilon}_0} \right)^{1/(1+N_s)} \geq K_{IC} \quad (3)$$

where $\bar{\dot{\epsilon}}$ is a time-averaged strain rate, N_s is an exponent that controls the strain-rate enhancement, and $\dot{\epsilon}_0$ is a reference strain rate below which the static value of the fracture toughness K_{IC} applies. In this work, the decrease in the fracture toughness caused by stress corrosion cracking was not considered, and the minimum value of K_{ID} is set to K_{IC} . As opposed to the actual strain rate, a time-averaged strain rate was used to smooth out short-term fluctuations in calculations of highly dynamic problems.

In an effort to validate the rate-dependent SPM, we performed an extensive experimental study using two different setups and various loading rates. The experiments include quasi-static punch tests with loading rates of 3 mm/min, 100 mm/min and 300 mm/min, and low-velocity impact tests with prescribed impact velocities from 2 m/s to 14 m/s. In total, 90 quasi-static punch tests were conducted on monolithic glass specimens, using an Instron universal testing machine to load the specimens by a flattened circular impactor. The low-velocity impact tests were conducted in an Instron 9350 drop tower impact system, using a standard instrumented striker with a half-spherical impactor nose that resulted in a total impacting mass of 6.551 kg. In the low-velocity impact tests, we tested two monolithic glass specimens (at 2-4 m/s), and nine laminated glass specimens consisting of two glass plates and a PVB interlayer (at 2-14 m/s). Both test setups employed the clamping system developed for the shock tube tests. Synchronised cameras were placed below the specimens to film the tests, and the images were used to obtain the displacements of the specimens by point tracking. High-speed camera images were used to capture the point of fracture initiation.

The quasi-static punch tests clearly demonstrated the stochastic fracture behaviour of glass, with a large variation in the fracture force and the position of fracture initiation. In addition, the tests demonstrated that the fracture force increased with the loading rate. The loading rate also appeared to alter the variance of the fracture force. However, the slope of the force-displacement curves appeared to be independent of the loading rate. The low-velocity impact tests also displayed a variation in the fracture strength of glass, with inconsistent failure occurrence and varying fracture initiation for equal impact velocities. The damage of the laminated glass specimens

generally increased with the impact velocity, leading to a larger out-of-plane displacement and more detaching glass fragments from the PVB interlayer. For the prescribed impact velocity of 14 m/s, we also obtained rupture of the PVB.

The rate-dependent SPM managed to successfully capture many of the trends observed in the experimental tests. For the quasi-static punch tests, the SPM was able to describe the change in median and variance of the fracture force with the loading rate. In addition, most of the experiments were found to lie within the predictions, regarding both the fracture force and the position of fracture initiation. In terms of the low-velocity impact tests, the fracture strengths were generally consistent with the SPM results, while the positions of fracture initiation were all found to lie within the corresponding predictions. We also obtained higher fracture strengths for fracture initiation some distance from the contact point. This result was in agreement with the experiments. Some of the experiments deviated from the SPM results, which might be caused by an imprecise description of the surface condition parameters in the SPM. Consequently, it may be necessary to perform measurements of the flaws in glass specimens, both in terms of density and size.

At this point, it is unclear whether the loading-rate dependency in the SPM will provide better predictions for the shock tube tests presented in Part 1. Preliminary SPM predictions of the shock tube tests proved to be more sensitive to the surface condition parameters than the strain-rate enhancement of the fracture toughness. Again, measurements of the surface flaws appear to be necessary.

Other contributions

The following contributions are related to, but not included in, the thesis.

Osnes, K., Hopperstad, O.S., Børvik, T. (2018). *Quasi-Static and Dynamic Testing of Annealed Float Glass*. Proceedings 2018 2, 495. Presented at the 18th International Conference on Experimental Mechanics (ICEM18), Brussels, Belgium.

Osnes, K., Børvik, T., Hopperstad, O.S. (2018). *Shock Tube Testing and Modelling of Annealed Float Glass*. EPJ Web of Conferences 183, 01035. Presented at the 12th International Conference on the Mechanical and Physical Behaviour of Materials under Dynamic Loading (DYMAT 2018), Arcachon, France.

4 Concluding remarks

The thesis deals with failure of monolithic and laminated window glass under various loading conditions and loading rates, with special emphasis on the mechanical behaviour under blast and impact loading. The work investigates the topic through both experimental tests and numerical simulations. The experiments were performed to create a basis for comparison with the simulations, and to better understand the failure processes of monolithic and laminated glass. The numerical work deals mainly with the prediction of fracture initiation of glass components by a strength prediction model (SPM). However, the post-fracture behaviour of laminated glass is also investigated through finite element (FE) simulations. The main scientific contributions and findings of the thesis are summarised in the following list.

- An experimental setup for testing of monolithic and laminated glass under blast and impact loading was developed. A custom-made fastening system ensured controlled boundary conditions with proper fastening and limited clamping pressure on the specimens. In addition, a validated point-tracking procedure was used to measure the displacement of the specimens without reducing the visibility of the crack initiation and propagation in the glass.
- An extensive experimental database was established for monolithic and laminated glass. The experimental tests on monolithic glass included quasi-static four point bending tests, pressure tests, punch tests, and dynamic tests including low-velocity impact tests and blast tests. For laminated glass, we performed low-velocity impact tests, and blast tests with and without the influence of fragment impact.
- The experiments demonstrated that the fracture strength of glass should be represented by a failure probability distribution, and that the distribution is dependent on the loading condition, the boundary condition, the loading rate, and the geometry of the monolithic or laminated glass specimen. The experimental study displayed that an increased median and variance of the failure probability distribution were achieved by an increased loading rate and a decreased glass surface area.
- Fracture initiation in monolithic glass generally induces complete failure, but laminated glass is able to maintain some structural integrity after glass fracture. Experiments proved that the post-fracture behaviour of laminated glass is strongly dependent on the fracture initiation in the glass and on the propagation of the cracks.
- The structural integrity of laminated window glass towards blast loading is significantly reduced if the window is pre-damaged by fragment impact. The pre-damage appeared to increase the detachment of larger glass fragments from the PVB interlayer, and caused more severe damage of the interlayer during blast loading.
- The SPM showed great potential concerning predictions of the fracture strength of glass components under various loading conditions, and can thus contribute to more predictive glass design. The rate dependency included in the last version of the SPM provided a

realistic rate enhancement of the fracture strength, and trends such as an increase in the mean and variance of the fracture force were recreated. Some experiments deviated from both the original SPM and the rate-dependent SPM, which might be explained by an improper description of the surface flaws.

- The numerical techniques investigated in FE simulations showed great promise regarding the recreation of the post-fracture behaviour of blast-loaded monolithic and laminated glass. By utilizing the node-splitting technique, the simulations managed to capture behaviours such as radial crack propagation and free-flying fragments. Simulations of laminated glass were able to describe fine cracking of the glass, delamination between the glass and the PVB interlayer, and separation of glass fragments from the interlayer. Thus, node splitting can be used to avoid obstacles associated with element erosion.

5 Suggestions for further work

The work carried out for this thesis has indicated a number of topics that would benefit from further research. Some suggestions for further work are listed below, and include investigations to improve the contributions of this thesis, or studies that were not included in the current research objectives.

- To improve the predictability of the strength prediction model (SPM), it is recommended to measure the surface conditions of glass plates in terms of sizes and densities of surface flaws. It would be valuable to establish a proper database that includes measurements of glass plates from different glass manufacturers. Through measurements of surface flaws, the underlying assumptions of the SPM can be investigated, such as non-interacting flaws, the size distribution of flaws, and the flaw shapes.
- The proposed method of including loading-rate dependency in the SPM should be investigated further, especially for higher loading rates than employed in the current experimental study.
- Effort should be put into increasing the understanding of stress corrosion, and other possible mechanisms for strain-rate enhancement of the fracture strength of glass.
- The influence of the glass and polymer material on the fracture behaviour of monolithic and laminated glass should be investigated. For use of heat-treated glass, it is recommended to measure the compressive surface stresses using optical methods.
- Delamination in laminated glass is particularly dependent on the ambient temperature and the loading rate, and experimental studies should be performed to investigate the sensitivity to these factors. Measurements of the delamination process may be performed using infrared thermography.
- The mechanical behaviour of PVB is expected to change after the autoclave process. However, material tests on non-treated PVB are often performed to obtain data for calibration of material models for use in FE simulations. This effect should be addressed experimentally.

- In the shock tube tests presented in this thesis, the negative phase of the blast pressure was negligible. Thus, blast experiments on glass components using explosives would be beneficial to study the effect of the negative phase experimentally.
- To determine the post-fracture behaviour of monolithic and laminated glass through finite element (FE) simulations with reasonable confidence, it is necessary to perform a more comprehensive study of the input parameters, both numerically and experimentally. In particular, studies on parameters included in the glass fracture criterion and the delamination criterion are needed.
- The numerical techniques employed in the FE simulations should be investigated and developed further, especially methods for describing glass fracture and delamination. Effort should be made to include temperature and loading-rate dependency in the models.
- In the FE simulations presented in this thesis, glass fracture was modelled using a deterministic failure criterion. To investigate the influence of stochastic glass fracture on the post-fracture behaviour, it would be beneficial to include a failure criterion that allows for fracture initiation at locations of non-maximum applied stress.
- It would be of interest to perform FE simulations of monolithic and laminated glass exposed to other extreme loading scenarios than blast loading, such as impact and ballistic loading. Simulations including failure of the polymeric interlayer would also be beneficial.
- Alternative numerical techniques for describing fracture in glass should be studied, such as phase field methods.

References

- [1] Haldimann, M., Luible, A., and Overend, M. Structural use of glass. 10th ed. Iabse, 2008. Chap. 4, pp. 85–86.
- [2] Belis, J., Mocibob, D., Luible, A., and Vandebroek, M. On the size and shape of initial out-of-plane curvatures in structural glass components. *Construction and Building Materials* 25.5 (2011), pp. 2700–2712.
- [3] Haldimann, M., Luible, A., and Overend, M. Structural use of glass. 10th ed. Iabse, 2008. Chap. 2, pp. 35–36.
- [4] Institution of Structural Engineers. Structural Use of Glass in Buildings. 2nd ed. Institution of Structural Engineers, 2014. Chap. 5, pp. 5–10.
- [5] Institution of Structural Engineers. Structural Use of Glass in Buildings. 2nd ed. Institution of Structural Engineers, 2014. Chap. 11, pp. 77–78.
- [6] Zhang, X., Hao, H., and Wang, Z. Experimental study of laminated glass window responses under impulsive and blast loading. *International Journal of Impact Engineering* 78 (2015), pp. 1–19.

- [7] Haldimann, M., Luible, A., and Overend, M. Structural use of glass. 10th ed. Iabse, 2008. Chap. 1, pp. 10–12.
- [8] Wachtman, J. B., Cannon, W. R., and Matthewson, M. J. Mechanical properties of ceramics. 2nd ed.
- [9] Overend, M, Parke, G., and Buhagiar, D. Predicting failure in glass - a general crack growth model. *Journal of Structural Engineering* 133.8 (2007), pp. 1146–1155.
- [10] Griffith, A. A. The phenomena of rupture and flow in solids. *Philosophical transactions of the royal society of London* 221 (1920), pp. 163–198.
- [11] Anderson, T. L. Fracture mechanics: Fundamentals and Applications. 3rd. CRC press, 2005. Chap. 2, pp. 48–49.
- [12] Irwin, G. R. Analysis of stresses and strains near the end of a crack transversing a plate. *Trans. ASME, Ser. E, J. Appl. Mech.* 24 (1957), pp. 361–364.
- [13] Wiederhorn, S. M. Fracture surface energy of glass. *Journal of the American Ceramic Society* 52.2 (1969), pp. 99–105.
- [14] Bradt, R. C. The fractography and crack patterns of broken glass. *Journal of failure analysis and prevention* 11.2 (2011), pp. 79–96.
- [15] Weibull, W. A statistical theory of strength of materials. *Ingeniörvetenskaps Akademiens Handlingar* 151 (1939), pp. 1–45.
- [16] Afferrante, L, Ciavarella, M, and Valenza, E. Is Weibull’s modulus really a material constant? Example case with interacting collinear cracks. *International Journal of Solids and Structures* 43.17 (2006), pp. 5147–5157.
- [17] Nurhuda, I, Lam, N., Gad, E., and Calderone, I. Estimation of strengths in large annealed glass panels. *International Journal of Solids and Structures* 47.18-19 (2010), pp. 2591–2599.
- [18] Yankelevsky, D. Z. Strength prediction of annealed glass plates – A new model. *Engineering Structures* 79 (2014), pp. 244–255.
- [19] Kinsella, D. T. and Persson, K. A numerical method for analysis of fracture statistics of glass and simulations of a double ring bending test. *Glass Structures & Engineering* 3.2 (2018), pp. 139–152.
- [20] Osnes, K., Børvik, T., and Hopperstad, O. S. Testing and modelling of annealed float glass under quasi-static and dynamic loading. *Engineering Fracture Mechanics* 201 (2018), pp. 107–129.
- [21] Wachtman, J. B., Cannon, W. R., and Matthewson, M. J. Mechanical properties of ceramics. 2nd ed.
- [22] Wiederhorn, S. and Bolz, L. Stress corrosion and static fatigue of glass. *Journal of the American Ceramic Society* 53.10 (1970), pp. 543–548.
- [23] Charles, R. Static fatigue of glass: I & II. *Journal of Applied Physics* 29.11 (1958), pp. 1554–1560.

- [24] Charles, R. Dynamic fatigue of glass. *Journal of Applied Physics* 29.12 (1958), pp. 1657–1662.
- [25] Ritter Jr, J. Dynamic Fatigue of Soda-Lime-Silica Glass. *Journal of Applied Physics* 40.1 (1969), pp. 340–344.
- [26] Chandan, H. C., Bradt, R., and Rindone, G. E. Dynamic fatigue of float glass. *Journal of the American Ceramic Society* 61.5-6 (1978), pp. 207–210.
- [27] Nie, X., Chen, W. W., Wereszczak, A. A., and Templeton, D. W. Effect of loading rate and surface conditions on the flexural strength of borosilicate glass. *Journal of the American Ceramic Society* 92.6 (2009), pp. 1287–1295.
- [28] Peroni, M., Solomos, G., Pizzinato, V., and Larcher, M. Experimental investigation of high strain-rate behaviour of glass. *Applied Mechanics and Materials*. Vol. 82. Trans Tech Publications. 2011, pp. 63–68.
- [29] Zhang, X., Zou, Y., Hao, H., Li, X., Ma, G., and Liu, K. Laboratory test on dynamic material properties of annealed float glass. *International Journal of Protective Structures* 3.4 (2012), pp. 407–430.
- [30] Daryadel, S. S., Mantena, P. R., Kim, K., Stoddard, D., and Rajendran, A. Dynamic response of glass under low-velocity impact and high strain-rate SHPB compression loading. *Journal of Non-Crystalline Solids* 432 (2016), pp. 432–439.
- [31] Feng, Z., Zhou, Y., Tan, R., Hou, H., Sun, T., Fezzaa, K., Huang, J., and Luo, S. Dynamic damage and fracture of a conductive glass under high-rate compression: A synchrotron based study. *Journal of Non-Crystalline Solids* 494 (2018), pp. 40–49.
- [32] Herndon, G., Allen, K., Roberts, A., Phillips, D., and Batzer, S. A. Automotive side glazing failure due to simulated human interaction. *Engineering Failure Analysis* 14.8 (2007), pp. 1701–1710.
- [33] Pyttel, T., Liebertz, H., and Cai, J. Failure criterion for laminated glass under impact loading and its application in finite element simulation. *International Journal of Impact Engineering* 38.4 (2011), pp. 252–263.
- [34] Liu, B., Xu, T., Xu, X., Wang, Y., Sun, Y., and Li, Y. Energy absorption mechanism of polyvinyl butyral laminated windshield subjected to head impact: experiment and numerical simulations. *International Journal of Impact Engineering* 90 (2016), pp. 26–36.
- [35] Yang, N., Wang, J., Zhao, G., Zhong, Y., and Wang, D. Experimental study of headform–PVB laminated windshield impact. *International journal of crashworthiness* 21.6 (2016), pp. 521–531.
- [36] Zhang, X., Hao, H., and Ma, G. Laboratory test and numerical simulation of laminated glass window vulnerability to debris impact. *International Journal of Impact Engineering* 55 (2013), pp. 49–62.
- [37] Van Dam, S., Pelfrene, J., Van Paepegem, W., and Lecompte, D. Mechanical response of laminated glass plates subjected to impact loading. *Proceedings of Challenging Glass 4 & COST Action TU0905 Final Conference*. 2014, pp. 473–480.

- [38] Masters, F. J., Gurley, K. R., Shah, N., and Fernandez, G. The vulnerability of residential window glass to lightweight windborne debris. *Engineering Structures* 32.4 (2010), pp. 911–921.
- [39] Van Dam, S., Pelfrene, J., De Pauw, S., and Van Paepegem, W. Experimental study on the dynamic behaviour of glass fitted with safety window film with a small-scale drop weight set-up. *International Journal of Impact Engineering* 73 (2014), pp. 101–111.
- [40] Larcher, M., Solomos, G., Casadei, F., and Gebbeken, N. Experimental and numerical investigations of laminated glass subjected to blast loading. *International Journal of Impact Engineering* 39.1 (2012), pp. 42–50.
- [41] Hooper, P., Sukhram, R., Blackman, B., and Dear, J. On the blast resistance of laminated glass. *International Journal of Solids and Structures* 49.6 (2012), pp. 899–918.
- [42] Zhang, X. and Hao, H. Experimental and numerical study of boundary and anchorage effect on laminated glass windows under blast loading. *Engineering Structures* 90 (2015), pp. 96–116.
- [43] Kumar, P. and Shukla, A. Dynamic response of glass panels subjected to shock loading. *Journal of Non-Crystalline Solids* 357.24 (2011), pp. 3917–3923.
- [44] Bermbach, T., Teich, M., and Gebbeken, N. Experimental investigation of energy dissipation mechanisms in laminated safety glass for combined blast-temperature loading scenarios. *Glass Structures & Engineering* 1.1 (2016), pp. 331–350.
- [45] Pelfrene, J., Kuntsche, J., Van Dam, S., Van Paepegem, W., and Schneider, J. Critical assessment of the post-breakage performance of blast loaded laminated glazing: experiments and simulations. *International Journal of Impact Engineering* 88 (2016), pp. 61–71.
- [46] Osnes, K., Holmen, J. K., Hopperstad, O. S., and Børvik, T. Fracture and fragmentation of blast-loaded laminated glass: An experimental and numerical study. *International Journal of Impact Engineering* 132 (2019), p. 103334.
- [47] Aune, V., Fagerholt, E., Langseth, M., and Børvik, T. A shock tube facility to generate blast loading on structures. *International Journal of Protective Structures* 7.3 (2016), pp. 340–366.
- [48] Osnes, K., Dey, S., Hopperstad, O. S., and Børvik, T. On the Dynamic Response of Laminated Glass Exposed to Impact Before Blast Loading. *Experimental Mechanics*, <http://doi.acm.org/10.1145/1671970.1921702>. (2019).
- [49] Hooper, P., Blackman, B., and Dear, J. The mechanical behaviour of poly (vinyl butyral) at different strain magnitudes and strain rates. *Journal of Materials Science* 47.8 (2012), pp. 3564–3576.
- [50] Zhang, X., Hao, H., Shi, Y., and Cui, J. The mechanical properties of Polyvinyl Butyral (PVB) at high strain rates. *Construction and building materials* 93 (2015), pp. 404–415.
- [51] Del Linz, P., Wang, Y., Hooper, P., Arora, H., Smith, D., Pascoe, L., Cormie, D., Blackman, B., and Dear, J. Determining material response for Polyvinyl Butyral (PVB) in blast loading situations. *Experimental Mechanics* 56.9 (2016), pp. 1501–1517.

- [52] Del Linz, P., Hooper, P. A., Arora, H., Wang, Y., Smith, D., Blackman, B. R., and Dear, J. P. Delamination properties of laminated glass windows subject to blast loading. *International Journal of Impact Engineering* 105 (2017), pp. 39–53.
- [53] Castori, G. and Speranzini, E. Structural analysis of failure behavior of laminated glass. *Composites Part B: Engineering* 125 (2017), pp. 89–99.
- [54] Serafinavičius, T., Lebet, J.-P., Louter, C., Lenkimas, T., and Kuranovas, A. Long-term laminated glass four point bending test with PVB, EVA and SG interlayers at different temperatures. *Procedia Engineering* 57 (2013), pp. 996–1004.
- [55] Franz, J and Schneider, J. Through-Cracked-Tensile tests with polyvinylbutyral (PVB) and different adhesion grades. *Engineered Transparency, International Conference at Glasstec, Düsseldorf, Germany*. 2014, pp. 135–142.
- [56] Samieian, M. A., Cormie, D., Smith, D., Wholey, W., Blackman, B. R., Dear, J. P., and Hooper, P. A. Temperature effects on laminated glass at high rate. *International Journal of Impact Engineering* 111 (2018), pp. 177–186.
- [57] *NS-EN 13541: Glass in building – Security Glazing – Testing and classification of resistance against explosion pressure*. Standard. CEN, 2012.
- [58] *NS-EN 13123-1: Windows, doors and shutters – Explosion resistance – Requirements and classification – Part 1: Shock tube*. Standard. CEN, 2001.
- [59] *NS-EN 13123-2: Windows, doors and shutters – Explosion resistance – Requirements and classification – Part 2: Range test*. Standard. CEN, 2004.
- [60] *NS-EN 13124-1: Windows, doors and shutters – Explosion resistance – Test method – Part 1: Shock tube*. Standard. CEN, 2001.
- [61] *NS-EN 13124-2: Windows, doors and shutters – Explosion resistance – Test method – Part 2: Range test*. Standard. CEN, 2004.
- [62] Holmen, J. K., Johnsen, J., Hopperstad, O. S., and Børvik, T. Influence of fragmentation on the capacity of aluminum alloy plates subjected to ballistic impact. *European Journal of Mechanics-A/Solids* 55 (2016), pp. 221–233.
- [63] *IMPETUS Afea Solver*. <http://www.impetus-afea.com/>. Accessed: 2019-03-18.
- [64] *eCorr User Manual*. <https://www.ntnu.edu/kt/ecorr>. Accessed: 2019-06-13.
- [65] Arnold, W and Rottenkolber, E. Fragment mass distribution of metal cased explosive charges. *International Journal of Impact Engineering* 35.12 (2008), pp. 1393–1398.
- [66] Grisaro, H. Y., Benamou, D., and Dancygier, A. N. Investigation of blast and fragmentation loading characteristics–Field tests. *Engineering Structures* 167 (2018), pp. 363–375.
- [67] Guo, Z. W., Huang, G. Y., Liu, C. M., and Feng, S. S. Velocity axial distribution of fragments from non-cylindrical symmetry explosive-filled casing. *International Journal of Impact Engineering* 118 (2018), pp. 1–10.
- [68] Bergström, J. and Boyce, M. Constitutive modeling of the time-dependent and cyclic loading of elastomers and application to soft biological tissues. *Mechanics of Materials* 33.9 (2001), pp. 523–530.

PART 1

Karoline Osnes, Tore Børvik, Odd Sture Hopperstad

Testing and modelling of annealed float glass under quasi-static and dynamic loading

Engineering Fracture Mechanics 201 (2018) 107-129.

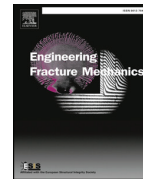
<https://doi.org/10.1016/j.engfracmech.2018.05.031>



Contents lists available at ScienceDirect

Engineering Fracture Mechanics

journal homepage: www.elsevier.com/locate/engfracmech



Testing and modelling of annealed float glass under quasi-static and dynamic loading



Karoline Osnes*, Tore Børvik, Odd Sture Hopperstad

Structural Impact Laboratory (SIMLab), Department of Structural Engineering, NTNU, Norwegian University of Science and Technology, NO-7491 Trondheim, Norway
Centre for Advanced Structural Analysis (CASA), NTNU, Norwegian University of Science and Technology, NO-7491 Trondheim, Norway

ARTICLE INFO

Keywords:

Glass
Brittle fracture
Probabilistics
Numerical simulation
Blast loading

ABSTRACT

In recent years, a considerable number of studies has been carried out to analyse the behaviour of laminated glass plates under blast loading by the use of the finite element method. This has proven to be quite challenging, as the response of the laminated glass is complex. The fracture strength of the glass layers govern much of the total response; however, a limited effort is often made to selecting this value in the analyses. The current work aims to identify the probabilistic fracture strength of the glass alone as a function of its geometry, boundary conditions and loading situation by the use of a newly proposed strength prediction model. It should be noted that the current study focuses on the initiation of fracture in glass plates, and no effort has been put into the description of crack propagation. To facilitate the validation of the model, three different experimental test series were carried out on annealed float glass. This included quasi-static four point bending tests on relatively small glass specimens, and quasi-static and blast pressure tests on larger glass plates. The experimental work demonstrated that the fracture strength of glass exhibits a large scatter within the same test setup. It also revealed that the fracture strength and its scatter were dependent on the geometry, and the boundary and loading conditions. The strength prediction model was able to successfully capture many of the trends observed in the quasi-static tests. Regarding the blast tests, the model was able to reproduce the experimental results reasonably well.

1. Introduction

Annealed float glass is widely used in window systems, but is a brittle material that offers little resistance to the intense blast waves produced by explosions. If the window fails, it breaks into numerous sharp fragments that can potentially cause major damage [1]. Laminated glass has been found to be effective at mitigating these risks and is now frequently used to increase the protection level by retaining the fragments on a polymer interlayer upon fracture. The polymer interlayer also provides additional resistance to the blast loading even after the glass layers have fractured [2–5]. Lately, much effort has been made to model laminated glass subjected to blast loading by the use of the Finite Element Method (FEM) [3–6]. This has proven to be challenging, as the behaviour of laminated glass is quite complex and dependent on many factors. These include the modelling of the supports, the material properties and failure criteria of both the glass and the polymer interlayer, and the delamination process between the glass and the polymer.

* Corresponding author at: Structural Impact Laboratory (SIMLab), Department of Structural Engineering, NTNU, Norwegian University of Science and Technology, NO-7491 Trondheim, Norway.

E-mail address: karoline.osnes@ntnu.no (K. Osnes).

<https://doi.org/10.1016/j.engfracmech.2018.05.031>

Received 17 November 2017; Received in revised form 7 May 2018; Accepted 19 May 2018

Available online 28 May 2018

0013-7944/ © 2018 Elsevier Ltd. All rights reserved.

Nomenclature			
α	in-plane flaw orientation	E	Young's modulus
δ	centre displacement in beam	F	applied load
η	distribution parameter	$f(\phi)$	angular flaw function
λ_s	surface flaw correction factor	F_f	failure load
μ	mean of the normal distribution	h	thickness
ν	Poisson's ratio	i_+	impulse of positive pressure phase
ϕ	angle of point on flaw	K_{IC}	fracture toughness
ρ	density	K_I	stress intensity factor for mode I loading
ρ_{flaw}	flaw density	L	length
σ	remote normal tensile stress	L_l	length of loading span
σ_n	in-plane normal stresses	L_s	length of support span
σ_x	normal stresses in x direction	N, c_i, w_i	normalized histogram parameters
σ_y	normal stresses in y direction	N_0	number of flaws on glass surface
σ_{fmax}	maximum tensile stress at failure	N_i	number of flaws with $a \geq a_i$
σ_{fmean}	mean tensile stress at failure	P_0	atmospheric pressure
σ_{fmin}	minimum tensile stress at failure	P_{max}	peak reflected overpressure
σ_f	tensile stress at failure	$P_{r,max}$	peak reflected pressure
τ	incubation time	$P_r(t)$	reflected pressure
τ_{xy}	in-plane shear stress	R	negative overpressure
a	flaw depth	Q	flaw shape parameter
a/c	flaw shape	R_1, R_2	random variable from 0 to 1
a_i	depth of flaw i	s	standard deviation of normal distribution
A_{jumbo}	area of jumbo plate	t	time
a_{max}	maximum flaw depth	t_a	arrival time of reflected pressure
b	decay coefficient	t_c	time of failure frame in model
c	flaw half-length	t_{frac}	time of fracture initiation
D_{max}	maximum centre displacement	w	width
		Y	geometric flaw shape factor

The identification of the glass plates' fracture strength is not straight forward, and is therefore frequently modelled as deterministic using a fixed fracture stress or strain [3,5]. This value is often based on a limited number of experimental tests, or simply adjusted to fit a representative experiment. It is widely known that the fracture strength of glass plates is probabilistic due to the presence of micro-structural surface flaws [7]. Fracture initiation in glass plates normally depends on the combination of the properties of the flaws and the applied normal stress. Consequently, the fracture may not occur at the point of maximum applied stress. Additionally, the glass strength will also be dependent on both the geometry of the plate and the boundary and loading conditions [8].

In most commercial Finite Element (FE) codes, the failure modelling is based on a deterministic approach. In other words, the given fracture strength applies to the entire glass plate. If this approach is to be used in a design process of glass, the fracture strength must be carefully chosen. It would naturally be advantageous to know the likelihood of the fracture strength specified in the FE model. The current study aims to obtain the probabilistic fracture strength of any glass plate as a function of its geometry, confinement and loading. This will hopefully make the identification of the fracture strength in an FE model more attainable. Note that no effort has been made to model the crack propagation in this work, and the modelling applies only to the initial fracture strength.

Traditionally, the probabilistic strength of brittle materials is described by the Weibull distribution [9], which requires calibration from experimental data. However, Nurhuda et al. [10] found that experimental tests involving glass plates with different test setups lead to different Weibull parameters. This suggests that the Weibull parameters are not material constants, but are dependent on both the dimension and the loading conditions of the glass specimens. Nevertheless, effort has been made to re-scale these parameters to fit different experiments than the ones from which the parameters were extracted, as in the work by Przybilla et al. [11]. The method proved suitable to convert the fracture stress distribution from a four-point to a three-point bending test series. The potential shortcoming is, however, the need for experimental tests with a sufficiently large population. Otherwise, an accurate description of the statistical distribution is not possible.

Recently, a strength prediction model of annealed glass plates was proposed by Yankelevsky [12], which aims to predict the glass strength without the need of material tests. The model is based on the existence of microscopic surface flaws in glass, and uses Monte Carlo simulations to determine the fracture strength for glass plates under certain loading conditions. It can also predict the origin of failure, and captures that this does not necessarily occur at the point of maximum applied stress. The resulting fracture strength provided by the model showed good correspondence with experimental four-point bending tests. In a further development of the model [13], both fracture strength and origin of fracture proved to be well predicted, when compared to a larger series of four-point bending tests.

The current work proposes a further development of this approach, and includes additional features and adjustments to the original model. In addition, experimental tests on annealed float glass have been carried out to facilitate validation of the strength prediction model. This includes quasi-static four-point bending tests on relatively small glass specimens, and quasi-static and dynamic

lateral pressure tests on larger glass plates. The dynamic pressure tests involve subjecting the glass plates to a blast pressure in the SIMLab Shock Tube Facility (SSTF) [14], while the quasi-static pressure tests employ a slowly increasing water pressure. The experimental work shows that the fracture strength of glass depends on both size and loading condition, and has a great variation within the same test setup.

2. Experimental study

2.1. Material

2.1.1. Glass

The glass plates and specimens used in the experimental work are made out of clear soda-lime-silica glass, which has gone through an annealing process. The mechanical properties of glass are dominated by brittle behaviour and glass behaves elastically to the point of failure. Due to the lack of plastic flow in glass, the energy absorption during crack propagation is small compared to e.g. metals [15]. Consequently, fracture in glass typically propagates fast with little chance of crack arrest. The theoretical strength of glass is much larger than its true strength, to which microscopic surface flaws are responsible. The existence of these microscopic flaws causes the material to fail normally in tension, and is also the reason for glass' stochastic fracture strength [8]. Table 1 presents some commonly employed material parameters for soda-lime-silica glass, which are used as nominal values in this work. The fracture toughness K_{IC} relates to the critical stress intensity factor for mode I loading. The stated value is reported in [16], and is based on the work by Wiederhorn [15].

2.1.2. Rubber

In the shock tube tests presented later in this study, Neoprene rubber strips with an International Rubber Hardness Degree (IRHD) of 50 ± 10 were placed on each side of the glass. Both the hardness and dimensions of the rubber strips were chosen based on test methods described in the European Standard for testing of security glazing subjected to blast pressure [18]. In order to recreate the shock tube tests by means of FEM (see Section 4.2), the boundary conditions had to be modelled with sufficient accuracy. Therefore, a series of compression tests was performed on the rubber to retrieve material data. Cylindrical specimens with 6 mm diameter and 4 mm height were tested at three different machine speeds. The tests were carried out in an Instron 5944 testing machine with a 2 kN load cell. Two cameras with a recording rate of 5 Hz were used to obtain the longitudinal and transverse deformation by the use of an in-house tracking algorithm in MATLAB.

The results for a selection of compression tests are presented in Fig. 1, which shows the true stress versus logarithmic strain for the three different loading rates. An incompressible material was assumed. Although the rates achieved in the shock tube tests could be higher than the ones presented here, a rate-insensitive and linear-elastic behaviour was later assumed for sufficiently small strains. A linear curve fit yields an initial stiffness of ~ 2 MPa.

2.2. Quasi-static four-point bending tests

Since fracture in annealed float glass is a stochastic process, quasi-static four-point bending tests were employed in order to investigate the scatter in material strength. Specimens of three different sizes were tested, and the nominal dimensions can be found in Table 2. The largest deviations from the values stated are 0.4%, 1.0% and -1.8% for the length, width and thickness, respectively. A nominal strain rate of $7 \times 10^{-5} \text{ s}^{-1}$ was achieved during testing for all specimen sizes. The specimens were cut with a glass cutter by the manufacturer, and the edges were not treated. In all of the tests, the most damaged edges, i.e., the scoring edges, were placed upwards in order to minimize failure at the edges.

Fig. 2 shows a schematic of the four-point bending tests. The setup is based on the ASTM standard C1161-13 [19], which is originally intended for testing of advanced ceramics. An Instron 5985 testing machine with a 5 kN load cell was used to load the specimens to failure, while an optoNCDT 2310-50 laser was used to measure the centre point displacement of the glass. Both the support and the loading cylinders were held in place by rubber bands. The cylinders were made out of high strength steel.

After failure of the specimens, the glass fragments were assembled in order to locate where failure initiated. The results for the specimens where failure started at the edges were excluded, as edge effects were not considered in this study. For studies concerning the edge flaws of glass specimens, we refer to the work of e.g. Lindqvist [20]. Fig. 3 shows two assembled specimens of medium size after failure; the specimen in Fig. 3a failed at the edge and the specimen in Fig. 3b, at the face. All edge-failed specimens were identified by crack branching from a point located at the edge, as seen in Fig. 3a. A total of 31 specimens of each size were tested, and 20, 21 and 30 tests were recognized as valid for the small, medium and large specimens, respectively. It was observed that the edge-failed specimens had a lower strength than the rest, with a reduction in mean failure load of 46.2%, 33.1% and 42.3% for the small, medium and large specimens, respectively.

Table 1
Material parameters for soda-lime-silica glass.

Density ρ (kg/m ³)	Young's modulus E (MPa)	Poisson's ratio ν	Fracture toughness K_{IC} (MPa $\sqrt{\text{m}}$)
2500 [17]	70000 [17]	0.2 [17]	0.75 [16]

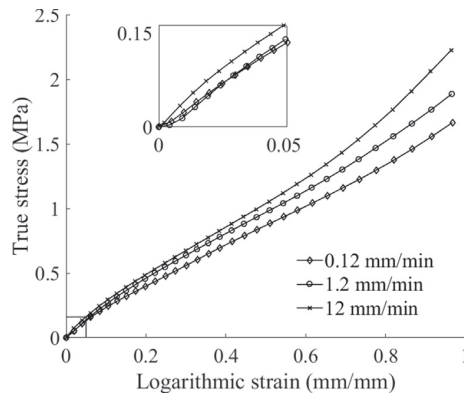


Fig. 1. True stress versus logarithmic strain curves for Neoprene rubber at three different machine rates.

Table 2
Nominal dimensions of specimens undergoing four-point bending.

Specimen	Length L (mm)	Support span L_s (mm)	Loading span L_l (mm)	Width w (mm)	Thickness h (mm)
Large	300	280	140	60	4
Medium	200	180	90	40	4
Small	100	80	40	20	4

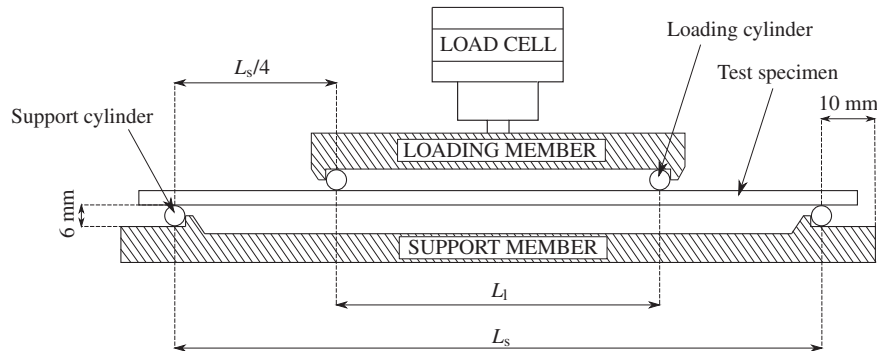


Fig. 2. Setup of the four-point bending tests.



Fig. 3. Typical glass specimens after failure in four-point bending tests: (a) failure at the edge and (b) failure at the face.

Fig. 4 shows histograms of the applied force at failure for the valid bending tests. The ordinate value refers to the probability density, i.e., a normalized occurrence calculated by $c_i/(Nw_i)$, where c_i is the number of elements in the bin, N is the total number of elements and w_i is the width of the bin. For a more attainable comparison of the fracture strength of the three specimen sizes, the maximum tensile stresses at failure, σ_f , were calculated from beam theory as

$$\sigma_f = \frac{3F_f L_s}{4wh^2} \tag{1}$$

where F_f is the failure load, L_s is the support span, w is the width and h is the thickness of the specimen. This results in multiplying the resulting failure load with the factor 0.22 mm^{-2} , 0.21 mm^{-2} and 0.19 mm^{-2} for the large, medium and small specimens, respectively. The extreme and mean values for the tensile stresses are presented in Table 3.

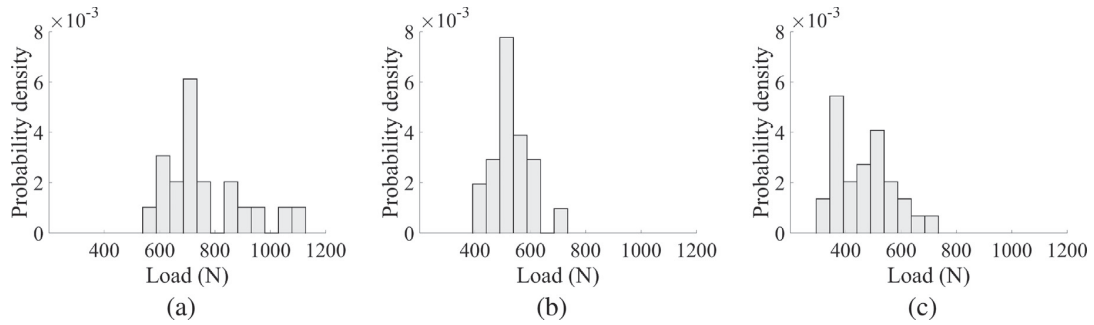


Fig. 4. The probability density distribution of the applied load at failure for (a) small (b) medium and (c) large specimens.

Table 3

Calculated tensile stresses from beam theory for small, medium and large specimens in the four-point bending tests (MPa).

	Small	Medium	Large
σ_{fmin}	110.8	86.39	67.70
σ_{fmean}	145.2	111.2	103.4
σ_{fmax}	207.2	144.7	153.8

Naturally, as the number of tests is rather limited, few definite conclusions can be made about the glass strength from the performed bending tests. However, one trend seems to apply, i.e., an increase in material strength with a decrease in surface area.

The bending tests also provided information about the stiffness of the tested glass material. Again from beam theory, Young’s modulus E can be calculated as

$$E = \frac{11FL_s^3}{64\delta wh^3} \tag{2}$$

where δ is the centre point displacement related to the applied load F . A mean value of 69.4 GPa was found, which is close to the nominal value stated in Table 1.

2.3. Blast loading

An illustration of an idealized reflected pressure-time history for a structure subjected to a blast wave is shown in Fig. 5. The pressure rises abruptly from atmospheric pressure P_0 to the peak reflected pressure $P_{r,max}$ at the arrival time t_a over a rise time close to zero. The pressure then decays to the atmospheric pressure P_0 over a duration t_{d+} , and further to a negative overpressure P_s and back again to P_0 over a duration t_{d-} . The first pressure phase is referred to as the positive phase, and the last as the negative phase. In the blast tests presented in this study, neither of the glass plates failed during the negative phase. Therefore, the time-window of interest is here limited to the positive phase of the reflected pressure. The positive phase is typically described by the modified Friedlander equation stated as [21]

$$P_r(t) = P_0 + P_{r,max} \left(1 - \frac{t-t_a}{t_{d+}} \right) \exp \left(\frac{-b(t-t_a)}{t_{d+}} \right), \quad t_a < t < t_a + t_{d+} \tag{3}$$

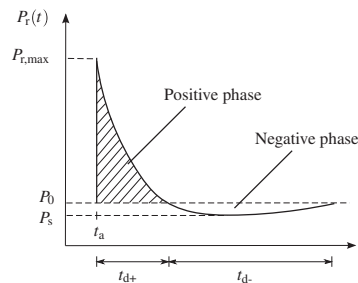


Fig. 5. Idealized pressure time history for the reflected blast wave from an explosion [21].

where b is the decay coefficient responsible for the curvature from maximum reflected pressure $P_{r,max}$. Typical expressions used to describe the negative phase of the blast wave can be found in Aune et al. [22]. The Friedlander equation will be used to describe the blast loads obtained in this study.

2.4. SIMLab shock tube facility

The SIMLab Shock Tube Facility (SSTF) was used to subject annealed glass plates to blast loading. The SSTF has proven to be a reliable alternative to explosive detonations, and enables a planar pressure loading to plated specimens. A detailed description of the SSTF and its performance can be found in [14]; however, a short description is given herein for completeness.

The purpose of the SSTF is to subject specimens to a pressure history similar to that from a far-field blast event within a controlled laboratory environment. The SSTF consists of a high-pressure chamber (called driver section), and a low-pressure chamber (denoted driven section). The driver and driven sections are separated by one or several diaphragms, which rupture when their capacity is reached. A high air pressure is built up in the driver section, and when the diaphragms fail, a series of pressure waves will run down the driven section and eventually take the form of a characteristic blast wave. When the blast wave reaches the specimen mounted at the rear end, it is reflected, and the reflected overpressure represents the pressure loading of the specimen. The intensity of the pressure load increases with both the build-up pressure and the volume of the driver section. Possible fragments from the specimen after loading and fracture are confined in a dump tank at the end of the driven section. A sketch of the SSTF and the general experimental setup is shown in Fig. 6. For the experiments presented in this study, the shortest driver length of 0.27 m was used in order to subject the glass plates to a sufficiently low pressure. The dump tank at the end of the driven section was closed during the experiments, and two Phantom v1610 high-speed cameras with a recording rate of 24 kHz were placed outside to film through the windows of the tank. To estimate the reflected pressure on the tested glass plates, two piezoelectric pressure sensors were placed 245 mm and 345 mm upstream the plate (see Fig. 6a). By assuming constant velocity of the blast wave between the furthest sensor and the plate, the reflected pressure could be determined [14]. The pressure measurements were logged with a frequency of both 500 kHz and 24 kHz. The latter was done in order to synchronize the cameras and the pressure measurements.

A custom-made fastening system was developed for tests on glass plates in the SSTF, as illustrated in Fig. 7. The glass plate is clamped between two 25 mm thick aluminium frames, denoted the inner and outer clamping frame. Neoprene rubber strips with a thickness of 4 mm and a width of 50 mm are glued to the clamping frames and positioned between the glass plate and the aluminium. The tested glass has in-plane dimensions of 400 mm × 400 mm, while the loaded area is 300 mm × 300 mm. The inner clamping frame is fastened to the end of the shock tube, while the outer frame is fastened with 12 equidistant M24 bolts through Ø25 mm holes

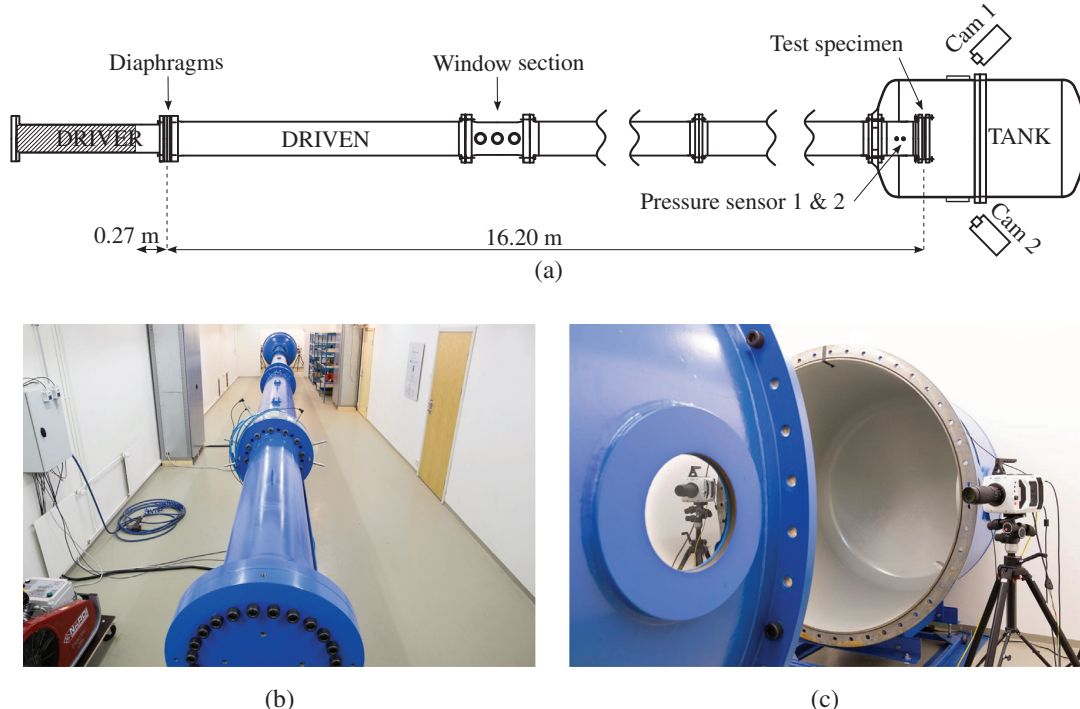


Fig. 6. Test setup in the SIMLab Shock Tube Facility (SSTF) [14]: (a) sketch of the shock tube seen from above, (b) the shock tube seen from the driver, (c) high speed cameras on each side of the tank.

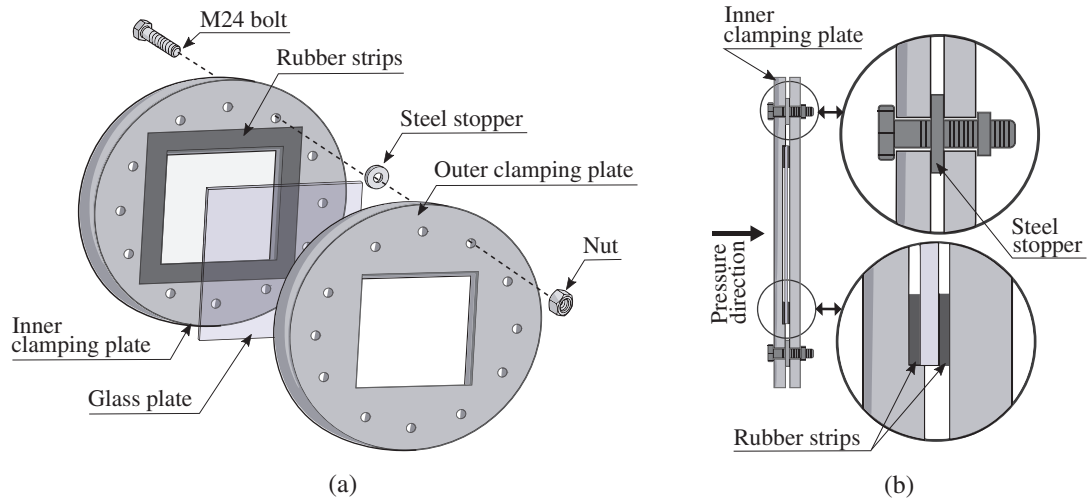


Fig. 7. The custom-made fastening system used in the blast experiments on glass in the SSTF: (a) disassembled setup showing one out of 12 bolts, stoppers and nuts, (b) assembled section observed from the side.

in both frames. For the tests on (3.8 mm thick) float glass, 6.6 mm thick steel washers, or stoppers, are used between the clamping frames in order to minimize the motion of the outer clamping frame during the tests by properly fasten it, while limiting the clamping pressure on the glass. The steel stoppers are threaded on the bolts, and have an outer diameter of 43 mm. Additionally, a part of the inner clamping frame was milled out to facilitate the setup, and is about 5.7 mm deep.

In the European Standard for testing of security glazing subjected to blast pressure [18], it is stated that a clamping pressure of $14 \pm 3 \text{ N/cm}^2$ should be applied. The thickness of the steel stoppers was chosen on the basis of this pressure, as the thickness governed the contraction of the rubber, and further the clamping pressure. To obtain this pressure exactly proved, however, to be challenging due to small variations in the thickness of the glass plates, rubber strips and clamping frames. Nevertheless, the steel stoppers offered proper tightening of the bolts during the tests without damaging the glass plate.

2.5. DIC measurements

In the shock tube tests, three-dimensional Digital Image Correlation (3D-DIC) was used to obtain the displacement of the glass plates as well as possible movements of the outer clamping frame. Checkerboard stickers with dimension $12 \text{ mm} \times 12 \text{ mm}$ were glued to the frame, and white circles with a central black dot, denoted optical targets, were spray-painted on the glass, see Fig. 8a. A point-tracking algorithm available in the in-house DIC code eCorr [23] was employed to track the optical targets utilizing photos recorded

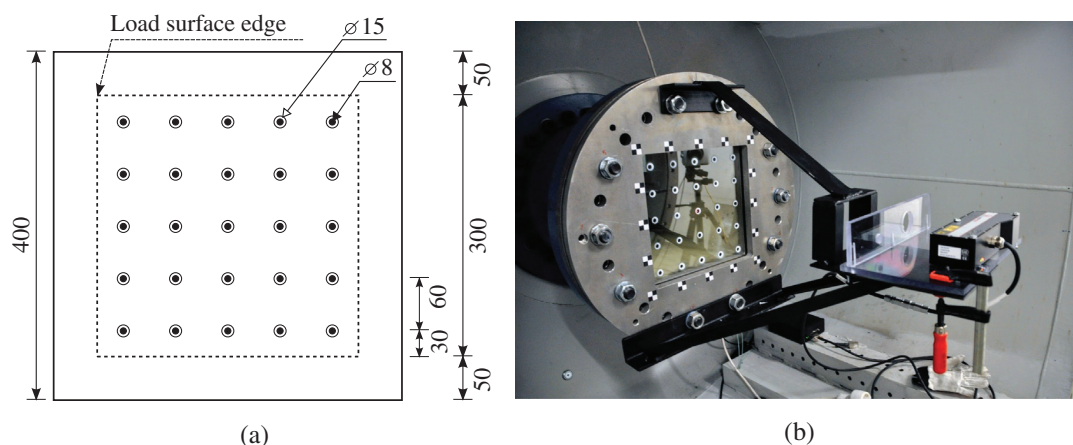


Fig. 8. Test setup for investigation of the point-tracking procedure: (a) optical targets used for point tracking of the glass (dimensions given in mm), (b) laser mounted to the end of the shock tube.

by the high-speed cameras in the tests. Optimally, a speckle pattern would be painted onto the glass to obtain a complete displacement field from 3D-DIC instead of point-based displacements. However, this would reduce the visibility of the fracture initiation and propagation in the glass during the tests. An evaluation of the point-tracking procedure was conducted in a preliminary study. A laser displacement sensor (optoNCDT 2310-50) was fastened to the outer clamping frame, as shown in Fig. 8b, and used to measure the displacement in the middle of the glass plate. The same measurement was done by the use of point tracking. Additionally, the movement of the clamping frame was tracked at the checkerboard stickers, also by point tracking. As the laser was mounted to the clamping frame, the middle point displacement obtained by point tracking was corrected for the displacement of the frame. Fig. 9 compares the two resulting displacements for a test where the glass did not fracture, and shows that the measurements are in good agreement. Some oscillations are present in the laser data due to vibrations in the laser mount. The results demonstrate that the point-tracking procedure yields reliable displacement data.

2.6. Blast tests

Twelve blast tests were performed in the SSTF on 400 mm × 400 mm float glass plates with a thickness of 3.8 mm (mean = 3.805 mm, SSD = 0.01 mm). The glass plates and the four-point bending specimens were delivered by the same glass manufacturer. Note that there is a small difference in the mean thickness of the four-point bending specimens and the current glass plates. Table 4 presents maximum reflected overpressure P_{\max} , time of fracture initiation t_{frac} , maximum centre displacement before fracture D_{\max} , maximum fragment velocity v_{frag} , impulse of the positive phase i_+ , and position of fracture initiation. Note that for the failed plates, the positive impulse i_+ was calculated only up until the point of fracture. The tests are divided into three classes (A, B and C), depending on the level of maximum reflected overpressure on the glass. The reflected overpressure was found by employing the logged pressure in the two sensors placed 245 and 345 mm from the plate, denoted sensor 01 and 02, respectively. The Friedlander equation (Eq. (3)) was fitted to the pressure data for the non-failed plates, see Fig. 10a, and a linear fit up to the time of failure was used for the failed plates, see Fig. 10b. Shortly after a glass plate failed in the tests, there was no longer a surface to reflect the pressure wave, and a Friedlander curve fit would not be applicable.

The fragment velocities were calculated based on the measured displacements from the point-tracking procedure. This required that the painted white and black circles were still trackable, which was not always the case. Therefore, these values are somewhat uncertain. In 10 out of 12 tests, the glass plate failed, and for most of the plates, failure initiated at the boundary. More specifically, it initiated under the rubber strips, see Fig. 11 for an example. The fracture sequences were similar for all boundary-failed plates, with circumferential crack formations in the corners, and subsequent propagation from the corners to the face. The latter is visualized in Fig. 11b–c. For comparison, photos from a test where failure initiated at the face of the plate is shown in Fig. 12. In these tests, cracks branched from the point of fracture initiation towards the edges, before circumferential cracks were formed. Note that the accuracy of the specified times is 1/24 ms due to the photo frequency.

2.7. Quasi-static pressure tests

It was also of interest to investigate the capacity of the glass plates exposed to uniform pressure without the effect of strain rate and inertia. This was done with the use of water pressure, which was slowly built up in a steel chamber with an opening on one side, see Fig. 13a. The test setup has many similar features as in the SSTF, including the same type and dimensions of the glass plates, the same loading area, the same dimensions and type of rubber strips, and threading of steel stoppers on bolts fastening the clamping plate. In this case, as for the SSTF, the steel stoppers were used to control the clamping pressure. The thickness of the steel stoppers was here 11.7 mm due to the design of the steel chamber. After tightening of the bolts, the weight of the steel clamping plate (11.1 kg) is transferred to both the stoppers and the bottom rubber strips. The point-tracking procedure was enabled in the tests by using two AVT Prosilica GC2450 cameras and the optical targets on the glass, see Fig. 13b. The pressure and camera recordings were synchronized, and logged with a rate of 15 Hz. The chamber was filled with water using a hand driven water pump to build up the pressure sufficiently slowly. A total of 11 glass plates were tested, and the resulting pressure-time history for one of these tests (Q-09) is shown in Fig. 14a. The oscillations in the pressure are due to the non-continuous filling of water and the fact that the chamber was not completely airtight. A dotted curve plot presenting the pressure-displacement history for the same test is presented in Fig. 14b.

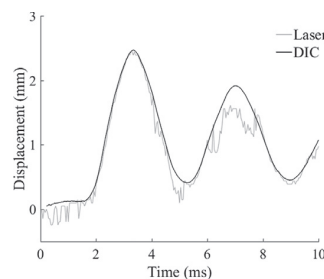
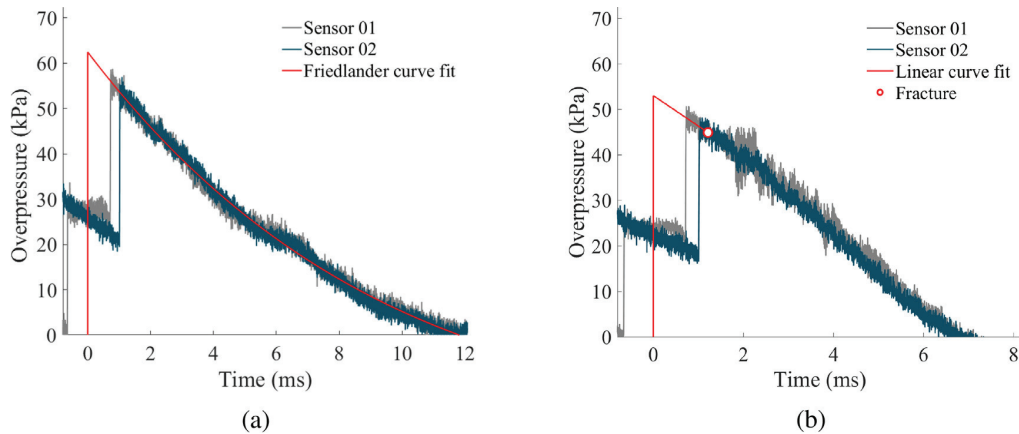


Fig. 9. Evaluation of the point-tracking procedure used to measure the mid-point displacement.

Table 4Summary of the blast tests on float glass for three classes of loads. Note that $t = 0$ corresponds to the time of arrival t_a of the blast wave.

Test	P_{\max} (kPa)	t_{frac} (ms)	D_{\max} (mm)	v_{frag} (m/s)	i_+ (kPa·ms)	Fracture initiation
A-01	53.0	1.21	4.52	15.8	59.2	Boundary
A-02	51.6	1.38	5.06	14.7	64.9	Boundary
B-01	63.7	0.88	3.23	24.5	52.5	Face, centre
B-02	64.6	1.25	5.40	18.8	73.2	Boundary
B-03	65.5	1.46	5.64	17.3	86.2	Boundary
B-04	62.5	×	5.44	×	293.9	No fracture
B-05	63.3	1.00	4.29	21.8	58.4	Face, above centre
B-06	62.9	0.92	3.68	19.3	54.1	Boundary
B-07	64.0	1.33	5.77	19.0	76.6	Boundary
B-08	62.9	×	5.96	×	294.2	No fracture
C-01	73.4	1.29	5.89	21.5	86.5	Boundary
C-02	73.2	1.33	6.48	22.3	88.9	Boundary

**Fig. 10.** Pressure measurements in two sensors close to the glass plate, including a representation of the reflected overpressure: (a) Friedlander curve fit for test B-04, (b) linear curve fit for test A-01.

The displacement corresponds to the upwards movement of the optical target in the middle of the plate. Selected photos from the test are further shown in Fig. 15. The capacity of each glass plate in terms of maximum applied pressure and mid-point displacement, denoted P_{\max} and D_{\max} , respectively, is listed in Table 5. Whether failure initiated at the face or boundary is also stated in this table. It is clear that the tested glass plates possessed a large scatter in fracture strength, as the strongest glass plate had more than twice the capacity of the weakest.

3. Modelling

3.1. Strength prediction model

A stochastic model for predicting the fracture strength of glass plates was recently proposed by Yankelevsky [12]. The strength prediction model presented here is based on this model, where some additional features and adjustments have been included. As for the model by Yankelevsky, stress corrosion and subcritical crack growth [24] are not considered in this study.

3.1.1. Background

Failure in glass is largely driven by the propagation of pre-existing microscopic flaws on the surface. These flaws, also denoted cracks, occur over the entire glass surface and the properties of each individual flaw will vary. The flaw characteristics on a glass surface will also vary from plate to plate. The fracture strength will consequently not be equal for every glass plate, and must therefore be described by a probability function. Moreover, the probability function will depend on the loading conditions and the size of the glass.

When tensile stresses are applied to the glass, and are normal to the flaws, the flaws will open and grow when the stresses are greater than a given threshold. Consequently, glass nearly always fails due to tensile stresses [8]. Because of this, it is natural to adopt the following failure criterion for glass [25]

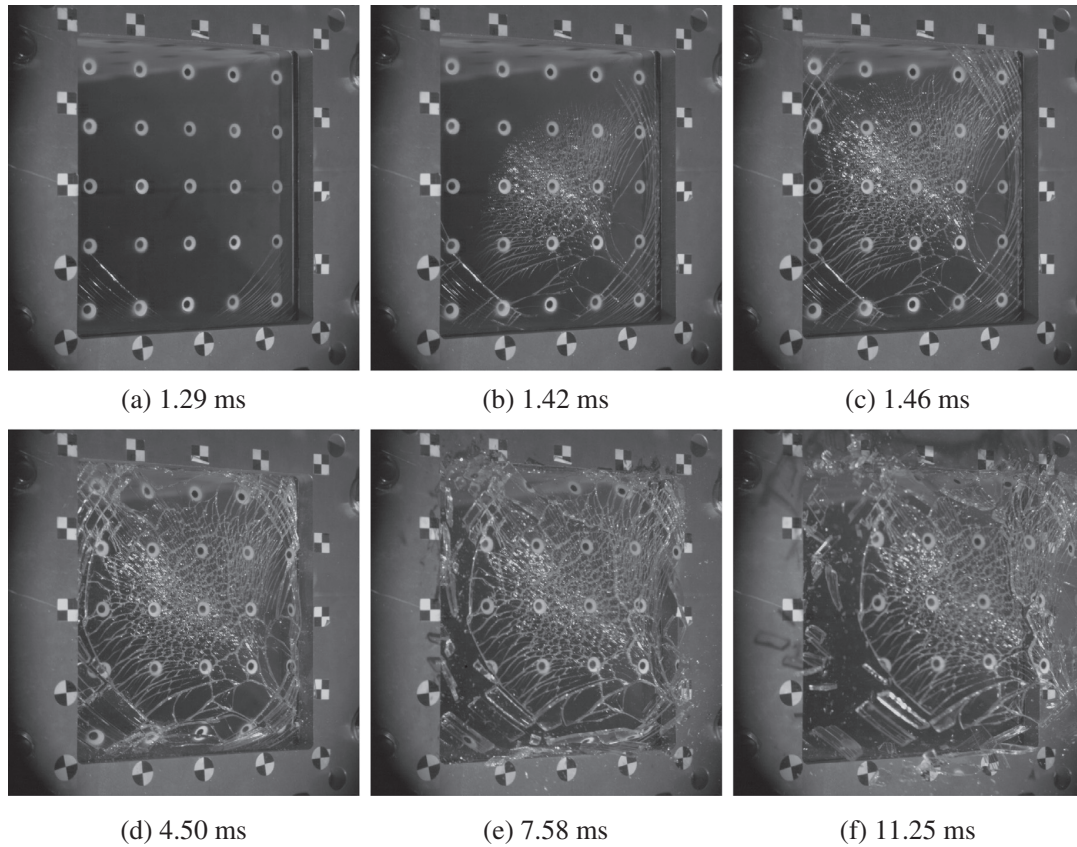


Fig. 11. Recorded photos in test A-01 captured at various points in time (see subcaptions) after t_a .

$$K_I = K_{IC} \quad (4)$$

where K_{IC} is the fracture toughness for mode I loading, i.e., the opening of a crack. K_I is the stress intensity factor for mode I loading, and is used to describe the stress state near the crack tip [26]. It is given by

$$K_I = Y\sigma\sqrt{\pi a} \quad (5)$$

where Y is a geometric factor which depends on the shape of the crack, and σ is the remote tensile stress normal to the crack. For a surface crack, a refers to the depth of the crack, as opposed to an embedded crack where a is the length. For an elliptic surface crack (see Fig. 16a) where the crack is small compared to the plate dimensions, Y can be calculated by the empirical expression [27]

$$Y = \frac{\lambda_s f(\phi)}{\sqrt{Q}}, \quad \lambda_s = \left[1.13 - 0.09 \left(\frac{a}{c} \right) \right] [1 + 0.1(1 - \sin\phi)^2]$$

$$Q = 1 + 1.464 \left(\frac{a}{c} \right)^{1.65}, \quad f(\phi) = \left[\sin^2(\phi) + \left(\frac{a}{c} \right)^2 \cos^2(\phi) \right]^{\frac{1}{4}} \quad (6)$$

where c is the half-length of the crack, λ_s is the surface correction factor, Q is the flaw shape parameter and $f(\phi)$ is an angular function depending on ϕ . The parameter ϕ defines the angle of a point on the elliptic crack, see Fig. 16b. Note that Eq. (4) expresses local failure, i.e., the onset of unstable crack growth in one flaw. In the strength prediction model, it is assumed that achieving failure in a single flaw is sufficient to induce failure in the entire glass plate. Since the chance of crack arrest in glass is very small, this is a fair assumption.

For a given loading scenario and geometry of a glass plate, the stress state before failure can be obtained by a finite element analysis. This, together with a small number of selected parameters, will be the input of the strength prediction model. Subsequently, the model simulates the flaw map, i.e., the distribution of surface flaws including their size, shape, location and orientation. Then, a Monte Carlo simulation is run, varying the flaw map, to establish the statistical strength probability. In the following, the various parts of the flaw map are discussed.

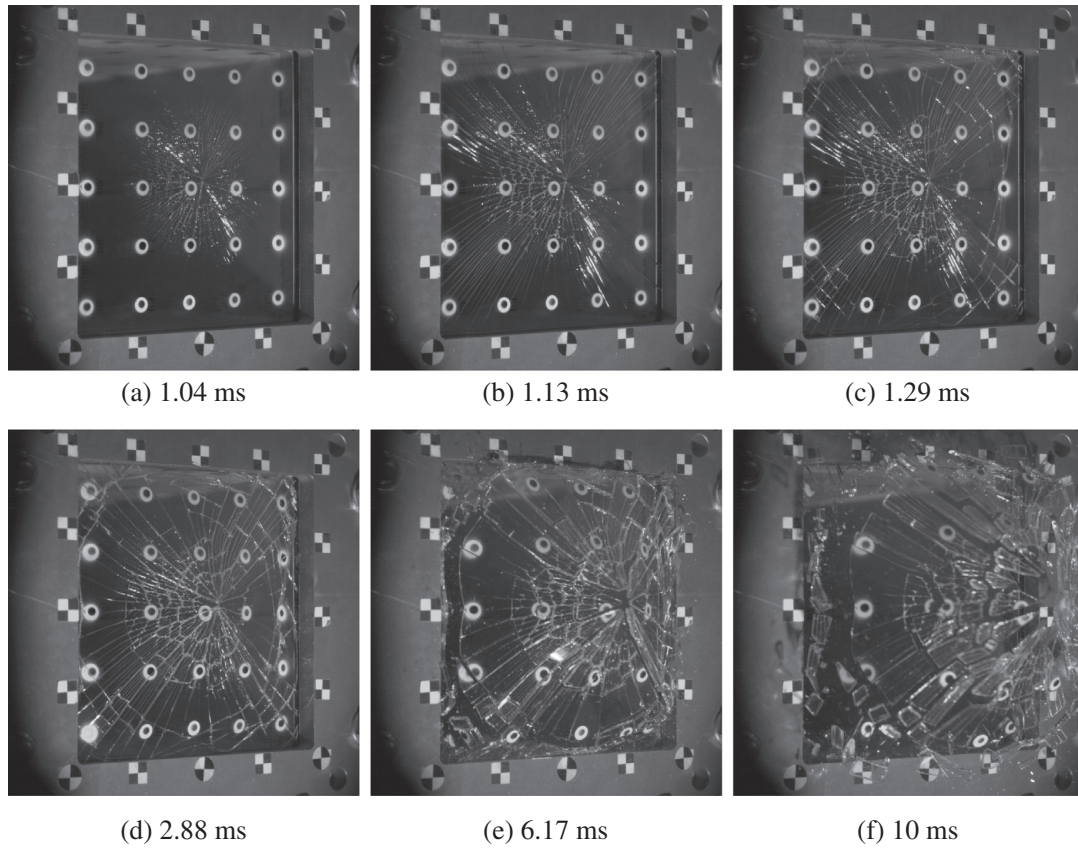


Fig. 12. Recorded photos in test B-01 captured at various points in time (see subcaptions) after t_a .

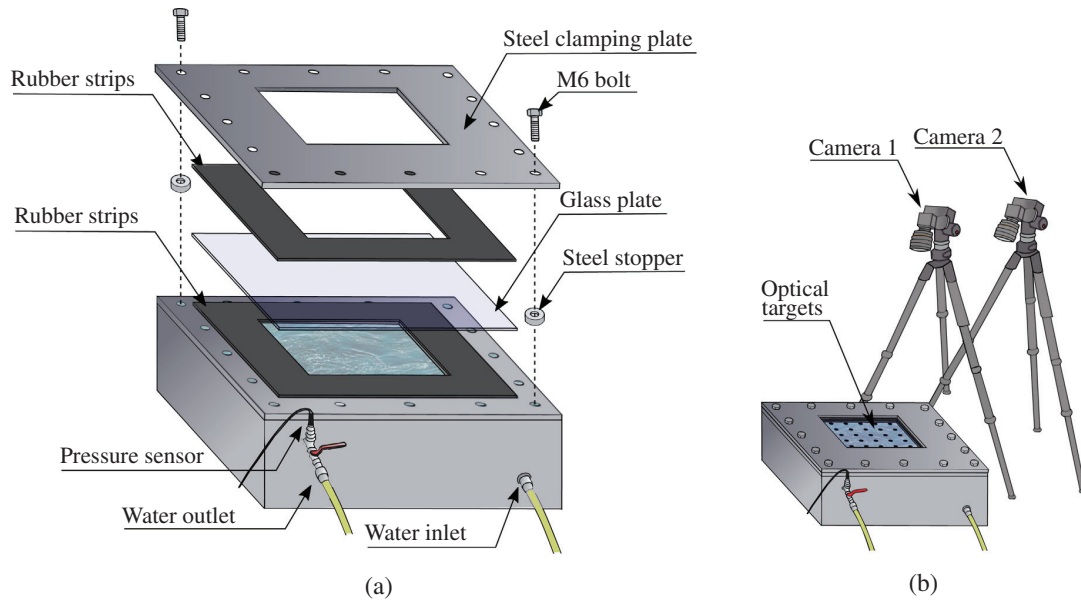


Fig. 13. Setup for quasi-static pressure tests: (a) assembly of water pressure chamber, (b) equipment for use of 3D-DIC.

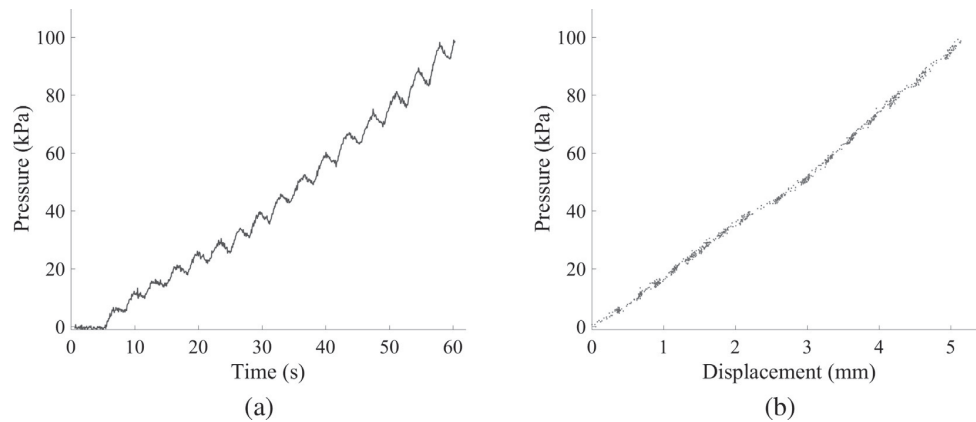


Fig. 14. Measurements from quasi-static pressure test Q-09: (a) pressure versus time, (b) pressure versus mid-point displacement.

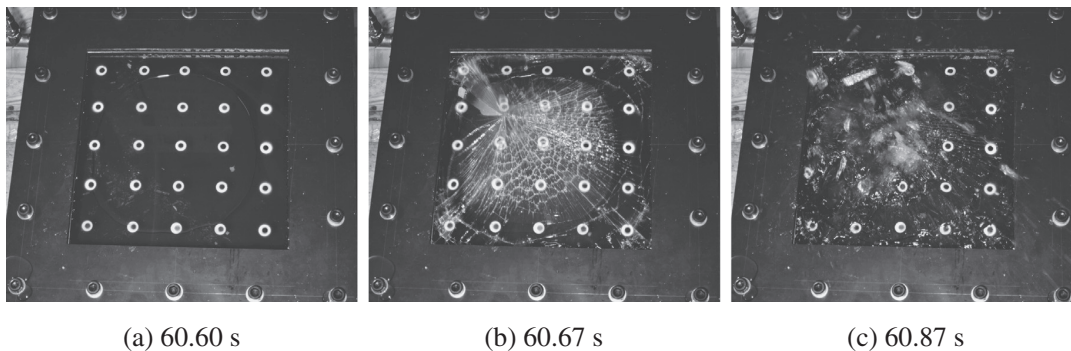


Fig. 15. Recorded photos in quasi-static pressure test Q-09 captured at various points in time (see subcaptions).

Table 5
Summary of results from the quasi-static pressure tests.

Test	P_{\max} (kPa)	D_{\max} (mm)	Fracture initiation
Q-01	96.9	5.19	Boundary
Q-02	66.5	3.64	Face, above centre
Q-03	65.2	3.54	Boundary
Q-04	48.4	2.69	Face, centre
Q-05	52.5	3.03	Boundary
Q-06	62.4	3.70	Face, below centre
Q-07	61.1	3.53	Face, left for centre
Q-08	83.6	4.62	Boundary
Q-09	98.9	5.19	Face, left and above centre
Q-10	83.8	4.67	Boundary
Q-11	62.3	3.72	Face, above centre

3.1.2. Flaw shape

In order to calculate the stress intensity factor K_I at each flaw on the glass surface, the shape of the flaws is required. In the strength prediction model, all flaws are idealized as elliptic, although in reality many may be irregularly shaped. It is further assumed that all cracks have a length-depth-ratio $a/c = 1$. The latter is supported by the work of Levenood [28], which studied the relationship between the fracture strength, the depth of the mirrored region¹ and the depth of the critical flaw in 80 glass specimens. Based on Levenood's results, we obtained the following averaged relationship: $\sigma_f \sqrt{a} = 0.577 \text{ MPa}\sqrt{\text{m}}$, where σ_f is the normal stress at failure. The maximum geometric factor Y calculated from Eq. (6) for flaws with $a/c = 1$, is equal to 0.729. The resulting critical stress intensity factor K_{IC} is thus

¹ The mirrored region is a smooth semi-circular area which forms during glass breakage normal to the applied stress and around the fracture induced surface flaw.

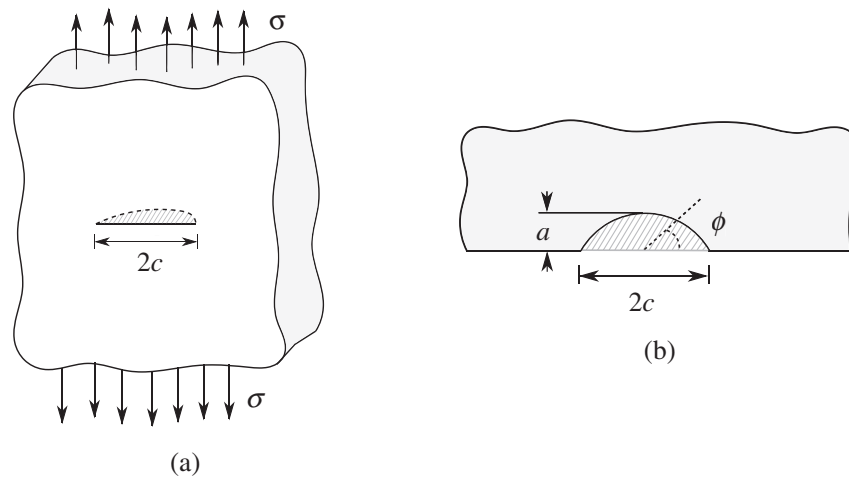


Fig. 16. (a) Elliptic surface crack in an infinitely large plate subjected to a remote stress σ . The dashed line refers to the outer edge of the crack placed inside the plate. (b) Section of the plate with denoted crack dimensions. Adapted from [25].

Table 6

Flaw characteristics identified for glass in the work by Wereszczak et al. [29].

Cutting procedure	Side	Density (flaws/cm ²)	Maximum flaw length (μm)
Scored and bent	Air	2.60	133
	Tin	2.37	162
Water jet	Air	1.18	105
	Tin	1.36	195

$$K_{IC} = Y\sigma_f\sqrt{a\pi} = 0.729 \cdot 0.577 \cdot \sqrt{\pi} = 0.746 \text{MPa}\sqrt{\text{m}}$$

which is identical to the value given in Table 1.

3.1.3. Flaw length and density

Yankelevsky [12] assumed that the maximum flaw length typically lies between 100 and 300 μm for standard soda lime glass, and considered 200 μm to be representative. To justify this assumption, the work by Wereszczak et al. [29] was highlighted. This work includes classification of both the density of the surface flaws and the maximum flaw for two soda lime glasses cut by two different procedures. The results are summarized in Table 6, and indicate that both the density and the maximum flaw length depend on the cutting procedure and whether measurements are done on the tin or the air side². The tin side of the glasses exhibited somewhat larger flaws than the air side, however, the number of flaws did not favour any of the sides. Moreover, the density of flaws was noticeably larger for the scored and bent plate. Whether this holds in general is uncertain.

It is assumed in the strength model that the flaws are distributed evenly over the glass surface. By using the maximum flaw and density presented in Table 6, and by assuming a uniform positioning, the distance between the flaws is much larger than the dimension of single flaws. This in turn leads to a flaw map with non-interacting cracks [25].

3.1.4. Flaw size distribution

In the work presented by Levengood [28], it was observed that specimens failing for small stresses were the least occurring. This indicates that glass plates exhibit a larger amount of small flaws than large ones. A possible way to describe this tendency, is to employ the distribution function [12]

$$\frac{N_i}{N_0} = \exp\left(\frac{-a_i}{\eta}\right) \quad (7)$$

where N_0 is the total number of flaws on a glass surface, a_i is the depth of a given flaw, N_i is the number of flaws that have depths larger or equal to a_i , and η is a distribution parameter.

² Window glasses of today typically have a tin side and an air side, because one side faces a tin bath through the floating process.

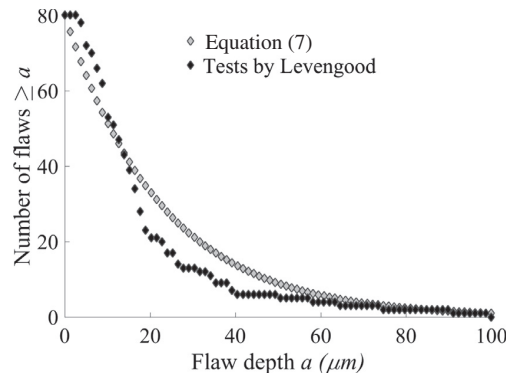


Fig. 17. Flaw size distribution governed by Eq. (7) versus tests by Levengood [28].

The majority of glass used for windows are cut from so-called jumbo plates with nominal lengths of 4500, 5100 or 6000 mm, and widths equal to 3210 mm [30]. It is assumed that there exists only one flaw of maximum size in each of the surfaces of the jumbo plates. N_0 thus becomes the total number of flaws on a jumbo plate surface, and η is given by the following expression

$$\eta = \frac{a_{\max}}{\ln(N_0)} \quad (8)$$

The fracture stresses recorded by Levengood ranged from 57.71 to 351.67 MPa. By employing the relationship $\sigma_f \sqrt{a} = 0.577 \text{ MPa}\sqrt{\text{m}}$, this corresponds to flaw depths from 2.69 to 99.67 μm . In Fig. 17, the flaw depth density defined by Eq. (7) is compared to the experimental results from [28]. N_0 is set to 80 and a_{\max} to 99.67 μm in accordance with Levengood's tests. Although the test results are not directly comparable with the flaw depth distribution in the jumbo plates, the resemblance of the two curves indicates that the assumed distribution function is reasonable. It should be noted that for simple problems, it would be possible to calculate the statistical strength probability directly from the flaw size distribution in Eq. (7). However, when the applied stresses in the glass vary in position and time, this is not straightforward. Therefore, we apply a procedure where the statistical strength is instead found by iterative calculations (in a Monte Carlo simulation). Each iteration corresponds to one glass plate.

3.1.5. Flaw orientation

It is fair to assume that the surface flaws do not favour any orientation. Consequently, every individual flaw is given an in-plane orientation pseudo-randomly at an angle α between 0 and π with respect to the x -axis. The remote stresses directed normal to a flaw, denoted σ_n , must therefore be calculated accordingly. σ_n is equal to

$$\sigma_n = \frac{\sigma_x + \sigma_y}{2} + \frac{\sigma_x - \sigma_y}{2} \cos(2\alpha) + \tau_{xy} \sin(2\alpha) \quad (9)$$

where σ_x and σ_y are the in-plane normal stresses in the x and y direction, respectively, and τ_{xy} is the in-plane shear stress.

3.2. Implementation of the strength prediction model

The following explains the procedure of implementing the strength prediction model, including the preparatory work necessary to apply it. The model itself was implemented in the programming language Python, and the stress state in the glass plates was retrieved by employing the FE software Abaqus [31].

3.2.1. Input

The simulation process starts by defining the dimensions of the glass plate as well as the boundary and loading conditions. An FE analysis is in turn performed (without any failure criterion) to obtain the stresses in all elements on the glass surface at a sufficient number of evenly spaced time intervals. If shell elements are used, the stresses are taken from the outer integration points, placed at the surface. The failure load and deflection of the glass are usually of interest, and the applied load and relevant displacements must therefore also be obtained by the FE analysis at the specified time intervals. Further, the said output from the FE analysis is used as input in the strength prediction model. Additionally, some parameters must be provided, and the following list summarizes these:

- Fracture toughness K_{IC}
- Flaw shape a/c
- Maximum flaw depth a_{\max}
- Flaw density ρ_{flaw}
- Size of the jumbo plate A_{jumbo}
- Number of plates to analyse

The size of the elements used for the glass plate is based on the flaw density and chosen such that each element will contain one flaw. For instance, if the flaw density is chosen as $1/\text{cm}^2$, the element size will be $10\text{ mm} \times 10\text{ mm}$. If this element size leads to an overly coarse mesh, the glass plate can be modelled with smaller elements and a clustering technique is used. That is, the same flaw is assigned to a group, or cluster, of neighbouring elements. The clustering procedure is performed in such a way that the chosen flaw density is still preserved. Note that the stresses are still obtained from each element, individually.

3.2.2. Procedure and output

Firstly, a hypothetical jumbo plate of a specified size is assigned N_0 number of flaws with varying depths and orientations on both surfaces. N_0 is equal to the specified flaw density multiplied by the area of the jumbo plate. The flaw depths on each surface of the jumbo plate are calculated based on Eqs. (7) and (8) as

$$a_i = a_{\max} \left(1 - \frac{\ln(N_i)}{\ln(N_0)} \right), \quad N_i = R_1(N_0 - 1) + 1, \quad R_1 \sim U([0,1]) \quad (10)$$

where R_1 refers to a random variable uniformly distributed on $[0, 1]$. The flaw orientations are further given by

$$\alpha_i = R_2\pi, \quad R_2 \sim U([0,1]) \quad (11)$$

where R_2 is another random variable uniformly distributed on $[0, 1]$.

Next, each surface element (or cluster of elements) in the glass plate from the FE model is assigned a flaw from the jumbo plate. This would correspond to the plate being cut out from the jumbo plate at a random location. The stresses normal to the flaws in each of the elements are then calculated from Eq. (9). The stress intensities K_I are further found by Eq. (5), where the normal stresses in the elements are treated as remote stresses on the flaws. This is done for every interval until the first element has reached the failure criterion given by Eq. (4). The time and stress intensity factor in the failed element corresponding to this interval are denoted t_c and $K_I(t_c)$, respectively. As $K_I(t_c)$ is most likely slightly larger than the fracture toughness K_{IC} , an interpolation of relevant parameters between t_c and the previous time t_{c-1} is carried out based on the values of the stress intensities, i.e., $K_I(t_c)$ and $K_I(t_{c-1})$. Next, the glass plate is assigned new flaws, which are taken from the same jumbo plate, and the above procedure is repeated. A visualization of assigned flaw depths and orientations for two glass surfaces from the same jumbo plate are visualized in Fig. 18. Here, the surface area is $400\text{ mm} \times 400\text{ mm}$, and the flaw density is set to $1\text{ flaw}/\text{cm}^2$. The above procedure is carried out until all flaws in the jumbo plate have been allocated, and a new one is constructed. The number of different jumbo plates used is dependent on the specified number of plates to analyse. Yankelevsky [12] stated that a total number of at least 5000 plates is required to give a converged and reliable result.

A number of different output parameters are available from the strength prediction model, and the most relevant are listed below. In addition to these, the failure percentage can be found for each studied case. The values of the following parameters are registered for every simulated plate:

- Coordinates of the failed element
- Normal stress at failure
- Displacement at failure
- Applied load at failure
- Time at failure

The above procedure is only valid for static problems, as the failure criterion given by Eqs. (4) and (5) may not hold for dynamic loading conditions. In the case of glass specimens exposed to rapid loading, the following condition presented in [32] is adopted

$$\frac{1}{\tau} \int_{t-\tau}^t K_I(\bar{t}) d\bar{t} \geq K_{IC} \quad (12)$$

Here, τ is denoted the incubation time, or the microstructural fracture time, and is in this case interpreted as the minimum time

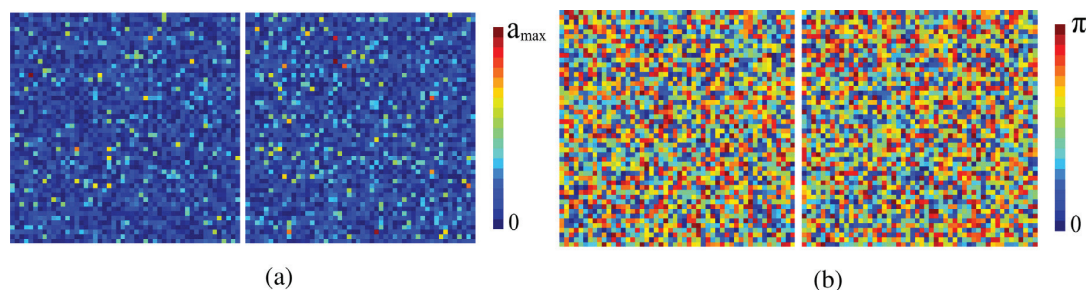


Fig. 18. Two randomly selected surfaces with assigned (a) flaw depth and (b) flaw orientation. The corresponding legend is shown on the right hand side of each subfigure.

required to initiate crack growth. Additionally, the criterion is employed to avoid that spurious peaks of stress result in failure of the glass. In order to introduce the aforementioned dynamic fracture criterion in the strength prediction model, it is discretized. Hence, to achieve failure in an element, the averaged value of the stress intensity K_I over a period greater than τ must be larger than or equal to the fracture toughness K_{IC} . This criterion naturally requires the determination of the incubation τ . Unfortunately, the authors have not succeeded in finding any records of this parameter for soda-lime glass in the literature. However, as a comparison, a values of $9 \mu\text{s}$ has been found for Homalite-100 [32].

4. Numerical study

4.1. Quasi-static four-point bending tests

In the following, the strength prediction model is employed in an attempt to find the strength distribution of the four-point bending tests presented in Section 2.2. The bending tests were first recreated in an Abaqus simulation, such that the stress state history could be used as input in the strength prediction model. Shell elements were employed for the glass specimens, while the loading and support cylinders were modelled as analytical rigid surfaces. The dimensions of the glass corresponded to the nominal values given in Table 2, while the element size was set to 1.25 mm, 2.5 mm and 5 mm for the small, medium and large specimens, respectively. Simpson's integration rule was employed with the use of 5 integration points over the thickness. The glass was modelled as linear-elastic with material parameters given in Table 1. The input parameters for the strength prediction model itself are presented in Table 7. Fig. 19 shows the histograms of the applied load at failure determined by the strength prediction model for the three specimen sizes. For comparison, the forces obtained in the laboratory tests are also included in the figure. Note that the ordinate, denoted probability density, refers to an occurrence, which is normalized to the model and test results individually. As can be seen, the failure loads from the tests are all within the capacity given by the strength prediction model. The normal stresses at failure determined by the strength prediction model are presented in Fig. 20. To facilitate an easier interpretation and comparison of the results, fitted normal probability density functions are included. The corresponding parameters are presented in the same figure, where μ and s are the mean and standard deviation of the normal distribution. As the normal distribution was found to give a better fit than e.g. the Weibull distribution, this was chosen in this study. However, both distributions highlighted the same trends of the strength prediction model. That is, a decreased surface area results in an increased mean and scatter of the fracture strength.

4.2. Shock tube tests

As for the four-point bending tests, FE simulations of the shock tube experiments were first run in order to obtain the stress state throughout the tests. This was in turn used as input in the strength prediction model. The following subsection describes the FE model of the test setup built in Abaqus.

4.2.1. FE model

The FE model of the test setup was based on several simplifications. Firstly, only the glass plate and rubber strips were modelled, see Fig. 21a. The clamping frames and steel stoppers were indirectly included in the model by restricting movement of the outer rubber surfaces in all directions. This is a fair assumption as the rubber strips were glued to the clamping frames and the movement of the clamping frames was close to zero during the tests. Secondly, to account for the clamping pressure in the test set up, the rubber was translated 0.005 mm towards the glass before loading. Thirdly, the rubber was modelled by a linear-elastic material model with a Young's modulus of 2 MPa and a Poisson's ratio of 0.46. Lastly, owing to the assumed linear-elastic behaviour of the rubber, only one (fully integrated) solid element was appropriate in the thickness direction. In order to properly describe the motion of the rubber along the frame, the elements had a cubic shape. The glass was modelled with $5 \text{ mm} \times 5 \text{ mm}$ shell elements, using the Simpson's integration rule with five integration points over the thickness. The material was chosen as linear-elastic with parameters in Table 1. It should be made clear that Young's modulus for glass is relatively insensitive to strain rate, as found by e.g. Zhang et al. [33], which makes it appropriate to use the static value. Note also that only a quarter of the plate could have been modelled due to symmetry. However, this was not done as each element was to be assigned an individual flaw. Three different loading scenarios were simulated; specifically the pressure histories obtained in test A-01, B-04 and C-01. To ensure that the FE models provided the correct behaviour, displacements in points corresponding to nine optical targets were compared to the DIC measurements. The nine points are shown in Fig. 21b, and are limited to three points in the FE model due to ideal symmetry of the deflection. The points are referred to as P0, P1 and P2. The displacements over time in tests A-01, B-04 and C-01 and the corresponding FE simulations are shown in Fig. 22. The dashed and solid lines refer to the FE model and the experimental tests, respectively. As can be seen, only test B-04 did not fracture at some point, and could therefore be compared throughout the entire course of displacement. The simulation fits well with the experimental test, however, there are some discrepancies after maximum displacement. As fracture will occur in the glass before this

Table 7
Input parameters for the strength prediction model

K_{IC}	a/c	a_{max}	ρ_{flaw}	A_{jumbo}	Number of plates
$0.75 \text{ MPa}\sqrt{\text{m}}$	1	$100 \mu\text{m}$	2 flaws/cm^2	$3210 \times 6000 \text{ mm}^2$	5000

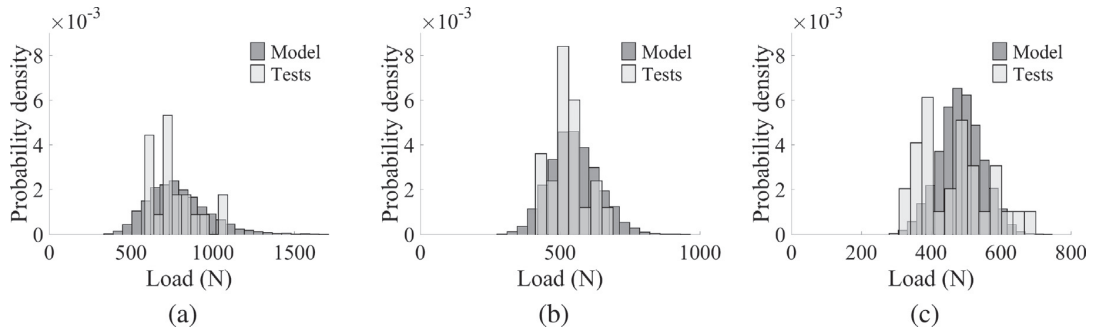


Fig. 19. The probability density distribution of forces at failure determined by the strength prediction model and laboratory tests for (a) small, (b) medium and (c) large specimens in four-point bending.

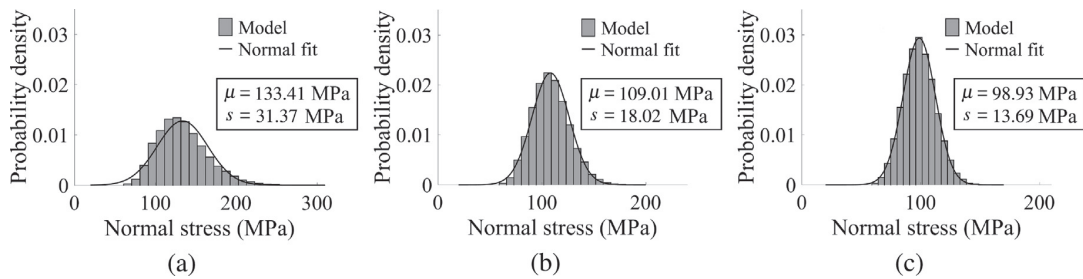


Fig. 20. The probability density distribution of normal stresses at failure determined by the strength prediction model for (a) small, (b) medium and (c) large specimens in four-point bending. A normal distribution function has also been fitted to the results.

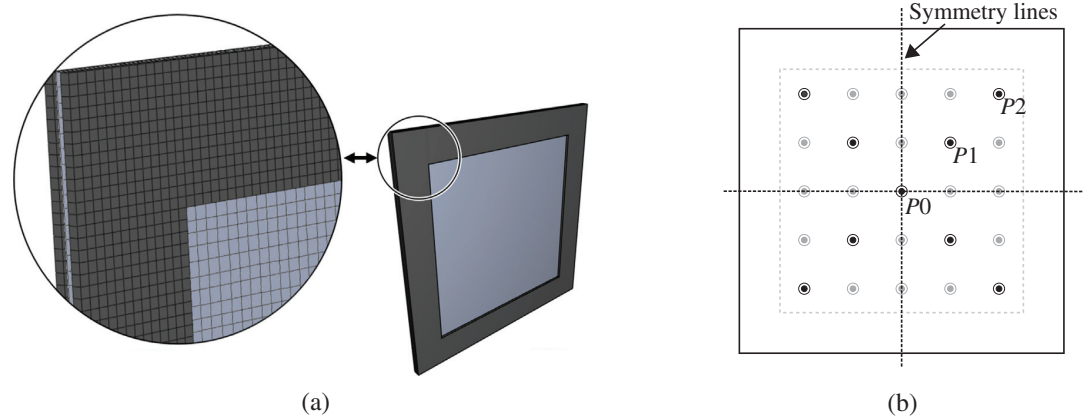


Fig. 21. The FE model of the test setup in the SSTF: (a) illustrating the mesh sizes, (b) illustrating points tracked in the FE model and the experiments, including symmetry lines.

point, this is irrelevant in the use of the strength prediction model. Simulations of test A-01 and C-01 also seem to match well before fracture. Consequently, the stress states from these simulations are used as input in the strength prediction model.

4.2.2. Strength prediction

The input parameters of the strength prediction model used for the shock tube tests were the same as for the four-point bending tests, with the exception of one additional parameter, the incubation time τ . This value was merely chosen to be 10 μ s. It proved, however, that the strength prediction model was not sensitive for a moderate change in τ .

In the four-point bending and quasi-static pressure tests, the load was gradually increased such that the ultimate capacity of the tested glass plates could be found. This was not the case for the shock tube tests, and the predicted and measured fracture strength could therefore not be directly compared. Instead, other properties were studied, such as the location and time of fracture initiation,

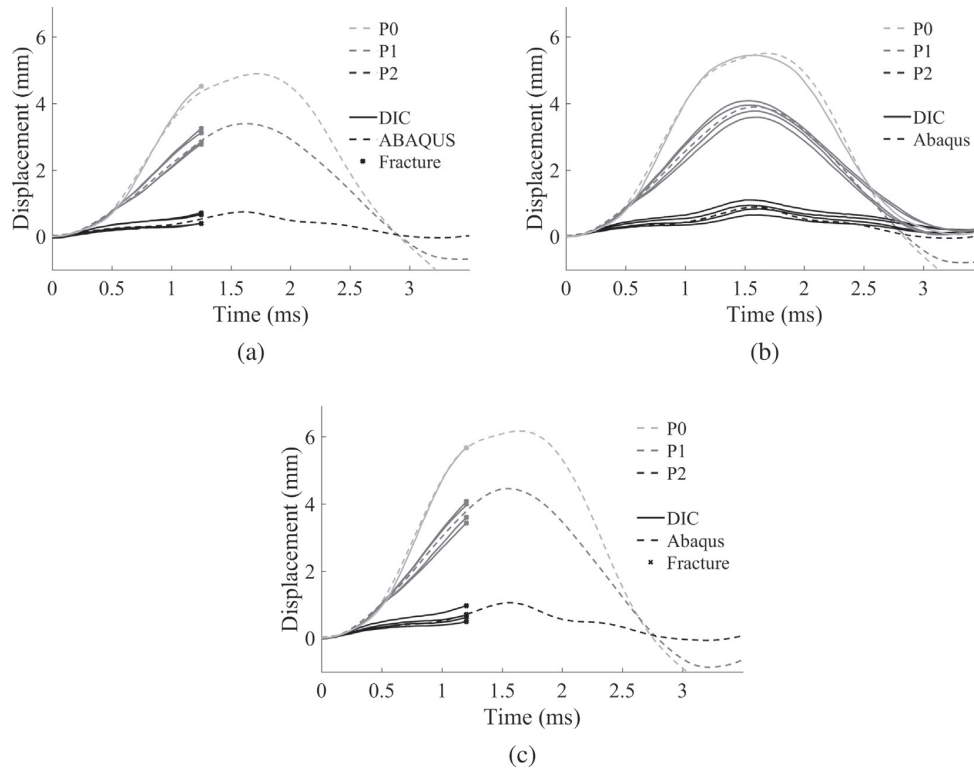


Fig. 22. Displacements from DIC and Abaqus simulations in points P0-P2 for tests (a) A-01, (b) B-04, (c) C-01.

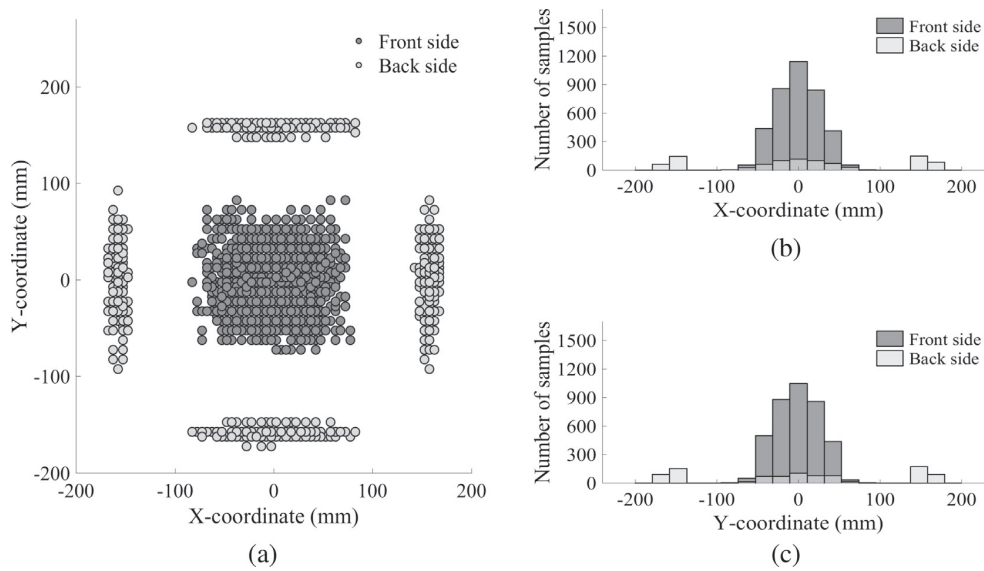


Fig. 23. Location of fracture initiation determined by the strength prediction model for test A-01 visualized as: (a) a surface map, (b) a histogram of occurrence on the X-axis, (c) a histogram of occurrence on the Y-axis. The origin is set at the plate’s centre.

and failure percentage.

Fig. 23a illustrates the predicted fracture locations for test A-01. The glass plates experienced tensile stresses on both sides, and the results distinguish therefore between failure on the front and back side of the plate. The back refers, in this study, to the side directly exposed to the pressure load. Fig. 23b and c illustrate the recurrence of the fracture locations by means of coordinate values in a histogram. The ordinate refers to the number of fictitious glass plates tested. As shown, most plates failed at the front and centre of the plate and the positioning is in addition symmetric. Compared to the actual shock tube tests, the location of front failures agreed well, as it occurred within the area proposed by the strength prediction model. Whether the position of back failure is in agreement with the tests was difficult to determine as the failure initiation occurred under the rubber strips. The failure percentages provided by the strength prediction model for tests A-01, B-04 and C-01 are presented in the first part of Table 8. As a comparison, the failure percentage for the actual tests of class A, B and C were 100% (2/2), 75% (6/8) and 100% (2/2), respectively. The percentage of plates that failed at the back side is also stated, which in the actual tests proved to be 100% (2/2), 50% (4/8) and 100% (2/2). Thus, the location of failure provided by the strength prediction model was not in particularly good agreement with the test results. However, it should be noted that to draw any definite conclusions, a much larger number of experimental tests must be carried out. Nevertheless, there are various possible reasons for the discrepancy, such as the glass being in direct contact with sharp edges of the clamping plate during the test. However, it may also be due to dynamic effects that are not sufficiently accounted for in the model. The strength of glass is generally increased when exposed to high strain rates [33,34], and the use of the criterion in Eq. (12) may not be suitable to correctly capture this trend. A rather limited study was thus conducted to investigate the effect of an increased fracture toughness, K_{IC} . The input of K_{IC} was set to 0.8 MPa \sqrt{m} , and the resulting failure percentage for test A-01 and B-04 was decreased to 77.7 and 99.2%, respectively, while the failure percentage for C-01 was unchanged. The failure percentages corresponding to the back of the plates were moderately increased for all tests, specifically 22.2%, 9.50% and 4.13% for A-01, B-04 and C-01, respectively. Note that the fracture toughness should in reality depend on the strain rate rather than being kept constant. Time of fracture is directly comparable in this case, and the range of predicted times for test A-01, B-04 and C-01 is shown in the last part of Table 8. The results are divided into back and front fracture initiation. For all tests in class A, B and C, the experimental time of fracture lies within or is equal to the predicted extreme values, see Table 4. An increase in fracture toughness, K_{IC} , to 0.8 MPa \sqrt{m} resulted in a somewhat increased time of fracture. However, the experimental values still remained within the predicted time ranges. The predicted normal stresses at failure for tests A-01, B-04 and C-01 are further shown in Fig. 24, and are divided into front and back failures. Here, it is clearly seen that for plates exposed to a lower peak reflected pressure $P_{r,max}$, a larger number of the plates failed at the back side. Fig. 25 further includes a normal probability density function fitted to the results for test C-01. The parameters of the fitting are also presented in the figure. Compared to the four-point bending tests, both the scatter and fracture stress are decreased, which was expected due to the rather large increase in surface area.

4.3. Quasi-static pressure tests

Finally, the strength prediction model is employed to find the strength distribution of the quasi-static pressure tests presented in Section 2.7. As for the previous tests, an Abaqus model of the test setup was first established. The model was the same as for the shock tube tests, except that the load was applied smoothly over a much longer period of time. Additionally, the weight of the clamping plate was applied to the glass edges as a uniform pressure.

To ensure that the Abaqus model provided the correct behaviour, the pressure-displacement histories from the simulation and test Q-09 were compared. The displacements were taken from three points corresponding to P0, P1 and P2 in Fig. 21b. Fig. 26 presents the resulting curves, where the dotted lines refer to the test, and the solid lines to the Abaqus simulation. As the curves are relatively coincident, we assume that the Abaqus simulation manages to describe the stress state in the plates up to fracture. Consequently, the stress state from the simulation was used as input for the strength prediction model. The input parameters were the same as for the four-point bending tests. Fig. 27 shows the location of the fracture initiation determined by the strength prediction model. The results are similar to those from the shock tube tests; however, the percentage of failure at the back side is larger for the current tests. Here, 34.3% failed at the back, while for the C-01 shock tube test, this value was 3.71%. As for the shock tube tests, the locations of all front failures for the quasi-static pressure tests occurred within the area estimated by the strength prediction model. The applied pressures at failure determined by the strength prediction model, together with the pressures obtained in the tests, are presented in Fig. 28 as a histogram. Note that the ordinate, denoted probability density, refers to an occurrence, which is normalized to the model and test results individually. The two tests Q-04 and Q-05 ended up on the outside of the model prediction. A possible reason for this could be that the prescribed initial flaws are smaller than the ones occurring in the tested glass plates. However, it may also imply that there are some effects that are not properly taken into account in the strength prediction model, such as subcritical crack growth. As the

Table 8

Failure percentages and time of fracture initiation t_{frac} determined by the strength prediction model for tests A-01, B-04 and C-01.

Test	Failure percentage		Time of fracture initiation t_{frac}	
	Total (%)	Back side (%)	Front side (ms)	Back side (ms)
A-01	94.2	19.8	0.88–1.92	0.95–1.73
B-04	99.8	4.62	0.82–1.71	0.85–1.54
C-01	100	3.71	0.76–1.41	0.75–1.33

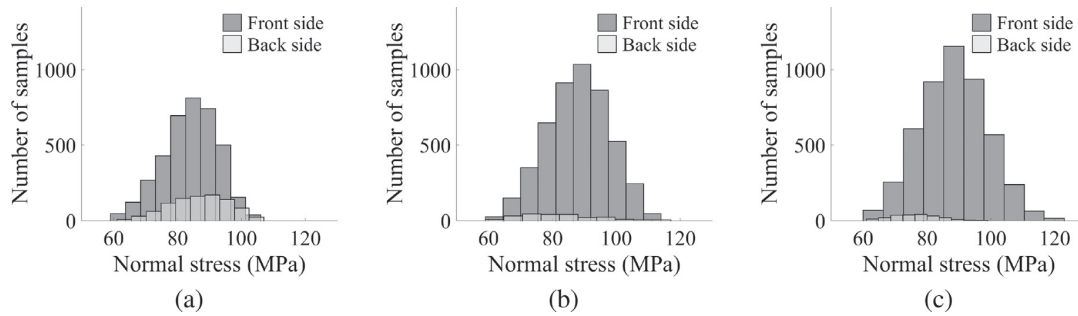


Fig. 24. The distribution of normal stresses at failure determined by the strength prediction model for tests (a) A-01, (b) B-04, (c) C-01.

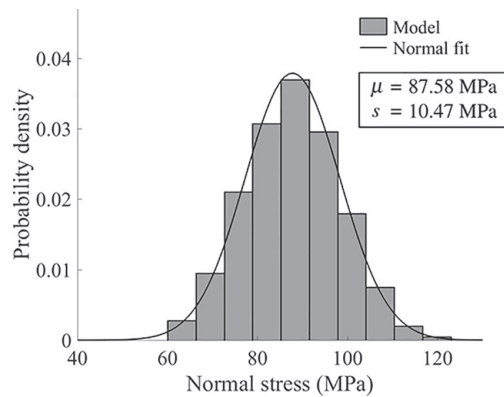


Fig. 25. The probability density distribution of normal stresses at failure determined by the strength prediction model for test C-01. A normal distribution function has also been fitted to the results.

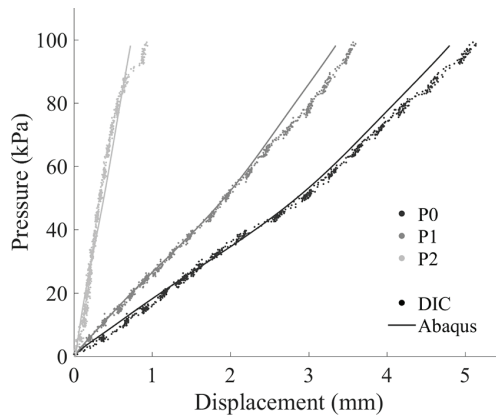


Fig. 26. Pressure versus displacement curves from DIC measurements and Abaqus simulations in points P0-P2 for test Q-09.

quasi-static tests took up to a minute to finish, it is possible that the initial flaws grew stably during the loading, and a smaller flaw size was required to induce failure. A histogram of the resulting normal stresses at failure is presented in Fig. 29a, and is divided into occurrences on the front and the back side of the glass plates. Failure at the largest value of normal stresses occurred in this case at the back side of the plate, while the smallest took place at the front. A histogram combining both sides, together with a fitted normal probability density function can be viewed in Fig. 29b. The parameters of the fitting are also presented. It should be mentioned that the probability density was almost identical when excluding the weight of the steel clamping plate. Compared to the shock tube tests, both the scatter and the fracture strength are slightly smaller.

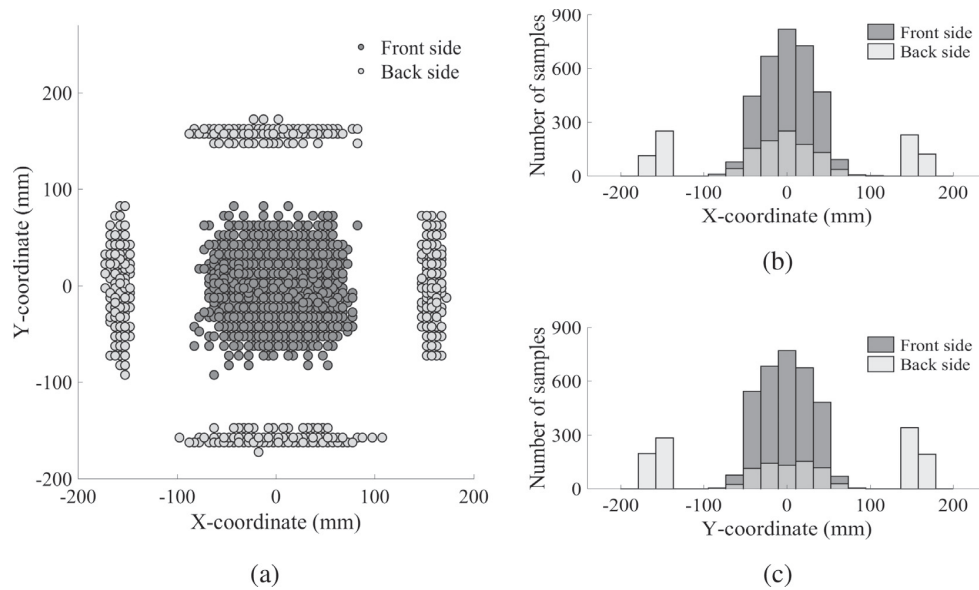


Fig. 27. Location of fracture initiation determined by the strength prediction model for the quasi-static pressure tests visualized as: (a) a surface map, (b) a histogram of occurrence on the X-axis, (c) a histogram of occurrence on the Y-axis. The origin is set at the plate's centre.

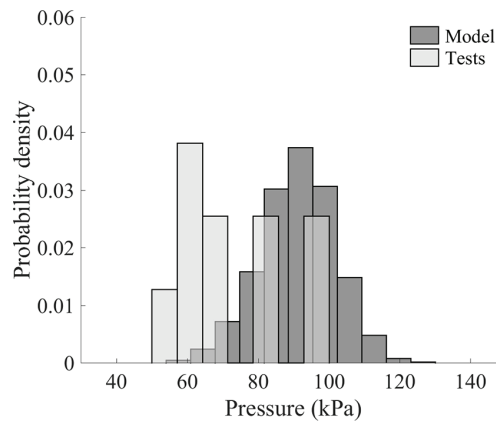


Fig. 28. The probability density distribution of applied pressures at failure determined by the strength prediction model and laboratory tests for the quasi-static pressure tests.

5. Discussion and concluding remarks

In this work, a further development of the strength prediction model proposed by Yankelevsky [12] has been presented. The model seeks to determine the fracture strength of glass without the need of experimental tests, and is based on the presence of microscopic surface flaws. These flaws are known to govern the fracture strength of glass, and lead to a highly probabilistic behaviour.

In an attempt to validate the strength prediction model, three different types of experiments on annealed float glass were conducted. These included quasi-static four-point bending tests on specimens of various size, and quasi-static and dynamic pressure tests on larger plates. As expected, the fracture strength varied within the same test setup, and was dependent on both the size of the glass plate and the loading condition.

The strength prediction model was able to successfully capture the trends observed in the quasi-static four-point bending tests. In the experiments, the mean strength seemed to increase with a decreasing specimen size; a trend the model also displayed. Additionally, the experimental fracture load was within the limits determined by the model. In the case of the quasi-static pressure tests, the fracture load obtained in the experiments was partly achieved by the strength prediction model. Specifically, the tests

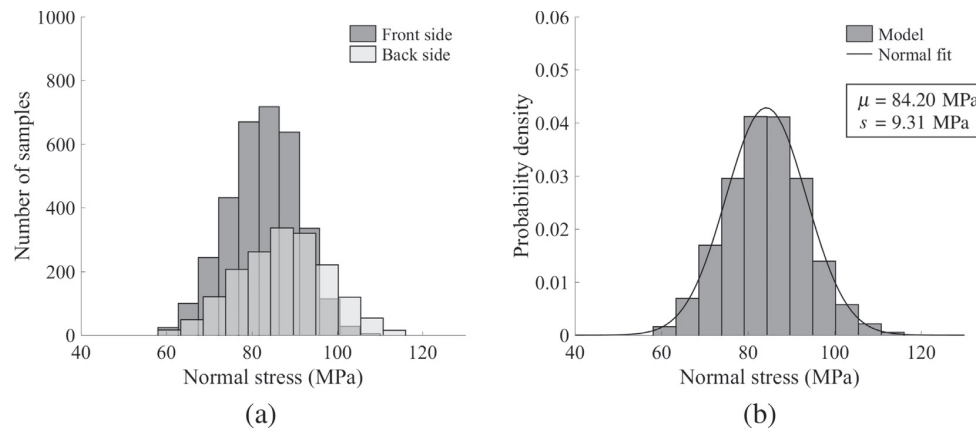


Fig. 29. The distribution of normal stresses at failure determined by the strength prediction model for the quasi-static pressure tests (a) divided in front and back failure, (b) including a fitted normal probability density function with corresponding parameters.

resulted in a slightly lower fracture strength than predicted by the model. This may be explained by an inaccurate value of the maximum flaw size. However, it may also be due to subcritical crack growth in the experiments, i.e., stable crack growth before failure. In fact, the quasi-static pressure tests lasted over twice as long as the longest-lasting bending tests. Consequently, this effect would be larger for the pressure tests.

Perhaps the largest source of error in the model arises in the modelling of the dynamic tests. The failure percentage determined by the model did not particularly coincide with the ones obtained in the experimental tests. It should, however, be noted that the number of experimental tests was limited. Nonetheless, the time and position of fracture initiation were captured by the strength prediction model. In order to consider dynamic effects, an incubation time, τ , was introduced. Since it was shown that the results were rather insensitive to the incubation time, a value of $10 \mu\text{s}$ was merely chosen. The strain rate effects on the glass' fracture strength may need to be included by different means, e.g. by including a fracture toughness dependent on strain rate. It was found that an increase in fracture toughness resulted in both increased fracture capacity and time to fracture.

The proposed model is simple, with few input parameters and cannot be expected to capture all effects arising in physical tests. It seems that the current model gives conservative solutions to the dynamic tests, whereas for the longer-lasting quasi-static tests, non-conservative solutions are obtained. Additionally, the chosen input parameters will need to be further investigated. This particularly applies to the flaw size and distribution. However, the model seems to have potential as it manages to display many of the trends found in the experiments. The model can therefore contribute to a greater understanding and a more predictive modelling of the stochastic behaviour of glass plates under quasi-static and dynamic loading. In addition, the time it takes to perform the analyses of the strength prediction model is only a fraction of the time it takes to perform actual tests. This makes the model even more appealing to the user.

In a further work by the authors, the strength prediction model will be coupled with a finite element solver, so that numerical simulations of both failure and crack propagation in window glasses exposed to dynamic loading can be predicted.

Acknowledgements

The present work has been carried out with financial support from CASA (project number 237885), Centre for Research-based Innovation (CRI), at the Norwegian University of Science and Technology (NTNU). The authors would like to acknowledge Mr. Trond Auestad and Mr. Tore With for assistance with the various experimental programmes. We would also like to thank the master students Mr. Kristoffer Aune Brekken, Mr. Petter Tønsberg Ingier, Ms. Nora Storebø Næss, Mr. Mathias Kolsaker and Mr. Ola Bratsberg for their contributions to this study. Acknowledgement are also expressed to Modum Glassindustri and Glassmester K. Larsen & Co for providing glass specimens for use in the experimental program.

References

- [1] Spiller K, Packer JA, Seica MV, Yankelevsky DZ. Prediction of annealed glass window response to blast loading. *Int J Impact Eng* 2016;88:189–200.
- [2] Zhang X, Hao H, Wang Z. Experimental study of laminated glass window responses under impulsive and blast loading. *Int J Impact Eng* 2015;78:1–19.
- [3] Larcher M, Solomos G, Casadei F, Gebbeken N. Experimental and numerical investigations of laminated glass subjected to blast loading. *Int J Impact Eng* 2012;39(1):42–50.
- [4] Hooper P, Sukhram R, Blackman B, Dear J. On the blast resistance of laminated glass. *Int J Solids Struct* 2012;49(6):899–918.
- [5] Pelfrene J, Kuntsche J, Van Dam S, Van Paepegem W, Schneider J. Critical assessment of the post-breakage performance of blast loaded laminated glazing: experiments and simulations. *Int J Impact Eng* 2016;88:61–71.
- [6] Hidallana-Gamage HD, Thambiratnam DP, Perera NJ. Failure analysis of laminated glass panels subjected to blast loads. *Eng Fail Anal* 2014;36:14–29.
- [7] Beason WL, Morgan JR. Glass failure prediction model. *J Struct Eng* 1984;110(2):197–212.
- [8] Wachtman JB, Cannon WR, Matthewson MJ. *Mechanical properties of ceramics*. 2nd ed. John Wiley & Sons; 2009.

- [9] Weibull W. A statistical distribution function of wide applicability. *J Appl Mech* 1951;103(730):293–7.
- [10] Nurhuda I, Lam N, Gad E, Calderone I. Estimation of strengths in large annealed glass panels. *Int J Solids Struct* 2010;47(18):2591–9.
- [11] Przybilla C, Fernández-Canteli A, Castillo E. Deriving the primary cumulative distribution function of fracture stress for brittle materials from 3-and 4-point bending tests. *J Eur Ceram Soc* 2011;31(4):451–60.
- [12] Yankelevsky DZ. Strength prediction of annealed glass plates – A new model. *Eng Struct* 2014;79:244–55.
- [13] Yankelevsky DZ, Spiller K, Packer J, Seica MV. Fracture characteristics of laboratory-tested soda lime glass specimens. *Can J Civ Eng* 2016;160:151–60.
- [14] Aune V, Fagerholt E, Langseth M, Børvik T. A shock tube facility to generate blast loading on structures. *Int J Protect Struct* 2016;7(3):340–66.
- [15] Wiederhorn SM. Fracture surface energy of glass. *J Am Ceram Soc* 1969;52(2):99–105.
- [16] Anstis G, Chantikul P, Lawn BR, Marshall D. A critical evaluation of indentation techniques for measuring fracture toughness: I. Direct crack measurements. *J Am Ceram Soc* 1981;64(9):533–8.
- [17] NS-EN 572-1: Glass in building – Basic soda-lime silicate glass products – Part 1: Definitions and general physical and mechanical properties, Standard, CEN; 2012.
- [18] NS-EN 13541: Glass in building – Security glazing – Testing and classification of resistance against explosion pressure, Standard, CEN; 2012.
- [19] ASTM C1161-13. Standard Test Method for Flexural Strength of Advanced Ceramics at Ambient Temperature, Standard. ASTM International, West Conshohocken, PA; 2013.
- [20] Lindqvist M, Louter C. Experimental study on glass edge machining flaw characterization. *Eng Fract Mech* 2014;127:56–70.
- [21] Cormie D, Mays G, Smith P. Blast effects on buildings. 2nd ed. Thomas Telford Publishing; 2009.
- [22] Aune V, Valsamos G, Casadei F, Larcher M, Langseth M, Børvik T. Numerical study on the structural response of blast-loaded thin aluminium and steel plates. *Int J Impact Eng* 2017;99:131–44.
- [23] Fagerholt E. Field measurements in mechanical testing using close-range photogrammetry and digital image analysis. PhD thesis. Norwegian University of Science and Technology (NTNU), Trondheim; 2012.
- [24] Yoda M. Subcritical crack growth of glass. *Eng Fract Mech* 1987;28(1):77–84.
- [25] Anderson TL. Fracture mechanics: fundamentals and applications. 3rd ed. CRC Press; 2005.
- [26] Irwin GR. Analysis of stresses and strains near the end of a crack traversing a plate. *J Appl Mech* 1957;24(3):361–4.
- [27] Newman J, Raju I. An empirical stress-intensity factor equation for the surface crack. *Eng Fract Mech* 1981;15(1-2):185–92.
- [28] Levengood W. Effect of origin flaw characteristics on glass strength. *J Appl Phys* 1958;29(5):820–6.
- [29] Wereszczak AA, Ferber MK, Musselwhite W. Method for identifying and mapping flaw size distributions on glass surfaces for predicting mechanical response. *Int J Appl Glass Sci* 2014;5(1):16–21.
- [30] NS-EN 572-1: Glass in building – Basic soda-lime silicate glass products – Part 2: Float glass, Standard, CEN; 2012.
- [31] Abaqus, Version 6.14. Dassault Systèmes Simulia Corporation. Providence, RI, USA; 2014.
- [32] Petrov YV, Morozov N, Smirnov V. Structural macromechanics approach in dynamics of fracture. *Fatigue Fract Eng Mater Struct* 2003;26(4):363–72.
- [33] Zhang X, Zou Y, Hao H, Li X, Ma G, Liu K. Laboratory test on dynamic material properties of annealed float glass. *Int J Prot Struct* 2012;3(4):407–30.
- [34] Peroni M, Solomos G, Pizzinato V, Larcher M. Experimental investigation of high strain-rate behaviour of glass. *Appl Mech Mater* 2011;82:63–8.

PART 2

Karoline Osnes, Sumita Dey, Odd Sture Hopperstad, Tore Børvik

On the dynamic response of laminated glass exposed to impact before blast loading

Experimental Mechanics 59 (2019) 1033-1046.

<https://doi.org/10.1007/s11340-019-00496-1>



On the Dynamic Response of Laminated Glass Exposed to Impact Before Blast Loading

K. Osnes^{1,2} · S. Dey³ · O. S. Hopperstad^{1,2} · T. Børvik^{1,2}

Received: 9 November 2018 / Accepted: 1 March 2019
© Society for Experimental Mechanics 2019

Abstract

In this study, the effect of fragment or bullet impact before blast loading on laminated glass is studied experimentally. First, laminated windows consisting of two 3.8 mm thick annealed float glass plates and a 1.52 mm thick PVB interlayer were blast loaded in a shock tube with various pressures as a reference. In these tests, the blast loading was successively increased until fracture occurred not only in the glass plates but also in the PVB interlayer. Second, a diamond drill was used to make a 5 mm diameter centrally placed hole in some windows before they were blast loaded with the same pressures as those used for the undamaged windows. Third, windows were impacted by 7.62 mm AP bullets, both with and without the brass jacket, before they were blast loaded. Such bullets may have similar mass and velocity to typical primary fragments from an explosive detonation. The results are finally compared with each other and discussed with respect to the blast protection offered. It is found that the capacity is significantly reduced if the laminated glass is perforated by a fragment or a bullet before it is blast loaded and that such impacts should be considered in the design of blast-resistant windows.

Keywords Laminated glass · Impact tests · Blast tests · Glass fracture · PVB failure

Introduction

Ordinary windows used in buildings typically consist of two layers of annealed float glass separated by a layer of argon gas. The glass material is highly brittle and offers limited

resistance to extreme loading conditions such as high-velocity impacts or blast waves generated by explosions [1]. Due to the lack of plastic deformation, the energy dissipated during crack propagation in glass is small, and the fracture propagates fast with little chance of crack arrest [2]. Thus, ordinary window glass will break into numerous sharp fragments that may travel at high velocities and potentially cause severe damage to the surroundings when they are exposed to extreme loadings. One way of reducing this risk is to apply laminated glass, which is a type of safety glass extensively used by e.g. the automotive industry as windshields or in protective structures for blast mitigation.

A laminated glass is simply made by sandwiching layers of polyvinyl butyral (PVB) or other structural interlayer materials in between two or more plates of annealed or strengthened float glass. The components are bonded permanently using both mechanical and chemical bonds. The main intention of the interlayer is to keep the sharp glass pieces bonded if the window breaks. Furthermore, the interlayer's low stiffness and ability to deform ensure that the glass breaks into small pieces instead of large and sharp fragments. Another very important feature of the interlayer is that it provides additional resistance even after the glass plates have fractured [3–5]. This property is particularly important in blast protection, as it prevents the blast pressure

✉ K. Osnes
karoline.osnes@ntnu.no

S. Dey
Sumita.Dey@forsvarsbygg.no

O. S. Hopperstad
odd.hopperstad@ntnu.no

T. Børvik
tore.borvik@ntnu.no

¹ Structural Impact Laboratory (SIMLab), Department of Structural Engineering, NTNU, Norwegian University of Science and Technology, NO-7491, Trondheim, Norway

² Centre for Advanced Structural Analysis (CASA), NTNU, Norwegian University of Science and Technology, NO-7491, Trondheim, Norway

³ Research and Development Department, Norwegian Defence Estates Agency, NO-0105, Oslo, Norway



from entering the building. If the blast pressure is allowed to freely enter any part of the building, it may be a severe threat to both the occupants and the structural integrity. This hazard was demonstrated during the terrorist attack against the Executive Government Quarter on the 22th of July, 2011, in Oslo, Norway (see, e.g., [6]), where only a few of the windows in the façade were blast protected.

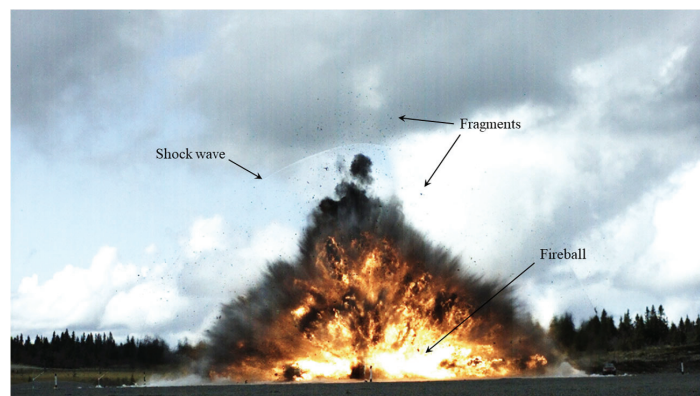
Whenever a chemical explosive detonates, a shock wave is generated and followed by a series of pressure waves, thus forming a blast wave. The detonation velocity is very high (typically several thousands of meters per second), and the blast wave propagates outwards from the source into the surrounding air. As the blast wave expands, it decays in intensity, increases in duration and decreases in velocity. The decrease in pressure occurs rapidly (approximately with the cube of the distance) due to geometrical effects and energy dissipation caused by heating of the air [7]. The blast wave is most often accompanied by primary and/or secondary fragments. Primary fragments are defined as parts initially contained in the explosive device (e.g., ball bearings) or parts from the fractured casing of the explosive (e.g., a shell or a vehicle), while secondary fragments are external objects picked up by the blast wave along its path. The primary fragments propagate with a high and rather constant velocity (up to several kilometres per second), having masses ranging from less than a gram to tens of grams [8–11]. The technical manual TM5-855 [8] reports expected average masses and velocities (from a warhead casing of 420 kg) ranging from 1.7 g to 83.1 g and 745 m/s to 1509 m/s, respectively. Arnold et al. [9] studied casings of different thicknesses and materials, and reported fragment masses from around 0.001 to 100 g. Field tests by Grisaro et al. [10], involving cased charges of approximately 11 kg, resulted in fragment masses up to 5 g and velocities ranging from approximately 1100 to 2053 m/s. The study by Guo et al. [11] on different explosive-filled casings recorded fragment velocities of approximately 950 to 1600 m/s.

Typical examples of secondary fragments include building debris or loose items on the ground, and they have in general a much lower velocity and a higher mass than primary fragments.

If the detonation is close-in, the shock wave may hit the structure before the fragments, while if the detonation is far-field, it is likely that the fragments will arrive before the shock wave. Under certain conditions, the shock wave and the fragments will arrive simultaneously, so the structure experiences the combined effect of impact and blast loading [12, 13]. What the outcome will be is a function of a number of factors, such as type of explosive/casing, standoff distance and weight of explosive/casing. This issue is still an open research topic [14–16]. An example of the detonation of a vehicle-borne improvised explosive device (VBIED), revealing the shock wave, the fragments and the fireball, is shown in Fig. 1. From this picture, it can clearly be seen that numerous fragments are propagating in front of the shock wave. Therefore, what happens with the blast protection if a fragment hits a laminated glass before the shock wave? Since high-velocity impact is a highly localized process, it is very likely that the fragment will break the glass plates and perforate the interlayer. This effect may allow the blast wave to rupture the laminate and enter the building when it arrives shortly after the impact. To the best of the authors' knowledge, the combined effect of fragment and blast loading on laminated glass has not been previously reported in the open literature.

Thus, in this study, the effect of impact before blast loading on laminated glass was studied experimentally. First, laminated windows consisting of two 3.8 mm thick annealed float glass plates and a 1.52 mm thick PVB interlayer were blast loaded in a shock tube at various pressures as a reference. In these tests, the blast loading was successively increased until fracture occurred not only in the glass plates but also in the interlayer. Second, a diamond drill was used to make a 5 mm diameter centrally placed hole in the windows

Fig. 1 Combined blast and fragment loading after detonation of a vehicle-borne improvised explosive device (VBIED). Courtesy of the Norwegian Defence Estate Agency (Forsvarsbygg)



before they were blast loaded with the same pressures as those used for the initially undamaged windows. Third, windows were impacted by 7.62 mm armour-piercing (AP) bullets, both with and without the brass jacket, before they were blast loaded. Such bullets may have similar mass and velocity to typical primary fragments (see, e.g., [9–11]). The results were finally compared with each other and discussed with respect to the blast protection offered. It is found that the degree of protection is significantly reduced if the laminated glass is perforated by fragments before it is blast loaded, and that the blast-resistant window design could give non-conservative results if the effects of fragment impact are not properly accounted for.

Materials

Annealed Float Glass

The glass plates used in this study are made of clear annealed soda-lime-silica float glass. Such glass plates are manufactured as large sheets (typically 3.21 m × 6 m [17]) by pouring molten material on a liquid tin bath where it solidifies in a controlled manner. The liquid tin ensures the uniform thickness of the sheets, and the dimensions are adjusted by stretching or compressing the molten material. The tin temperature is then lowered in a controlled manner until the glass sheet has hardened. This annealing process is important to relieve internal residual stresses introduced during manufacturing. Annealed float glass is a brittle material and has linear elastic behaviour to the point of failure. Fracture in glass typically initiates at microscopic flaws located on the surface, causing the fracture strength to be highly stochastic [18]. Since the opening of a flaw is the predecessor to crack propagation, glass plates primarily fail in tension [19]. Commonly used material parameters for float glass are found in the European Standard NS-EN 572-1 [20]. It reports a density of 2500 kg/m³, an elastic modulus of 70000 MPa, and a Poisson's ratio of 0.2. The fracture toughness of glass is reported in Anstis et al. [21], based on quasi-static tests by Wiederhorn [2]. The value is stated as 0.75 MPa√m and correlates with the critical stress intensity factor for mode I loading, i.e., the opening of a flaw. It should, however, be mentioned that the fracture strength of glass is strain rate sensitive [22, 23], which could affect the fracture toughness.

PVB

The laminated glass used in this study includes an interlayer of polyvinyl butyral (PVB), which is the most commonly used interlayer in laminated glass [5]; however, other materials can also be used (such as ionoplast, polycarbonate and similar materials). PVB displays highly non-linear and

time-dependent behaviour and may undergo large strains before failure. The material has a viscoelastic behaviour, and exhibits a different response under low and high strain rates [24, 25]. It should be noted that there is close to no permanent deformation of the PVB material a sufficient amount of time after loading [25]. Furthermore, PVB is a nearly incompressible material [3] and is also highly temperature dependent [26].

Laminated Glass

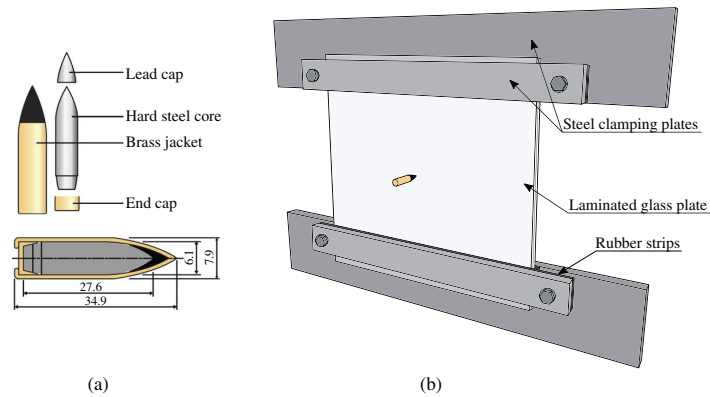
Laminated glass is a combination of two or more glass plates bonded together with a polymer interlayer (usually PVB). Normally several layers of 0.38 mm thick PVB films are used. If the glass breaks, the glass fragments are contained on the surface of the polymer, offering an increased level of protection against impact and blast loading. The post-fracture behaviour of laminated glass is a complicated process that depends on many different factors. Delamination will occur between the glass and the polymer, which in turn allows stretching of the interlayer [5]. If the interlayer is flexible, as in the case of PVB, it can deform significantly and absorb energy. If the applied load is sufficiently large, detachment of glass fragments can occur. This effect is dependent on the adhesion level, which in turn depends on the production process [27]. The production of laminated glass involves at least five main steps: (1) The glass is cut into required shapes, designs and sizes following given specifications. (2) Using feeding devices and a roller table, the glass is conveyed to washing machines. In this stage, wider gaps between glass panes are automatically minimized. (3) The glass panes are thoroughly cleaned and dried using automated machines. (4) The clean and dry glass panes are transferred to a clean room with conditioned temperature and humidity, where the PVB film rolls are stored. Together with the PVB films, the glass panes are accurately aligned according to their geometry. The laminated glass is then placed on a nip roller where it is heated and compressed simultaneously to remove air in between the layers. (5) The nipped specimen is transferred to the autoclave cart. In this final stage, controlled cycles of heat and pressure are applied to adhere the layers together and make the laminated glass clear.

Experimental Setups

Ballistic Impact Tests

In an attempt to mimic an impact of a primary fragment from an explosion, two different approaches were exploited. First, a glazier used a 5 mm diameter diamond drill to make a hole in the centre of the laminated glass. This process

Fig. 2 Illustration of the ballistic test setup: **a** 7.62 mm AP bullet (dimensions given in mm) [29], **b** clamping of the laminated glass plate



could be performed without damaging the glass plates outside the central region, except maybe for some micro-cracks not visible to the naked eye. Two laminated windows were tested in this configuration. Second, a smooth-bored Mauser rifle was used to fire 7.62 mm armour-piercing (AP) bullets at the centre of the laminated glass plates. A total of four laminated windows were impacted by bullets. The applied AP bullet consists of a brass jacket, a lead tip, an end cap and a hardened steel core [28, 29]. The mass of the hardened steel core is 5 ± 0.25 g, while the mass of the whole bullet is 10.5 ± 0.25 g. The dimensions of the bullet are given in Fig. 2(a). In two of the tests, only the hard core of the AP bullet was used to impact the laminated glass. In this case, the 6.1 mm diameter hard steel core was encased in a 0.3 g plastic sabot before inserted into the cartridge [30, 31]. The ammunition was adjusted by removing some of the powder before firing the core-only (CO) bullet, with the intention of having approximately the same initial velocity for the CO and AP bullets. It is assumed that the hardened steel core, having a Rockwell C hardness of 63, will not considerably deform as a result of the impact.

During testing, the laminated glass plate was clamped at the top and bottom between steel platens with 4 mm thick Neoprene rubber strips in between, as shown in Fig. 2(b). Each test was recorded with a Phantom v2511 high-speed camera with a recording rate of 100,000 fps. Both the initial and the residual velocity of the bullet were measured using a point-tracking procedure in the digital image correlation (DIC) software eCorr [32]. This approach was also used to measure the pitch angle of the bullet prior to impact.

Blast Loading

The detonation of a chemical explosive results in a rapid release of energy and the development of a blast wave. The resulting reflected overpressure on a surface (i.e., the blast loading) is dependent on parameters such as the

size of the charge and the standoff distance. An idealized reflected pressure-time history for a structure subjected to a blast wave is shown in Fig. 3. The maximum reflected pressure $P_{r, \max}$ occurs at the arrival time t_a and rises from atmospheric pressure P_0 over a time period close to zero. Subsequently, the pressure decays to atmospheric pressure P_0 over a time period t_{d+} and further down to the negative overpressure P_s over a time period t_{d-} . The first pressure overpressure P_s over a time period t_{d-} . The first pressure phase is referred to as the positive phase, while the last is referred to as the negative phase. The positive pressure phase is frequently described by the modified Friedlander equation [7], given by

$$P_r(t) = P_0 + P_{r, \max} \left(1 - \frac{t - t_a}{t_{d+}} \right) \exp \left(\frac{-b(t - t_a)}{t_{d+}} \right) \quad (1)$$

where b governs the curvature from $P_{r, \max}$. In this study, the obtained blast loadings have a negligible negative pressure phase, and the modified Friedlander equation is sufficient to describe the pressure loading. It should, however, be noted that the negative phase may have a pronounced effect on the blast response of glass plates (see, e.g., [33]). In further references to Eq. 1, we will employ the reflected

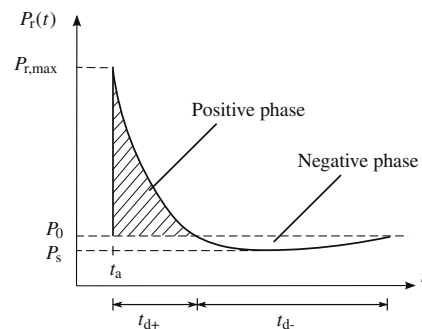


Fig. 3 Idealized pressure-time history for the reflected blast wave from an explosion [7]



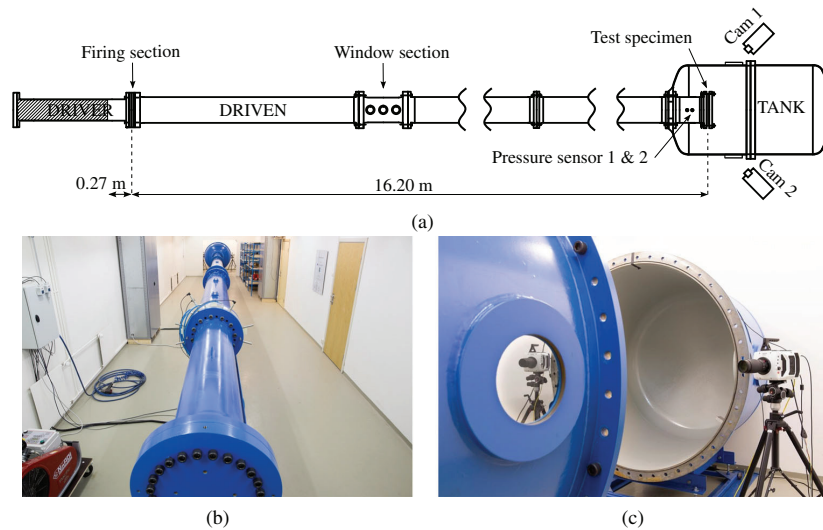


Fig. 4 Test setup in the SIMLab Shock Tube Facility (SSTF) [18, 34]: **a** sketch of the shock tube seen from above, **b** the shock tube seen from the driver, and **c** high-speed cameras on each side of the tank

overpressure, i.e., $P(t) = P_r(t) - P_0$. Additionally, the time of arrival t_a is set to 0. The maximum reflected overpressure will be denoted P_{\max} .

Blast Load Tests

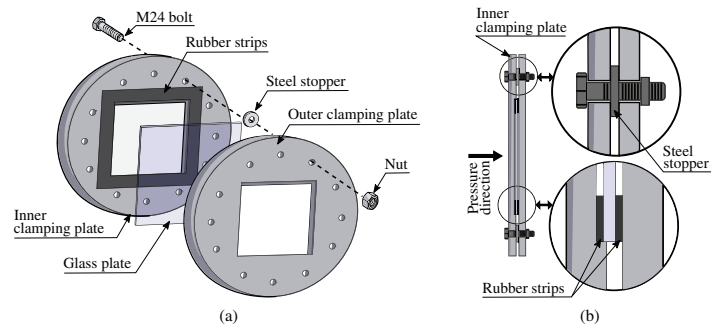
The SIMLab Shock Tube Facility (SSTF) was used to subject the laminated glass plates to blast loading similar to that from a far-field explosion. The SSTF has earlier been proven to produce planar pressure loadings onto specimens, and is a reliable and safe alternative to explosive detonations. The following text provides some information about the SSTF, and the reader is also referred to the work by Osnes et al. [18] or Aune et al. [34] for a more thorough description.

Figure 4 shows pictures of the SSTF and includes a sketch of the different parts of the shock tube as well. It consists of a high-pressure chamber (the driver), a firing section, a low-pressure chamber (the driven), a window section, and finally, a dump tank. The test specimen is attached to the end of the driven and is positioned inside the tank. The tests are carried out in the following order: (1) one or more plastic diaphragms are placed inside the firing section to separate the driver and driven; (2) air pressure (with a magnitude of P_d) is built up in the driver; (3) the diaphragms are ruptured by controlled venting of the firing section; (4) pressure waves travel down the driven and eventually take the form of a characteristic blast wave; (5) the blast wave is reflected at the specimen mounted at the end of the driven, and the pressure intensity is

increased. The reflected overpressure represents the loading experienced by the specimen. To estimate the loading, pressure data from two pressure sensors (with a logging frequency of 500 kHz) are used to fit the Friedlander equation (Eq. 1) and extrapolated to the arrival time of the blast wave at the specimen. The arrival time is estimated by assuming a constant velocity of the blast wave between the pressure sensors and the specimen. The two pressure sensors (denoted Sensors 1 and 2) are placed 245 mm and 345 mm upstream from the plate and 150 mm above the midpoint of the tested specimen; see Fig. 4(a). The pressure loading is dependent on the built-up driver pressure P_d and the volume of the driver, both of which can be varied to achieve the desired pressure loading [34]. During testing of the laminated glass, the tank is closed, and two Phantom v1610 or v2511 high-speed cameras, synchronized to each other and to the pressure recordings, are placed outside to film through windows in the tank. The recording rate of the cameras is set to either 24 kHz (v1610) or 37 kHz (v2511) in these tests. The pressure is measured by Kistler 603B piezoelectric pressure sensors with Kistler 5064 charge amplifiers and a data acquisition system from National Instruments (NI USB-6356). More details regarding the pressure measurements in the shock tube are given by Aune et al. [34].

The fastening system shown in Fig. 5 has been developed to test glass plates in the SSTF. The specimen is clamped between two 25 mm thick steel plates, referred to as the inner and outer clamping plate. The inner clamping plate is placed closest to the driven and includes a 5.7 mm deep

Fig. 5 Illustration of the fastening system used in the blast experiments on glass in the SSTF [18]: **a** disassembled setup showing one of 12 bolts, stoppers and nuts, **b** assembled section observed from the side



milled-out area to facilitate the setup. Neoprene rubber strips with a thickness of 4 mm and a width of 50 mm are glued to each clamping plate and positioned on each side of the glass. In these tests, the in-plane area of the glass specimen is 400 mm × 400 mm, while the loaded area is 300 mm × 300 mm. The outer clamping plate is fastened with 12 M24 bolts with a fixed distance of 260 mm from the centre of the glass specimen. The total radius of the clamping plates is 325 mm. On each of the bolts, we placed steel stoppers (with a diameter of 43 mm and a thickness of 11.8 mm) in order to limit the pressure on the rubber and glass while simultaneously being able to properly tighten the clamping plates together. The thickness of the steel stoppers was motivated by a clamping pressure of 14 ± 3 N/cm², specified in the European standard for testing of security glazing [35]. Since the thickness of the steel stoppers will control the compression of the rubber strips, it will also control the clamping pressure. To obtain the exact clamping pressure proved, however, to be difficult due to small variations in the thickness of the glass plate, rubber strips and clamping plate. Nonetheless, the stoppers provided a fixed test setup with proper fastening without damaging the glass plates prior to testing.

DIC Measurements

A three-dimensional point-tracking procedure was employed to obtain the deformation of the laminated glass plates during blast loading. A total of 25 white circles with a central black dot (denoted optical targets) were painted on the glass, while the in-house 3D digital image correlation (DIC) software eCorr [32] was used to track their displacements. The optical targets had a diameter of 15 mm, while the distance between them was *c/c* 60 mm in both the transverse and longitudinal direction. This procedure was previously validated and proven valid against laser measurements [18]. Note that a point-tracking procedure is chosen instead of a more traditional 3D-DIC measurement technique, which gives the complete displacement field.

This selection is done because the traditional method needs a speckle pattern that would partly obstruct the visibility of the crack initiation and propagation during blast loading of the brittle glass plates.

Test Programme

In this study, a total of 11 laminated glass plates were tested in the SSTF. Five of them were initially undamaged, while two included a 5 mm diameter centrally placed hole generated by a diamond drill. The last four laminated glass plates were centrally impacted by 7.62 mm AP bullets (with and without the brass jacket) fired from a Mauser rifle. Note that the blast loading was applied to the same side as the bullet impact, i.e., the front side. All plates had in-plane dimensions of 400 mm × 400 mm and included two 3.8 mm thick annealed float glass plates with a 1.52 mm thick PVB interlayer. Table 1 presents an overview of the tests performed in the SSTF, with information about the desired driver pressure P_d and the imposed damage. Note that the actual driver pressure may differ slightly

Table 1 Overview of the experiments performed in the SSTF

Test	P_d (kPa)	Imposed damage
L01a	860	Undamaged
L01b	860	Undamaged
L02	1000	Undamaged
L03	1200	Undamaged
L04	1500	Undamaged
H01	860	5 mm drilled hole
H02	1000	5 mm drilled hole
AP01	860	Bullet (7.62 mm AP) perforation
AP02	1000	Bullet (7.62 mm AP) perforation
CO01	860	Bullet (core only) perforation
CO02	1000	Bullet (core only) perforation



Table 2 Initial (v_i) and residual (v_r) velocities in the ballistic impact tests

Test	v_i (m/s)	v_r (m/s)	Shock tube test
1	891.7	858.3	AP01
2	892.3	859.0	AP02
3	732.7	658.7	CO01
4	671.7	571.9	CO02

from the desired pressure since the diaphragms are not instantaneously removed and that the volume of the driver will increase slightly due to deformation of the diaphragms before rupture. The initial volume of the driver was the same for all the tests (i.e., a driver length of 0.27 m [34]).

Experimental Results

Ballistic Impact Tests

Table 2 presents the measured initial (v_i) and residual (v_r) velocities of the bullet from the four ballistic impact tests. It is seen that the reduction in bullet velocity during the perforation process is rather low, meaning that the applied laminated glass does not offer much ballistic resistance. This finding demonstrates that perforation of similar laminated glass by a fragment generated by a high-explosive detonation is very likely. Table 2 also shows that the tests with the full AP bullet (i.e., Test 1 and Test 2) had higher initial velocities than those with the CO bullet (i.e., Test 3 and Test 4) resulting from an imprecise adjustment of the ammunition. As a consequence, the initial kinetic energy of the AP bullets was more than three times that of the CO bullets. Additionally, the bullet in Test 4 impacted the laminated glass with a pitch angle of 4.5 degrees, which is normally considered too high in standard ballistic testing. However, this is of minor importance in this study, as the main purpose of the ballistic tests was to impact and

perforate the laminated glass before blast loading. Consider also that a fragment will have an arbitrary shape and impact angle and that the perforation capability depends somewhat on these factors. Moreover, the appearance, i.e., the crack pattern and the penetration channel, turned out to be highly similar for the four ballistic impact tests. This similarity is shown in Fig. 6, which presents pictures of the laminated glass after ballistic testing. The pictured side is the one being impacted, i.e., the front side. It was observed that the diameter of the holes induced in the PVB interlayer by the perforating bullets was smaller than the 5 mm diameter hole drilled into the laminated glass due to the viscoelastic material behaviour of the PVB.

Figure 7 shows high-speed camera images from Test 1 (AP bullet) and Test 3 (CO bullet) at six different time points. The pixel-to-millimetre ratio in the images is approximately 32.5, while the resolution is 1024×224 pixels. The pitch angle prior to impact was negligible in these tests. It appears that the front plate of the laminated glass was crushed more extensively by the CO bullet than by the full AP bullet, presumably due to the plastic sabot not being stripped before impact. Further, the amount of fracture at the backside seems larger for the AP bullet tests than for the CO bullet tests, which was probably a result of the larger projectile diameter. In both cases, severe local fragmentation from both sides of the laminated glass was observed. The high-speed camera images reveal that the amount of damage in the hard bullet core after the impact was negligible. Finally, it appears that the brass jacket of the full AP bullet was partly stripped during the perforation process.

Blast Load Tests

Figure 8 presents the pressure readings in Sensor 1 from all 11 blast tests, subdivided into four plots based on the driver pressure P_d . Note that the sensor is located 245 mm from the specimen and therefore registers both the incident blast wave (at $t < 0$) and the reflected blast wave (at $t >$

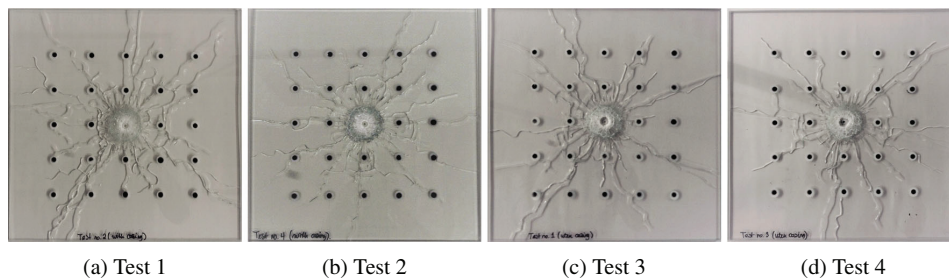


Fig. 6 Laminated glass plates after the ballistic impact tests. The two first plates in (a) and (b) were impacted by AP bullets, while the two last plates in (c) and (d) were impacted by CO bullets

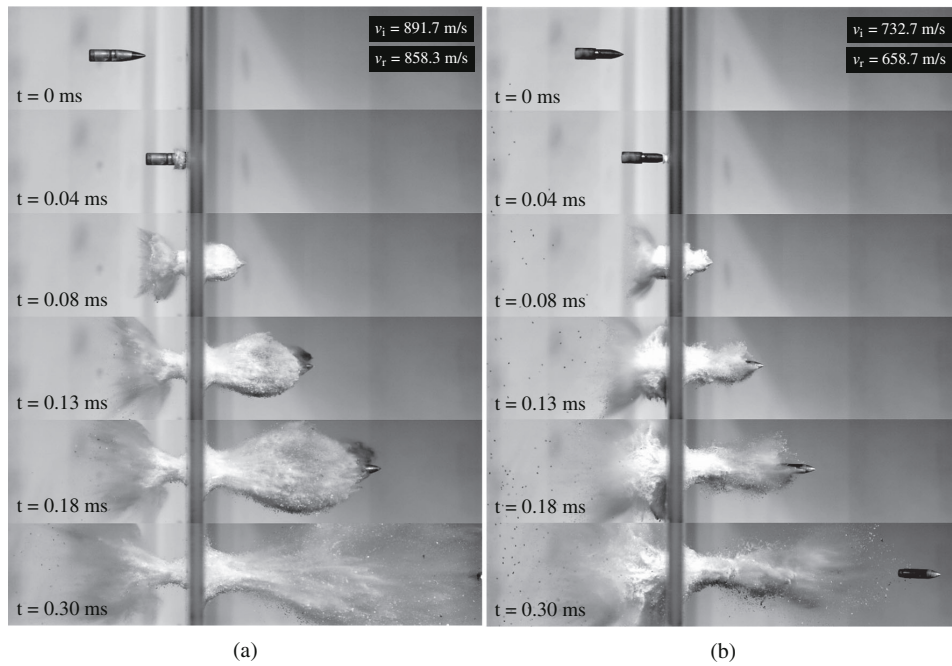


Fig. 7 High-speed camera images of the perforation process of the laminated glass by **a** an AP bullet (Test 1) and **b** a CO bullet (Test 3)

0). The figure also includes curve fits of the Friedlander equation (Eq. 1), which represent the reflected overpressure (i.e., the blast loading) on the laminated glass plates. It is

seen that tests with the same desired driver pressure P_d resulted in an almost identical pressure reading in Sensor 1 and consequently the same parameters of the Friedlander

Fig. 8 Pressure measurements in Sensor 1, including a representation of the reflected overpressure by a curve fit of the Friedlander equation for tests with P_d equal to **a** 860 kPa, **b** 1000 kPa, **c** 1200 kPa and **d** 1500 kPa

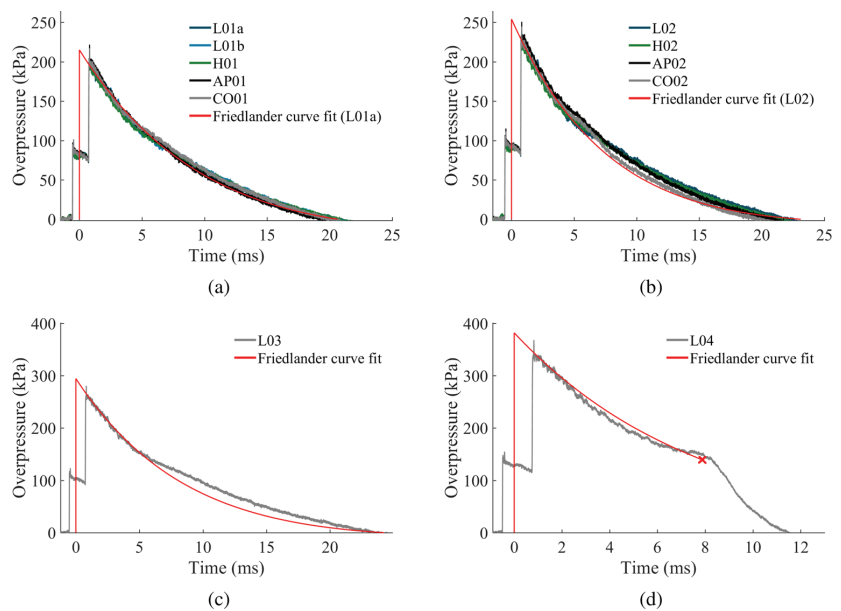
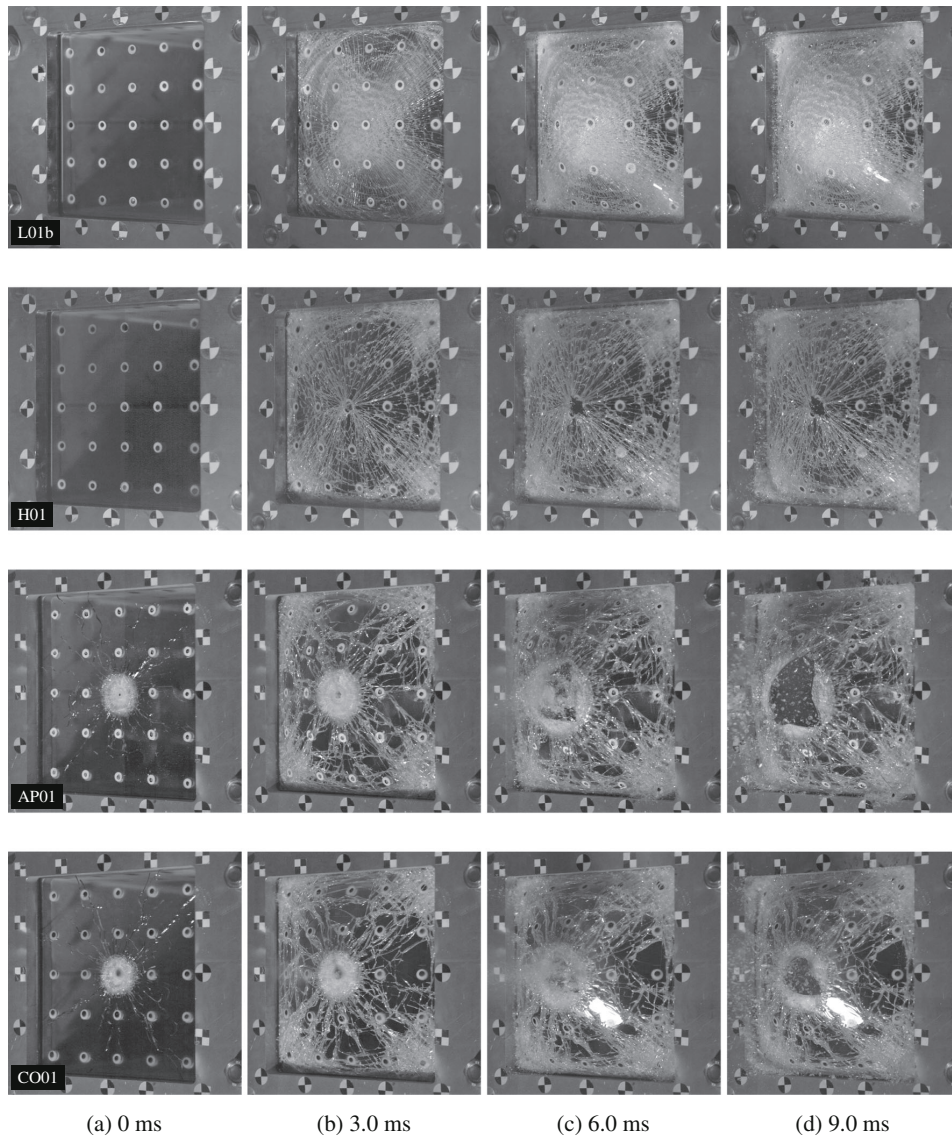


Table 3 Parameters of the Friedlander equation for the blast tests in the SSTF

Test	P_d (kPa)	P_{max} (kPa)	t_d (ms)	b (-)
L01a	860	215.2	20.62	1.42
L02	1000	254.2	20.78	1.51
L03	1200	294.5	24.02	2.04
L04	1500	382.1	×	×

equation, confirming the repeatability of the SSTF. In the tests with a desired driver pressure P_d of 860 kPa and 1000 kPa, the actual driver pressure was 859 ± 2 % kPa and 1001 ± 3.7 % kPa, respectively. The maximum reflected overpressure was 215.2 ± 2.5 % kPa and 254.2 ± 4 % kPa. The Friedlander parameters are presented in Table 3. Note that the setup for Tests L01a and L01b was identical. However, no glass fracture was observed in Test L01a, whereas for Test L01b, both glass plates fractured, demonstrating

**Fig. 9** Recorded photos of tests with $P_d = 860$ kPa captured at various points in time (see subcaptions) after t_d

the stochastic fracture behaviour of glass. The Friedlander equation for Test L04 (Fig. 8(d)) is only partially fitted due to a rapid drop in pressure after approximately 8 ms (indicated by a cross on the Friedlander curve fit). This sudden drop in pressure is due to a complete rupture of the PVB interlayer, which in turn allows the pressure to freely pass through the laminated glass, as there is no longer a surface on which to reflect the pressure.

We start by considering the five blast tests on the laminated glass without imposed damage (see Table 1). At the lowest overpressures, i.e., $P_{\max} < 300$ kPa, the PVB interlayer was intact after testing, meaning that the pressure did not pass through the protection even if both glass plates fractured and the laminated glass was severely damaged. However, as already mentioned, at an overpressure of approximately 380 kPa, the PVB interlayer

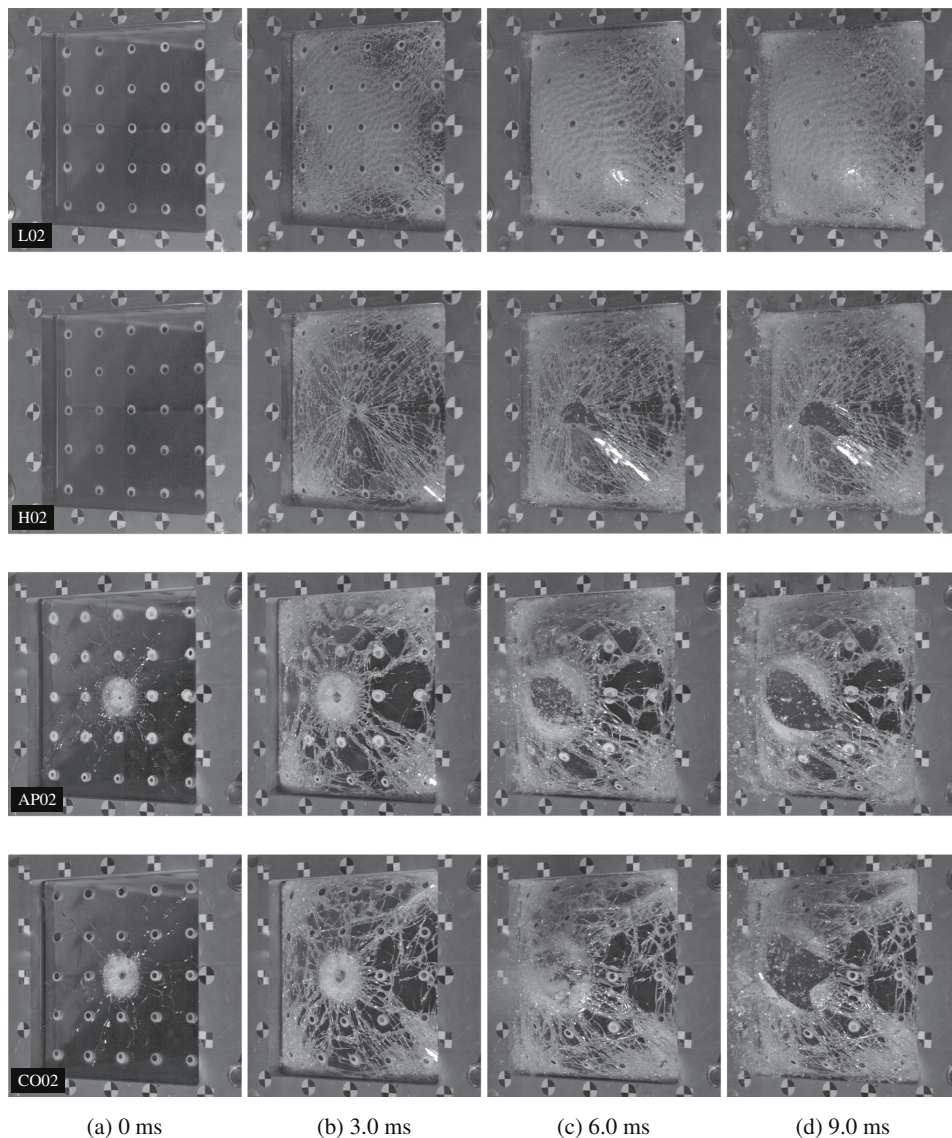


Fig. 10 Recorded photos of tests with $P_d = 1000$ kPa captured at various points in time (see subcaptions) after t_d



ruptured, allowing the pressure to freely pass through the protection. Thus, for this test setup, the total capacity of the initially undamaged laminated glass lies at an overpressure somewhere between 300 kPa and 380 kPa. It should be mentioned that although the fracture process of the glass plates is known to be highly stochastic [18], the rupturing of the PVB interlayer is assumed not to be. High-speed camera pictures at various points in time from the tests on the initially undamaged laminated glass are given in Figs. 9, 10 and 11. The pixel-to-millimetre ratio in the images is approximately 1.9, while the resolution is 768×800 pixels. It is seen that before the PVB interlayer ruptures in Test L04 (see Fig. 11), a large number of glass fragments are detached and launched from the protection. This phenomenon occurs on both sides of the PVB interlayer. Detachment of glass fragments is also observed in Test L03. The fragments have similar sizes, but the number of fragments is smaller than that in Test L04. Moreover, Tests L01b and L02 generated more powder-like fragments. Pictures from Test L01a, where failure did not occur in any of the glass plates, are not shown for brevity.

Next, we compare the response of the pre-damaged and the undamaged laminated glass plates exposed to blast loading. The pressure readings in Fig. 8(a–b) suggest that there is no particular pressure decrease at Sensor 1 due to the imposed damage in the laminated glass. However, the overall response of the plates is highly altered. This finding is illustrated in Figs. 9 and 10, which include pictures at four points in time from the different tests. The pictures

show that the specimens without imposed damage (L01b and L02) fractured into tiny fragments over most of the plate surface, whereas for the damaged plates, the fragments were in general much larger and more similar to those observed from ordinary annealed float glass [18]. More seriously, the pre-induced damage led to tearing of the PVB interlayer already at the lowest blast loading ($P_{\max} = 215$ kPa) and more so as the pressure was increased. Furthermore, the laminated glass pre-damaged by bullets were, as expected, more destroyed than those pre-damaged by drilled holes. In the former, the PVB ruptured over a larger area, and the glass fractured into larger pieces. This in turn led to detachment of more and larger glass fragments. It was also observed that fracture in the plates with pre-drilled holes initiated exactly at the hole. This observation indicates that the drilling generated micro-cracks since fracture initiation normally results from stress concentrations around pre-existing cracks. For the bullet-impacted plates, several cracks were clearly visible before testing (see Fig. 6), and fracture in the glass initiated at several places at the same time.

In contrast to Test L04, none of the pre-damaged plates exhibited complete rupture of the PVB interlayer, and a rapid drop in pressure at Sensor 1 was not observed. This result is probably because Sensor 1 is located some distance from the centre of the laminated glass and because there was still some glass surface from which to reflect pressure in these tests. It is reasonable to believe that if the pressure sensor was located closer to the plate's centre, a pressure drop would have been visible.

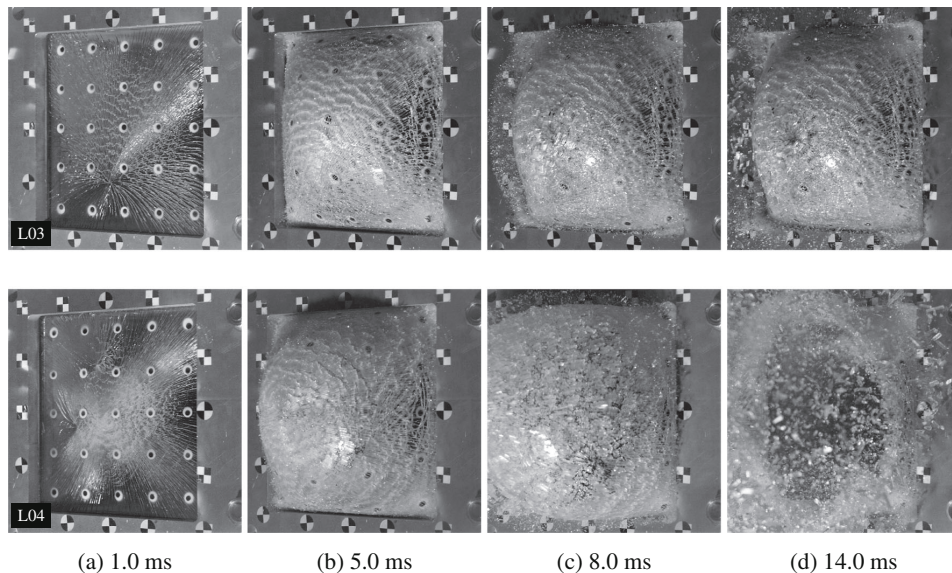


Fig. 11 Recorded photos of Tests L03 and L04 with $P_d = 1500$ kPa captured at various points in time (see subcaptions) after t_d

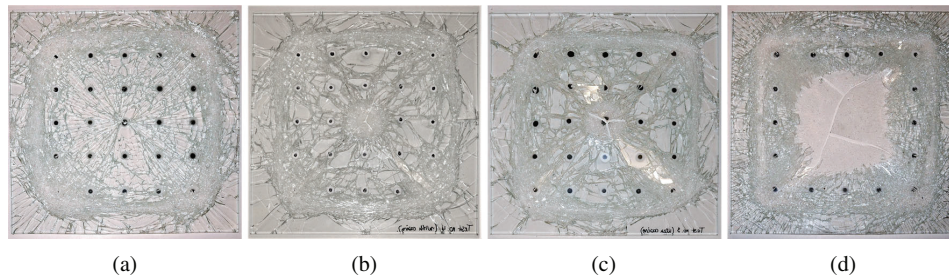


Fig. 12 Pictures of typical laminated glass specimens after blast loading for Tests **a** H02, **b** AP02, **c** CO02 and **d** L04. The pictured side is the one facing towards the cameras in the shock tube tests (backside)

It is clear from the pictures in Figs. 9 and 10 that the protective capability of the laminated glass is severely decreased if pre-damaged by fragment or bullet impact before being blast loaded since larger glass splinters are generated and detached from the PVB interlayer. Additionally, the pressure can freely pass through the protection in all cases. At these pressures, the initially undamaged laminated glass is still intact. Pictures of some representative laminated glass specimens after blast loading are shown in Fig. 12. It is seen that the PVB displays viscoelastic behaviour, with nearly no permanent deformation some time after the blast tests. The specimens also appear to be highly damaged, especially the one from Test L04. It should, however, be kept in mind that since the SSTF is a closed system, the blast wave will not disappear after the first impact. Instead, it will propagate back and forth inside the shock tube until equilibrium is re-established, and the laminated glass may be impacted several times but with decreased intensity. Thus, pictures after testing such as those shown in Fig. 12 can be misleading, as the damage may be exaggerated.

Finally, Fig. 13 presents average out-of-plane displacements versus time for four optical targets (shown in Fig. 13(c)) during blast loading. These results are obtained by using

the point-tracking procedure described earlier. The central optical target could not be tracked due to the pre-damage. As seen, when the glass plates do not fail (i.e., Test L01a), the displacements are negligible. However, when they do fail, the displacements become significant, and the blast loading is carried by membrane stretching of the ductile interlayer. Furthermore, when the laminated glass was pre-damaged, the displacement seemed to increase with the degree of initial damage, as the displacements of the glass plates pre-damaged by bullets were higher than those for the glass plates pre-damaged by a drilled hole. The displacement of the initially undamaged laminated glass plates that failed falls between those of the plates with pre-drilled holes and the plates pre-damaged by the bullets. It must be emphasized that the latter would not necessarily hold for a rerun of the undamaged plate tests. As previously mentioned, fracture in glass is a highly stochastic process, which results in variation in the position of fracture initiation. Furthermore, the position of initiation will affect the rest of the displacement history. It is also expected that the properties of the pre-induced damage will affect the overall behaviour of the laminated glass. These properties include the size, the amount, and the location of the damage.

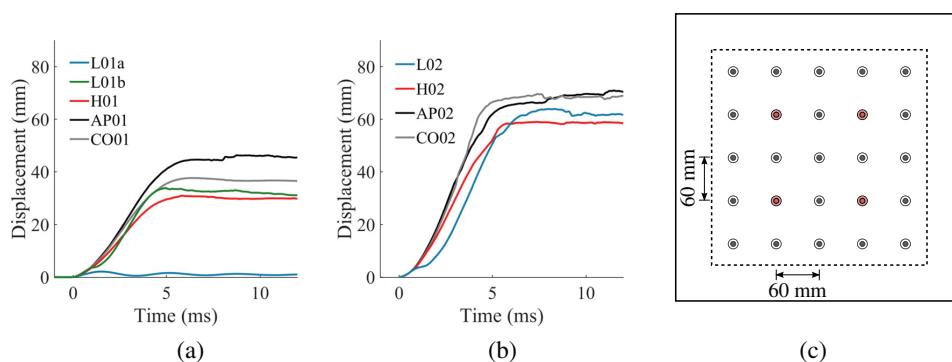


Fig. 13 Average out-of-plane displacement of four optical targets from tests with P_d equal to **a** 860 kPa and **b** 1000 kPa, while **c** shows the position of the four optical targets (marked in red) on the glass surface used in the measurements



Concluding Remarks

Whenever a high explosive detonates, an intense blast wave accompanied by free-flying fragments is generated. These fragments may have velocities and masses similar to bullets fired from rifles. Since the velocity of the propagating blast wave decays rapidly, the fragments will break through the shock front and impact any target before arrival of the blast wave if the detonation is far-field. If this target is laminated glass, mainly intended for blast protection, the fragment will most likely fracture the glass plates and perforate the interlayer. Upon arrival of the subsequent blast wave, the PVB interlayer in the damaged window may rupture completely, allowing the pressure to enter the structure together with large glass fragments detached from the laminate. Thus, the protective capability of the laminated glass may be lost if pre-damaged by fragment or bullet impact before being blast loaded.

This supposition has been proven experimentally in the current study. First, we blast loaded laminated glass (consisting of two 3.8 mm thick annealed float glass plates and a 1.52 mm thick PVB interlayer) successively in a shock tube until the laminate ruptured to determine the capacity against blast loading. Then, we pre-damaged several laminated glass specimens, either by drilling a 5 mm hole in the centre of the specimens using a diamond drill or by firing two different types of bullets at them. Lastly, the pre-damaged plates were blast loaded using the same pressures as those in the tests of the initially undamaged windows. It was found that the glass in the pre-damaged plates broke into larger fragments than the glass in the undamaged ones. This effect seemed to increase the amount and size of glass fragments detached from the PVB interlayer. Furthermore, the damage to the PVB was severely increased with the amount of pre-damage in the laminated glass. This in turn allowed the blast pressure to pass freely through the barrier. The protective capacity of the laminated glass is thus clearly reduced if it is pre-damaged by a fragment or a bullet. It is therefore highly recommended to consider fragment impact as well in the design of blast-protective windows.

Acknowledgements The present work has been carried out with financial support from the Centre of Advanced Structural Analysis (CASA), Centre for Research-based Innovation, at the Norwegian University of Science and Technology (NTNU) and the Research Council of Norway through project no. 237885 (CASA). The authors would like to acknowledge Mr. Trond Auestad for assisting with the experimental programme, and Modum Glassindustri for providing the glass specimens.

References

- Hooper PA, Sukhran RAM, Blackman BRK, Dear JP (2012) On the blast resistance of laminated glass. *Int J Solids Struct* 49(6):899–918
- Wiederhorn SM (1969) Fracture surface energy of glass. *J Am Ceram Soc* 52(2):99–105
- Larcher M, Solomos G, Casadei F, Gebbeken N (2012) Experimental and numerical investigations of laminated glass subjected to blast loading. *Int J Impact Eng* 39(1):42–50
- Zhang X, Hao H, Wang Z (2015) Experimental study of laminated glass window responses under impulsive and blast loading. *Int J Impact Eng* 78:1–19
- Pelfrene J, Kuntsche J, Van Dam S, Van Paepegem W, Schneider J (2016) Critical assessment of the post-breakage performance of blast loaded laminated glazing: experiments and simulations. *Int J Impact Eng* 88:61–71
- Wikipedia. https://en.wikipedia.org/wiki/2011_Norway_attacks, Accessed: 2018-07-07
- Cormie D, Mays G, Smith PD (2009) *Blast Effects on Buildings*, 2nd edn. Thomas Telford Publishing, Westminster
- U.S. Army, TM5-855-1, *Fundamentals of protective design for conventional weapons*, Chapter 7: Fragmentation, Technical Manual
- Arnold W, Rottenkolber E (2008) Fragment mass distribution of metal cased explosive charges. *Int J Impact Eng* 35(12):1393–1398
- Grisaro HY, Benamou D, Dancygier AN (2018) Investigation of blast and fragmentation loading characteristics—field tests. *Eng Struct* 167:363–375
- Guo ZW, Huang GY, Liu CM, Feng SS (2018) Velocity axial distribution of fragments from non-cylindrical symmetry explosive-filled casing. *Int J Impact Eng* 118:1–10
- Nyström U, Gylltoft K (2009) Numerical studies of the combined effects of blast and fragment loading. *Int J Impact Eng* 36(8):995–1005
- Grisaro HY, Dancygier AN (2018) Characteristics of combined blast and fragments loading. *Int J Impact Eng* 116:51–64
- Leppänen J (2005) Experiments and numerical analyses of blast and fragment impacts on concrete. *Int J Impact Eng* 31(7):843–860
- Hutchinson MD (2009) The escape of blast from fragmenting munitions casings. *Int J Impact Eng* 36(2):185–192
- Grisaro HY, Dancygier AN (2018) Spatial mass distribution of fragments striking a protective structure. *Int J Impact Eng* 112:1–14
- NS-EN 572-1: Glass in building – Basic soda-lime silicate glass products – Part 2: Float glass, Standard CEN (2012)
- Osnes K, Børvik T, Hopperstad OS (2018) Testing and modelling of annealed float glass under quasi-static and dynamic loading. *Eng Fract Mech* 201:107–129
- Wachtman JB, Cannon WR, Matthewson MJ (2009) *Mechanical Properties of Ceramics*, 2nd edn. Wiley, Hoboken
- NS-EN 572-1: Glass in building – Basic soda-lime silicate glass products – Part 1: Definitions and general physical and mechanical properties Standard CEN (2012)
- Anstis G, Chantikul P, Lawn BR, Marshall D (1981) A critical evaluation of indentation techniques for measuring fracture toughness: I, Direct crack measurements. *J Am Ceram Soc* 64(9):533–538
- Peroni M, Solomos G, Pizzinato V, Larcher M (2011) Experimental investigation of high strain-rate behaviour of glass. In: *Applied Mechanics and Materials*, vol 82. Trans Tech Publ, pp 63–68
- Zhang X, Zou Y, Hao H, Li X, Ma G, Liu K (2012) Laboratory test on dynamic material properties of annealed float glass. *International Journal of Protective Structures* 3(4):407–430
- Del Linz P, Wang Y, Hooper P, Arora H, Smith D, Pascoe L, Cormie D, Blackman B, Dear J (2016) Determining material response for Polyvinyl Butyral (PVB) in blast loading situations. *Exp Mech* 56(9):1501–1517
- Zhang X, Hao H, Shi Y, Cui J (2015) The mechanical properties of polyvinyl butyral (PVB) at high strain rates. *Constr Build Mater* 93:404–415



26. Hooper PA, Blackman BRK, Dear JP (2012) The mechanical behaviour of poly (vinyl butyral) at different strain magnitudes and strain rates. *J Mater Sci* 47(8):3564–3576
27. Franz J, Schneider J (2014) Through-cracked-tensile tests with polyvinylbutyral (PVB) and different adhesion grades. In: *Engineered Transparency International Conference at Glasstec*, pp 135–142
28. Børvik T, Dey S, Clausen A (2009) Perforation resistance of five different high-strength steel plates subjected to small-arms projectiles. *Int J Impact Eng* 36(7):948–964
29. Holmen JK, Johnsen J, Jupp S, Hopperstad OS, Børvik T (2013) Effects of heat treatment on the ballistic properties of AA6070 aluminium alloy. *Int J Impact Eng* 57:119–133
30. Forrestal M, Børvik T, Warren T (2010) Perforation of 7075-T651 aluminum armor plates with 7.62 mm APM2 bullets. *Exp Mech* 50(8):1245–1251
31. Børvik T, Forrestal M, Warren T (2010) Perforation of 5083-H116 aluminum armor plates with ogive-nose rods and 7.62 mm APM2 bullets. *Exp Mech* 50(7):969–978
32. Fagerholt E (2012) Field measurements in mechanical testing using close-range photogrammetry and digital image analysis, Ph.D. thesis, Norwegian University of Science and Technology (NTNU) Trondheim
33. Krauthammer T, Altenberg A (2000) Negative phase blast effects on glass panels. *Int J Impact Eng* 24(1):1–17
34. Aune V, Fagerholt E, Langseth M, Børvik T (2016) A shock tube facility to generate blast loading on structures. *International Journal of Protective Structures* 7(3):340–366
35. NS-EN 13541: Glass in building – Security glazing- Testing and classification of resistance against explosion pressure, Standard CEN (2012)

Publisher's Note Springer Nature remains neutral with regard to jurisdictional claims in published maps and institutional affiliations.



PART 3

Karoline Osnes, Jens Kristian Holmen, Odd Sture Hopperstad, Tore Børvik

Fracture and fragmentation of blast-loaded laminated glass: an experimental and numerical study

International Journal of Impact Engineering 132 (2019) 103334.

<https://doi.org/10.1016/j.ijimpeng.2019.103334>



Contents lists available at ScienceDirect

International Journal of Impact Engineering

journal homepage: www.elsevier.com/locate/ijimpeng

Fracture and fragmentation of blast-loaded laminated glass: An experimental and numerical study

Karoline Osnes^{*,a,b}, Jens Kristian Holmen^a, Odd Sture Hopperstad^{a,b}, Tore Børvik^{a,b}^a Structural Impact Laboratory (SIMLab), Department of Structural Engineering, Norwegian University of Science and Technology (NTNU), Trondheim, NO-7491, Norway^b Centre for Advanced Structural Analysis (CASA), NTNU, NO-7491, Trondheim, Norway

ARTICLE INFO

Keywords:

Blast experiments
Laminated glass
Shock tube
Numerical simulations
Node splitting

ABSTRACT

In this study, we use the explicit finite element method in combination with higher order elements and 3D node splitting to simulate fracture and fragmentation of blast-loaded laminated glass. Node splitting is a modelling technique where elements are separated instead of being eroded when a fracture criterion is reached. The resulting FE simulations are thus capable of describing behaviours such as fragmentation without loss of mass or momentum, fine cracking of the glass plates, and delamination and separation between the glass and the polymer interlayer. The simulations are compared to blast experiments conducted in a shock tube. In total, 15 laminated glass specimens (consisting of annealed float glass plates and PVB) were tested at five different pressure levels. The time and position of fracture initiation in the glass plates varied, which in turn resulted in varying post-fracture behaviour within the different pressure levels. The simulations were in good agreement with the blast tests, revealing the potential of the selected numerical method. Additional simulations of monolithic (i.e., non-laminated) glass plates were conducted and compared to experiments that were presented in an earlier study. Again, these simulations displayed a highly comparable response to the experiments, and were able to describe crack branching, formation of large glass splinters and free-flying fragments.

1. Introduction

In recent years, extreme conditions such as blast and impact loading have become important aspects in structural design. Window systems are generally considered the most vulnerable part of a structural facade, as they mainly consist of annealed float glass. Glass is a brittle material, and when it fails, it will break in a sudden manner into numerous sharp fragments. Laminated glass is often used as an alternative to increase the safety of window systems in the event of an explosion or an impact, and consists of two or more glass plates bonded together with a polymer interlayer, usually polyvinyl butural (PVB). The polymer interlayer retains broken glass fragments and increases the loading resistance of the window system. If a flexible polymer is used (e.g., PVB), deformation of the interlayer absorbs energy, which in turn reduces the energy transmitted to the rest of the structure. The post-fracture behaviour of laminated glass subjected to blast loading is a complex process and has been a topic of research for several years. The open literature includes many experimental studies on blast-loaded laminated glass, both field tests [1–4] and shock tube tests [5–7]. In a recent study by Osnes et al. [8], the combined effect of fragment impact and blast loading on laminated glass was studied experimentally. A number of researchers

have used finite element (FE) simulations with the aim of recreating the mechanical behaviour observed in the experiments. Among them, Larcher et al. [1] studied the behaviour of a solid element model, a shell element model and a smeared model, and concluded that the solid element model gave the most accurate result. Hooper et al. [2] developed a shell element model where the stiffness of the glass layer was set to zero when it fractured. The technique gave comparable results to experiments. Zhang et al. [4] studied the failure mechanisms of laminated window systems through FE simulations, and found that the boundary conditions dominate the behaviour. The study emphasised the importance of accurate modelling of the window frame. Pelfrene et al. [7] developed a detailed FE model of a blast-loaded laminated glass, and investigated the possibility of delamination between the glass and the PVB. The numerical model was able to capture many aspects of the post-fracture behaviour. However, the authors emphasised the need of a very fine mesh to model the fracture and delamination processes accurately when using element erosion. Another study of importance is the experimental and numerical investigation of pre-cracked laminated glass specimens under tensile loading by Del Linz et al. [9]. The authors found that the delamination process in terms of delamination energy is dependent on the loading rate. Franz and Schneider [10] performed

* Corresponding author at: Centre for Advanced Structural Analysis (CASA), NTNU, NO-7491, Trondheim, Norway.

E-mail address: karoline.osnes@ntnu.no (K. Osnes).<https://doi.org/10.1016/j.ijimpeng.2019.103334>

Received 29 March 2019; Received in revised form 19 June 2019; Accepted 28 June 2019

Available online 29 June 2019

0734-743X/© 2019 The Authors. Published by Elsevier Ltd. This is an open access article under the CC BY license (<http://creativecommons.org/licenses/by/4.0/>).

similar experiments and showed that the delamination properties are strongly dependent on the adhesion level between the PVB and the glass. The delamination properties are also found to be dependent on the ambient temperature [11]. Other aspects to consider is the probabilistic fracture strength of glass, which arises from microscopic flaws located on the surface [12]. In a recent work by Osnes et al. [13], the strength of glass plates exposed to an arbitrary loading history was estimated by a stochastic strength model. The model utilises stress fields from FE simulations and performs virtual experiments on a large number of glass plates. The stochastic strength model is based on the work of Yankelevsky [14].

In the current study, we use the explicit finite element method combined with higher-order elements and node splitting in simulations of blast-loaded laminated glass specimens. Node splitting is an alternative to element erosion, in which elements are separated instead of deleted when a fracture criterion is reached. By employing node splitting, a number of obstacles associated with element erosion are avoided. To further demonstrate the use of the modelling techniques, we also run simulations of blast-loaded monolithic (i.e., non-laminated) glass plates. The simulations of both laminated and monolithic glass are compared to blast experiments performed in a shock tube [15]. A total of 15 laminated glass specimens (made from annealed float glass plates and PVB) were tested at five different pressure levels. The time and position of fracture initiation varied in the tests, which in turn resulted in varying post-fracture behaviour within the different pressure levels. The experiments on monolithic glass were presented in an earlier study by Osnes et al. [13]. In the FE simulations presented in this study, glass fracture takes place upon reaching a deterministic failure criterion. Since the fracture strength of glass is probabilistic, this is a simplification of the problem. However, as the main purpose of the numerical study is to investigate the applicability of the selected simulation method, this simplification is deemed justifiable, even if the stochastic fracture behaviour of glass should be considered in the design of laminated glass components.

2. Materials

2.1. Float glass

The laminated glass used in this study consists of clear soda-lime silica float glass, which has undergone an annealing process. This process results in glass plates with nearly no internal residual stresses. Float glass is a brittle material and has a linear elastic behaviour until it fails suddenly into sharp fragments. Fracture in glass typically initiates in microscopic flaws randomly located on the surface, which results in a highly stochastic fracture behaviour [13]. The flaws also cause glass plates to primarily fail in tension, since crack propagation is induced by mode I loading (i.e., opening of a flaw) [12]. Commonly used material parameters for float glass are presented in Table 1 [16]. The fracture toughness K_{IC} is the critical stress intensity factor for mode I loading. The value stated in the table is based on quasi-static tests by Wiederhorn [17]. It should, however, be noted that the fracture strength of glass is found to be strain-rate sensitive [18,19], which could affect the fracture toughness. The strain-rate dependency is believed to be caused by a type of stress-corrosion [20], i.e., a phenomenon driven by water vapour in the surroundings [21].

Table 1
Material parameters for soda-lime-silica glass.

Density ρ	Young's modulus E	Poisson's ratio ν	Fracture toughness K_{IC}
2500 kg/m ³	70000 MPa	0.2	0.75 MPa \sqrt{m}

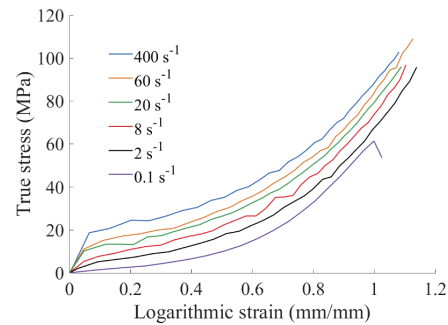


Fig. 1. Selected tensile tests on PVB performed by Hooper et al. [22] and Del Linz et al. [24]. The legend refers to the nominal strain rate.

2.2. Polyvinyl butyral (PVB)

The laminated glass used in this study includes an interlayer made from polyvinyl butyral (PVB). It is the most commonly used interlayer in laminated window glass, and is also frequently used as a component in automobile windshields [7]. PVB is a highly flexible material, and may undergo large strains before failure. Additionally, it exhibits temperature and strain-rate dependent nonlinear behaviour [22–24] with hardly any permanent deformation some time after loading [23]. PVB is usually considered to be nearly incompressible [1], and it has been reported that the failure strain of PVB decreases with increasing strain rate [23]. The viscoelastic response of PVB is illustrated in Fig. 1, which shows true stress-logarithmic strain curves from uniaxial tensile tests at different strain rates. It is seen that the curves from the high strain-rate tests include a point where the stiffness changes. This effect is not observed at low strain rates. The uniaxial tensile tests presented in Fig. 1 were performed on PVB dogbone specimens by Hooper et al. [22] and Del Linz et al. [24].

2.3. Laminated glass

Laminated glass consists of two or more glass plates bonded together with a polymer interlayer (usually PVB). The bonding is mainly a result of a process including heat and pressure in an autoclave. Compared to monolithic glass, laminated glass has several beneficial attributes. If the glass breaks, the glass fragments adhere to the polymer, resulting in a safer glass solution, especially against blast and impact loading. The interlayer also provides additional resistance by distributing forces over a larger area of the plate. A flexible interlayer, such as PVB, can also absorb energy during loading and in turn reduce the energy transmitted to the rest of the structure (e.g., building or automobile). The pre-fracture behaviour of laminated glass is relatively simple, with linear-elastic behaviour of the glass plates [1]. The interlayer transfers shear forces between the glass layers to a varying extent depending on the stiffness of the interlayer. After fracture of the glass plates, the behaviour is more complex. Delamination occurs between the glass and the interlayer around the cracks in the glass, which leads to stretching of the interlayer. A strong adhesion between the interlayer and glass might not be desirable as this can lead to stretching over a small area and tearing of the interlayer [7]. However, a sufficient adhesion level must be achieved to limit the amount of detaching glass fragments. The adhesion level is dependent on the autoclave process and the applied polymer type.

3. Experimental study

3.1. Blast loading

In the event of a chemical explosion, a shock wave is generated and followed by a series of pressure waves, thus forming a blast wave. The blast pressure, i.e., the pressure profile of the blast wave, is dependent on factors such as the standoff distance and the size of the explosive charge. When the distance from the detonation increases, the intensity of the blast pressure decreases, while the duration increases. The blast pressure can be categorised as either an incident blast pressure or a reflected blast pressure. The loading experienced by a structure is the reflected overpressure, i.e., the reflected blast pressure relative to the atmospheric pressure. The loading history typically consists of a positive overpressure phase and a negative overpressure phase, where the latter will have a lower intensity and often a longer duration. The positive overpressure phase can be described by the modified Friedlander equation [25], given by

$$P(t) = P_{\max} \left(1 - \frac{t}{t_{d+}} \right) \exp \left(-b \frac{t}{t_{d+}} \right) \quad (1)$$

where P_{\max} is the maximum reflected overpressure, t_{d+} is the duration of the positive phase, and b is the decay coefficient used to describe the shape of the overpressure-time curve. Note that $t = 0$ refers to the arrival time of the blast wave. The negative phase is negligible compared to the positive phase in the experiments presented in this study. Thus, the modified Friedlander equation is sufficient to describe the blast loading on the laminated glass specimens. It should, however, be noted that the negative phase may have a pronounced effect on the blast response of glass plates (see, e.g., [26]).

3.2. Blast testing

The laminated glass was subjected to pressure loads generated by a shock tube, which is located at SIMLab at the Norwegian University of Science and Technology (NTNU). The produced loading history is similar to that of far-field explosions, and the shock tube is thus a safe alternative to explosive detonations [15]. Fig. 2 shows a sketch of the shock tube. It consists of a high-pressure chamber (the driver section), a firing section, a low-pressure chamber (the driven section), a window section, and a dump tank (with a volume of 5.1 m³). The laminated glass specimen is attached to the end of the driven section which is positioned inside the dump tank. The pressure load is produced by built-up air pressure (in the driver section) that is sent down the driven section and transformed into a characteristic blast wave. When the blast wave reaches the test specimen, it is reflected and the pressure intensifies. The reflected overpressure represents the loading experienced by the laminated glass. We refer to the work by Aune et al. [15] for a detailed description and validation of the shock tube, and for the general experimental setup. The current blast tests were filmed by two synchronised high-speed cameras of type Phantom v1610 (with a recording rate of 24 kHz) or Phantom v2511 (with a recording rate of 37 kHz). The reflected overpressure is estimated by curve fitting the Friedlander equation (Eq. (1)) to data from two piezoelectric pressure sensors (denoted sensors 1 and 2 in Fig. 2). The sensors are placed 245 mm and 345 mm upstream the laminated glass specimen, and have a recording rate of 500 kHz. A validation of the curve-fitting procedure can be found in Aune et al. [15]. The validation was performed using a massive steel plate equipped with several pressure sensors. The Friedlander curve fit based on sensors 1 and 2 showed excellent agreement with pressure measurements directly on the massive steel plate. Note that, if the displacements of the specimen are large during loading,

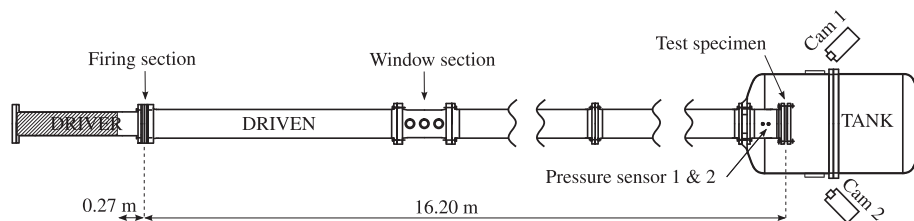


Fig. 2. Sketch of the shock tube seen from above [15].

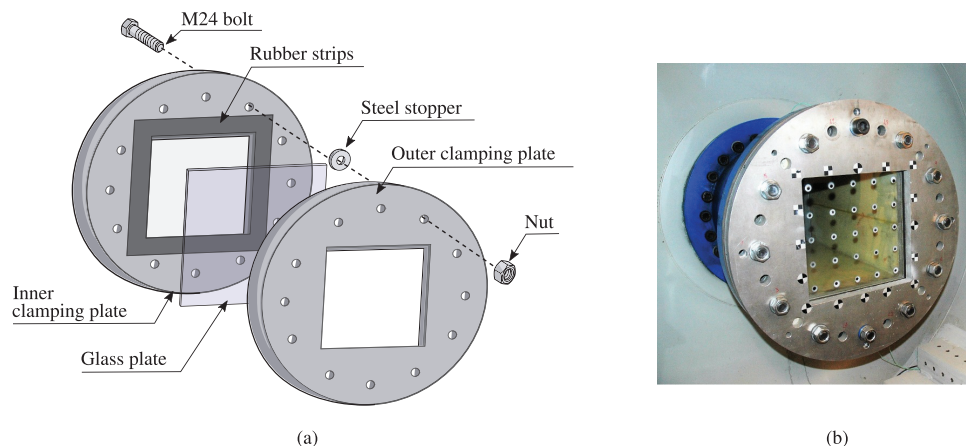


Fig. 3. The custom-made fastening system for glass testing [13]: (a) disassembled, (b) assembled, showing the optical targets on the glass surface.

Table 2
Results from the blast tests on laminated glass for the five different classes of loads.

Test	P_{\max} (kPa)	t_{d+} (ms)	b (-)	t_{frac} (ms)	D_{\max} (mm)	i_+ (kPa · ms)	Comment
A-01	167.8	18.89	1.18	×	3.74	1109.3	No fracture
A-02	168.7	18.78	1.15	×	3.55	1117.9	No fracture
A-03	169.7	19.37	1.18	×	3.56	1150.3	No fracture
A-04	172.4	18.87	1.21	0.92	5.79	1129.2	Fracture in back plate
B-01	204.3	19.60	1.39	×	4.25	1324.5	No fracture
B-02	205.5	19.65	1.29	×	4.59	1371.7	No fracture
B-03	206.3	20.01	1.35	×	4.38	1379.9	No fracture
C-01	215.2	20.62	1.42	×	4.54	1456.2	No fracture
C-02	215.6	20.78	1.51	0.75	69.67	1462.8	Fracture in both plates
D-01	231.7	21.40	1.63	1.08	93.80 ^a	1541.4	Fracture in both plates
D-02	237.4	20.23	1.44	0.63	95.41	1567.8	Fracture in both plates
D-03	237.7	21.09	1.48	0.75	121.61 ^a	1619.5	Fracture in both plates
D-04	238.9	21.40	1.52	1.08	92.53	1634.6	Fracture in both plates
E-01	254.2	23.10	2.21	1.03	99.18	1674.5	Fracture in both plates
E-02	258.9	24.20	1.98	0.42	111.61 ^a	1786.8	Fracture in both plates

^a The middle optical target was no longer traceable after the specified D_{\max} .

there may be an interaction between the specimen and the air, i.e., a fluid-structure interaction (FSI) effect. This interaction could cause a disagreement between the actual and the curve-fitted reflected overpressure. More details regarding the pressure measurements in the shock tube can be found in the work by Aune et al. [15].

Fig. 3 shows a custom-made fastening system for blast testing of glass specimens in the shock tube. The specimen is clamped between two 25 mm thick aluminium plates. Neoprene rubber strips (with a thickness of 4 mm, width of 50 mm, and a hardness of IRHD 50 ± 10) are glued to the clamping plates and hence positioned on each side of the glass. The inner clamping plate is placed closest to the driven section, and includes a 5.7 mm deep milled-out area to facilitate the setup. To properly fasten the outer clamping plate while limiting the clamping pressure on the glass, steel stoppers are placed on the bolts that connect the two clamping plates together. In total, twelve equidistant M24 bolts are used. The glass specimen has dimensions 400 mm × 400 mm, while the loaded area is 300 mm × 300 mm. For more details on the experimental setup, we refer to Osnes et al. [13].

To measure the deformation of the laminated glass and possible movements of the clamping plate during testing, we employed three-dimensional digital image correlation (3D-DIC). Checkerboard stickers with dimensions 12 mm × 12 mm were placed on the outer clamping plate, and 25 white circles with a central black dot, denoted optical targets, were spray-painted on the glass, see Fig. 3b. The distance between the circles was c/c 60 mm in both in-plane directions. A point-tracking procedure, available in the in-house 3D-DIC software eCorr [27], was used to track the optical targets and the checkerboard stickers

from the high-speed images of the tests. If a speckle pattern was painted on the laminated glass, we could have obtained the displacement field from 3D-DIC. However, this was not done, as it would reduce the visibility of fracture initiation and propagation in the glass plates during the tests. The point-tracking procedure was validated in Ref. [13].

3.3. Experimental results

Fifteen laminated glass specimens, consisting of two 3.8 mm thick glass plates and a 1.52 mm thick PVB interlayer, were tested. Table 2 presents results from these tests in terms of the maximum reflected overpressure P_{\max} , Friedlander parameters t_{d+} and b , time of fracture initiation t_{frac} , maximum mid-point displacement D_{\max} , and impulse of the positive pressure phase i_+ . The table also includes a comment on whether fracture occurred in the glass plates or not. PVB fracture was not visible in any of the tests. The glass plate closest to the cameras, i.e., farthest away from the pressure load, is referred to as the back plate in this study. The maximum mid-point displacements were corrected for the average displacements of the outer clamping frame. This correction did not significantly alter the results since the average frame displacement never exceeded 0.2 mm.

The experimental programme is divided into five classes, denoted A, B, C, D and E, based on the intensity of the maximum reflected overpressure. The logging frequency of the high-speed cameras was 37 kHz for tests B-01, C-01 and E-01. For the remaining tests, the logging frequency was 24 kHz. The velocity of the shock wave was measured to be between 427 m/s and 463 m/s, resulting in a Mach number above 1 in

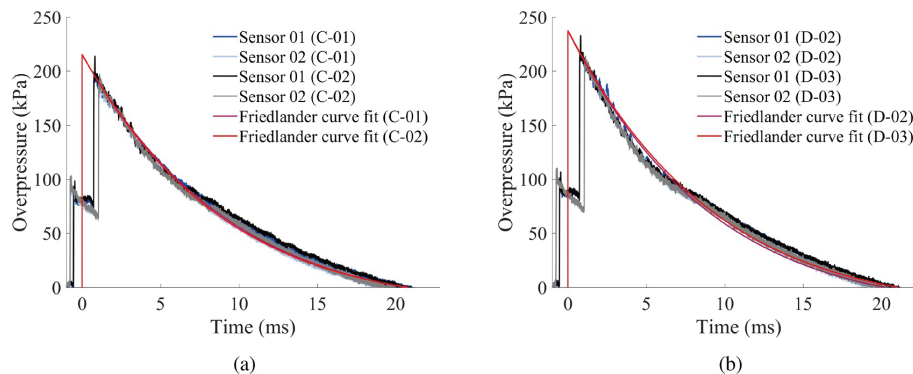


Fig. 4. Pressure measurements in sensors 1 and 2, including a representation of the reflected overpressure (Friedlander curve fit) for tests (a) C-01 and C-02, (b) D-02 and D-03.

all tests. These measurements were based on the recorded time used by the shock wave to travel between sensors 1 and 2, and the known distance between them. Examples of pressure data from the two sensors, including a Friedlander curve fit, are presented in Fig. 4. Note that the sensors are located some distance from the specimen, and therefore registers both the incident blast wave (at $t < 0$) and the reflected blast wave (at $t > 0$). The specimen is loaded by the reflected overpressure, represented by the fitted Friedlander curve. The results from Fig. 4

show that the pressure-time curves are highly similar despite the markedly different response of the plates within a class.

In tests D-01, D-03 and E-02, the mid-point optical target was no longer traceable after the specified D_{max} due to small glass fragments obstructing the visibility of the targets. Therefore, the true D_{max} might have been larger in these tests. The complete mid-point displacement versus time curves for all tests are displayed in Fig. 5. It is clear that the displacements are limited if fracture is not present in both glass plates.

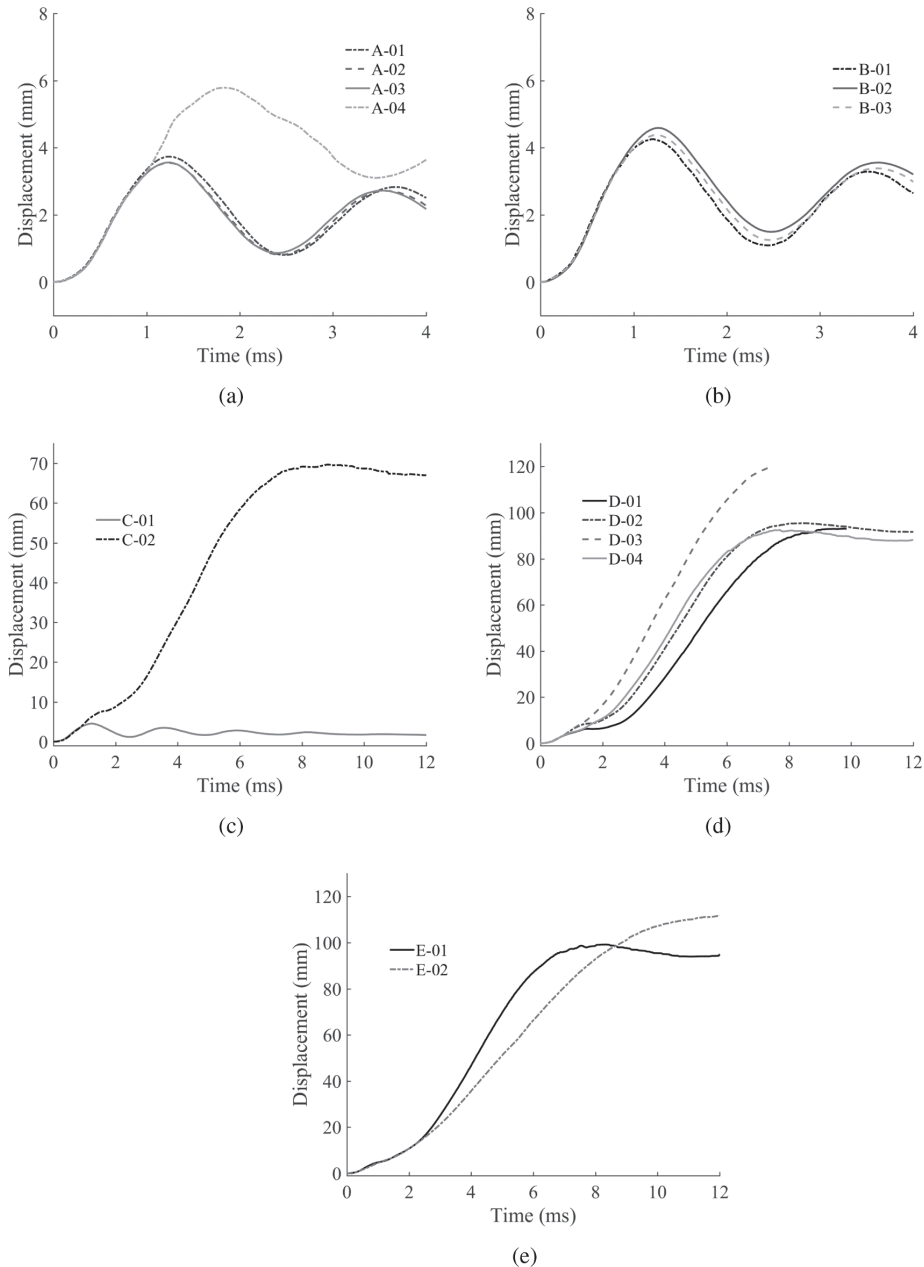


Fig. 5. Mid-point displacement versus time curves for all tests in class (a) A, (b) B, (c) C, (d) D and (e) E.

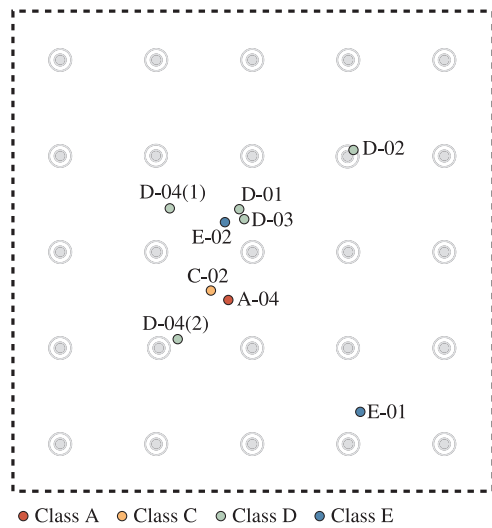


Fig. 6. Position of fracture initiation in the laminated glass based on all blast tests.

In test A-04, fracture occurred only in the back plate. This resulted in a different behaviour compared to the rest of the plates in class A for which no fracture occurred. Fig. 5 also illustrates that the displacements of the laminated glass specimens differ despite the pressure load being similar. This difference is caused by a variation in the position and time of fracture initiation in the tests. It seems that the fracture initiation governs a great deal of the subsequent behaviour of the laminated glass. When fracture is absent, the behaviour is similar. Furthermore, the tests depict the probabilistic fracture strength of glass. Fracture occurred (in the back plate) in one test of class A, but not for any of the tests of class B. In addition, fracture occurred (in both plates) for only one of the two tests of class C.

Fig. 6 shows the points of fracture initiation in the different tests. The dashed lines in the figure refer to the outer edges of the loading area, while the grey circles show the position of the optical targets. Note that for test D-04, fracture initiated at two different places at approximately the same time, referred to as (1) and (2). All fractures initiated in the back plate. The information from Table 2 and Figs. 5 and 6 suggest that a laminated glass displays a larger displacement when fracture initiates early and at the mid-point.

Detailed photo series from one of the high-speed cameras of tests A-04, C-02, D-03 and E-01 are presented in Figs. 7–10. As previously mentioned, only the back glass plate fractured in test A-04 (see Fig. 7). This implies that the PVB was not activated and therefore not allowed

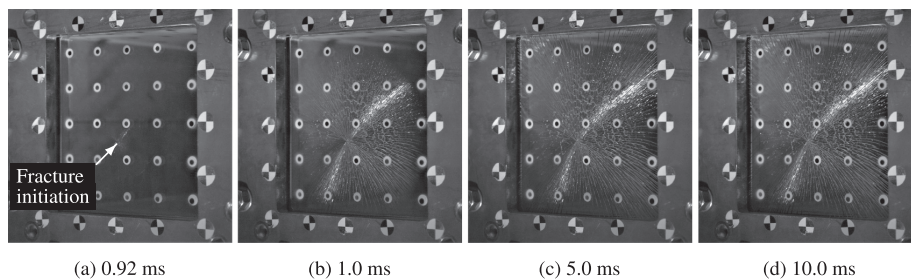


Fig. 7. Recorded photos in test A-04 captured at various points in time (see subcaptions).

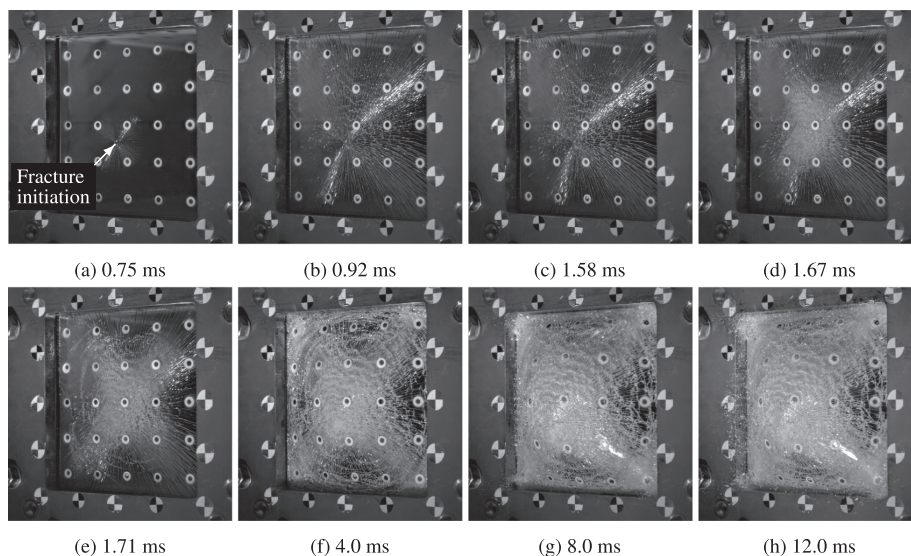


Fig. 8. Recorded photos in test C-02 captured at various points in time (see subcaptions).

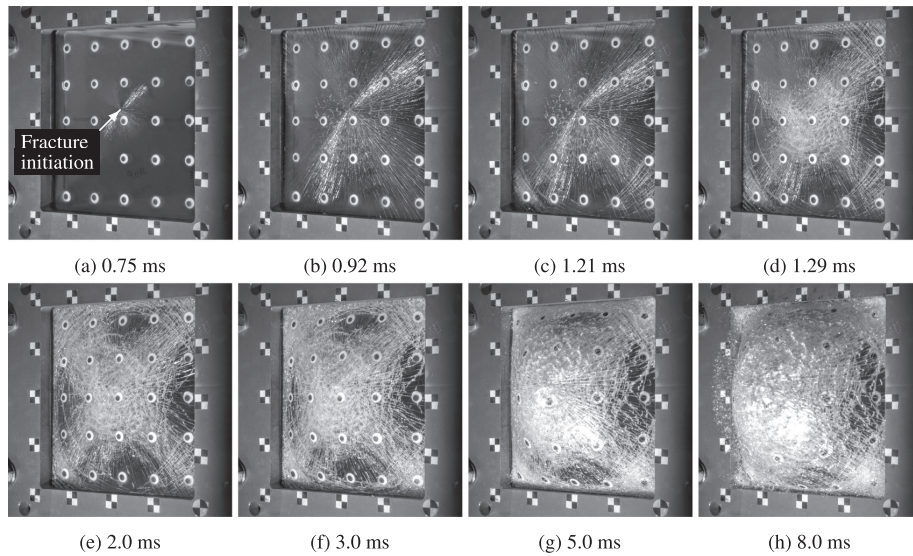


Fig. 9. Recorded photos in test D-03 captured at various points in time (see subcaptions).

to deform as a membrane. The glass fracture initiated close to the midpoint (a), and the cracks propagated towards the frame (b-c). Afterwards, there was no visible change in the appearance (d). In test C-02, both glass plates fractured and the PVB deformed significantly (see Fig. 8). Fracture initiated close to the mid-point of the back plate (a), with radial cracks propagating towards the edges (b-c). After some time, the front plate failed (d), and circumferential cracks formed in both glass plates (e-f). Towards the end of the test, nearly the entire plate was cracked into small pieces, owing to the significant deformation of the PVB. Delamination was also clearly visible (g-h). In test D-03, a slightly different sequence of events was obtained (see Fig. 9). As

in test C-02, fracture initiated close to the mid-point (a), with subsequent radial crack propagation (b). However, forming of circumferential cracks occurred earlier and closer to the corners (c-f). Delamination was also observed in this test (g-h). In test E-01 (Fig. 10), fracture initiation occurred far from the mid-point (a), giving a highly different fracture pattern than in tests C-02 and D-03, with non-radial cracks propagating from the initiation point (b-c). After some time the appearance was similar to tests C-02 and D-03, with fracture in the front plate (d), growth of circumferential cracks (e), cracking into small fragments in both glass plates (f), and subsequent delamination (g-h).

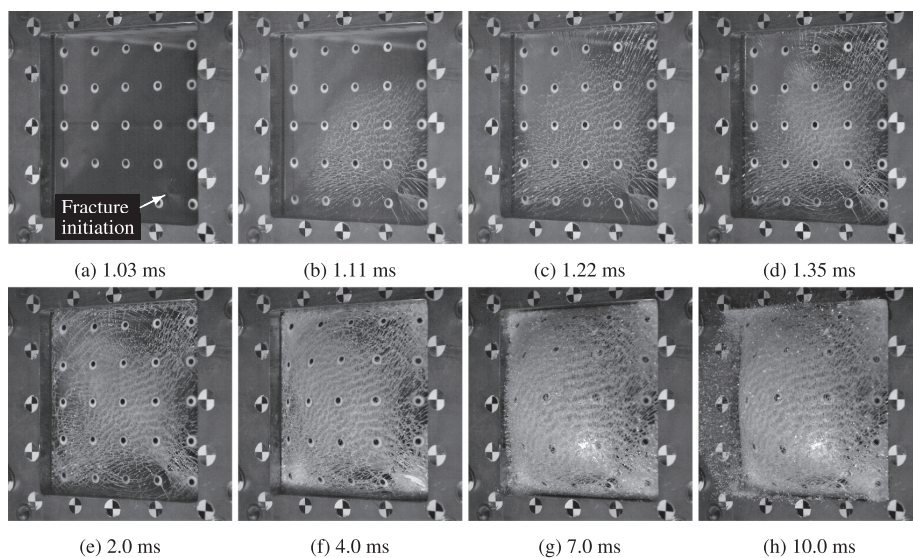


Fig. 10. Recorded photos in test E-01 captured at various points in time (see subcaptions).

4. Material modelling

4.1. Float glass

In this study, the float glass is modelled as a linear elastic material with a brittle failure criterion. The elastic behaviour is determined by Young's modulus E and Poisson's ratio ν given in Table 1. Fracture initiation occurs when a damage parameter D has evolved from 0 to 1 in an integration point, and is defined as

$$D = \frac{1}{t_s} \int_0^{t_s} H \left(\sigma_1 - \sigma_s \right) \left(\frac{\sigma_1}{\sigma_s} \right)^{\alpha_s} dt \quad (2)$$

where σ_1 is the major principal stress, σ_s is the given stress threshold for fracture initiation, t_s is the fracture initiation time threshold and α_s is an exponent that controls the time to initiate fracture. The parameter t_s is introduced as a means to avoid that spurious peaks of stress result in fracture. Further, H is the Heaviside function, which ensures that damage does not evolve if σ_1 is less than σ_s . In regards to float glass, $D = 1$ generally corresponds to the growth of a pre-existing microscopic surface flaw into a macroscopic crack. The brittle failure criterion is motivated by the work of Tuler and Butcher [28].

When node splitting is applied, an initiated crack is made-up of new nodes and free element faces. Subsequently, propagation of a crack will occur if the stress intensity factor K_I in the integration points surrounding a crack tip reaches a critical value given by

$$K_I > K_{IC} \quad (3)$$

where K_{IC} is the fracture toughness for mode I loading. A crack tip is defined as a node that has not yet been split and belongs to at least one created element face. Note that the criterion given by Eq. (3) is only checked in the integration points closest to the crack in elements that are connected to a crack tip node. Based on the stress field in a linear elastic cracked body [29], the stress intensity factor K_I is calculated by

$$K_I = \alpha \sigma_1 \sqrt{\pi d} \quad (4)$$

where d is the distance from the integration points to the crack tip node and α is a constant determined by empirical calibration for the employed element type. The failure model is based on a deterministic approach, i.e., all glass elements are appointed the same fracture strength σ_s . Since the fracture strength of glass is known to be probabilistic [12], this will lead to a simplification of the glass failure modelling.

4.2. Polyvinyl butyral (PVB)

A viscoelastic material model, consisting of a hyperelastic spring in parallel with a nonlinear (viscous) dashpot, is used for the PVB material. The model employs a corotated formulation, i.e.,

$$\hat{\sigma} = \mathbf{R}^T \sigma \mathbf{R} \quad (5)$$

where $\hat{\sigma}$ is the corotated Cauchy stress tensor, σ is the Cauchy stress tensor, and \mathbf{R} is the rotation tensor. The stress tensor $\hat{\sigma}$ is given by the sum of the stresses in the hyperelastic spring $\hat{\sigma}_A$ and the nonlinear dashpot $\hat{\sigma}_B$ as

$$\hat{\sigma} = \hat{\sigma}_A + \hat{\sigma}_B \quad (6)$$

The stress contribution $\hat{\sigma}_A$ is calculated as

$$\hat{\sigma}_A = \frac{\mu}{J \lambda_c^*} \frac{\mathcal{L}^{-1}(\lambda_c^*/\lambda_L)}{\mathcal{L}^{-1}(1/\lambda_L)} \mathbf{C}_{dev}^* + \frac{1}{J} K \ln(J) \mathbf{I} \quad (7)$$

where μ , λ_L and K are the initial shear modulus, locking stretch and bulk modulus, respectively. Further, \mathcal{L}^{-1} is the inverse Langevin function, J is the Jacobian given by the determinant of the deformation gradient \mathbf{F} , and \mathbf{I} is the identity tensor. The tensor \mathbf{C}_{dev}^* is the deviatoric part of the isochoric right Cauchy-Green deformation tensor, and is defined as

$$\mathbf{C}_{dev}^* = \mathbf{C}^* - \frac{1}{3} \text{tr}(\mathbf{C}^*) \mathbf{I}, \quad \mathbf{C}^* = J^{-2/3} \mathbf{C}, \quad \mathbf{C} = \mathbf{F}^T \mathbf{F} \quad (8)$$

Additionally, λ_c^* is an average chain stretch expressed as

$$\lambda_c^* = \sqrt{\frac{\text{tr}(\mathbf{C}^*)}{3}} \quad (9)$$

The viscous stress contribution $\hat{\sigma}_B$ is calculated as

$$\hat{\sigma}_B = b_0 (\lambda_c^* - 1)^{b_1} \left(\frac{\dot{\gamma}_{dev}^{eff}}{\dot{\gamma}_0} \right)^{b_2} \left(\frac{\hat{\mathbf{D}}_{dev}}{\dot{\gamma}_{dev}^{eff}} \right) \quad (10)$$

where b_0 , b_1 , b_2 and $\dot{\gamma}_0$ are the viscous flow stress parameters, and $\dot{\gamma}_{dev}^{eff}$ is an effective time-averaged deviatoric shear strain rate. The latter is defined as

$$\dot{\gamma}_{dev}^{eff} = \sqrt{\frac{1}{3} \hat{\mathbf{D}}_{dev} : \hat{\mathbf{D}}_{dev}} \quad (11)$$

where $\hat{\mathbf{D}}_{dev}$ is a time-averaged corotated deviatoric rate of deformation tensor calculated as

$$\hat{\mathbf{D}}_{dev} = \frac{1}{c_{dec}} \int_0^t \hat{\mathbf{D}}_{dev} \exp\left(-\frac{t-\tau}{c_{dec}}\right) d\tau \quad (12)$$

Here, c_{dec} is a viscous decay parameter and $\hat{\mathbf{D}}_{dev}$ is the corotated deviatoric rate of deformation tensor defined as

$$\hat{\mathbf{D}}_{dev} = \hat{\mathbf{D}} - \frac{1}{3} \text{tr}(\hat{\mathbf{D}}) \mathbf{I}, \quad \hat{\mathbf{D}} = \mathbf{R}^T \mathbf{D} \mathbf{R} \quad (13)$$

where \mathbf{D} is the rate of deformation tensor. The presented model is motivated by a constitutive model by Bergström and Boyce [30]. In the original model, the viscous part is comprised of a Maxwell element instead of a single dashpot. By removing the spring in the Maxwell element, the viscous stress is given explicitly; however, the need for numerical damping is introduced.

4.3. Adhesion and delamination

Adhesion between the PVB interlayer and the glass is modelled by merging the nodes in the PVB to the glass surface. Delamination, i.e., separation of the PVB nodes from the glass surface, can take place when the following criterion is reached.

$$\left(\frac{\max\{\sigma\}}{\sigma_{fail}} \right)^2 + \left(\frac{\tau}{\tau_{fail}} \right)^2 \geq \frac{1}{\xi^2} \quad (14)$$

Here, σ_{fail} is the tensile failure stress, τ_{fail} is the shear failure stress and ξ is a scale factor calculated as

$$\xi = \max(1, \sqrt{\Delta/\Delta_{ref}}) \quad (15)$$

where Δ is the local characteristic element size of the PVB and Δ_{ref} is the given element reference size. The scale factor ξ is included as a form of regularization, i.e., to account for a coarse mesh and its inability to generate possible stress concentrations. By including ξ , the stresses required to induce delamination is reduced if $\Delta > \Delta_{ref}$. Further, σ and τ are the normal and shear stresses calculated from the nodal forces at the PVB-glass interface. They are expressed as

$$\sigma = \mathbf{t} \cdot \mathbf{n}, \quad \tau = \sqrt{\|\mathbf{t}\|^2 - \sigma^2} \quad (16)$$

where \mathbf{t} is the surface traction and \mathbf{n} is the node normal. After reaching the criterion defined by Eq. (14), a certain amount of energy must be consumed before delamination occurs. At this point, the stresses are equal to $\sigma = \sigma_{del}$ and $\tau = \tau_{del}$. Now, the stresses start to unload, following a linear function of the crack opening distance δ (along the direction given by \mathbf{t}). This relationship is illustrated in Fig. 11, and is given by

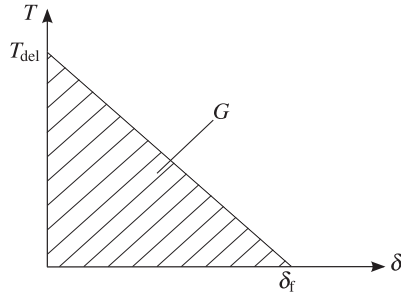


Fig. 11. Illustration of the stress unloading from reaching the criterion defined by Eq. (14).

$$T = T_{\text{del}} \left(1 - \frac{\delta}{\delta_f} \right), \quad T_{\text{del}} = \sqrt{\sigma_{\text{del}}^2 + \tau_{\text{del}}^2} \quad (17)$$

where T is the magnitude of the surface traction \mathbf{t} , and T_{del} is T after reaching the criterion defined by Eq. (14). The crack opening distance when delamination occurs is δ_f . The consumed energy (over the crack area) is thus defined as

$$G = \frac{1}{2} T_{\text{del}} \delta_f = \sqrt{\left(\frac{\sigma_{\text{del}}}{\sigma_{\text{fail}}} G_I \right)^2 + \left(\frac{\tau_{\text{del}}}{\tau_{\text{fail}}} G_{II} \right)^2} \quad (18)$$

where G_I and G_{II} are the given energy release per unit area for mode I and II loading. Note that the criterion is rate independent.

5. Finite element modelling

5.1. Finite element solver

In the current work, all numerical studies were carried out using the nonlinear explicit FE code IMPETUS Afea Solver [31]. The code is particularly suitable for simulations involving large deformations of structures and components under extreme loading conditions, due to the implementation of special features such as higher order elements and a node-splitting technique. Higher order elements provide additional robustness and accuracy, and can describe bending with only one element over the thickness, while node splitting enables modelling of fracture and crack propagation by separation of elements instead of deletion through element erosion. Node splitting involves generating new nodes and free element surfaces, and will occur when an integration point reaches a specified failure criterion. A crack will initiate at the nearest exterior node by splitting it into two nodes and separating neighbouring elements. After crack initiation, the software loops over all integration points surrounding the splitted node and calculates a stress (or strain) magnitude-weighted average direction of the major principal stress (or strain). Separation of elements (i.e., the crack) occurs in a direction as close as possible to the normal of the average major principal stress (or strain) direction [32]. In this study, the crack direction is chosen to be stress dependent. Holmen et al. [32,33] applied the 3D node splitting technique, in combination with higher order elements, in ballistic impact simulations of aluminum and steel plates. IMPETUS Afea Solver is compatible with graphic processing units (GPUs) for an increased computational speed, and version 4.0.2452 of the solver was used in this study.

5.2. Calibration of material model for PVB

The following calibration is based on a selection of uniaxial tensile tests on PVB dogbone specimens performed by Hooper et al. [22] and Del Linz et al. [24] (Fig. 1). The viscoelastic material model presented

Table 3

Fitted material parameters for the viscoelastic material model. >

K (MPa)	μ (MPa)	λ_d (-)	$\dot{\gamma}_0$ (s^{-1})	c_{dec} (s)	b_0 (MPa)	b_1 (-)	b_2 (-)
200	5	2	0.392	5×10^{-5}	11.54	0.152	0.197

in Section 4.2 was calibrated to the tensile test data by a combined curve-fitting and inverse-modelling approach. The fitted parameters are presented in Table 3. Simulations of the tensile tests were run to illustrate the agreement between the experiments and the calibrated model. The PVB specimen was modelled with symmetry along its length and width. One 27-node hexahedral element was used over the thickness since this is the element type that will be used in the blast simulations. Metallic grips were used to clamp the PVB to the testing machine in the experiments, and these were indirectly included by removing parts of the grip section in the model. Fig. 12 depicts the effective (von Mises) stress field in a simulation with a nominal strain rate of 400 s^{-1} at three different levels of deformation (given by the logarithmic strain). The figure shows that the PVB specimen is able to deform greatly without necking, and that it has a close-to homogeneous stress field in the gauge area.

Fig. 13 displays the true stress versus logarithmic strain curves from the experiments and the simulations. Just like in the experiments, the true stress in the simulations was obtained from the reaction forces at the boundary of the specimen, and the logarithmic strain was found from the deformation of the gauge area. To investigate the versatility of the viscoelastic material model, we also simulated compressive Split Hopkinson Pressure Bar (SHPB) tests performed by Xu et al. [34]. The experiments were designed to minimise the friction between the bars and the PVB specimens, so we used a relatively low friction coefficient of 0.05 in our simulations. Fig. 14 compares the stress-strain curves from tests and simulations at three different strain rates. Note that the stress-strain data in Ref. [34] were given in terms of nominal values. The nominal stress and nominal strain in the simulations are calculated from the reaction force and displacement of the bars. As seen in the figure, the overall agreement between the simulation and experiment is good and deemed satisfactory for our purposes, despite some discrepancy at higher strains.

Note that the material tests were performed on PVB that was not treated in an autoclave. PVB is known to change from semitransparent to transparent after being subjected to heat and pressure, and one might therefore also expect some changes in the mechanical properties. This was shown in a study by Morison [35], where PVB specimens (both untreated and treated in an autoclave) were tested at four different loading rates. It was found that both the transition force (i.e., the force when the stiffness of the stress-strain curve changes) and the initial stiffness increased when the PVB was treated. This effect will be investigated numerically later on in the study.

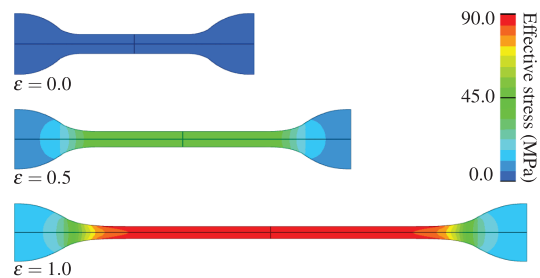


Fig. 12. Effective stress field in a simulation of a PVB tensile test with nominal strain rate of 400 s^{-1} at three different levels of deformation.

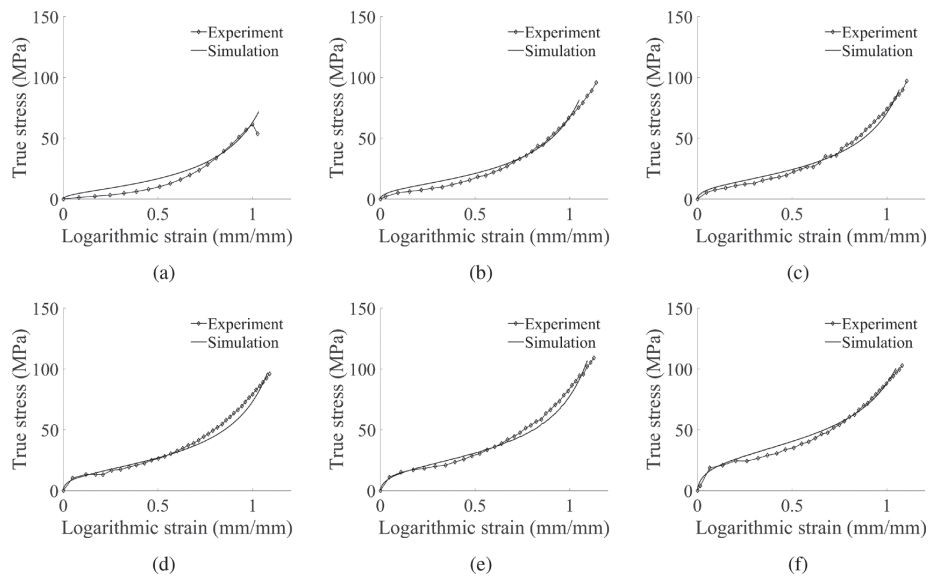


Fig. 13. True stress versus logarithmic strain curves from experimental tensile tests [22,24] and corresponding simulations with nominal strain rates: (a) 0.1 s^{-1} , (b) 2 s^{-1} , (c) 8 s^{-1} , (d) 20 s^{-1} , (e) 60 s^{-1} and (f) 400 s^{-1} .

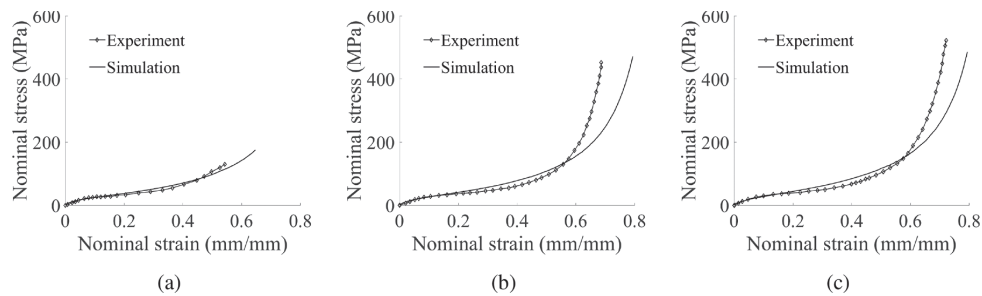


Fig. 14. Nominal stress versus strain curves from experimental compression tests [34] and corresponding simulations with nominal strain rates: (a) 700 s^{-1} , (b) 1200 s^{-1} and (c) 2200 s^{-1} .

5.3. Fracture stress of float glass

As mentioned in Section 4.1, the selected failure criterion for glass is based on a deterministic approach. Since the fracture strength of glass is probabilistic, this criterion represents a simplification. However, the approach was deemed satisfactory, as the main intention of the numerical study was to demonstrate the selected simulation techniques.

In the following two sections, we will present numerical studies on both monolithic (i.e., non-laminated) glass and laminated glass. The glass material is the same for both cases, i.e., 3.8 mm thick soda-lime silica float glass. For failure modelling of the glass plates, the fracture stress σ_s was chosen as 60 MPa and 90 MPa for the monolithic and laminated glass case, respectively. Two experimental tests were used to calibrate the failure criterion through an inverse modelling approach, which resulted in the two different values for σ_s . In the calibration process, we focused on a qualitative assessment of the simulation, in addition to the time of fracture initiation in the glass. The laminated glass case corresponds to test D-03. Details about the monolithic tests will be presented in the following section.

To justify the use of the values for σ_s , we carried out a statistical prediction of the fracture strength of the glass for the two cases. The analyses were done through the use of a stochastic strength model

presented by Osnes et al. [13]. The input to the model is the stress field from an FE simulation of each of the two experimental tests. In these FE simulations, glass fracture is not included. The basis of the stochastic strength model is that fracture generally initiates in microscopic surface flaws under tensile loading. As a result, fracture depends on the applied normal stresses and the properties of the surface flaws. In the model, the information from the FE simulations is combined with an artificial flaw map, i.e., information about the location, size, and orientation of the flaws. The flaw map is varied over a number of iterations, i.e., virtual experiments. The stress intensity factor is evaluated and compared to the fracture toughness in every flaw within each iteration. The stochastic strength model outputs a prediction of the location and time of fracture initiation, and the probability distribution of the fracture load and fracture stress. More details regarding the stochastic strength model can be found in Ref. [13]. The number of employed iterations was set to 5000, and the calculation time was approximately 2 min for each of the two failure predictions. The statistical failure prediction that corresponds to the two experimental tests is presented in Fig. 15. According to the stochastic strength model, the failure stress for both the monolithic and the laminated glass test (D-03) is between $\sim 55 \text{ MPa}$ and $\sim 120 \text{ MPa}$, see Fig. 15a. Therefore, the two values chosen for σ_s fall within the predicted values. Fig. 15b and c illustrates the predicted

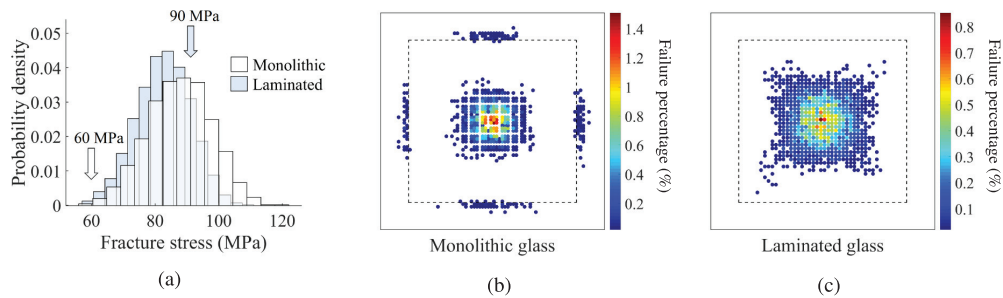


Fig. 15. Results from the stochastic strength model [13] in terms of (a) the probability density of fracture stresses, and the position of fracture initiation for (b) a monolithic glass and (c) a laminated glass (D-03).

position of fracture initiation, with the color bar representing the percentage of failure at the specific locations. It is seen that fracture initiation in the tests of class D falls within the predicted ones, see Figs. 6 and 15c.

5.4. Modelling of monolithic glass blast test

We chose to simulate the behaviour of monolithic float glass plates as an initial numerical study of the blast tests. To compare the simulations with representative test results, we used two experiments from an earlier study on blast-loaded monolithic glass that can be found in Ref. [13]. In the first experiment, no fracture was visible, while in the second experiment, fracture initiated close to the mid-point of the plate. The peak reflected overpressure P_{max} in the tests was 62.5 kPa for the unfractured plate and 63.7 kPa for the fractured plate.

The glass was modelled as linear elastic with the parameters presented in Table 1. The boundary conditions of the glass plate consisted of rubber strips with restriction in displacement at the outer surfaces, and four 5.7 mm thick rigid plates at the edges. The latter was included to mimic the milled-out area of the inner clamping plate. It was deemed unnecessary to include the entire clamping in the model since the rubber was glued to the clamping plates. Fig. 16a shows the FE model with the meshes of the different components. The rubber was modelled with $7\text{ mm} \times 7\text{ mm} \times 4\text{ mm}$ 64-node hexahedral elements, while for the glass we used $4\text{ mm} \times 4\text{ mm} \times 3.8\text{ mm}$ 40-node pentahedron elements. Pentahedron elements were chosen to allow crack growth to happen in several directions. The pressure loading is described by the Friedlander equation defined in Eq. (1), and the pressure was applied normal to the loading area of the glass. The Friedlander parameters t_{d+} and b were set to 11.82 ms and 0.73, respectively [13]. It should be

noted that we employ a purely Lagrangian (uncoupled) approach, and potential FSI effects are therefore neglected in this study. In other words, we assume that the pressure is unaltered by the deformation of the specimen. Generally, a coupled approach results in reduced deformations, in which the extent is dependent on the amount of FSI effects present [36].

The rubber material was modelled as linear elastic with a Young's modulus of 2 MPa, and a Poisson's ratio of 0.46 [13]. This results in a simplification of the material behaviour of the rubber, but it was proved sufficient to recreate the boundary conditions in the experiments. This is demonstrated in Fig. 17a, where displacements of the diagonal optical targets (denoted P0, P1 and P2 in Fig. 16b) in the simulation and the experiment of the unfractured glass plate are compared. The agreement between the simulation and the experiment is good. However, there is a small deviation during the spring-back of the plate (after around 3 ms), presumably due to the simplification of the rubber material model. Note that the displacements are taken from both sides of the symmetry lines, resulting in a total of nine points, see Fig. 16b. The displacements of points P0, P1 and P2 are as expected perfectly symmetric in the simulation of the unfractured plate, while some variation can be seen in the experiment.

In the simulation of the fractured plate, the fracture stress σ_s was set to 60 MPa (see Section 5.3), the fracture toughness K_{IC} to $0.75\text{ MPa}\sqrt{\text{m}}$ (see Table 1), and the fracture initiation parameters t_s and α_s to $2 \times 10^{-7}\text{ s}$ and 0.5, respectively. The parameters t_s and α_s were chosen as they resulted in a highly realistic fracture pattern. The displacements of points P0, P1 and P2 in both the experiment and simulation are presented in Fig. 17b. Note that the displacement in P2 was no longer traceable after about 4 ms, and is therefore not visible after this point. The response of the experiment and simulation is highly similar.

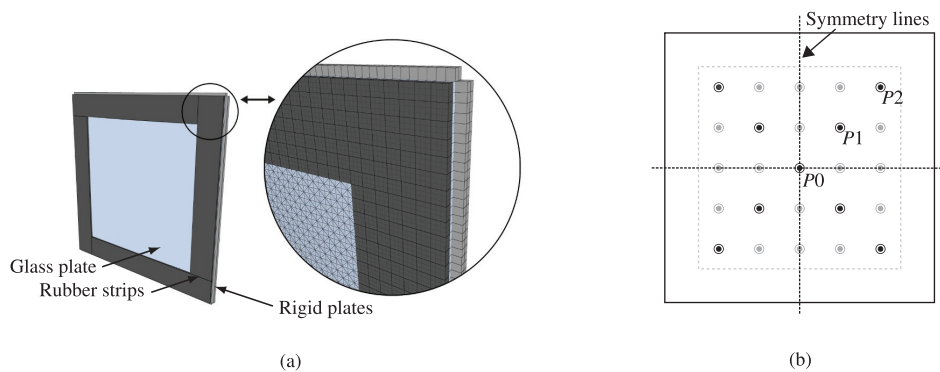


Fig. 16. FE model of the blast tests on monolithic float glass plates: (a) illustration of the mesh sizes, (b) points tracked in the FE model and the experiments, including symmetry lines.

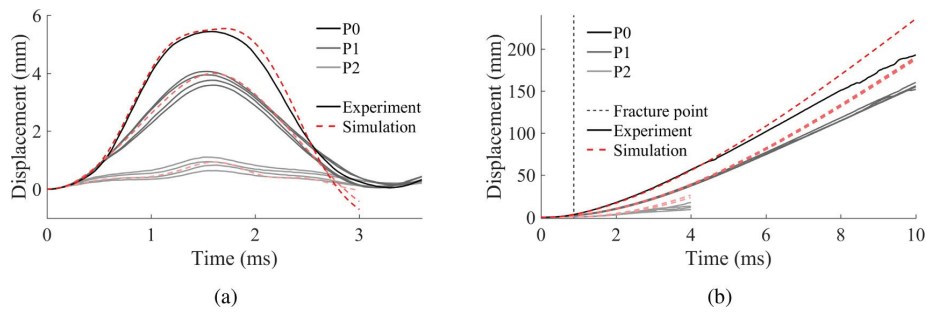


Fig. 17. Displacements of points P0, P1 and P2 versus time in experiment and simulation of (a) the unfractured plate and (b) the fractured monolithic glass plate [13].

However, some deviations are seen towards the end due to difference in position of fracture initiation and subsequent crack propagation in the glass. Fig. 18 compares pictures from the experiment and the simulation at three different stages throughout the test. The simulation captures many of the mechanisms seen in the experiment, including crack branching from the initiation point, formation of large glass splinters and free-flying fragments.

As previously mentioned, the employed fracture model is deterministic, which results in fracture initiation in the point of maximum major principal stress (i.e., in the mid-point of the glass plate). Since the glass plate in the experiment fractured close to the mid-point, it was possible to obtain a good agreement between the experiment and the corresponding simulation. In the aforementioned study on blast-loaded monolithic glass [13], fracture frequently initiated under the rubber strips. To obtain a comparable simulation for those tests, we would

have to include additional features such as distribution of initial damage to enable fracture initiation to happen away from the centre. Nevertheless, the presented simulation illustrates that node splitting enables a highly realistic description of the fracture and fragmentation in glass without loss of mass or momentum.

A small parametric study was carried out to investigate the sensitivity of the monolithic glass model. The study considered the glass mesh size, the fracture initiation parameters t_s and σ_s , the fracture toughness K_{IC} and the fracture stress σ_s . Each parameter was given a lower and higher value compared to the base model. Additionally, a simulation with $\sigma_s = 90$ MPa was run, because this was the employed fracture stress for the laminated glass model, see Section 5.5. Fig. 19 presents a picture from each simulation (including the base model) at 5 ms after impact of the blast wave. The parametric study suggests that the brittle fracture criterion is most sensitive to the value of t_s , σ_s , and

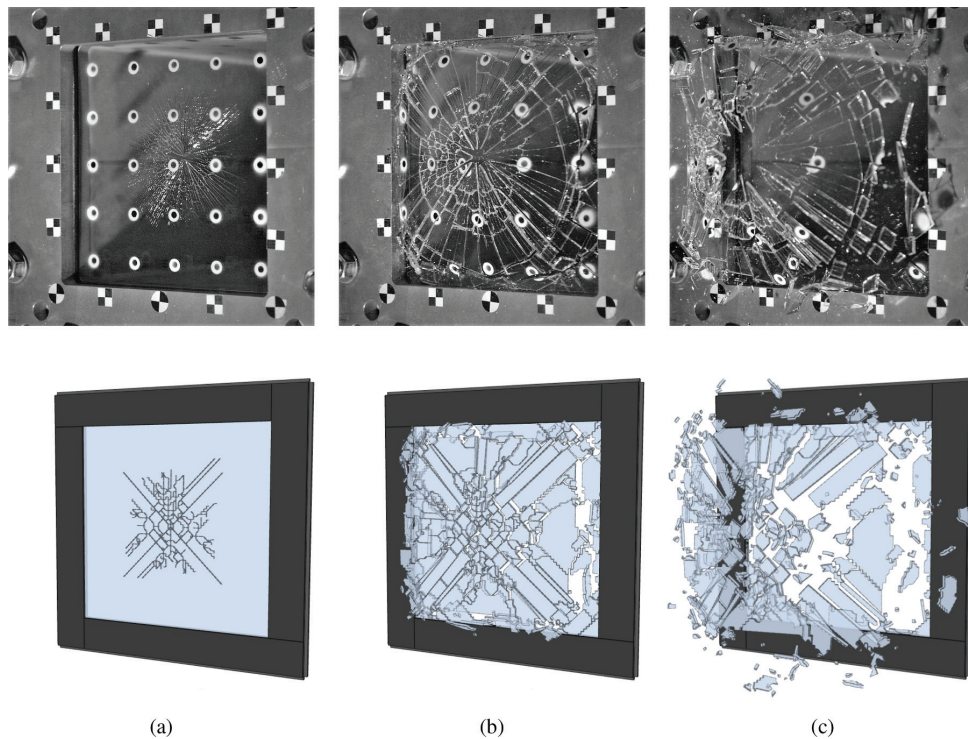


Fig. 18. Pictures of the fractured plate in the experiment and simulation at: (a) 0.9 ms, (b) 5 ms and (c) 10 ms.

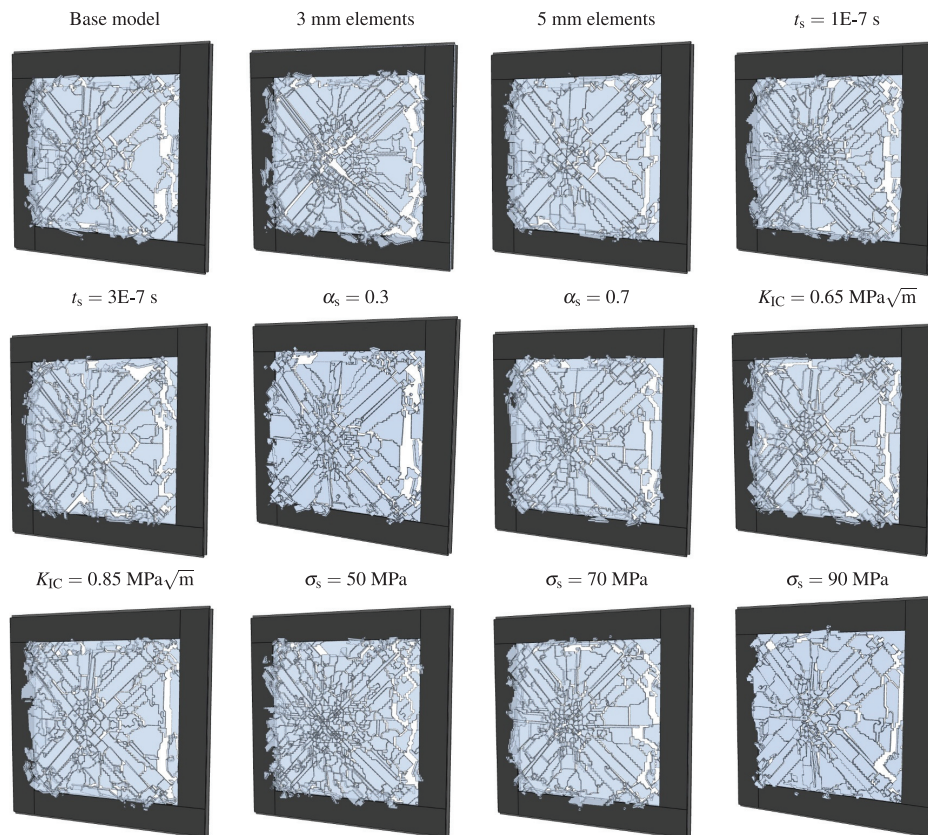


Fig. 19. Parametric study of blast-loaded monolithic glass. Pictures are taken at $t = 5$ ms. The base model utilised 4 mm elements and the parameters $t_s = 2 \times 10^{-7}$ s, $\alpha_s = 0.5$, $K_{IC} = 0.75 \text{ MPa}\sqrt{\text{m}}$ and $\sigma_s = 60 \text{ MPa}$.

the mesh size. The coarser mesh leads to fewer fragments, while a finer mesh gave an increased number of fragments, especially around the centre. The lower value of t_s also resulted in more fragments around the centre, not unlike the finer mesh model. This finding suggests that to get a similar cracking pattern for a finer mesh, one should increase the value of t_s . A fracture stress σ_s equal to 50 MPa gave excessive fracture over most of the plate, while σ_s equal to 70 MPa and 90 MPa gave similar results compared to the base model. The time of fracture

initiation naturally varied somewhat for the different values of σ_s .

5.5. Modelling of laminated glass blast tests

The numerical model of the laminated glass is similar to the monolithic glass model presented in Section 5.4. Differences include an increased fracture stress for the glass ($\sigma_s = 90 \text{ MPa}$), and naturally, the additional glass and PVB layer with adhesion and a delamination

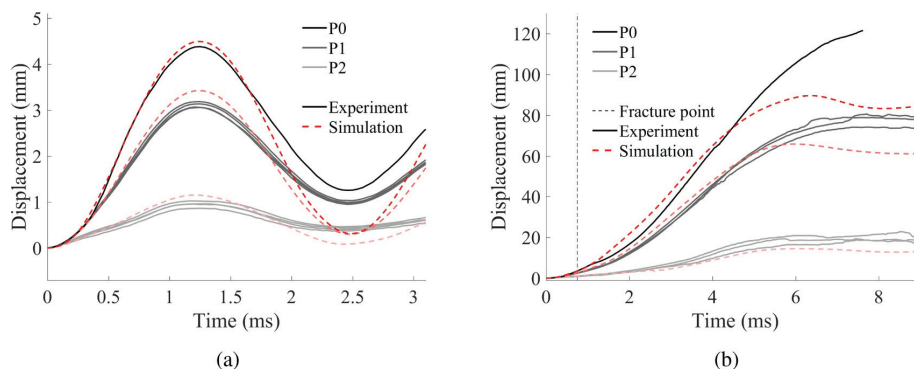


Fig. 20. Displacements of points P0, P1 and P2 versus time in experiment and simulation for test (a) B-03 and (b) D-03.

Table 4
The parameters of the delamination criterion.

σ_{fail}	τ_{fail}	G_I	G_{II}	Δ_{ver}
12 MPa	10 MPa	1 N/mm	1 N/mm	2 mm

criterion. The loading was applied in the same manner as for the monolithic glass, but with the use of parameters from Table 2. We also chose to utilise the symmetry of the problem in these simulations to save computational time. Consequently, only one fourth of the experimental setup was modelled. The employed material model for the PVB with fitted parameters was presented in Section 5.2. The PVB layer was modelled with one 27-node hexahedral element over the thickness. The

pre-fracture behaviour of the laminated glass was examined first. We chose to model test B-03, and the resulting displacements of points P0, P1 and P2 in the experiment and corresponding simulation are presented in Fig. 20a. The simulation manages to recreate the overall experimental behaviour. However, just like in the unfractured monolithic glass simulation, there is some deviation during the spring-back of the plate (at around 2.5 ms). Still, the results indicate that the chosen PVB model and the fitted parameters are reasonable.

The parameters of the delamination criterion were chosen through a trial-and-error approach, and are presented in Table 4. These parameters lead to a realistic description of fracture and delamination, and are in the same range as parameters reported in studies of pre-cracked laminated glass specimens [9,10]. The chosen parameters did not lead to highly localised stretching of the PVB layer between glass elements,

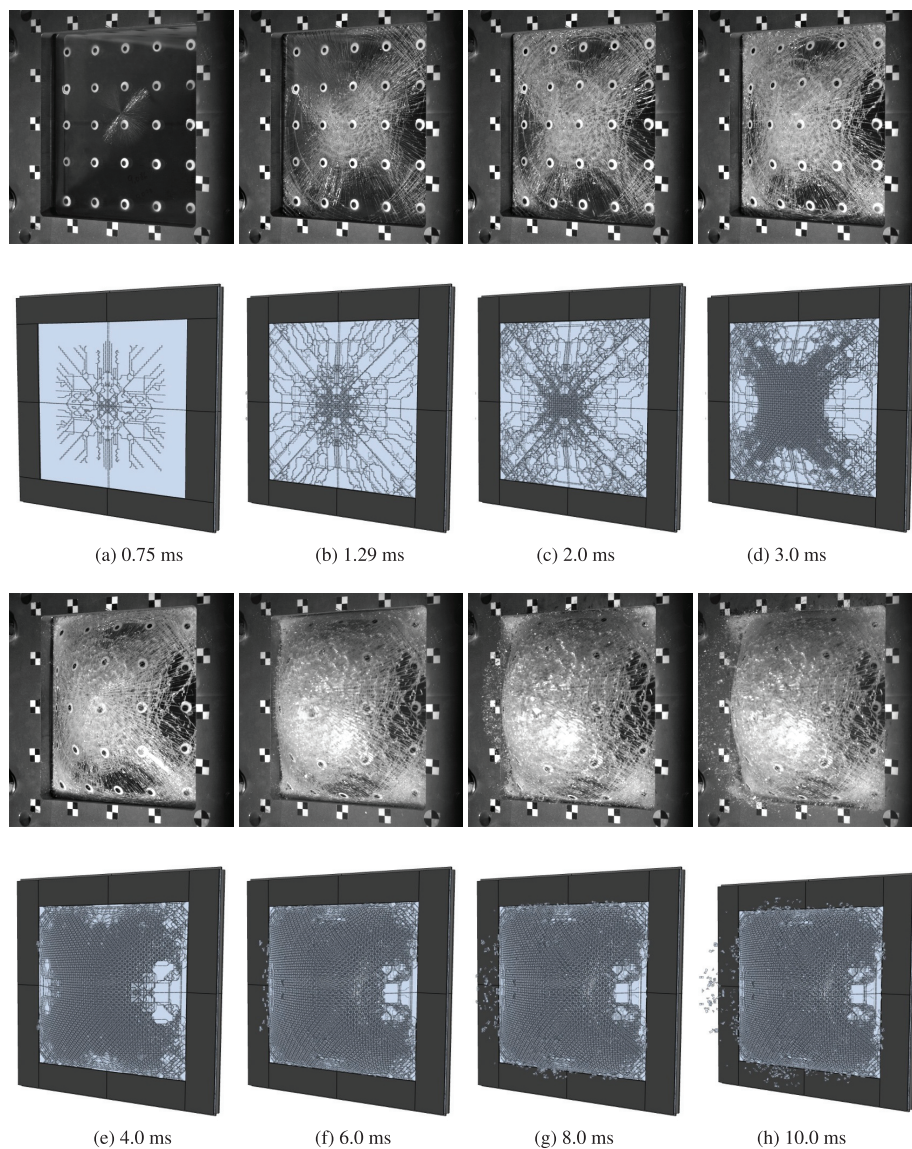


Fig. 21. Pictures of test D-03 and corresponding simulation at various points in time (see subcaptions).

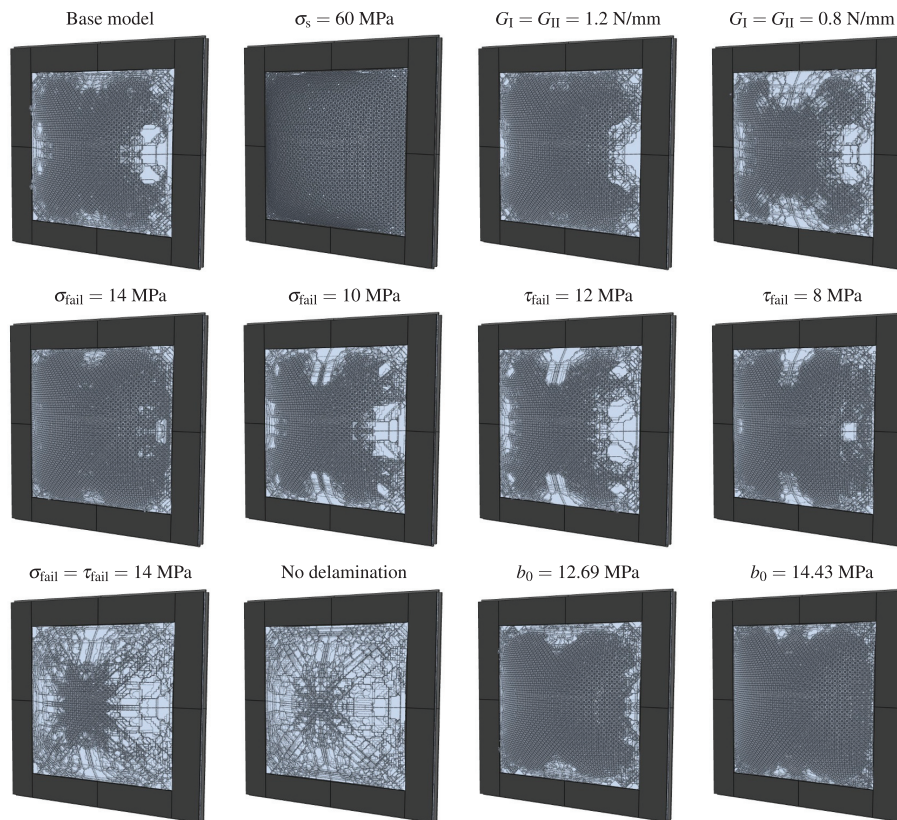


Fig. 22. Parametric study of blast-loaded laminated glass. The base model utilised the parameters $\sigma_s = 90$ MPa, $\sigma_{\text{fail}} = 12$ MPa, $\tau_{\text{fail}} = 10$ MPa, $G_I = G_{II} = 1$ N/mm and $b_0 = 11.54$ MPa. Pictures are taken at $t = 4$ ms.

which could be a problem with strong adhesion, i.e., delamination parameters that are too high. The element reference size Δ_{ref} was set to the same size as the PVB elements. Thus, according to Eq. (15), the scale factor ξ was equal to unity in these simulations.

For the simulation of a laminated glass that fractures, we chose to model test D-03, since fracture occurred close to the mid-point and delamination was observed in the test. Fig. 20b presents the displacements of points P0, P1 and P2 in the experiment and simulation. The behaviour is similar at the beginning, but deviates somewhat towards the end of the test. This result indicates that the cracking of the glass is more pronounced in the experiment than in the simulation, which leads to different levels of deformation in the PVB. Nevertheless, the displacements measured from the simulation follows the overall trend from the experiment, with a gradual increase from the start before it approaches a close-to constant value between 6 ms and 8 ms. Fig. 21 compares pictures from the experiment and the simulation at eight different points in time throughout the test. The simulation captures many of the mechanisms observed in the experiment, including fine cracking of the glass and detachment of glass fragments from the PVB. Additionally, the failure mode is highly comparable to the experiment, with extensive cracking in the centre and formation of diagonal cracks towards the boundary. Note that the back glass plate and the PVB are made partly transparent so that fracture in both glass plates is visible.

A parametric study was performed to investigate the sensitivity of

the laminated glass model. The study considered the delamination parameters σ_{fail} , τ_{fail} , G_I and G_{II} , and the viscous flow stress parameter b_0 in the PVB material model. The latter was included in an attempt to study the influence of the autoclave process on the laminated glass model. Increasing the value of b_0 leads to an increase in the transition force and the initial stiffness of the uniaxial stress-strain curve. This effect is observed experimentally for PVB after the autoclave process, as discussed in Section 5.2. In the current parametric study, we investigated the use of a higher and a lower value of the delamination parameters, in addition to excluding the delamination criterion altogether. For the viscous flow stress parameter b_0 , two increased values were used. Additionally, a simulation with $\sigma_s = 60$ MPa was run, since this was the fracture stress we employed for the monolithic glass model in Section 5.4.

Fig. 22 presents pictures from each simulation (including the base model) at 4 ms after impact of the blast wave. We see that an increase in G_I and G_{II} leads to more cracking of the glass, whereas a decrease leads to less cracking. The response is reasonable because increased values of G_I and G_{II} imply that more energy has to be consumed before delamination can occur. This results in later and less delamination, which in turn requires the glass and the PVB to deform together. In this way, the glass fractures more extensively. Keep in mind that some delamination should be present to achieve a realistic fracture behaviour. If the delamination parameters σ_{fail} and τ_{fail} are increased excessively, or if no

delamination criterion is applied at all, the cracking of the glass becomes rather limited. With little delamination present, the glass fragments seem to prevent excessive deformation of the PVB, which reduces the cracking of the glass plates.

Furthermore, the parametric study suggests that mode II failure is dominating in terms of delamination. By increasing τ_{fail} alone, we are approaching the response with no delamination criterion. In other words, an increase in τ_{fail} leads to less delamination and less cracking of the glass. An equal change in σ_{fail} alone seems to have an opposite effect, as an increased value yields more cracking of the glass, whereas a decreased value results in less cracking. By increasing the value of b_0 , the amount of cracking is increased, presumably as a result of a less flexible PVB and a decreased amount of delamination compared to the base model. For a reduction in the fracture stress, i.e., $\sigma_c = 60$ MPa, the glass plates undergo more cracking, which results from fracture initiation with subsequent fracture propagation at an earlier point compared to the base model. From the parametric study, it is evident that the behaviour of the laminated glass model is quite sensitive to all of the investigated parameters. It also appears that several combinations of the different parameters can result in a similar behaviour. It is therefore deemed necessary to investigate the input parameters in a more detailed manner in future studies, both through numerical simulations and experimental tests. Nevertheless, the numerical study reveals the potential of the selected numerical techniques.

6. Conclusions

In this study, we have investigated the possibility of simulating fracture and fragmentation of blast loaded laminated and monolithic (i.e., non-laminated) glass using explicit finite element analysis. In the simulations, we applied modelling techniques such as higher order elements and node splitting. The study also investigates the behaviour of blast-loaded laminated glass experimentally in a shock tube. In total, 15 laminated glass specimens, consisting of annealed float glass and PVB, were tested at five different pressure levels. The different tests displayed a variation in fracture initiation and subsequent post-fracture behaviour within the different pressure levels, demonstrating the stochastic fracture behaviour of glass.

The simulations of monolithic glass were able to capture behaviours such as crack branching from the fracture initiation point, formation of large glass splinters and free-flying glass fragments. We also conducted a parametric study to investigate the sensitivity of the FE model concerning the mesh density and the parameters in the failure criterion for glass. We observed that the model was most sensitive to the mesh density, the fracture stress σ_c and the fracture initiation parameter t_g . The simulations of the laminated glass were able to describe behaviours such as fine cracking of the glass plates, delamination between the glass and the PVB interlayer, and separation of glass elements from the interlayer. Just like in the monolithic glass simulations, a parametric study was carried out. In this case, we focused on the parameters of the delamination criterion. It was observed that the simulations were quite sensitive to all of the investigated parameters. Additionally, several effects that are known to be strain-rate sensitive (e.g., delamination and fracture toughness) were assumed rate independent in the FE model. Despite the fact that there are uncertainties linked to the selected method, the presented modelling techniques show great potential regarding simulations of blast-loaded glass. Finally, it is uncertain how the autoclave process on the laminated glass affects the PVB material. In the FE simulations of the laminated glass, we employed material tests of untreated PVB to calibrate the PVB material model. However, one might expect some change in the mechanical properties after this process. This effect should therefore be a topic of further investigation.

Acknowledgements

The present work has been carried out with financial support from the Centre of Advanced Structural Analysis (CASA), Centre for Research-based Innovation, at the Norwegian University of Science and Technology (NTNU) and the Research Council of Norway through project no. 237885 (CASA). The authors would like to acknowledge Mr. Trond Auestad for assisting with the experimental programme and Modum Glassindustri for providing the glass specimens. We also would like to thank Dr. Lars Olovsson at IMPETUS Afea AB for valuable assistance with the FE code.

References

- [1] Larcher M, Solomos G, Casadei F, Gebbeken N. Experimental and numerical investigations of laminated glass subjected to blast loading. *Int J Impact Eng* 2012;39(1):42–50.
- [2] Hooper P, Sukhram R, Blackman B, Dear J. On the blast resistance of laminated glass. *Int J Solids Struct* 2012;49(6):899–918.
- [3] Zhang X, Hao H. Experimental and numerical study of boundary and anchorage effect on laminated glass windows under blast loading. *Eng Struct* 2015;90:96–116.
- [4] Zhang X, Hao H, Wang Z. Experimental study of laminated glass window responses under impulsive and blast loading. *Int J Impact Eng* 2015;78:1–19.
- [5] Kumar P, Shukla A. Dynamic response of glass panels subjected to shock loading. *J Non-Cryst Solids* 2011;357(24):3917–23.
- [6] Bermbach T, Teich M, Gebbeken N. Experimental investigation of energy dissipation mechanisms in laminated safety glass for combined blast-temperature loading scenarios. *Glass Struct Eng* 2016;1(1):331–50.
- [7] Pelfrene J, Kuntsche J, Van Dam S, Van Paepegem W, Schneider J. Critical assessment of the post-breakage performance of blast loaded laminated glazing: experiments and simulations. *Int J Impact Eng* 2016;88:61–71.
- [8] Osnes K, Dey S, Hopperstad O, Børvik T. On the dynamic response of laminated glass exposed to impact before blast loading. *Exp Mech* 2019. <https://doi.org/10.1007/s11340-019-00496-1>.
- [9] Del Linz P, Hooper PA, Arora H, Wang Y, Smith D, Blackman BR, et al. Delamination properties of laminated glass windows subject to blast loading. *Int J Impact Eng* 2017;105:39–53.
- [10] Franz J, Schneider J. Through-cracked-tensile tests with polyvinylbutyral (PVB) and different adhesion grades. Engineered transparency, international conference at glasstec, Düsseldorf, Germany. 2014. p. 135–42.
- [11] Samieian MA, Cormie D, Smith D, Wholey W, Blackman BR, Dear JP, et al. Temperature effects on laminated glass at high rate. *Int J Impact Eng* 2018;111:177–86.
- [12] Wachtman JB, Cannon WR, Matthewson MJ. *Mechanical properties of ceramics*. 2nd ed. John Wiley & Sons; 2009.
- [13] Osnes K, Børvik T, Hopperstad OS. Testing and modelling of annealed float glass under quasi-static and dynamic loading. *Eng Fract Mech* 2018;201:107–29.
- [14] Yankelevsky DZ. Strength prediction of annealed glass plates – anew model. *Eng Struct* 2014;79:244–55.
- [15] Aune V, Fagerholt E, Langseth M, Børvik T. A shock tube facility to generate blast loading on structures. *Int J Protect Struct* 2016;7(3):340–66.
- [16] NS-EN 572-1: Glass in building – Basic soda-lime silicate glass products – Part 1: Definitions and general physical and mechanical properties. Standard. CEN; 2012.
- [17] Wiederhorn SM. Fracture surface energy of glass. *J Am Ceram Soc* 1969;52(2):99–105.
- [18] Peroni M, Solomos G, Pizzinato V, Larcher M. Experimental investigation of high strain-rate behaviour of glass. *Applied mechanics and materials*. vol. 82. Trans Tech Publ; 2011. p. 63–8.
- [19] Zhang X, Zou Y, Hao H, Li X, Ma G, Liu K. Laboratory test on dynamic material properties of annealed float glass. *Int J Protect Struct* 2012;3(4):407–30.
- [20] Wiederhorn S, Bolz L. Stress corrosion and static fatigue of glass. *J Am Ceram Soc* 1970;53(10):543–8.
- [21] Charles R. Static fatigue of glass: I & II. *J Appl Phys* 1958;29(11):1554–60.
- [22] Hooper P, Blackman B, Dear J. The mechanical behaviour of poly (vinyl butyral) at different strain magnitudes and strain rates. *J Mater Sci* 2012;47(8):3564–76.
- [23] Zhang X, Hao H, Shi Y, Cui J. The mechanical properties of polyvinyl butyral (PVB) at high strain rates. *Constr Build Mater* 2015;93:404–15.
- [24] Del Linz P, Wang Y, Hooper P, Arora H, Smith D, Pascoe L, et al. Determining material response for polyvinyl butyral (pnb) in blast loading situations. *Exp Mech* 2016;56(9):1501–17.
- [25] Cormie D, Mays G, Smith P. *Blast effects on buildings*. 2nd ed. Thomas Telford Publishing; 2009.
- [26] Krauthammer T, Altenberg A. Negative phase blast effects on glass panels. *Int J Impact Eng* 2000;24(1):1–17.
- [27] eCorr User Manual. Accessed: 2019-03-15. <https://www.ntnu.edu/kt/ecorr>.
- [28] Tuler FR, Butcher BM. A criterion for the time dependence of dynamic fracture. *Int*

- J Fract Mech 1968;4(4):431–7.
- [29] Anderson TL. Fracture mechanics: fundamentals and applications. 3rd ed. 2005. p. 42. CRC press.
- [30] Bergström J, Boyce M. Constitutive modeling of the time-dependent and cyclic loading of elastomers and application to soft biological tissues. Mech Mater 2001;33(9):523–30.
- [31] IMPETUS Afea Solver. Accessed: 2019-03-18. <http://www.impetus-afea.com/>.
- [32] Holmen JK, Johnsen J, Hopperstad O, Børvik T. Influence of fragmentation on the capacity of aluminum alloy plates subjected to ballistic impact. Eur J Mech A/Solids 2016;55:221–33.
- [33] Holmen JK, Solberg JK, Hopperstad OS, Børvik T. Ballistic impact of layered and case-hardened steel plates. Int J Impact Eng 2017;110:4–14.
- [34] Xu J, Li Y, Ge D, Liu B, Zhu M. Experimental investigation on constitutive behavior of PVB under impact loading. Int J Impact Eng 2011;38(2):106–14.
- [35] Morison C. The resistance of laminated glass to blast pressure loading and the coefficients for single degree of freedom analysis of laminated glass. United Kingdom: Cranfield University; 2007. Ph.D. Thesis.
- [36] Børvik T, Hanssen A, Langseth M, Olovsson L. Response of structures to planar blast loads—a finite element engineering approach. Comput Struct 2009;87(9–10):507–20.

PART 4

Karoline Osnes, Odd Sture Hopperstad, Tore Børvik

Rate dependent failure of monolithic and laminated glass: an experimental and numerical study

Submitted for possible journal publication.

Rate dependent failure of monolithic and laminated glass: an experimental and numerical study

K. Osnes^{a,b,*}, O.S. Hopperstad^{a,b}, T. Børvik^{a,b}

^aStructural Impact Laboratory (SIMLab), Department of Structural Engineering, Norwegian University of Science and Technology (NTNU), NO-7491, Trondheim, Norway
^bCentre for Advanced Structural Analysis (CASA), NTNU, NO-7491, Trondheim, Norway

Abstract

Glass is a brittle material known to possess large scatter in its fracture strength, which is caused by the existence of microscopic surface flaws. Fracture in glass generally originates from stress concentrations around these flaws, which cause the fracture strength to be dependent on the flaw properties and the stress state on the glass surface. The fracture strength is also reported to increase with the loading rate. The current study aims to determine the probabilistic fracture strength of glass plates exposed to arbitrary loading and loading rates by a proposed rate-dependent strength prediction model (SPM). The SPM is based on the existence of microscopic surface flaws, and performs virtual experiments on glass plates through Monte Carlo simulations. To validate the SPM in some measure, we performed quasi-static punch tests and low-velocity impact tests on monolithic and laminated glass. The experimental work clearly demonstrated the stochastic fracture strength of glass, in addition to the load-rate dependency. The SPM managed to capture many of the trends observed in the experiments, such as the increase in fracture strength with the loading rate and the positions of fracture initiation in the glass.

Keywords: Glass, Stochastic failure, Rate dependency, Impact loading, Numerical simulation

1. Introduction

The use of glass in buildings has increased significantly over the past few decades. Traditionally, glass has only been used as a window component inside a load-carrying frame, but in modern designs, glass is frequently used as load-carrying elements, such as roofs, beams, columns and floors [1, 2]. This development has introduced new challenges to the structural design process, and calls for a better understanding of glass' load-carrying capacity. In addition, if the structure is required to withstand extreme loading, such as blast or impact, the rate dependent nature of glass fracture will further complicate the design process. Laminated glass is often used as opposed to monolithic glass when additional capacity and safety is required. Laminated glass consists of two or more glass plates bonded together by a polymeric interlayer, and is able to maintain some structural integrity even after glass fracture [3–5].

Glass is a brittle material known to possess a highly stochastic fracture behaviour caused by the presence of microscopic surface flaws [6]. Fracture generally initiates in these flaws under tensile loading, and the fracture strength of glass is therefore dependent on the flaw properties and the applied stresses.

As a result, the probability of fracture in glass is dependent on the geometry, the boundary conditions and the loading history. Fracture in glass originates from an amplification of stresses around the surface flaws, causing the flaws to grow in an unstable manner [7]. However, studies have also shown that the surface flaws may grow slowly and steadily under tensile loads before sudden failure occurs. This phenomenon is known as stress corrosion cracking, or static fatigue, and is caused by a chemical reaction between the glass (at the flaw tip) and water vapour in the environment [8]. Stress corrosion cracking is also known to cause a loading-rate dependency of the fracture strength of glass, and can reduce the fracture strength significantly under long-term loading. Charles [9] proposed a phenomenological model that relates the fracture stress and the fracture time for soda-lime-silica glass rods under quasi-static tensile loading, and showed later that the model could also be applied for dynamic loads [10]. In these tests, Charles used loading rates up to 13 mm/min. Ritter [11] later showed that Charles' model correctly predicted the rate dependency of the fracture strength for similar tests performed with loading rates up to 50 mm/min. Chandan et al. [12] found that the relationship derived by Charles could describe the rate enhancement of the fracture stress in bending tests with stress rates ranging from 10^{-1} MPa/s to 10^7 MPa/s. More recent studies have also demonstrated the loading-rate dependency of the fracture

*Corresponding author

Email address: karoline.osnes@ntnu.no (K. Osnes)

strength of glass. Among them, Nie et al. [13] investigated the fracture strength of borosilicate glass at four different loading rates between 0.7 MPa/s and 4×10^6 MPa/s. It was found that the fracture strength increased with the loading rate, and that the rate dependency was larger for loading rates between 0.7 and 2500 MPa/s than above 2500 MPa/s. The increased tensile strength of glass with the loading rate was also observed by Peroni et al. [14] and Zhang et al. [15]. Zhang et al. [15] performed both quasi-static and dynamic split tensile tests, and observed that the dynamic amplification of the fracture strength increased significantly for strain rates over 350 s^{-1} . Although glass plates are less prone to fail in compression [6], it is worth noting that the compressive strength of glass is also reported to increase with the loading rate [15–17]. To accurately determine the loading-rate dependency of glass and other brittle materials can be challenging [18] and might lead to inconsistent findings across various experimental studies. More dynamic material tests, which are performed in a precise manner, are therefore necessary to better understand the effects of loading rate on the fracture behaviour of glass.

There are several reports on component tests of glass exposed to extreme loading in the open literature. Among them, we find studies on impact-loaded laminated windshields [19–21], automobile side glazing [22], laminated window glass [4, 23, 24], monolithic window glass with safety film [25] and regular monolithic window glass [16, 26]. A number of researchers have also studied the response of monolithic and laminated window glass exposed to blast loading generated by explosive detonations [3, 4, 27, 28] or pressure loading produced in a shock tube [5, 29–32]. Blast experiments in combination with fragment impact are also available [33].

In order to design glass solutions capable of withstanding extreme loading, we need models or numerical tools that can predict the fracture strength of glass under dynamic conditions. In this study, we seek to predict the initiation of unstable fracture in glass plates exposed to arbitrary loading and loading rates. Recently, we presented a strength prediction model (SPM), which is based on the existence of microscopic surface flaws and uses Monte Carlo simulations to predetermine fracture initiation in glass [31]. The SPM is an extension of a model proposed by Yankelevsky [34], and includes some additional features and adjustments. Results obtained with the model were in good agreement with quasi-static tests on glass, and the model managed to reproduce trends from dynamic tests reasonably well. However, in order to obtain more accurate predictions for dynamic loading, it was deemed necessary to include strain-rate dependency in the model. Thus, in this work we present an extended version of the SPM where the rate dependency of glass fracture is taken into account.

In an effort to validate the rate-dependent SPM, we have performed experiments on both monolithic and laminated glass

under various loading conditions and loading rates. The experimental work includes quasi-static punch tests of monolithic glass at three different loading rates from 3 mm/min to 300 mm/min, and low-velocity impact tests on monolithic and laminated glass using velocities ranging from 2 m/s to 14 m/s. The experimental results clearly demonstrate the stochastic fracture behaviour and the loading-rate dependency of the fracture strength. The rate-dependent SPM provided results that were in good agreement with the experimental results, both in terms of the fracture strength and the position of fracture initiation.

2. Material

2.1. Float glass

The glass specimens used in this study are made up by clear annealed soda-lime-silica float glass. Glass is a brittle material and it behaves in a linear elastic manner until it fails suddenly into sharp fragments. Furthermore, glass has a highly stochastic fracture behaviour, which normally results from crack propagation of pre-existing microscopic surface flaws under mode I loading (i.e., opening of a flaw) [6]. Consequently, glass plates primarily fail in tension, and the fracture strength is dependent on the applied stresses and the properties of the surface flaws [31]. The fracture strength has also been reported in many studies to be dependent on the loading rate [9–15], while the stiffness in terms of the Young’s modulus is found to be rate independent [15]. Table 1 presents commonly used material parameters for soda-lime-silica float glass [35]. The fracture toughness K_{IC} is the critical stress intensity factor for the onset of sudden, or unstable, crack growth under mode I loading. The stated value is typically denoted the static fracture toughness, and is reported by e.g., Wiederhorn [36] for quasi-static tests at room temperature. In this study, we used glass specimens provided by two different glass suppliers. The glass from supplier 1 is generally used in automobile windshields, while the glass from supplier 2 is used in both safety and regular window solutions.

Table 1: Material parameters for soda-lime-silica glass.

Density	Young’s modulus	Poisson’s ratio	Fracture toughness
ρ	E	ν	K_{IC}
2500 kg/m ³	70000 MPa	0.2	0.75 MPa√m

2.2. Polyvinyl butyral (PVB)

The laminated glass specimens used in this study include a polymeric interlayer consisting of polyvinyl butyral (PVB). PVB is widely used as a component in both laminated window glass and automobile windshields; however, depending on the application, other polymeric materials (e.g., ionoplast and

polycarbonate) can also be used. PVB is a flexible material and exhibits a nonlinear behaviour that is highly dependent on the loading rate and the temperature [37–39]. In addition, PVB is considered to be nearly incompressible and displays close to no permanent deformation after loading [38]. The material behaviour is distinctly different at low and high strain rates, in which high strain rates generate a nonlinear time-dependent behaviour that includes an initial region with an increased stiffness. This initial region is not observed at lower loading rates [37–39].

2.3. Laminated glass

Laminated glass is made by sandwiching layers of PVB or other polymeric materials in between two or more plates of glass. The layers are bonded together mechanically and chemically through a process including heat and pressure in an autoclave. The main intention of the interlayer is to increase the loading resistance and to retain broken glass fragments on the interlayer if the glass fractures. In addition, if a flexible polymer is used (e.g., PVB) deformation of the interlayer can absorb energy and in turn reduce the loading transmitted to the rest of the structure. A deformable interlayer also ensures that the glass breaks into small pieces instead of large and hazardous fragments [32]. The post-fracture behaviour of laminated glass is largely controlled by the adhesion between the polymer and the glass layers. A weak adhesion level may lead to an excessive amount of detaching glass fragments, while if the adhesion is too strong, the interlayer can rupture due to stretching over a small area [5]. The adhesion level is dependent on the autoclave process and the polymer type applied, which will affect

the delamination process [40]. Delamination is also dependent on the loading rate [41] and the ambient temperature [42].

3. Experimental study

3.1. Quasi-static punch tests

An Instron universal testing machine was used to perform quasi-static punch tests with a massive wooden (oak) impactor on monolithic glass specimens in three different test series at different loading rates. The crosshead velocity of the test machine was set to 3 mm/min, 100 mm/min and 300 mm/min, and 30 tests were performed for each loading rate. The in-plane dimensions of the glass specimens were 400 mm × 400 mm, while the thickness was approximately 1.75 mm. All 90 glass specimens were delivered by the same glass supplier (supplier 1). Neoprene rubber strips (with thickness 4 mm and width 50 mm) were glued onto two 25 mm thick aluminium clamping plates and positioned on each side of the glass specimen. Prior to testing, we ensured that the glass specimens did not have any visible flaws or defects, and that all glass fragments from previous tests were removed. Twelve equidistant M24 bolts were used to fasten the clamping plates together using a torque of 75 Nm. In order to properly tighten the bolts, while limiting the clamping pressure on the glass specimens, we placed steel stoppers on the bolts between the clamping plates. The experimental setup is illustrated in Figure 1a, while an illustration of the impactor nose is shown in Figure 1b. Note that the bottom part of the impactor nose contains a flat area.

Two synchronised Basler acA2440-75um cameras and a Phantom v2511 high-speed camera were placed below the glass

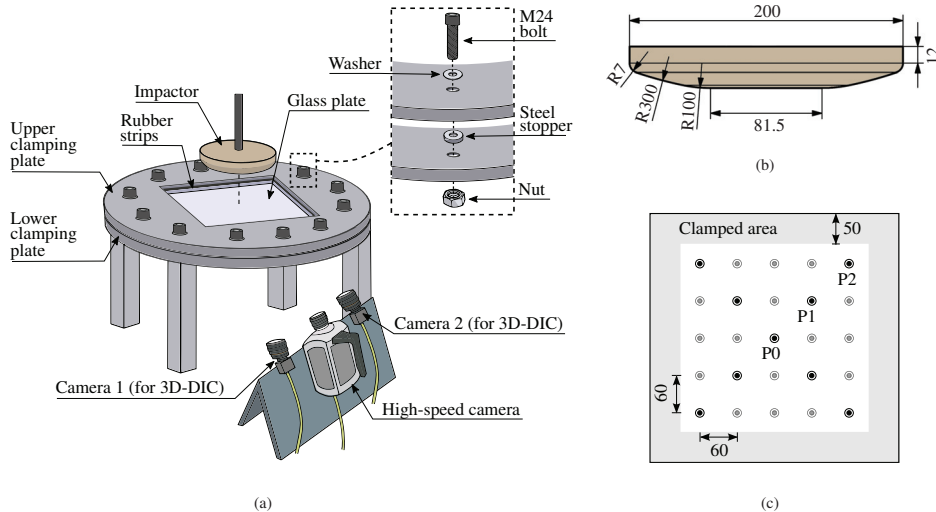


Figure 1: Quasi-static punch tests: illustration of (a) the setup and camera positions, (b) the impactor nose, (c) glass specimen with optical targets and denoted clamped area (units: mm).

specimen to film the tests. The frame rate of the synchronised cameras was set to 1 Hz for the 3 mm/min tests and 20 Hz for the 100 mm/min and 300 mm/min tests. For the high-speed camera, we used a frame rate of 100 kHz. The high-speed camera images were used to capture the fracture initiation and propagation in the glass, while the synchronised camera images were used to obtain the out-of-plane displacement of the specimens in discrete points (denoted optical targets) by means of a point-tracking procedure. This procedure is available in the in-house three dimensional digital image correlation (3D-DIC) code eCorr [44]. The optical targets consist of a white circle with a central black dot, and were spray-painted on the glass 60 mm relative to each other, see Figure 1c. Note that the grey area in the figure indicates the clamped area of the glass, i.e., the position of the rubber strips. Later in the article, we will refer to the diagonal optical targets as shown in the figure. The central optical target is referred to as P0, while the four optical targets positioned 60 mm from the centre are referred to as P1, and P2 are the four points positioned in the corners. A validation of the point-tracking procedure can be found in Ref. [31].

As a reference to the low-velocity impact tests (see Section 3.2), we performed one quasi-static punch test at 3 mm/min with the same impactor nose and monolithic glass as in the low-velocity impact tests. The reference test was otherwise per-

formed with the same experimental setup as in the quasi-static punch tests.

3.2. Low-velocity impact tests

Eleven low-velocity impact tests were performed in an Instron CEAST 9350 drop tower impact system [45] on monolithic (two tests) and laminated (nine tests) glass specimens. The impact velocities ranged from approximately 2 m/s to 14 m/s. The glass specimens were delivered by glass supplier 2. The in-plane dimensions of the glass specimens were the same as for the quasi-static punch tests, i.e., 400 mm \times 400 mm, while the thickness of the glass plate was approximately 3.8 mm. The laminated glass consisted of two 3.8 mm thick glass plates and a 1.52 mm thick PVB layer, resulting in a total thickness of 9.12 mm. We used the same fastening system as in the quasi-static punch tests; however, the thickness of the steel stoppers was adjusted to obtain approximately the same clamping pressure as for the thinner specimens.

The drop tower can impart kinetic energies up to 1800 J, using impact velocities up to 24 m/s and masses up to approximately 70 kg. The experimental setup is illustrated in Figure 2a. In the current tests, we applied the standard instrumented striker and striker-holder with a mass of 1.435 kg and 4.300 kg, respectively. By including an aluminium impactor nose with a

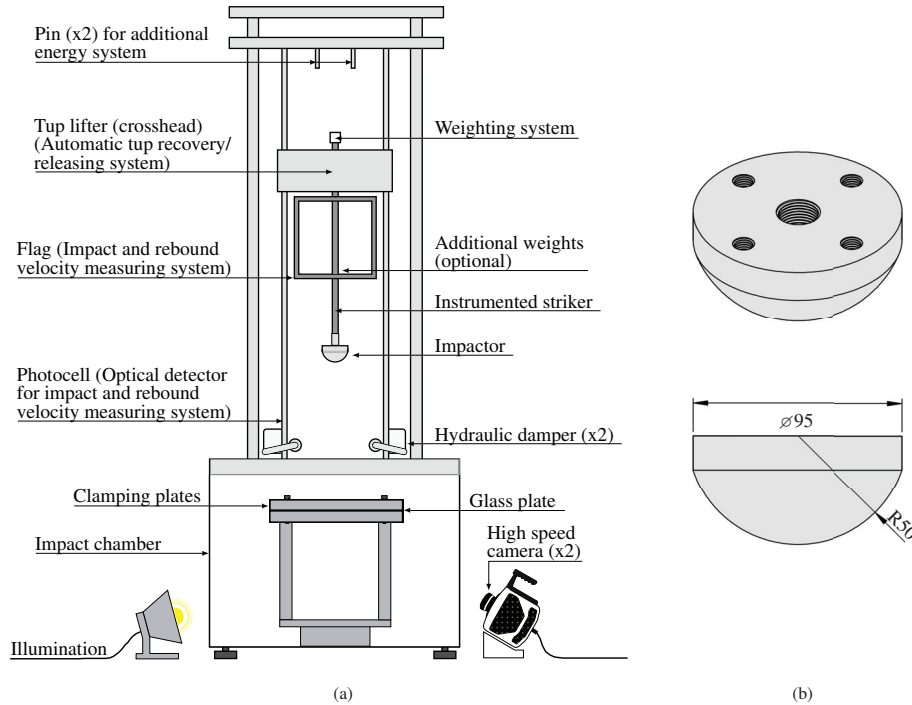


Figure 2: Low-velocity impact tests: illustration of (a) the drop tower impact system [43], (b) the impactor nose (units: mm).

mass of 0.816 kg (see Figure 2b), we achieved a total impacting mass m_p of 6.551 kg. The striker was instrumented with a load cell (using a recording rate of 500 kHz) positioned approximately 225 mm above the impactor nose tip. A stopping mechanism was activated to avoid damaging the striker if the displacement exceeded a certain limit. The contact force F between the striker and the glass specimen was calculated based on dynamic equilibrium as [46]

$$F = \left(1 + \frac{m_2}{m_1}\right)P \quad (1)$$

where m_1 and m_2 are the mass above and below the load cell, respectively, and P is the force measured in the load cell. The sum of the masses $m_1 = 5.243$ kg and $m_2 = 1.308$ kg equals the impacting mass m_p . To obtain the velocities and displacements in the tests, we employed the following numerical integration scheme [47].

$$v_{n+1} = v_n - \left(\frac{F_{n+1} + F_n}{2m_p} - g\right)\Delta t \quad (2)$$

$$d_{n+1} = d_n + \left(\frac{v_{n+1} + v_n}{2}\right)\Delta t \quad (3)$$

Here, v is the velocity and d is the displacement of the striker, F is the contact force, m_p is the impacting mass, $g = 9.81$ m/s² is the gravitational acceleration, and Δt is the time between recordings of the load cell. The subscripts $n + 1$ and n refer to the current and previous recordings, respectively.

Two synchronised Phantom v1610 high-speed cameras (with a recording rate of 25 kHz) were placed below the glass specimen to film the impact tests. The high-speed camera images were used to obtain the out-of plane displacement of the specimens through the point-tracking procedure described above, and to reveal the fracture initiation and propagation in the glass.

4. Experimental results

4.1. Quasi-static punch tests

The force-displacement histories for the three quasi-static punch test series, including their fracture points, are shown in Figure 3a. Note that the slope of the curves is similar for all tests and independent of the loading rate. Additionally, the results clearly illustrate the probabilistic fracture strength of glass as the fracture forces vary between approximately 590 N (in

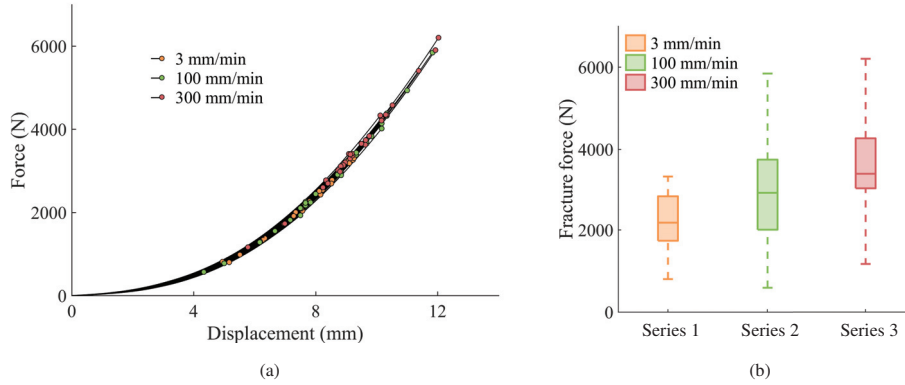


Figure 3: Results from the quasi-static punch tests: (a) force-displacement curves including fracture points, (b) box plot of the fracture forces.

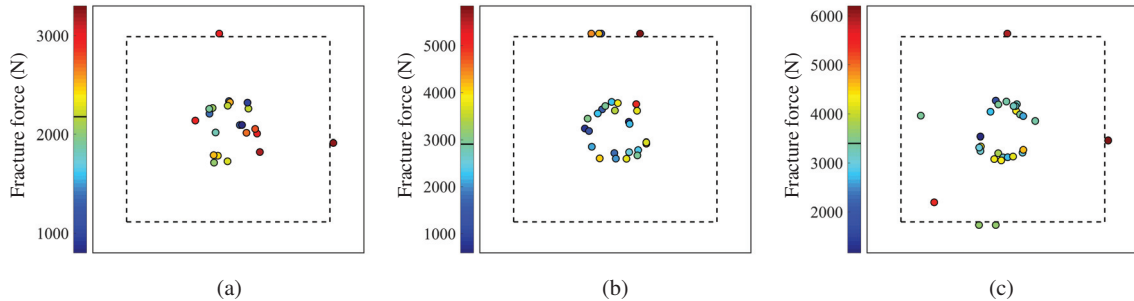


Figure 4: Point of fracture initiation with the corresponding fracture force for test series with a loading rate of (a) 3 mm/min, (b) 100 mm/min, (c) 300 mm/min.

test series 2) and 6200 N (in test series 3). Further, Figure 3b presents box plots of the fracture force for each of the three loading rates. The outer edges of the box refer to the 25th and 75th percentile, the inner line indicates the median and the dashed lines represent the rest of the data. The results in Figure 3b suggest that the median fracture force increases with the loading rate. The variance of the fracture force is also larger for series 2 and 3 compares to series 1. Furthermore, the tests display a distinct variation in the position of fracture initiation. Figure 4 illustrates the fracture positions and the corresponding fracture force for each test. The dashed lines in the figure refer to the edges of the clamped area, and the black line on the color bars denotes the median fracture force. It is seen that fracture initiated in either the face or the boundary (i.e., inside the clamped area) of the specimens, and that the fracture force is generally above the median value for boundary failures. The

reference test (see Section 3.1) reached a fracture force of 1305 N and fracture initiated close to the midpoint.

Figure 5 presents high-speed camera images that represent the different failure responses that occurred in the quasi-static punch tests, i.e., face and boundary failures at both low and high fracture forces. The time t_0 refers to the time in which fracture was first visible. Figure 5a is taken from test series 1, while Figures 5b-d are taken from test series 2. The images illustrate that a larger fracture force generates smaller fragments, which results from a higher level of stored elastic energy at the point of fracture. Moreover, fracture initiation at the face resulted in radial cracks from the initiation point and cracks along the edges of the flat area of the impactor nose (Figures 5a and 5c). For the tests with fracture initiation at the boundary, circumferential cracks formed at the boundary with subsequent fracture propagation towards the face of the plate (Figures 5b and 5d).

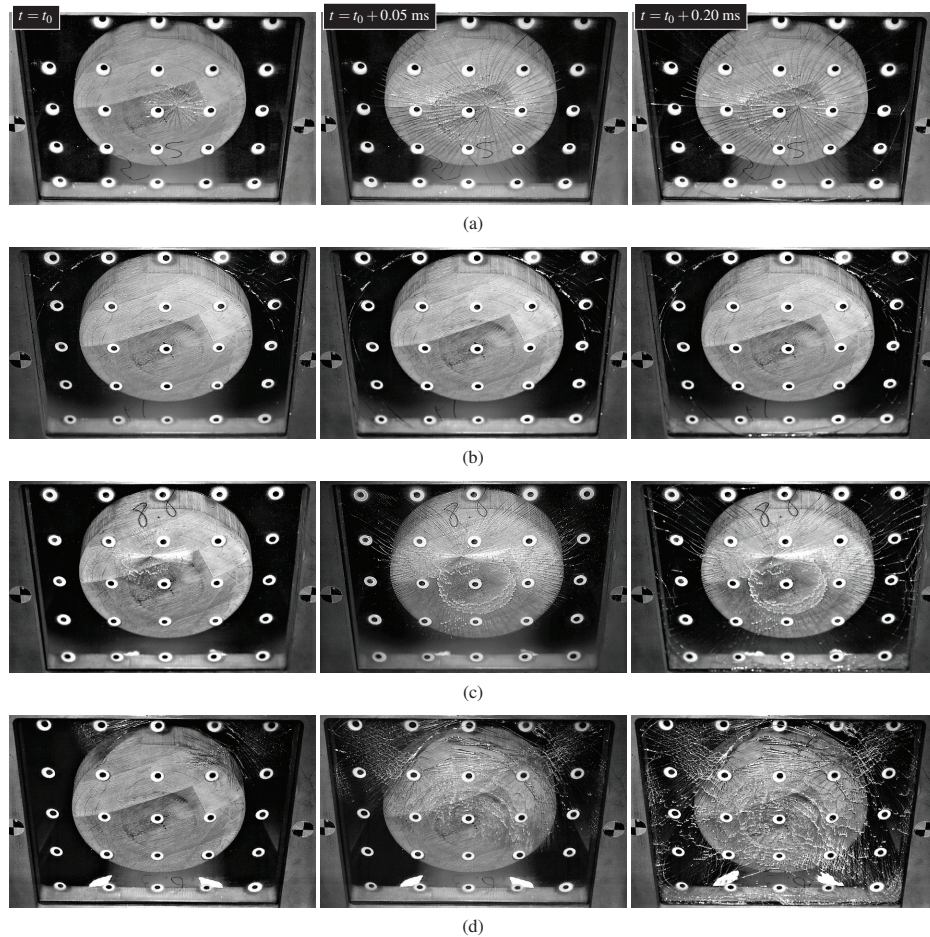


Figure 5: Typical images from quasi-static punch tests with a fracture force of (a) 801 N, (b) 1316 N, (c) 2946 N and (d) 5844 N, where fracture initiated at the face in (a) and (c), and at the boundary in (b) and (d).

4.2. Low-velocity impact tests

Table 2 presents the prescribed and the measured impact velocities at contact in the low-velocity impact tests, whereas Figures 6 and 7 display the force-time and velocity-time histories, separated into specimen type and prescribed velocities. The force and velocity histories are presented by grey and red lines, respectively, while the fracture initiation points are shown as dashed blue vertical lines. Harmonic oscillations are present in all of the tests, which are caused by dynamic coupling between the impactor, the specimens and the supports [48]. Note that the presented experimental data have not been filtered. Both of the monolithic glass plates fractured at the appointed impact velocity, which is shown by a decrease in the force level, see Figure 6. In addition, we observe a steady decrease in the velocity from contact and up to fracture initiation and a subsequent increase afterwards. This increase is caused by limited resistance in the monolithic glass after fracture initiation, and the impactor enters into free falling before being stopped by the stopping mechanism. Since the PVB offers additional resistance, we did not observe an increase in velocity after fracture of the laminated glass specimens, see Figure 7. The specimen in the first test on laminated glass did not fracture at the prescribed impact velocity. Consequently, at a time approximately equal to 2 ms, the velocity gets negative, see Figure 7a. This means that the impactor bounces back and travels in the oppo-

Table 2: Impact velocities in the low-velocity impact tests on monolithic (M) and laminated (L) glass.

Glass specimen type	M	M	L	L
Prescribed velocity (m/s)	2	4	2	3
Measured velocity (m/s)	2.32	4.11	2.32 / 2.31	3.20
Glass specimen type	L	L	L	L
Prescribed velocity (m/s)	4	6	10	14
Measured velocity (m/s)	4.03 / 4.02	5.86	9.91 / 9.93	14.08

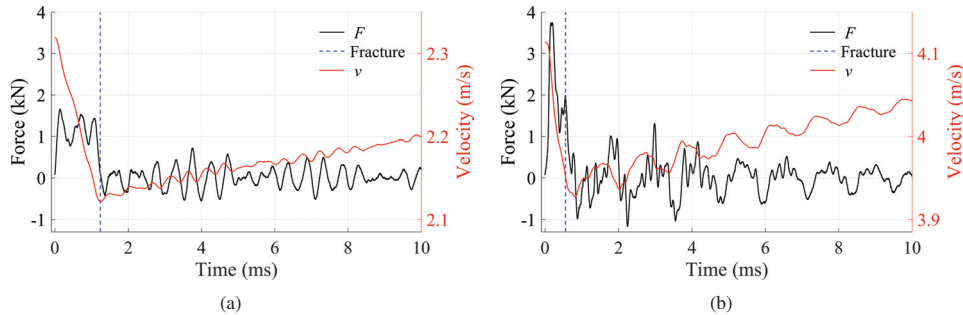


Figure 6: Contact force and velocity versus time for monolithic glass tests with prescribed impact velocities (a) 2 m/s and (b) 4 m/s.

site direction. At approximately 5 ms, there is no longer any contact between the impactor and the specimen, and the force reaches 0 kN. For the rest of the tests, there is contact during the presented histories. Moreover, in the test with a prescribed impact velocity of 14 m/s, the PVB ruptures after around 6.5 ms, as evidenced by a jump in the velocity-time curve and a large drop in force after this point, see Figure 7f. After the test was finished, a half-spherical tear with a radius of approximately 35 mm was visible in the PVB around the midpoint of the specimen.

The calculations by Equations (1)-(3) were validated by comparing the calculated displacement to the measured displacement of the striker. The measurements were performed by installing an additional camera to film the striker and using point tracking to trace its movement. It was found that the displacements were identical throughout the presented histories.

In all of the low-velocity impact tests, fracture initiated close to the midpoint, see Figure 8 for an illustration. The dashed lines in the figure indicate the edges of the clamped area, while the grey circles denote the position of the optical targets. It was also observed that the initiation occurred generally closer to the midpoint as the impactor velocity was increased. In addition, for the same impact velocity, fracture that initiated farthest from the midpoint resulted in a higher fracture strength. Note that the figure also includes the fracture initiation point for the reference test.

Figure 9 presents high-speed camera images from a test on a monolithic glass specimen with an impact velocity of 4.11 m/s. Both tests on monolithic glass had a similar response, with fracture initiation a short distance from the midpoint and propagation of radial and circumferential cracks. Figures 10 and 11 provide images from two tests on laminated glass specimens with an impact velocity of 4.02 m/s and 14.08 m/s. The response of all of the laminated glass specimens that fractured exhibited fracture initiation close to the midpoint in the upper glass plate, radial cracks propagating towards the edges, circumferential cracks forming in both glass plates, and detaching glass

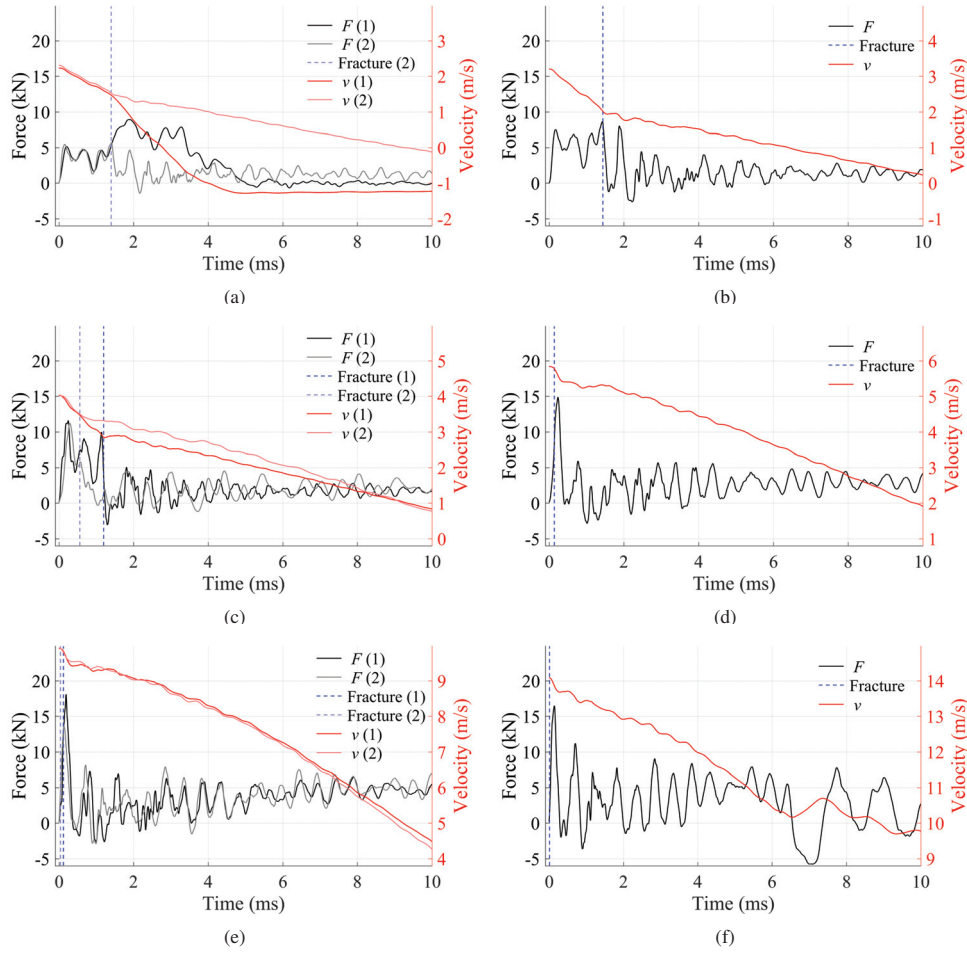


Figure 7: Contact force and velocity versus time for laminated glass tests with prescribed impact velocities (a) 2 m/s, (b) 3 m/s, (c) 4 m/s, (d) 6 m/s, (e) 10 m/s, (f) 14 m/s.

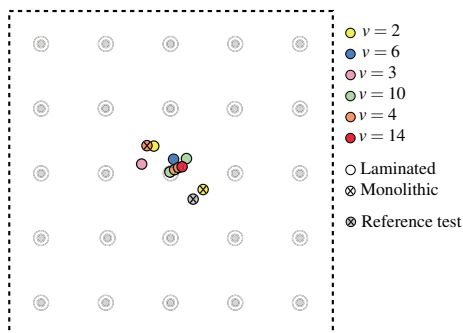


Figure 8: Position of fracture initiation in the low-velocity impact tests and the reference test (units: m/s).

fragments from the PVB interlayer. As expected, an increased impact velocity resulted in more severe damage, i.e., a larger out-of-plane displacement and more detachment of glass fragments. Additionally, by increasing the impact velocity, fracture seemed to occur earlier in the lower glass plate, resulting in a less refined fracture pattern. The upper glass plate is defined as the plate in direct contact with the impactor.

5. Numerical modelling

5.1. Strength prediction model

A model for predicting the fracture strength of glass was recently presented by Osnes et al. [31], and is an extension of the work by Yankelevsky [34]. The model, referred to as the strength prediction model (SPM), performs virtual experiments

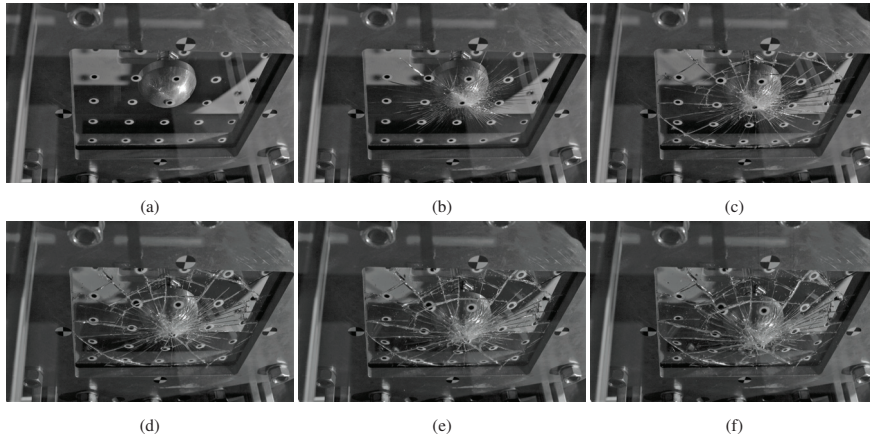


Figure 9: Images from a test on monolithic glass with impact velocity of 4.11 m/s at (a) 0.52 ms, (b) 0.60 ms, (c) 2.44 ms, (d) 6.00 ms, (e) 8.00 ms, and (f) 10.0 ms after contact.

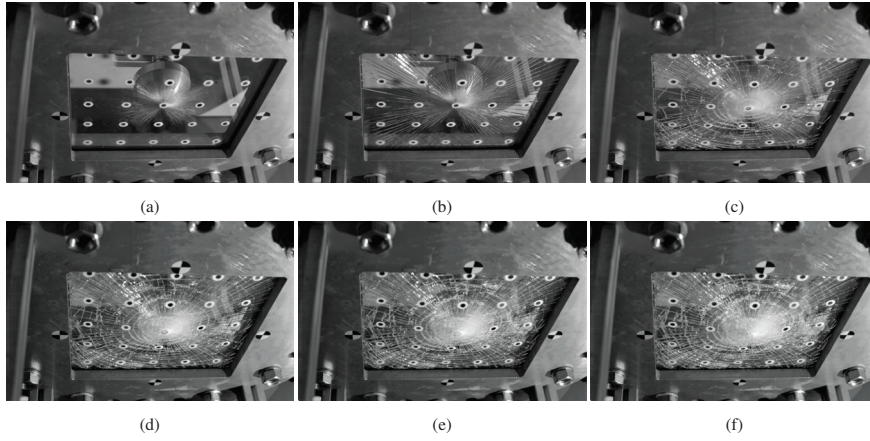


Figure 10: Images from a test on laminated glass with impact velocity of 4.02 m/s at (a) 0.60 ms, (b) 0.68 ms, (c) 2.52 ms, (d) 6.00 ms, (e) 8.00 ms, and (f) 10.0 ms after contact.

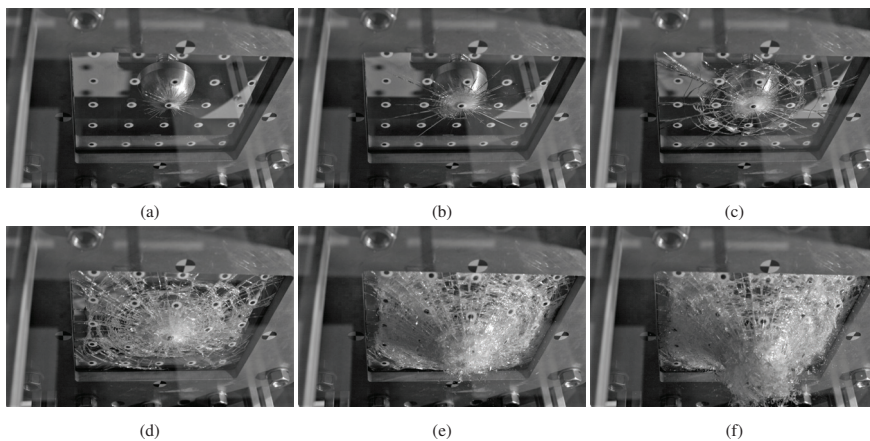


Figure 11: Images from a test on laminated glass with impact velocity of 14.08 m/s at (a) 0.01 ms, (b) 0.08 ms, (c) 0.16 ms, (d) 1.92 ms, (e) 6.00 ms, and (f) 10.0 ms after contact.

on glass by combining outputs from an FE simulation and information about artificial surface flaws in a Monte Carlo simulation. The model calculates the onset of unstable fracture, and can thus estimate the probability distribution of the fracture stress, the fracture force and fracture displacement, and the position of fracture initiation. Since the chance of crack arrest in glass is small, initiation of unstable fracture is often associated with failure in the entire plate. A detailed description of the SPM, including a comparison with experimental results, can be found in Ref. [31], but a short description is given herein for completeness. Due to the nature of fracture in glass, we can apply linear elastic fracture mechanics [7] to calculate the fracture strength of glass (i.e., the initiation of unstable crack growth) by

$$K_I \geq K_{IC}, \quad K_I = Y \sigma \sqrt{\pi a} \quad (4)$$

where K_I is the stress intensity factor for mode I loading, K_{IC} is the corresponding fracture toughness, Y is a geometrical factor depending on the flaw shape, σ is the remote tensile stress normal to a flaw, and a is the depth of a surface flaw. Thus, for $K_I = K_{IC}$, σ is equal to the fracture stress. In the model, the surface flaws are assumed to have a semi-circular shape, and the geometrical factor Y is calculated from an empirical expression proposed by Newman and Raju [49]. The required input of the SPM is given in the following list.

- Fracture toughness K_{IC} (MPa $\sqrt{\text{m}}$)
- Maximum flaw depth a_{max} (mm)
- Flaw density ρ_{flaw} (flaws/mm²)
- Size of the jumbo plate A_{jumbo} (mm²)
- Number of iterations, i.e., virtual experiments
- Stress history from an FE simulation (over k frames)

The parameter A_{jumbo} refers to the area of a larger plate in which the analysed specimens are cut from, and are typically about 14.5-19.3 m² [50]. The output from the FE simulation is issued from a specified number of evenly spaced time intervals, referred to as frames. It should be noted that the number of frames k must be large enough to capture the stress history in a sufficient manner. In the model, each surface of a hypothetical jumbo plate is first assigned a number of artificial flaws with varying sizes, which follows the Mott's distribution function dependent on ρ_{flaw} and a_{max} . Each flaw is also given a random in-plane orientation at an angle between 0 and π . It is assumed that each surface of the jumbo plate contains one flaw of size a_{max} . The jumbo plate is then cut into the sizes of the analysed plate and each element, or cluster of elements [31], is assigned one flaw at random. In each iteration, the stress history and the information about the flaws are combined, and the fracture criterion (Equation 4) is checked for every flaw in each frame.

When (or if) failure is reached, the necessary information is saved and another iteration begins. According to Yankelevsky [34], 5000 iterations are required to obtain a converged failure probability distribution.

5.2. Rate dependency

The fracture strength of glass is reported to increase with the loading rate [9–15]. Consequently, to obtain more realistic failure predictions for dynamic loading, we have introduced a strain-rate dependent dynamic fracture toughness K_{ID} . Exactly how the loading rate affects the fracture strength of glass is still an open topic of research [18], and the following procedure is a first attempt to add rate dependency to the SPM. The proposed dynamic fracture toughness K_{ID} is given as

$$K_{ID} = K_{IC} \left(\frac{\bar{\dot{\epsilon}}}{\dot{\epsilon}_0} \right)^{1/(1+N_s)} \geq K_{IC} \quad (5)$$

where $\bar{\dot{\epsilon}}$ is a time-averaged strain rate, N_s is an exponent that controls the strain-rate enhancement, and $\dot{\epsilon}_0$ is a reference strain rate below which the static value of the fracture toughness K_{IC} applies. The relationship is based on the works by Charles [9, 10] on stress corrosion in glass, and by assuming a constant loading rate. A similar approach was used by Cormie et al. [51] to account for the strain-rate enhancement of the fracture strength of glass under blast loading. It should be noted that a decrease in fracture strength caused by stress corrosion is not considered in the rate-dependent SPM at this point, and the minimum value of K_{ID} is set to K_{IC} . Further, the time-averaged strain rate is calculated as [32]

$$\bar{\dot{\epsilon}} = \frac{1}{t_c} \int_0^t \dot{\epsilon} \exp\left(-\frac{\tau-t}{t_c}\right) d\tau \quad (6)$$

where t_c is a decay parameter and $\dot{\epsilon}$ is the strain rate. A time-averaged strain rate is used to avoid spurious stress peaks in calculations of dynamic problems. Furthermore, by performing the integration from $t = 0$ to $t = t_n + \Delta t_{n+1}$, Equation (6) can be written in a discretised manner as

$$\bar{\dot{\epsilon}}_{n+1} = \bar{\dot{\epsilon}}_n \exp\left(-\frac{\Delta t_{n+1}}{t_c}\right) + \dot{\epsilon}_{n+1} \left(1 - \exp\left(-\frac{\Delta t_{n+1}}{t_c}\right)\right) \quad (7)$$

where $\dot{\epsilon}_{n+1}$ is the strain rate calculated as

$$\dot{\epsilon}_{n+1} = \frac{\epsilon_{n+1} - \epsilon_n}{\Delta t_{n+1}}, \quad \Delta t_{n+1} = t_{n+1} - t_n \quad (8)$$

Note that for $\Delta t_{n+1} \gg t_c$, the time-averaged strain rate becomes equal to the strain rate. In addition, the strain has the same direction as the normal stress σ , i.e., in the normal direction to a surface flaw. The subscripts n and $n+1$ refer to the previous time t_n and the current time t_{n+1} .

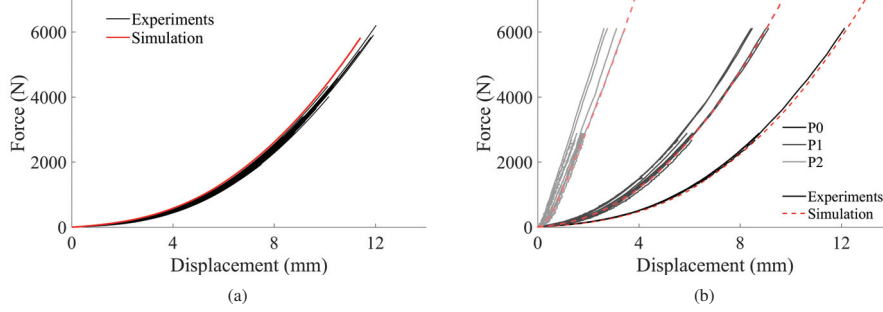


Figure 12: Comparison of an FE simulation and quasi-static punch tests in terms of force versus (a) displacement of the impactor, and (b) displacement of optical targets.

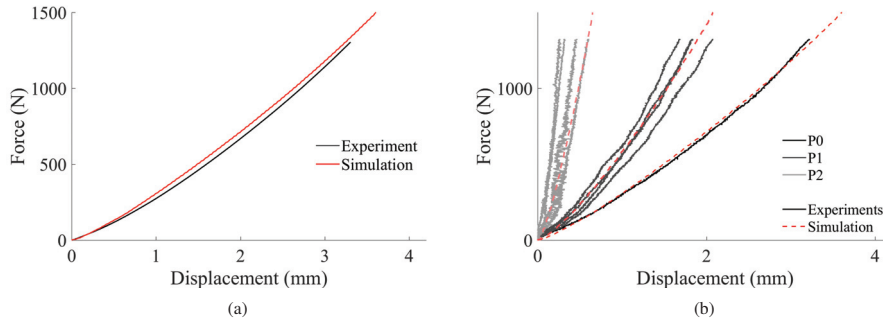


Figure 13: Comparison of an FE simulation and the reference test in terms of force versus (a) displacement of the impactor, and (b) displacement of optical targets.

6. Numerical study

In the numerical study, we investigate whether the rate-dependent SPM is able to recreate the fracture strength observed in the experimental tests. Therefore, each test series was first recreated by an FE simulation to retrieve the stress history in the glass to be used as input to the SPM. Note that no fracture criterion is used for the glass in the FE models. All FE simulations were performed using the explicit solver of Abaqus (version 2017).

6.1. Finite element simulations

6.1.1. Quasi-static punch tests

The FE model of the quasi-static punch tests consisted of an impactor nose, a glass plate, and two rubber parts positioned on each side of the glass. The impactor nose was modelled as an analytical rigid surface, while the glass was made-up by $5 \text{ mm} \times 5 \text{ mm} \times 1.75 \text{ mm}$ shell elements with five integration points over the thickness. The rubber consisted of $5 \text{ mm} \times 5 \text{ mm} \times 0.7 \text{ mm}$ fully integrated solid elements. The movement of the outer surfaces of the rubber was restricted in all directions as a way of indirectly including the rest of the fastening system.

Both the glass and the rubber were modelled with a linear elastic material model. Table 1 presents the parameters employed for the glass, while for the rubber, we used a Young's modulus of 2 MPa and a Poisson's ratio of 0.46 [31]. Although a linear-elastic material model might simplify the description of the rubber behaviour, it was deemed sufficient in this study due to limited deformation of the rubber. The impactor was prescribed a gradually increasing velocity over a short time period before reaching a constant value. Furthermore, the FE model of the reference test was identical to the quasi-static punch test model, except for the shape of the impactor nose.

Figure 12a compares the force versus displacement of the impactor in the quasi-static punch tests and the corresponding simulations. Figure 12b further presents the force versus displacement of the optical targets P0, P1 and P2 (see Figure 1c) in the FE simulations and three selected experiments, one for each loading rate. Note that the experimental data is not visible after fracture, and that the three tests fractured at different time points. In addition, the displacement in P1 and P2 are not perfectly symmetric in the tests, as in the simulations. Nevertheless, the agreement between the simulations and the experiments is in general good, which suggests that the applied FE

model is able to recreate the experiments before fracture. The stress histories could therefore be used as input to the SPM. The same comparison is also made for the reference test, see Figure 13. Again, the results indicate that the FE model provides the correct behaviour and the stress history could be used further.

6.1.2. Low-velocity impact tests

The FE model of the low-velocity impact tests was similar to the quasi-static punch test model presented in Section 6.1.1. Differences include a different impactor nose shape with a prescribed initial velocity, and, naturally, the additional glass and PVB layer for the laminated glass specimens. In order to avoid that stress singularities would arise at the midpoint of the glass specimen, a small part of the impactor tip was made flat. The PVB was made-up by $10 \text{ mm} \times 10 \text{ mm} \times 0.5 \text{ mm}$ solid elements, and the glass and the PVB layers were merged together

by a tied constraint at the inner surfaces. The PVB layer was modelled using a non-linear viscoelastic material model, consisting of a hyperelastic part described by the Arruda-Boyce model, and a viscoelastic part defined by the Bergström-Boyce creep model. The complete model is described in the work by Bergström and Boyce [52], while details on the implementation in Abaqus can be found in Refs. [53, 54]. Table 3 presents the input parameters that we used for the viscoelastic material model, where μ is the shear modulus, λ_m is the locking stretch, D described the compressibility, A is the creep parameter, m is the effective stress exponent, and C is the creep strain exponent. The input parameters were obtained by a combination of curve fitting and inverse modelling of tensile tests on PVB by Hooper et al. [37] and Del Linz et al. [39]. Figures 14 and 15 compare the displacements of the optical targets P0, P1 and P2, and the velocity of the impactor in the FE simulations and the experiments on monolithic and laminated glass specimens with a prescribed impact velocity of 2 m/s. The experimental data is removed after the fracture point (denoted by a blue dashed line); hence, only one test could be compared throughout the entire course of the displacement. For the mono-

Table 3: Input parameters for the PVB material model

μ	λ_m	D	A	m	C
4.18	2.0	0.01	0.001	3.0	-1.0

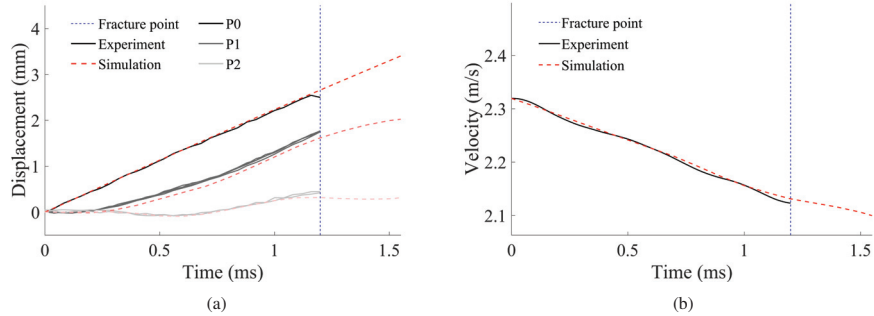


Figure 14: Comparison of an FE simulation and an experiment on monolithic glass ($v = 2.32 \text{ m/s}$) in terms of (a) displacement in optical targets and (b) velocity of impactor.

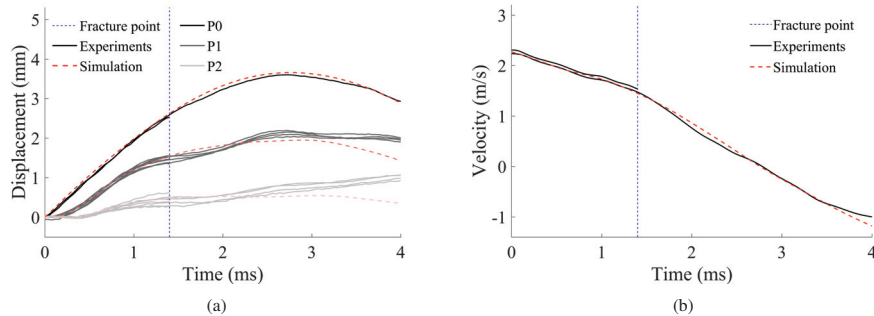


Figure 15: Comparison of an FE simulation and experiments on laminated glass ($v = 2.31$ and 2.32 m/s) in terms of (a) displacement in optical targets and (b) velocity of impactor.

Table 4: Input parameters for the rate-dependent SPM

Glass supplier	K_{IC}	a_{max}	ρ_{flaw}	A_{jumbo}	Iterations	N_s	$\dot{\epsilon}_0$
Supplier 1	0.75 MPa \sqrt{m}	50 μm	1 flaws/cm ²	3210 \times 6000 mm ²	5000	16	10 ⁻⁵ s ⁻¹
Supplier 2	0.75 MPa \sqrt{m}	75 μm	2 flaws/cm ²	3210 \times 6000 mm ²	5000	16	10 ⁻⁵ s ⁻¹

lithic glass test, it is seen that the curves are fairly coincident, and we could therefore assume that the FE simulation manages to describe the stress state in the glass before fracture. The FE simulation of the laminated glass tests also fits well with the experiments. However, there is some disagreement after maximum displacement in points P1 and P2, which may be due to the simplified modelling of the rubber material. If the glass fractures, it will most likely occur before this point, and the FE model was considered sufficiently accurate. The stress history could therefore be used as input to the SPM. A similar comparison was made for the rest of the low-velocity impact tests, showing similar accuracy, but is not presented here for brevity.

6.2. Rate-dependent strength prediction

Table 4 presents the input parameters of the rate-dependent SPM for glass from each of the two glass suppliers. Recall that glass from supplier 1 was used for the quasi-static punch tests, while glass from supplier 2 was used for the low-velocity impact tests and the reference test. Most of the input is the same for the two suppliers; however, the parameters that describe the surface condition of the glass specimens, i.e., a_{max} and ρ_{flaw} , are different. The surface condition parameters for specimens from supplier 1 were chosen through inverse modelling of the quasi-static punch tests at 3 mm/min, while for the specimens from supplier 2 we applied inverse-modelling of the reference test. The results imply that the surface condition is better for the glass from supplier 1 than for the glass from supplier 2. However, to have more confidence in the input parameters, measurements of the flaw sizes and flaw densities should be performed, and will therefore be a topic of further investigation. A method for performing such measurements was presented in the work by Wereszczak et al. [55]. Furthermore, the value of the exponent N_s was set to 16, which is consistent with the work of Charles [9, 10], while the reference strain rate $\dot{\epsilon}_0$ was chosen as 10⁻⁵ s⁻¹ since the value is typically defined as the beginning of the quasi-static loading domain [56].

6.2.1. Quasi-static punch tests

Figure 16 presents results from SPM simulations of the quasi-static punch tests, and includes three plots for each of the three loading rates. Figure 16a compares box plots of the fracture force from the experiments and the strength predictions. In the box plot representing the SPM results, the box and the dashed lines denote 99% of the data, making the dots outside

the remaining 1%. The box edges refer to the 25th and 75th percentile and the inner line indicates the median. The 3 mm/min test series proved to be independent of the loading rate, as it obtained the same results with and without the strain-rate enhancement of the fracture toughness defined in Equation (5). The predictions of the 100 mm/min and 300 mm/min test series obtained a 42% and 57% increase in the median fracture force compared to the 3 mm/min test series, respectively. Furthermore, for the prediction of the 100 mm/min test series, we achieved one extreme outlier with a fracture force of approximately 10000 N. However, for an easier representation of the results, this value was removed from the plots in Figure 16.

From the box plots, we observe that the SPM manages to recreate the increase in the fracture force and its variance with the loading rate, and that most experimental values are captured by the model. However, for the 100 mm/min test series, the minimum fracture force in the experiment is not predicted by the model, possibly due to a larger surface flaw than described by the appointed a_{max} . Note that the predictions of the 100 mm/min and 300 mm/min series without the rate dependency would be identical to the 3 mm/min prediction, demonstrating the importance of including rate enhancement for high loading rates. Furthermore, Figure 16b presents the predicted positions of fracture initiation, in which the colours denote the percentage of failure occurrence at the given position. Fracture initiate primarily around the flat area of the impactor nose, but also at the boundary, which is in accordance with the experimental tests, see Figure 4. Fracture initiation takes place in tension, which corresponds to the lower side of the glass for face fractures, and the upper side of the glass for boundary fractures. Moreover, Figure 16c shows the predicted fracture initiation with colours indicating the median fracture force. The model predicts that fracture can occur at both high and low forces at the face and the boundary of the glass plate, but the lowest fracture forces are primarily caused by fracture initiation at the face. This is also in agreement with the experiments. Furthermore, the predictions suggest that the position of fracture initiation is independent of the employed loading rates, and that the number of face failures versus boundary failures is relatively constant. Whether or not this also holds for the experiments is unclear due to the limited number of tests.

Results from the SPM simulation of the reference test are shown in Figure 17, which includes a box plot of the fracture

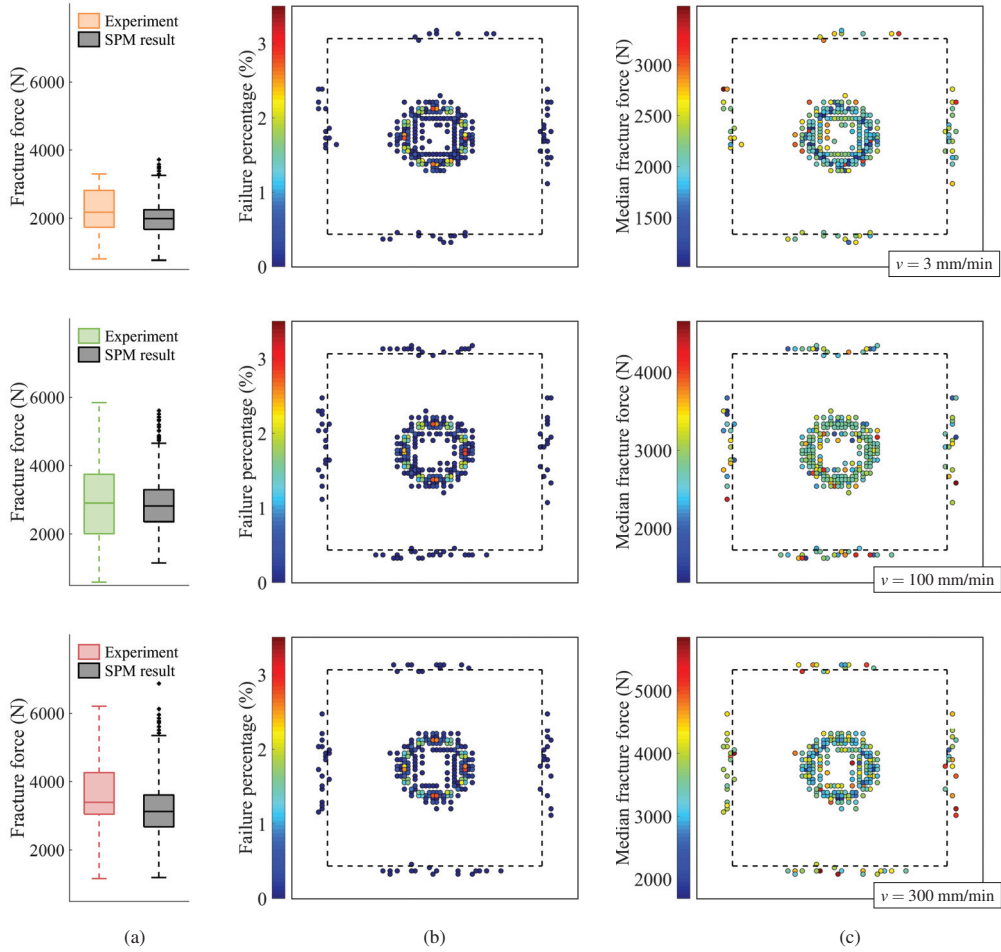


Figure 16: SPM results for the quasi-static punch tests: (a) fracture force compared to the experiments, (b) fracture initiation indicating failure percentage and (c) median fracture force.

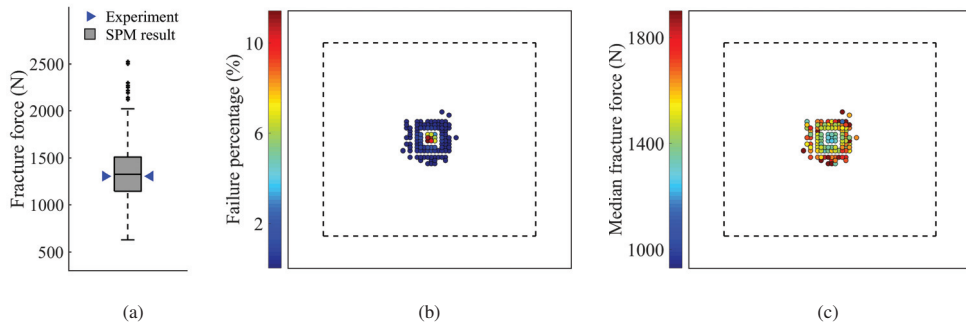


Figure 17: SPM results for the reference tests: (a) fracture force compared to the experiment, (b) fracture initiation indicating failure percentage and (c) median fracture force.

force and illustrations of the fracture initiation with denoted failure percentage and median fracture force. The box plot includes the obtained fracture force from the experiment, indicated by two blue arrows. The fracture initiation plots illustrate that fracture initiates most frequently at the midpoint, but can also occur a distance of approximately 40 mm away. Consequently, the fracture initiation in the experiment appears within the predicted ones. Additionally, the simulation predicts that the lowest fracture forces are mainly obtained at the midpoint. By comparing the results to the quasi-static punch tests, we can clearly see how the shape of the impactor nose influences the results. Compared to the quasi-static punch tests, the fracture initiates closer to the midpoint without boundary failures, and the scatter of the obtained fracture forces is lower.

6.2.2. Low-velocity impact tests

In the SPM simulations of the low-velocity impact tests, we made use of the time-averaged strain rate $\bar{\dot{\epsilon}}$, see Equation (6) in Section 5.2. For these simulations, it was therefore necessary to define the decay parameter t_c , and the value was set to 10^{-4} s. By using the time-averaged strain rate with the appointed t_c instead of the actual strain rate, we obtained fracture slightly earlier without significantly altering the fracture strength distribution. Results from the SPM simulations of the low-velocity impact tests are presented in Figures 18 to 20, and include box plots of the fracture strength, and illustrations of the fracture

positions with colours denoting the failure percentage and median fracture strength. The fracture strength is given here in terms of both the impactor displacement and time at fracture. Note that the median in the box plots for the SPM predictions of the 4 m/s test on monolithic glass, and 3 m/s and 4 m/s tests on laminated glass nearly coincide with the 25th percentile.

From the box plots, we observe that the model predictions are generally in good agreement with the experimental results. However, some of the SPM results deviate from the experiments. Both of the tests on laminated glass with a prescribed velocity of 4 m/s fall outside the 99 percentile from the model prediction, see Figure 19. In addition, the SPM simulations predicted that fracture would occur in all of the virtual experiments. Since fracture did not occur in one of the laminated specimens tested at 2 m/s, this is a conservative result. Nevertheless, the SPM model appears to correctly predict many of the trends observed in the experiments. This includes a more localised failure occurrence when increasing the impactor velocity and overall obtaining higher fracture strengths for fracture initiation far from the midpoint. Additionally, the fracture initiation points in the experiments are all found to lie within the corresponding predictions, see Figure 8. Most of the laminated glass specimens experience fracture initiation in the upper glass plate, which is also in accordance with the experiments.

Although the SPM results appear to deviate from some of the low-velocity impact tests and fit very well with others, it

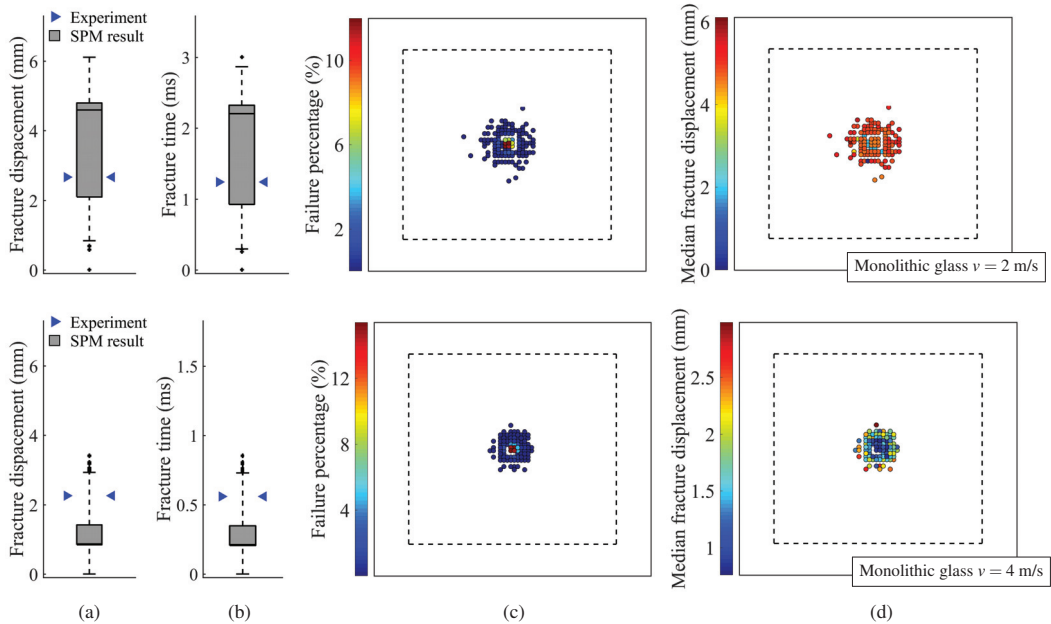


Figure 18: SPM results for the low-velocity impact tests on monolithic glass: (a) fracture displacement and (b) fracture time compared to the experiments, (c) fracture initiation indicating failure percentage and (d) median fracture force.

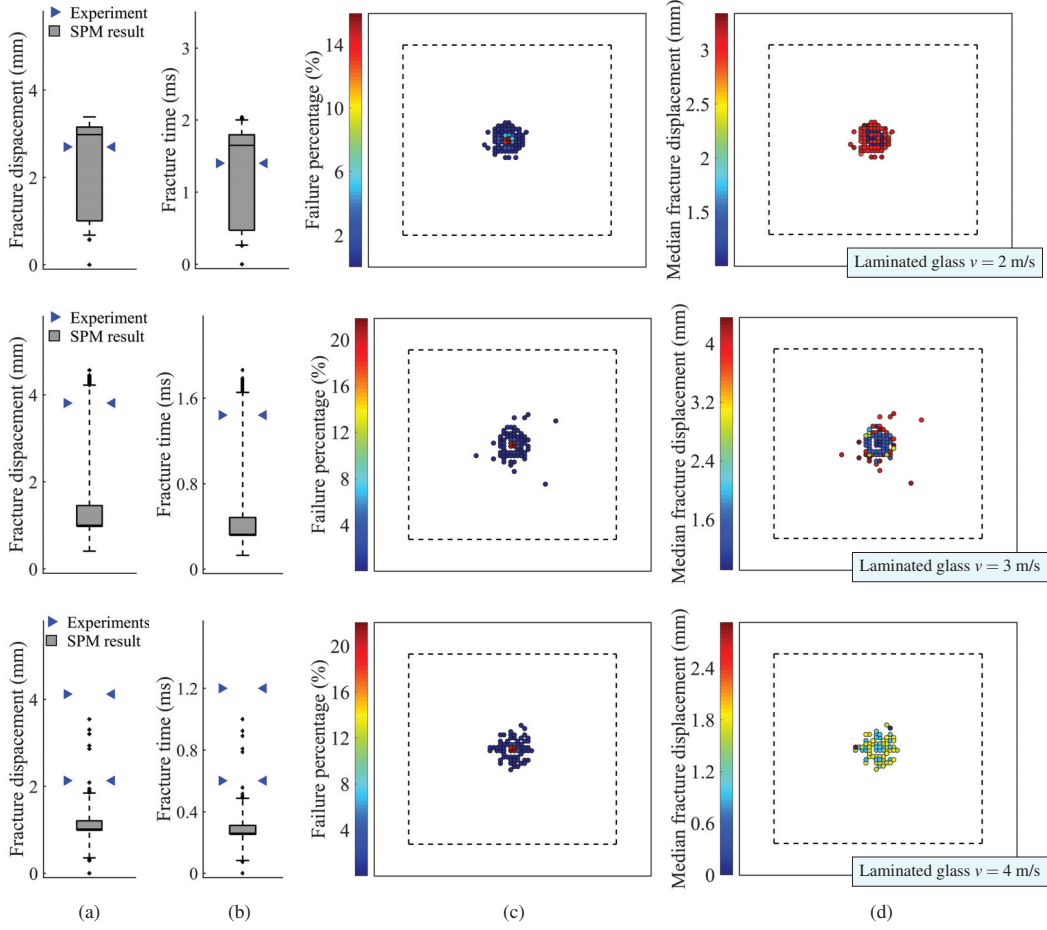


Figure 19: SPM results for the low-velocity impact tests on laminated glass with $v = 2-4$ m/s: (a) fracture displacement and (b) fracture time compared to the experiments, (c) fracture initiation indicating failure percentage and (d) median fracture force.

is important to bear in mind that we have a limited amount of experimental data. Therefore, to draw any definite conclusions, a much larger experimental study should be carried out. However, the disagreement with some of the experiments and the SPM results could be explained by a number of possible reasons. The applied flaw parameters might not reflect the actual surface condition of the tested glass specimens. Additionally, the SPM is a relatively simple model, and it might not be able to capture all effects arising in the physical tests. That being said, the study demonstrates that to obtain realistic strength predictions, a rate enhancement must be included in one way or another. Figure 21 presents results from SPM simulations with and without strain-rate enhancement for two selected low-velocity impact tests, and illustrates that if rate dependency is not included, we clearly underestimate the fracture strength.

On a last note, the results from the SPM should be independent of the mesh used in the FE models. We therefore carried out a small mesh sensitivity study for two of the presented cases, i.e., the quasi-static punch tests at 100 mm/min, and the low-velocity impact test at 4.11 m/s on monolithic glass. We performed two new simulations using a refined mesh consisting of elements with half the size compared to the original mesh. Figure 22 presents the results, and demonstrates that the predictions are close-to mesh independent for the investigated mesh densities, since the width of the dashed lines were approximately the same and the predicted median fracture strength was within 2% of each other.

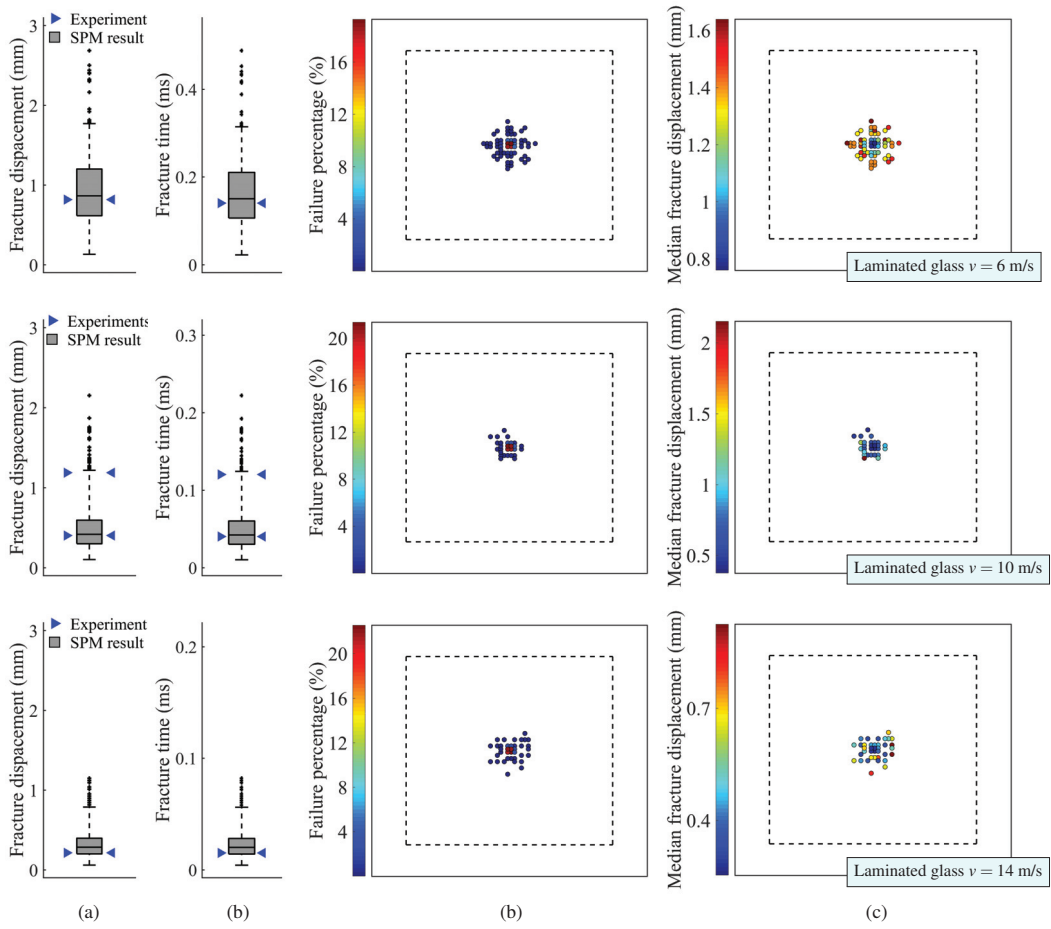


Figure 20: SPM results for the low-velocity impact tests on laminated glass with $v = 6-14$ m/s: (a) fracture displacement and (b) fracture time compared to the experiments, (c) fracture initiation indicating failure percentage and (d) median fracture force.

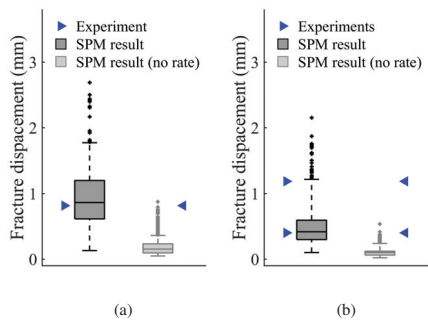


Figure 21: Strength predictions with and without rate-dependency for the low-velocity impact tests on laminated glass with a prescribed impact velocity of: (a) 6 m/s, (b) 10 m/s.

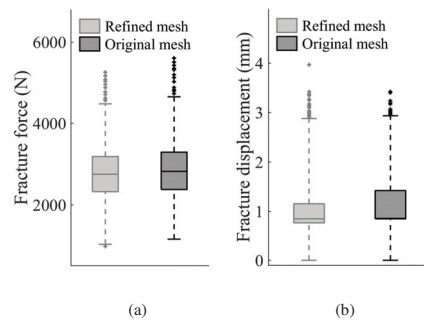


Figure 22: Mesh sensitivity study for the strength predictions of the (a) 100 mm/min quasi-static punch test, and (b) low-velocity impact test at 4.11 m/s on monolithic glass.

7. Concluding remarks

In this study, we have proposed an extension to account for rate dependency in a strength prediction model (SPM) for monolithic and laminated glass [31]. The SPM aims to predict fracture initiation in glass exposed to arbitrary loading, and is based on the existence of microscopic surface flaws. These surface flaws are known to govern fracture initiation in glass and cause a highly stochastic fracture behaviour. By combining stress histories from an FE simulation and information about artificial surface flaws, the SPM can output the probabilistic fracture strength of glass through numerous virtual experiments. To account for rate dependency in the SPM, we proposed an approach that is based on works by Charles [9, 10] on stress corrosion in glass.

In an effort to validate the rate-dependent SPM, we performed experiments on both monolithic and laminated glass specimens under various loading conditions and loading rates. In total, 90 quasi-static punch tests were conducted on monolithic glass at loading rates of 3 mm/min, 100 mm/min and 300 mm/min. We also performed low-velocity impact tests on monolithic glass with impact velocities of 2 m/s and 4 m/s, and laminated glass with impact velocities ranging from 2 m/s to 14 m/s. The quasi-static punch tests demonstrated the stochastic fracture strength of glass by a large variation in both the fracture force and the position of fracture initiation. Additionally, the median and the variance of the fracture force appeared to increase with the loading rate. The stochastic fracture behaviour of glass was also demonstrated by the low-velocity impact tests, since the same loading conditions resulted in different fracture strengths. The position of fracture initiation also varied. As expected, an increased impact velocity resulted in more severe damage in the laminated glass specimens, with a larger out-of-plane displacement and more detaching glass fragments from the polymeric interlayer. For the highest impact velocity, we also obtained tearing of the interlayer.

The rate-dependent SPM was able to successfully capture many of the trends observed in the experimental tests. For the quasi-static punch tests, the SPM managed to recreate the increase in the fracture force and its variance with the loading rate, and most of the experiments occurred within the predictions, both in terms of the fracture force and the position of fracture initiation. For the low-velocity impact tests, the predicted fracture strengths were generally in very good agreement with the experiments, and the fracture initiation from the experiments were all found to lie within the predictions. In addition, higher fracture strengths were obtained for fracture initiation some distance from the midpoint of the specimen, which was also in accordance with the experiments.

However, we observed that some of the experiments deviated from the SPM results, which might be explained by an

insufficient description of the surface flaws in the model. Consequently, it may be necessary to perform measurements of the surface condition of glass plates to obtain more realistic input parameters. In addition, to better validate the SPM, a more extensive experimental study should be performed, including experiments with higher loading rates than presented in this study. It is also worth mentioning that the proposed rate-dependent SPM is a relatively simple model, and might not be able to capture all effects arising in physical tests. However, it is apparent from the numerical study that some form of rate dependency must be included in order to obtain reasonable results. All things considered, the SPM appears to have great potential as it manages to correctly display a number of trends in the experiments. The model can therefore contribute to more predictive modelling of the probabilistic fracture strength of glass under both quasi-static and dynamic loading conditions.

Acknowledgements

The present work has been carried out with financial support from the Centre of Advanced Structural Analysis (CASA), Centre for Research-based Innovation, at the Norwegian University of Science and Technology (NTNU) and the Research Council of Norway through project no. 237885 (CASA). The authors would like to thank Mr. Trond Auestad and master students Tormod Grue, Simen Kjernlie, Jonas Rudshaug, Eyvind Hustvedt Evensen and Ruben Løland Sælen for assisting with the experimental programme. Acknowledgements are also expressed to Modum Glassindustri and Dr. Octavian Knoll at the BMW Group Research and Innovation Center for providing glass specimens for use in the experimental programme.

References

- [1] M. Haldimann, A. Luible, M. Overend, *Structural use of glass*, 10th Edition, Iabse, 2008, Ch. 4, pp. 85–86.
- [2] J. Belis, D. Mocibob, A. Luible, M. Vandebroek, On the size and shape of initial out-of-plane curvatures in structural glass components, *Construction and Building Materials* 25 (5) (2011) 2700–2712.
- [3] M. Larcher, G. Solomos, F. Casadei, N. Gebbeken, Experimental and numerical investigations of laminated glass subjected to blast loading, *International Journal of Impact Engineering* 39 (1) (2012) 42–50.
- [4] X. Zhang, H. Hao, Z. Wang, Experimental study of laminated glass window responses under impulsive and blast loading, *International Journal of Impact Engineering* 78 (2015) 1–19.
- [5] J. Pelfrene, J. Kuntsche, S. Van Dam, W. Van Paepegem, J. Schneider, Critical assessment of the post-breakage performance of blast loaded laminated glazing: experiments and simulations, *International Journal of Impact Engineering* 88 (2016) 61–71.
- [6] J. B. Wachtman, W. R. Cannon, M. J. Matthewson, *Mechanical properties of ceramics*, 2nd Edition, John Wiley & Sons, 2009.
- [7] T. L. Anderson, *Fracture mechanics: Fundamentals and applications*, 3rd Edition, CRC press, 2005, Ch. 2, pp. 48–49.
- [8] S. Wiederhorn, L. Bolz, Stress corrosion and static fatigue of glass, *Journal of the American Ceramic Society* 53 (10) (1970) 543–548.

- [9] R. Charles, Static fatigue of glass: I & II, *Journal of Applied Physics* 29 (11) (1958) 1554–1560.
- [10] R. Charles, Dynamic fatigue of glass, *Journal of Applied Physics* 29 (12) (1958) 1657–1662.
- [11] J. Ritter Jr, Dynamic fatigue of soda-lime-silica glass, *Journal of Applied Physics* 40 (1) (1969) 340–344.
- [12] H. C. Chandan, R. Bradt, G. E. Rindone, Dynamic fatigue of float glass, *Journal of the American Ceramic Society* 61 (5-6) (1978) 207–210.
- [13] X. Nie, W. W. Chen, A. A. Wereszczak, D. W. Templeton, Effect of loading rate and surface conditions on the flexural strength of borosilicate glass, *Journal of the American Ceramic Society* 92 (6) (2009) 1287–1295.
- [14] M. Peroni, G. Solomos, V. Pizzinato, M. Larcher, Experimental investigation of high strain-rate behaviour of glass, in: *Applied Mechanics and Materials*, Vol. 82, Trans Tech Publications, 2011, pp. 63–68.
- [15] X. Zhang, Y. Zou, H. Hao, X. Li, G. Ma, K. Liu, Laboratory test on dynamic material properties of annealed float glass, *International Journal of Protective Structures* 3 (4) (2012) 407–430.
- [16] S. S. Daryadel, P. R. Mantena, K. Kim, D. Stoddard, A. Rajendran, Dynamic response of glass under low-velocity impact and high strain-rate SHPB compression loading, *Journal of Non-Crystalline Solids* 432 (2016) 432–439.
- [17] Z. Feng, Y. Zhou, R. Tan, H. Hou, T. Sun, K. Fezzaa, J. Huang, S. Luo, Dynamic damage and fracture of a conductive glass under high-rate compression: A synchrotron based study, *Journal of Non-Crystalline Solids* 494 (2018) 40–49.
- [18] P. Forquin, Brittle materials at high-loading rates: an open area of research, *Philosophical Transactions of the Royal Society A: Mathematical, Physical and Engineering Sciences* 375 (2017) 1–12.
- [19] T. Pyttel, H. Liebertz, J. Cai, Failure criterion for laminated glass under impact loading and its application in finite element simulation, *International Journal of Impact Engineering* 38 (4) (2011) 252–263.
- [20] B. Liu, T. Xu, X. Xu, Y. Wang, Y. Sun, Y. Li, Energy absorption mechanism of polyvinyl butyral laminated windshield subjected to head impact: experiment and numerical simulations, *International Journal of Impact Engineering* 90 (2016) 26–36.
- [21] N. Yang, J. Wang, G. Zhao, Y. Zhong, D. Wang, Experimental study of headform-pvb laminated windshield impact, *International journal of crashworthiness* 21 (6) (2016) 521–531.
- [22] G. Herndon, K. Allen, A. Roberts, D. Phillips, S. A. Batzer, Automotive side glazing failure due to simulated human interaction, *Engineering Failure Analysis* 14 (8) (2007) 1701–1710.
- [23] X. Zhang, H. Hao, G. Ma, Laboratory test and numerical simulation of laminated glass window vulnerability to debris impact, *International Journal of Impact Engineering* 55 (2013) 49–62.
- [24] S. Van Dam, J. Pelfrene, W. Van Paepegem, D. Lecompte, Mechanical response of laminated glass plates subjected to impact loading, in: *Proceedings of Challenging Glass 4 & COST Action TU0905 Final Conference*, 2014, pp. 473–480.
- [25] S. Van Dam, J. Pelfrene, S. De Pauw, W. Van Paepegem, Experimental study on the dynamic behaviour of glass fitted with safety window film with a small-scale drop weight set-up, *International Journal of Impact Engineering* 73 (2014) 101–111.
- [26] F. J. Masters, K. R. Gurley, N. Shah, G. Fernandez, The vulnerability of residential window glass to lightweight windborne debris, *Engineering Structures* 32 (4) (2010) 911–921.
- [27] P. Hooper, R. Sukhran, B. Blackman, J. Dear, On the blast resistance of laminated glass, *International Journal of Solids and Structures* 49 (6) (2012) 899–918.
- [28] X. Zhang, H. Hao, Experimental and numerical study of boundary and anchorage effect on laminated glass windows under blast loading, *Engineering Structures* 90 (2015) 96–116.
- [29] P. Kumar, A. Shukla, Dynamic response of glass panels subjected to shock loading, *Journal of Non-Crystalline Solids* 357 (24) (2011) 3917–3923.
- [30] T. Bernbach, M. Teich, N. Gebbeken, Experimental investigation of energy dissipation mechanisms in laminated safety glass for combined blast-temperature loading scenarios, *Glass Structures & Engineering* 1 (1) (2016) 331–350.
- [31] K. Osnes, T. Børvik, O. S. Hopperstad, Testing and modelling of annealed float glass under quasi-static and dynamic loading, *Engineering Fracture Mechanics* 201 (2018) 107–129.
- [32] K. Osnes, J. K. Holmen, O. S. Hopperstad, T. Børvik, Fracture and fragmentation of blast-loaded laminated glass: An experimental and numerical study, *International Journal of Impact Engineering* 132 (2019) 103334.
- [33] K. Osnes, S. Dey, O. S. Hopperstad, T. Børvik, On the dynamic response of laminated glass exposed to impact before blast loading, *Experimental Mechanics*, <http://doi.acm.org/10.1145/1671970.1921702>.
- [34] D. Z. Yankelevsky, Strength prediction of annealed glass plates – A new model, *Engineering Structures* 79 (2014) 244–255.
- [35] NS-EN 572-1: Glass in building – Basic soda-lime silicate glass products – Part 1: Definitions and general physical and mechanical properties, Standard, CEN (2012).
- [36] S. M. Wiederhorn, Fracture surface energy of glass, *Journal of the American Ceramic Society* 52 (2) (1969) 99–105.
- [37] P. Hooper, B. Blackman, J. Dear, The mechanical behaviour of poly (vinyl butyral) at different strain magnitudes and strain rates, *Journal of Materials Science* 47 (8) (2012) 3564–3576.
- [38] X. Zhang, H. Hao, Y. Shi, J. Cui, The mechanical properties of polyvinyl butyral (PVB) at high strain rates, *Construction and building materials* 93 (2015) 404–415.
- [39] P. Del Linz, Y. Wang, P. Hooper, H. Arora, D. Smith, L. Pascoe, D. Cormie, B. Blackman, J. Dear, Determining material response for Polyvinyl Butyral (PVB) in blast loading situations, *Experimental Mechanics* 56 (9) (2016) 1501–1517.
- [40] J. Franz, J. Schneider, Through-cracked-tensile tests with polyvinylbutyral (PVB) and different adhesion grades, in: *Engineered Transparency, International Conference at Glasstec, Düsseldorf, Germany, 2014*, pp. 135–142.
- [41] P. Del Linz, P. A. Hooper, H. Arora, Y. Wang, D. Smith, B. R. Blackman, J. P. Dear, Delamination properties of laminated glass windows subject to blast loading, *International Journal of Impact Engineering* 105 (2017) 39–53.
- [42] M. A. Samieian, D. Cormie, D. Smith, W. Wholey, B. R. Blackman, J. P. Dear, P. A. Hooper, Temperature effects on laminated glass at high rate, *International Journal of Impact Engineering* 111 (2018) 177–186.
- [43] A. Reyes, T. Børvik, Low velocity impact on crash components with steel skins and polymer foam cores, *International Journal of Impact Engineering*.
- [44] eCorr User Manual, <https://www.ntnu.edu/kt/ecorr>, accessed: 2019-06-13.
- [45] Instron, CEAST 9350 Series, Droptower Impact Systems, <http://www.instron.se/sv-se/products> (2011).
- [46] J. K. Holmen, L. Olovsson, T. Børvik, Discrete modeling of low-velocity penetration in sand, *Computers and Geotechnics* 86 (2017) 21–32.
- [47] J. K. Holmen, O. S. Hopperstad, T. Børvik, Low-velocity impact on multi-layered dual-phase steel plates, *International Journal of Impact Engineering* 78 (2015) 161–177.
- [48] C. Lopes, O. Seresta, Y. Coquet, Z. Gürdal, P. Camanho, B. Thuis, Low-velocity impact damage on dispersed stacking sequence laminates. Part I: Experiments, *Composites Science and Technology* 69 (7-8) (2009) 926–936.
- [49] J. Newman Jr, I. Raju, An empirical stress-intensity factor equation for the surface crack, *Engineering fracture mechanics* 15 (1-2) (1981) 185–192.
- [50] NS-EN 572-2: Glass in building – Basic soda-lime silicate glass products – Part 2: Float glass, Standard, CEN (2012).
- [51] D. Cormie, G. Mays, P. Smith, Blast effects on buildings, 2nd Edition, Thomas Telford Publishing, 2009.

- [52] J. Bergström, M. Boyce, Constitutive modeling of the time-dependent and cyclic loading of elastomers and application to soft biological tissues, *Mechanics of Materials* 33 (9) (2001) 523–530.
- [53] Abaqus 2017, Abaqus Analysis User's Guide 22.5.1, Dassault Systèmes, Providence, RI, USA (2017).
- [54] Abaqus 2017, Abaqus Analysis User's Guide 22.8.2, Dassault Systèmes, Providence, RI, USA (2017).
- [55] A. A. Wereszczak, M. K. Ferber, W. Musselwhite, Method for identifying and mapping flaw size distributions on glass surfaces for predicting mechanical response, *International Journal of Applied Glass Science* 5 (1) (2014) 16–21.
- [56] M. A. Meyers, *Dynamic behavior of materials*, John Wiley & Sons, 1994, Ch. 12, pp. 298–299.

**DEPARTMENT OF STRUCTURAL ENGINEERING
NORWEGIAN UNIVERSITY OF SCIENCE AND TECHNOLOGY**

N-7491 TRONDHEIM, NORWAY
Telephone: +47 73 59 47 00

"Reliability Analysis of Structural Systems using Nonlinear Finite Element Methods",
C. A. Holm, 1990:23, ISBN 82-7119-178-0.

"Uniform Stratified Flow Interaction with a Submerged Horizontal Cylinder",
Ø. Arntsen, 1990:32, ISBN 82-7119-188-8.

"Large Displacement Analysis of Flexible and Rigid Systems Considering
Displacement-Dependent Loads and Nonlinear Constraints",
K. M. Mathisen, 1990:33, ISBN 82-7119-189-6.

"Solid Mechanics and Material Models including Large Deformations",
E. Levold, 1990:56, ISBN 82-7119-214-0, ISSN 0802-3271.

"Inelastic Deformation Capacity of Flexurally-Loaded Aluminium Alloy Structures",
T. Welo, 1990:62, ISBN 82-7119-220-5, ISSN 0802-3271.

"Visualization of Results from Mechanical Engineering Analysis",
K. Aamnes, 1990:63, ISBN 82-7119-221-3, ISSN 0802-3271.

"Object-Oriented Product Modeling for Structural Design",
S. I. Dale, 1991:6, ISBN 82-7119-258-2, ISSN 0802-3271.

"Parallel Techniques for Solving Finite Element Problems on Transputer Networks",
T. H. Hansen, 1991:19, ISBN 82-7119-273-6, ISSN 0802-3271.

"Statistical Description and Estimation of Ocean Drift Ice Environments",
R. Korsnes, 1991:24, ISBN 82-7119-278-7, ISSN 0802-3271.

"Properties of concrete related to fatigue damage: with emphasis on high strength
concrete",
G. Petkovic, 1991:35, ISBN 82-7119-290-6, ISSN 0802-3271.

"Turbidity Current Modelling",
B. Brørs, 1991:38, ISBN 82-7119-293-0, ISSN 0802-3271.

"Zero-Slump Concrete: Rheology, Degree of Compaction and Strength. Effects of
Fillers as Part Cement-Replacement",
C. Sørensen, 1992:8, ISBN 82-7119-357-0, ISSN 0802-3271.

"Nonlinear Analysis of Reinforced Concrete Structures Exposed to Transient Loading",
K. V. Høiseith, 1992:15, ISBN 82-7119-364-3, ISSN 0802-3271.

"Finite Element Formulations and Solution Algorithms for Buckling and Collapse
Analysis of Thin Shells",
R. O. Bjærum, 1992:30, ISBN 82-7119-380-5, ISSN 0802-3271.

"Response Statistics of Nonlinear Dynamic Systems",
J. M. Johnsen, 1992:42, ISBN 82-7119-393-7, ISSN 0802-3271.

"Digital Models in Engineering. A Study on why and how engineers build and operate
digital models for decision support",
J. Høyte, 1992:75, ISBN 82-7119-429-1, ISSN 0802-3271.

"Sparse Solution of Finite Element Equations",
A. C. Damhaug, 1992:76, ISBN 82-7119-430-5, ISSN 0802-3271.

"Some Aspects of Floating Ice Related to Sea Surface Operations in the Barents Sea",
S. Løset, 1992:95, ISBN 82-7119-452-6, ISSN 0802-3271.

"Modelling of Cyclic Plasticity with Application to Steel and Aluminium Structures",
O. S. Hopperstad, 1993:7, ISBN 82-7119-461-5, ISSN 0802-3271.

"The Free Formulation: Linear Theory and Extensions with Applications to Tetrahedral
Elements
with Rotational Freedoms",
G. Skeie, 1993:17, ISBN 82-7119-472-0, ISSN 0802-3271.

"Høyfast betongs motstand mot piggdekkslitasje. Analyse av resultater fra prøving i
Veisliter'n",
T. Tveter, 1993:62, ISBN 82-7119-522-0, ISSN 0802-3271.

"A Nonlinear Finite Element Based on Free Formulation Theory for Analysis of
Sandwich Structures",
O. Aamlid, 1993:72, ISBN 82-7119-534-4, ISSN 0802-3271.

"The Effect of Curing Temperature and Silica Fume on Chloride Migration and Pore
Structure of High Strength Concrete",
C. J. Hauck, 1993:90, ISBN 82-7119-553-0, ISSN 0802-3271.

"Failure of Concrete under Compressive Strain Gradients",
G. Markeset, 1993:110, ISBN 82-7119-575-1, ISSN 0802-3271.

"An experimental study of internal tidal amphidromes in Vestfjorden",
J. H. Nilsen, 1994:39, ISBN 82-7119-640-5, ISSN 0802-3271.

"Structural analysis of oil wells with emphasis on conductor design",
H. Larsen, 1994:46, ISBN 82-7119-648-0, ISSN 0802-3271.

"Adaptive methods for non-linear finite element analysis of shell structures",
K. M. Okstad, 1994:66, ISBN 82-7119-670-7, ISSN 0802-3271.

"On constitutive modelling in nonlinear analysis of concrete structures",
O. Fyrileiv, 1994:115, ISBN 82-7119-725-8, ISSN 0802-3271.

"Fluctuating wind load and response of a line-like engineering structure with emphasis
on motion-induced wind forces",
J. Bogunovic Jakobsen, 1995:62, ISBN 82-7119-809-2, ISSN 0802-3271.

"An experimental study of beam-columns subjected to combined torsion, bending and
axial actions",
A. Aalberg, 1995:66, ISBN 82-7119-813-0, ISSN 0802-3271.

"Scaling and cracking in unsealed freeze/thaw testing of Portland cement and silica
fume concretes",
S. Jacobsen, 1995:101, ISBN 82-7119-851-3, ISSN 0802-3271.

"Damping of water waves by submerged vegetation. A case study of laminaria
hyperborea",
A. M. Dubi, 1995:108, ISBN 82-7119-859-9, ISSN 0802-3271.

"The dynamics of a slope current in the Barents Sea",
Sheng Li, 1995:109, ISBN 82-7119-860-2, ISSN 0802-3271.

"Modellering av delmaterialenes betydning for betongens konsistens",
Ernst Mørtzell, 1996:12, ISBN 82-7119-894-7, ISSN 0802-3271.

"Bending of thin-walled aluminium extrusions",
Birgit Søvik Opheim, 1996:60, ISBN 82-7119-947-1, ISSN 0802-3271.

"Material modelling of aluminium for crashworthiness analysis",
Torodd Berstad, 1996:89, ISBN 82-7119-980-3, ISSN 0802-3271.

"Estimation of structural parameters from response measurements on submerged
floating tunnels",
Rolf Magne Larssen, 1996:119, ISBN 82-471-0014-2, ISSN 0802-3271.

"Numerical modelling of plain and reinforced concrete by damage mechanics",
Mario A. Polanco-Loria, 1997:20, ISBN 82-471-0049-5, ISSN 0802-3271.

"Nonlinear random vibrations - numerical analysis by path integration methods",
Vibeke Moe, 1997:26, ISBN 82-471-0056-8, ISSN 0802-3271.

“Numerical prediction of vortex-induced vibration by the finite element method”,
Joar Martin Dalheim, 1997:63, ISBN 82-471-0096-7, ISSN 0802-3271.

“Time domain calculations of buffeting response for wind sensitive structures”,
Ketil Aas-Jakobsen, 1997:148, ISBN 82-471-0189-0, ISSN 0802-3271.

"A numerical study of flow about fixed and flexibly mounted circular cylinders",
Trond Stokka Meling, 1998:48, ISBN 82-471-0244-7, ISSN 0802-3271.

“Estimation of chloride penetration into concrete bridges in coastal areas”,
Per Egil Steen, 1998:89, ISBN 82-471-0290-0, ISSN 0802-3271.

“Stress-resultant material models for reinforced concrete plates and shells”,
Jan Arve Øverli, 1998:95, ISBN 82-471-0297-8, ISSN 0802-3271.

“Chloride binding in concrete. Effect of surrounding environment and concrete composition”,
Claus Kenneth Larsen, 1998:101, ISBN 82-471-0337-0, ISSN 0802-3271.

“Rotational capacity of aluminium alloy beams”,
Lars A. Moen, 1999:1, ISBN 82-471-0365-6, ISSN 0802-3271.

“Stretch Bending of Aluminium Extrusions”,
Arild H. Clausen, 1999:29, ISBN 82-471-0396-6, ISSN 0802-3271.

“Aluminium and Steel Beams under Concentrated Loading”,
Tore Tryland, 1999:30, ISBN 82-471-0397-4, ISSN 0802-3271.

"Engineering Models of Elastoplasticity and Fracture for Aluminium Alloys",
Odd-Geir Lademo, 1999:39, ISBN 82-471-0406-7, ISSN 0802-3271.

"Kapasitet og duktilitet av dybelforbindelser i trekonstruksjoner",
Jan Siem, 1999:46, ISBN 82-471-0414-8, ISSN 0802-3271.

“Etablering av distribuert ingeniørarbeid; Teknologiske og organisatoriske erfaringer fra en norsk ingeniørbedrift”,
Lars Line, 1999:52, ISBN 82-471-0420-2, ISSN 0802-3271.

“Estimation of Earthquake-Induced Response”,
Símón Ólafsson, 1999:73, ISBN 82-471-0443-1, ISSN 0802-3271.

“Coastal Concrete Bridges: Moisture State, Chloride Permeability and Aging Effects”
Ragnhild Holen Relling, 1999:74, ISBN 82-471-0445-8, ISSN 0802-3271.

”Capacity Assessment of Titanium Pipes Subjected to Bending and External Pressure”,
Arve Bjørset, 1999:100, ISBN 82-471-0473-3, ISSN 0802-3271.

“Validation of Numerical Collapse Behaviour of Thin-Walled Corrugated Panels”,
Håvar Ilstad, 1999:101, ISBN 82-471-0474-1, ISSN 0802-3271.

“Strength and Ductility of Welded Structures in Aluminium Alloys”,
Miroslaw Matusiak, 1999:113, ISBN 82-471-0487-3, ISSN 0802-3271.

“Thermal Dilation and Autogenous Deformation as Driving Forces to Self-Induced
Stresses in High Performance Concrete”,
Øyvind Bjøntegaard, 1999:121, ISBN 82-7984-002-8, ISSN 0802-3271.

“Some Aspects of Ski Base Sliding Friction and Ski Base Structure”,
Dag Anders Moldestad, 1999:137, ISBN 82-7984-019-2, ISSN 0802-3271.

"Electrode reactions and corrosion resistance for steel in mortar and concrete",
Roy Antonsen, 2000:10, ISBN 82-7984-030-3, ISSN 0802-3271.

"Hydro-Physical Conditions in Kelp Forests and the Effect on Wave Damping and
Dune Erosion. A case study on Laminaria Hyperborea",
Stig Magnar Løvås, 2000:28, ISBN 82-7984-050-8, ISSN 0802-3271.

"Random Vibration and the Path Integral Method",
Christian Skaug, 2000:39, ISBN 82-7984-061-3, ISSN 0802-3271.

"Buckling and geometrical nonlinear beam-type analyses of timber structures",
Trond Even Eggen, 2000:56, ISBN 82-7984-081-8, ISSN 0802-3271.

”Structural Crashworthiness of Aluminium Foam-Based Components”,
Arve Grønsund Hanssen, 2000:76, ISBN 82-7984-102-4, ISSN 0809-103X.

“Measurements and simulations of the consolidation in first-year sea ice ridges, and
some aspects of mechanical behaviour”,
Knut V. Høyland, 2000:94, ISBN 82-7984-121-0, ISSN 0809-103X.

”Kinematics in Regular and Irregular Waves based on a Lagrangian Formulation”,
Svein Helge Gjosund, 2000-86, ISBN 82-7984-112-1, ISSN 0809-103X.

”Self-Induced Cracking Problems in Hardening Concrete Structures”,
Daniela Bosnjak, 2000-121, ISBN 82-7984-151-2, ISSN 0809-103X.

"Ballistic Penetration and Perforation of Steel Plates",
Tore Børvik, 2000:124, ISBN 82-7984-154-7, ISSN 0809-103X.

"Freeze-Thaw resistance of Concrete. Effect of: Curing Conditions, Moisture Exchange
and Materials",
Terje Finnerup Rønning, 2001:14, ISBN 82-7984-165-2, ISSN 0809-103X

"Structural behaviour of post tensioned concrete structures. Flat slab. Slabs on ground",
Steinar Trygstad, 2001:52, ISBN 82-471-5314-9, ISSN 0809-103X.

"Slipforming of Vertical Concrete Structures. Friction between concrete and slipform panel",
Kjell Tore Fosså, 2001:61, ISBN 82-471-5325-4, ISSN 0809-103X.

"Some numerical methods for the simulation of laminar and turbulent incompressible flows",
Jens Holmen, 2002:6, ISBN 82-471-5396-3, ISSN 0809-103X.

"Improved Fatigue Performance of Threaded Drillstring Connections by Cold Rolling",
Steinar Kristoffersen, 2002:11, ISBN: 82-421-5402-1, ISSN 0809-103X.

"Deformations in Concrete Cantilever Bridges: Observations and Theoretical Modelling",
Peter F. Takács, 2002:23, ISBN 82-471-5415-3, ISSN 0809-103X.

"Stiffened aluminium plates subjected to impact loading",
Hilde Giæver Hildrum, 2002:69, ISBN 82-471-5467-6, ISSN 0809-103X.

"Full- and model scale study of wind effects on a medium-rise building in a built up area",
Jónas Thór Snæbjörnsson, 2002:95, ISBN82-471-5495-1, ISSN 0809-103X.

"Evaluation of Concepts for Loading of Hydrocarbons in Ice-infested water",
Arnor Jensen, 2002:114, ISBN 82-417-5506-0, ISSN 0809-103X.

"Numerical and Physical Modelling of Oil Spreading in Broken Ice",
Janne K. Økland Gjosteen, 2002:130, ISBN 82-471-5523-0, ISSN 0809-103X.

"Diagnosis and protection of corroding steel in concrete",
Franz Pruckner, 20002:140, ISBN 82-471-5555-4, ISSN 0809-103X.

"Tensile and Compressive Creep of Young Concrete: Testing and Modelling",
Dawood Atrushi, 2003:17, ISBN 82-471-5565-6, ISSN 0809-103X.

"Rheology of Particle Suspensions. Fresh Concrete, Mortar and Cement Paste with Various Types of Lignosulfonates",
Jon Elvar Wallevik, 2003:18, ISBN 82-471-5566-4, ISSN 0809-103X.

"Oblique Loading of Aluminium Crash Components",
Aase Reyes, 2003:15, ISBN 82-471-5562-1, ISSN 0809-103X.

"Utilization of Ethiopian Natural Pozzolans",
Surafel Ketema Desta, 2003:26, ISSN 82-471-5574-5, ISSN:0809-103X.

“Behaviour and strength prediction of reinforced concrete structures with discontinuity regions”, Helge Brå, 2004:11, ISBN 82-471-6222-9, ISSN 1503-8181.

“High-strength steel plates subjected to projectile impact. An experimental and numerical study”, Sumita Dey, 2004:38, ISBN 82-471-6282-2 (printed version), ISBN 82-471-6281-4 (electronic version), ISSN 1503-8181.

“Alkali-reactive and inert fillers in concrete. Rheology of fresh mixtures and expansive reactions.”

Bård M. Pedersen, 2004:92, ISBN 82-471-6401-9 (printed version), ISBN 82-471-6400-0 (electronic version), ISSN 1503-8181.

“On the Shear Capacity of Steel Girders with Large Web Openings”.

Nils Christian Hagen, 2005:9 ISBN 82-471-6878-2 (printed version), ISBN 82-471-6877-4 (electronic version), ISSN 1503-8181.

”Behaviour of aluminium extrusions subjected to axial loading”.

Østen Jensen, 2005:7, ISBN 82-471-6873-1 (printed version), ISBN 82-471-6872-3 (electronic version), ISSN 1503-8181.

”Thermal Aspects of corrosion of Steel in Concrete”.

Jan-Magnus Østvik, 2005:5, ISBN 82-471-6869-3 (printed version), ISBN 82-471-6868 (electronic version), ISSN 1503-8181.

”Mechanical and adaptive behaviour of bone in relation to hip replacement.” A study of bone remodelling and bone grafting.

Sébastien Muller, 2005:34, ISBN 82-471-6933-9 (printed version), ISBN 82-471-6932-0 (electronic version), ISSN 1503-8181.

“Analysis of geometrical nonlinearities with applications to timber structures”.

Lars Wollebæk, 2005:74, ISBN 82-471-7050-5 (printed version), ISBN 82-471-7019-1 (electronic version), ISSN 1503-8181.

“Pedestrian induced lateral vibrations of slender footbridges”.

Anders Rönquist, 2005:102, ISBN 82-471-7082-5 (printed version), ISBN 82-471-7081-7 (electronic version), ISSN 1503-8181.

“Initial Strength Development of Fly Ash and Limestone Blended Cements at Various Temperatures Predicted by Ultrasonic Pulse Velocity”.

Tom Ivar Fredvik, 2005:112, ISBN 82-471-7105-8 (printed version), ISBN 82-471-7103-1 (electronic version), ISSN 1503-8181.

“Behaviour and modelling of thin-walled cast components”.

Cato Dørum, 2005:128, ISBN 82-471-7140-6 (printed version), ISBN 82-471-7139-2 (electronic version), ISSN 1503-8181.

- “Behaviour and modelling of selfpiercing riveted connections”,
Raffaele Porcaro, 2005:165, ISBN 82-471-7219-4 (printed version), ISBN 82-471-7218-6 (electronic version), ISSN 1503-8181.
- ”Behaviour and Modelling of Aluminium Plates subjected to Compressive Load”,
Lars Rønning, 2005:154, ISBN 82-471-7169-1 (printed version), ISBN 82-471-7195-3 (electronic version), ISSN 1503-8181.
- ”Bumper beam-longitudinal system subjected to offset impact loading”,
Satyanarayana Kokkula, 2005:193, ISBN 82-471-7280-1 (printed version), ISBN 82-471-7279-8 (electronic version), ISSN 1503-8181.
- “Control of Chloride Penetration into Concrete Structures at Early Age”,
Guofei Liu, 2006:46, ISBN 82-471-7838-9 (printed version), ISBN 82-471-7837-0 (electronic version), ISSN 1503-8181.
- “Modelling of Welded Thin-Walled Aluminium Structures”,
Ting Wang, 2006:78, ISBN 82-471-7907-5 (printed version), ISBN 82-471-7906-7 (electronic version), ISSN 1503-8181.
- ”Time-variant reliability of dynamic systems by importance sampling and probabilistic analysis of ice loads”,
Anna Ivanova Olsen, 2006:139, ISBN 82-471-8041-3 (printed version), ISBN 82-471-8040-5 (electronic version), ISSN 1503-8181.
- “Fatigue life prediction of an aluminium alloy automotive component using finite element analysis of surface topography”,
Sigmund Kyrre Ås, 2006:25, ISBN 82-471-7791-9 (printed version), ISBN 82-471-7791-9 (electronic version), ISSN 1503-8181.
- ”Constitutive models of elastoplasticity and fracture for aluminium alloys under strain path change”,
Dasharatha Achani, 2006:76, ISBN 82-471-7903-2 (printed version), ISBN 82-471-7902-4 (electronic version), ISSN 1503-8181.
- “Simulations of 2D dynamic brittle fracture by the Element-free Galerkin method and linear fracture mechanics”,
Tommy Karlsson, 2006:125, ISBN 82-471-8011-1 (printed version), ISBN 82-471-8010-3 (electronic version), ISSN 1503-8181.
- “Penetration and Perforation of Granite Targets by Hard Projectiles”,
Chong Chiang Seah, 2006:188, ISBN 82-471-8150-9 (printed version), ISBN 82-471-8149-5 (electronic version), ISSN 1503-8181.

“Deformations, strain capacity and cracking of concrete in plastic and early hardening phases”,

Tor Arne Hammer, 2007:234, ISBN 978-82-471-5191-4 (printed version), ISBN 978-82-471-5207-2 (electronic version), ISSN 1503-8181.

“Crashworthiness of dual-phase high-strength steel: Material and Component behaviour”, Venkatapathi Tarigopula, 2007:230, ISBN 82-471-5076-4 (printed version), ISBN 82-471-5093-1 (electronic version), ISSN 1503-8181.

“Fibre reinforcement in load carrying concrete structures”,

Åse Lyslo Døssland, 2008:50, ISBN 978-82-471-6910-0 (printed version), ISBN 978-82-471-6924-7 (electronic version), ISSN 1503-8181.

“Low-velocity penetration of aluminium plates”,

Frode Grytten, 2008:46, ISBN 978-82-471-6826-4 (printed version), ISBN 978-82-471-6843-1 (electronic version), ISSN 1503-8181.

“Robustness studies of structures subjected to large deformations”,

Ørjan Fyllingen, 2008:24, ISBN 978-82-471-6339-9 (printed version), ISBN 978-82-471-6342-9 (electronic version), ISSN 1503-8181.

“Constitutive modelling of morsellised bone”,

Knut Birger Lunde, 2008:92, ISBN 978-82-471-7829-4 (printed version), ISBN 978-82-471-7832-4 (electronic version), ISSN 1503-8181.

“Experimental Investigations of Wind Loading on a Suspension Bridge Girder”,

Bjørn Isaksen, 2008:131, ISBN 978-82-471-8656-5 (printed version), ISBN 978-82-471-8673-2 (electronic version), ISSN 1503-8181.

“Cracking Risk of Concrete Structures in The Hardening Phase”,

Guomin Ji, 2008:198, ISBN 978-82-471-1079-9 (printed version), ISBN 978-82-471-1080-5 (electronic version), ISSN 1503-8181.

“Modelling and numerical analysis of the porcine and human mitral apparatus”,

Victorien Emile Prot, 2008:249, ISBN 978-82-471-1192-5 (printed version), ISBN 978-82-471-1193-2 (electronic version), ISSN 1503-8181.

“Strength analysis of net structures”,

Heidi Moe, 2009:48, ISBN 978-82-471-1468-1 (printed version), ISBN 978-82-471-1469-8 (electronic version), ISSN 1503-8181.

“Numerical analysis of ductile fracture in surface cracked shells”,

Espen Berg, 2009:80, ISBN 978-82-471-1537-4 (printed version), ISBN 978-82-471-1538-1 (electronic version), ISSN 1503-8181.

“Subject specific finite element analysis of bone – for evaluation of the healing of a leg lengthening and evaluation of femoral stem design”,
Sune Hansborg Pettersen, 2009:99, ISBN 978-82-471-1579-4 (printed version), ISBN 978-82-471-1580-0 (electronic version), ISSN 1503-8181.

“Evaluation of fracture parameters for notched multi-layered structures”,
Lingyun Shang, 2009:137, ISBN 978-82-471-1662-3 (printed version), ISBN 978-82-471-1663-0 (electronic version), ISSN 1503-8181.

“Modelling of Dynamic Material Behaviour and Fracture of Aluminium Alloys for Structural Applications”
Yan Chen, 2009:69, ISBN 978-82-471-1515-2 (printed version), ISBN 978-82-471-1516-9 (electronic version), ISSN 1503-8181.

“Nanomechanics of polymer and composite particles”
Jianying He 2009:213, ISBN 978-82-471-1828-3 (printed version), ISBN 978-82-471-1829-0 (electronic version), ISSN 1503-8181.

“Mechanical properties of clear wood from Norway spruce”
Kristian Berbom Dahl 2009:250, ISBN 978-82-471-1911-2 (printed version) ISBN 978-82-471-1912-9 (electronic version), ISSN 1503-8181.

“Modeling of the degradation of TiB₂ mechanical properties by residual stresses and liquid Al penetration along grain boundaries”
Micol Pezzotta 2009:254, ISBN 978-82-471-1923-5 (printed version) ISBN 978-82-471-1924-2 (electronic version) ISSN 1503-8181.

“Effect of welding residual stress on fracture”
Xiabo Ren 2010:77, ISBN 978-82-471-2115-3 (printed version) ISBN 978-82-471-2116-0 (electronic version), ISSN 1503-8181.

“Pan-based carbon fiber as anode material in cathodic protection system for concrete structures”
Mahdi Chini 2010:122, ISBN 978-82-471-2210-5 (printed version) ISBN 978-82-471-2213-6 (electronic version), ISSN 1503-8181.

“Structural Behaviour of deteriorated and retrofitted concrete structures”
Irina Vasililjeva Sæther 2010:171, ISBN 978-82-471-2315-7 (printed version) ISBN 978-82-471-2316-4 (electronic version) ISSN 1503-8181.

“Prediction of local snow loads on roofs”
Vivian Meløysund 2010:247, ISBN 978-82-471-2490-1 (printed version) ISBN 978-82-471-2491-8 (electronic version) ISSN 1503-8181.

“Behaviour and modelling of polymers for crash applications”
Virgile Delhaye 2010:251, ISBN 978-82-471-2501-4 (printed version) ISBN 978-82-471-2502-1 (electronic version) ISSN 1503-8181.

“Blended cement with reduced CO₂ emission – Utilizing the Fly Ash-Limestone Synergy”,
Klaartje De Weerd 2011:32, ISBN 978-82-471-2584-7 (printed version) ISBN 978-82-471-2584-4 (electronic version) ISSN 1503-8181.

“Chloride induced reinforcement corrosion in concrete” Concept of critical chloride content – methods and mechanisms.
Ueli Angst 2011:113, ISBN 978-82-471-2769-9 (printed version) ISBN 978-82-471-2763-6 (electronic version) ISSN 1503-8181.

“A thermo-electric-Mechanical study of the carbon anode and contact interface for Energy savings in the production of aluminium”.
Dag Herman Andersen 2011:157, ISBN 978-82-471-2859-6 (printed version) ISBN 978-82-471-2860-2 (electronic version) ISSN 1503-8181.

“Structural Capacity of Anchorage Ties in Masonry Veneer Walls Subjected to Earthquake”. The implications of Eurocode 8 and Eurocode 6 on a typical Norwegian veneer wall.
Ahmed Mohamed Yousry Hamed 2011:181, ISBN 978-82-471-2911-1 (printed version) ISBN 978-82-471-2912-8 (electronic ver.) ISSN 1503-8181.

“Work-hardening behaviour in age-hardenable Al-Zn-Mg(-Cu) alloys”.
Ida Westermann , 2011:247, ISBN 978-82-471-3056-8 (printed ver.) ISBN 978-82-471-3057-5 (electronic ver.) ISSN 1503-8181.

“Behaviour and modelling of selfpiercing riveted connections using aluminium rivets”.
Nguyen-Hieu Hoang, 2011:266, ISBN 978-82-471-3097-1 (printed ver.) ISBN 978-82-471-3099-5 (electronic ver.) ISSN 1503-8181.

“Fibre reinforced concrete”.
Sindre Sandbakk, 2011:297, ISBN 978-82-471-3167-1 (printed ver.) ISBN 978-82-471-3168-8 (electronic ver) ISSN 1503:8181.

“Dynamic behaviour of cablesupported bridges subjected to strong natural wind”.
Ole Andre Øiseth, 2011:315, ISBN 978-82-471-3209-8 (printed ver.) ISBN 978-82-471-3210-4 (electronic ver.) ISSN 1503-8181.

“Constitutive modeling of solargrade silicon materials”
Julien Cochard, 2011:307, ISBN 978-82-471-3189-3 (printed ver). ISBN 978-82-471-3190-9 (electronic ver.) ISSN 1503-8181.

“Constitutive behavior and fracture of shape memory alloys”
Jim Stian Olsen, 2012:57, ISBN 978-82-471-3382-8 (printed ver.) ISBN 978-82-471-3383-5 (electronic ver.) ISSN 1503-8181.

“Field measurements in mechanical testing using close-range photogrammetry and digital image analysis”

Egil Fagerholt, 2012:95, ISBN 978-82-471-3466-5 (printed ver.) ISBN 978-82-471-3467-2 (electronic ver.) ISSN 1503-8181.

“Towards a better understanding of the ultimate behaviour of lightweight aggregate concrete in compression and bending”

Håvard Nedrelid, 2012:123, ISBN 978-82-471-3527-3 (printed ver.) ISBN 978-82-471-3528-0 (electronic ver.) ISSN 1503-8181.

“Numerical simulations of blood flow in the left side of the heart”

Sigrid Kaarstad Dahl, 2012:135, ISBN 978-82-471-3553-2 (printed ver.) ISBN 978-82-471-3555-6 (electronic ver.) ISSN 1503-8181.

“Moisture induced stresses in glulam”

Vanessa Angst-Nicollier, 2012:139, ISBN 978-82-471-3562-4 (printed ver.) ISBN 978-82-471-3563-1 (electronic ver.) ISSN 1503-8181.

“Biomechanical aspects of distraction osteogenesis”

Valentina La Russa, 2012:250, ISBN 978-82-471-3807-6 (printed ver.) ISBN 978-82-471-3808-3 (electronic ver.) ISSN 1503-8181.

“Ductile fracture in dual-phase steel. Theoretical, experimental and numerical study”

Gaute Gruben, 2012:257, ISBN 978-82-471-3822-9 (printed ver.) ISBN 978-82-471-3823-6 (electronic ver.) ISSN 1503-8181.

“Damping in Timber Structures”

Nathalie Labonnote, 2012:263, ISBN 978-82-471-3836-6 (printed ver.) ISBN 978-82-471-3837-3 (electronic ver.) ISSN 1503-8181.

“Biomechanical modeling of fetal veins: The umbilical vein and ductus venosus bifurcation”

Paul Roger Leinan, 2012:299, ISBN 978-82-471-3915-8 (printed ver.) ISBN 978-82-471-3916-5 (electronic ver.) ISSN 1503-8181.

“Large-Deformation behaviour of thermoplastics at various stress states”

Anne Serine Ognedal, 2012:298, ISBN 978-82-471-3913-4 (printed ver.) ISBN 978-82-471-3914-1 (electronic ver.) ISSN 1503-8181.

“Hardening accelerator for fly ash blended cement”

Kien Dinh Hoang, 2012:366, ISBN 978-82-471-4063-5 (printed ver.) ISBN 978-82-471-4064-2 (electronic ver.) ISSN 1503-8181.

“From molecular structure to mechanical properties”

Jianyang Wu, 2013:186, ISBN 978-82-471-4485-5 (printed ver.) ISBN 978-82-471-4486-2 (electronic ver.) ISSN 1503-8181.

“Experimental and numerical study of hybrid concrete structures”

Linn Grepstad Nes, 2013:259, ISBN 978-82-471-4644-6 (printed ver.) ISBN 978-82-471-4645-3 (electronic ver.) ISSN 1503-8181.

“Mechanics of ultra-thin multi crystalline silicon wafers”

Saber Saffar, 2013:199, ISBN 978-82-471-4511-1 (printed ver.) ISBN 978-82-471-4513-5 (electronic ver.) ISSN 1503-8181.

“Through process modelling of welded aluminium structures”

Anizahyati Alisibramulisi, 2013:325, ISBN 978-82-471-4788-7 (printed ver.) ISBN 978-82-471-4789-4 (electronic ver.) ISSN 1503-8181.

“Combined blast and fragment loading on steel plates”

Knut Gaarder Rakvåg, 2013:361, ISBN 978-82-471-4872-3 (printed ver.) ISBN 978-82-4873-0 (electronic ver.) ISSN 1503-8181.

“Characterization and modelling of the anisotropic behaviour of high-strength aluminium alloy”

Marion Fourmeau, 2014:37, ISBN 978-82-326-0008-3 (printed ver.) ISBN 978-82-326-0009-0 (electronic ver.) ISSN 1503-8181.

“Behaviour of threaded steel fasteners at elevated deformation rates”

Henning Fransplass, 2014:65, ISBN 978-82-326-0054-0 (printed ver.) ISBN 978-82-326-0055-7 (electronic ver.) ISSN 1503-8181.

“Sedimentation and Bleeding”

Ya Peng, 2014:89, ISBN 978-82-326-0102-8 (printed ver.) ISBN 978-82-326-0103-5 (electronic ver.) ISSN 1503-8181.

“Impact against X65 offshore pipelines”

Martin Kristoffersen, 2014:362, ISBN 978-82-326-0636-8 (printed ver.) ISBN 978-82-326-0637-5 (electronic ver.) ISSN 1503-8181.

“Formability of aluminium alloy subjected to prestrain by rolling”

Dmitry Vysochinskiy, 2014:363, ISBN 978-82-326-0638-2 (printed ver.) ISBN 978-82-326-0639-9 (electronic ver.) ISSN 1503-8181.

“Experimental and numerical study of Yielding, Work-Hardening and anisotropy in textured AA6xxx alloys using crystal plasticity models”

Mikhail Khadyko, 2015:28, ISBN 978-82-326-0724-2 (printed ver.) ISBN 978-82-326-0725-9 (electronic ver.) ISSN 1503-8181.

“Behaviour and Modelling of AA6xxx Aluminium Alloys Under a Wide Range of Temperatures and Strain Rates”

Vincent Vilamosa, 2015:63, ISBN 978-82-326-0786-0 (printed ver.) ISBN 978-82-326-0787-7 (electronic ver.) ISSN 1503-8181.

“A Probabilistic Approach in Failure Modelling of Aluminium High Pressure Die-Castings”

Octavian Knoll, 2015:137, ISBN 978-82-326-0930-7 (printed ver.) ISBN 978-82-326-0931-4 (electronic ver.) ISSN 1503-8181.

“Ice Abrasion on Marine Concrete Structures”

Egil Møen, 2015:189, ISBN 978-82-326-1034-1 (printed ver.) ISBN 978-82-326-1035-8 (electronic ver.) ISSN 1503-8181.

“Fibre Orientation in Steel-Fibre-Reinforced Concrete”

Giedrius Zirgulis, 2015:229, ISBN 978-82-326-1114-0 (printed ver.) ISBN 978-82-326-1115-7 (electronic ver.) ISSN 1503-8181.

“Effect of spatial variation and possible interference of localised corrosion on the residual capacity of a reinforced concrete beam”

Mohammad Mahdi Kioumarsi, 2015:282, ISBN 978-82-326-1220-8 (printed ver.) ISBN 978-82-1221-5 (electronic ver.) ISSN 1503-8181.

“The role of concrete resistivity in chloride-induced macro-cell corrosion”

Karla Horbostel, 2015:324, ISBN 978-82-326-1304-5 (printed ver.) ISBN 978-82-326-1305-2 (electronic ver.) ISSN 1503-8181.

“Flowable fibre-reinforced concrete for structural applications”

Elena Vidal Sarmiento, 2015:335, ISBN 978-82-326-1324-3 (printed ver.) ISBN 978-82-326-1325-0 (electronic ver.) ISSN 1503-8181.

“Development of chushed sand for concrete production with microproportioning”

Rolands Cepuritis, 2016:19, ISBN 978-82-326-1382-3 (printed ver.) ISBN 978-82-326-1383-0 (electronic ver.) ISSN 1503-8181.

“Withdrawal properties of threaded rods embedded in glued-laminated timber elements”

Haris Stamatopoulos, 2016:48, ISBN 978-82-326-1436-3 (printed ver.) ISBN 978-82-326-1437-0 (electronic ver.) ISSN 1503-8181.

“An Experimental and numerical study of thermoplastics at large deformation”

Marius Andersen, 2016:191, ISBN 978-82-326-1720-3 (printed ver.) ISBN 978-82-326-1721-0 (electronic ver.) ISSN 1503-8181.

“Modeling and Simulation of Ballistic Impact”

Jens Kristian Holmen, 2016:240, ISBN 978-82-326-1818-7 (printed ver.) ISBN 978-82-326-1819-4 (electronic ver.) ISSN 1503-8181.

“Early age crack assessment of concrete structures”

Anja B. Estensen Klausen, 2016:256, ISBN 978-82-326-1850-7 (printed ver.) ISBN 978-82-326-1851-4 (electronic ver.) ISSN 1503-8181.

“Uncertainty quantification and sensitivity analysis for cardiovascular models”

Vinzenz Gregor Eck, 2016:234, ISBN 978-82-326-1806-4 (printed ver.) ISBN 978-82-326-1807-1 (electronic ver.) ISSN 1503-8181.

“Dynamic behaviour of existing and new railway catenary systems under Norwegian conditions”

Petter Røe Nåvik, 2016:298, ISBN 978-82-326-1935-1 (printed ver.) ISBN 978-82-326-1934-4 (electronic ver.) ISSN 1503-8181.

“Mechanical behaviour of particle-filled elastomers at various temperatures”

Arne Ilseng, 2016:295, ISBN 978-82-326-1928-3 (printed ver.) ISBN 978-82-326-1929-0 (electronic ver.) ISSN 1503-8181.

“Nanotechnology for Anti-Icing Application”

Zhiwei He, 2016:348, ISBN 978-82-326-2038-8 (printed ver.) ISBN 978-82-326-2019-5 (electronic ver.) ISSN 1503-8181.

“Conduction Mechanisms in Conductive Adhesives with Metal-Coated Polymer Spheres”

Sigurd Rolland Pettersen, 2016:349, ISBN 978-82-326-2040-1 (printed ver.) ISBN 978-82-326-2041-8 (electronic ver.) ISSN 1503-8181.

“The interaction between calcium lignosulfonate and cement”

Alessia Colombo, 2017:20, ISBN 978-82-326-2122-4 (printed ver.) ISBN 978-82-326-2123-1 (electronic ver.) ISSN 1503-8181.

“Behaviour and Modelling of Flexible Structures Subjected to Blast Loading”

Vegard Aune, 2017:101, ISBN 978-82-326-2274-0 (printed ver.) ISBN 978-82-326-2275-7 (electronic ver.) ISSN 1503-8181.

“Behaviour of steel connections under quasi-static and impact loading”

Erik Løhre Grimsmo, 2017:159, ISBN 978-82-326-2390-7 (printed ver.) ISBN 978-82-326-2391-4 (electronic ver.) ISSN 1503-8181.

“An experimental and numerical study of cortical bone at the macro and Nano-scale”

Masoud Ramenzanzadehkoldeh, 2017:208, ISBN 978-82-326-2488-1 (printed ver.) ISBN 978-82-326-2489-8 (electronic ver.) ISSN 1503-8181.

“Optoelectrical Properties of a Novel Organic Semiconductor: 6,13-Dichloropentacene”

Mao Wang, 2017:130, ISBN 978-82-326-2332-7 (printed ver.) ISBN 978-82-326-2333-4 (electronic ver.) ISSN 1503-8181.

“Core-shell structured microgels and their behavior at oil and water interface”

Yi Gong, 2017:182, ISBN 978-82-326-2436-2 (printed ver.) ISBN 978-82-326-2437-9 (electronic ver.) ISSN 1503-8181.

“Aspects of design of reinforced concrete structures using nonlinear finite element analyses”

Morten Engen, 2017:149, ISBN 978-82-326-2370-9 (printed ver.) ISBN 978-82-326-2371-6 (electronic ver.) ISSN 1503-8181.

“Numerical studies on ductile failure of aluminium alloys”

Lars Edvard Dæhli, 2017:284, ISBN 978-82-326-2636-6 (printed ver.) ISBN 978-82-326-2637-3 (electronic ver.) ISSN 1503-8181.

“Modelling and Assessment of Hydrogen Embrittlement in Steels and Nickel Alloys”

Haiyang Yu, 2017:278, ISBN 978-82-326-2624-3 (printed. ver.) ISBN 978-82-326-2625-0 (electronic ver.) ISSN 1503-8181.

“Network arch timber bridges with light timber deck on transverse crossbeams”

Anna Weronika Ostrycharczyk, 2017:318, ISBN 978-82-326-2704-2 (printed ver.) ISBN 978-82-326-2705-9 (electronic ver.) ISSN 1503-8181.

“Splicing of Large Glued Laminated Timber Elements by Use of Long Threaded Rods”

Martin Cepelka, 2017:320, ISBN 978-82-326-2708-0 (printed ver.) ISBN 978-82-326-2709-7 (electronic ver.) ISSN 1503-8181.

“Thermomechanical behaviour of semi-crystalline polymers: experiments, modelling and simulation”

Joakim Johnsen, 2017:317, ISBN 978-82-326-2702-8 (printed ver.) ISBN 978-82-326-2703-5 (electronic ver.) ISSN 1503-8181.

“Small-Scale Plasticity under Hydrogen Environment”

Kai Zhao, 2017:356, ISBN 978-82-326-2782-0 (printed ver.) ISBN 978-82-326-2783-7 (electronic er.) ISSN 1503-8181.

“Risk and Reliability Based Calibration of Structural Design Codes”

Michele Baravalle, 2017:342, ISBN 978-82-326-2752-3 (printed ver.) ISBN 978-82-326-2753-0 (electronic ver.) ISSN 1503-8181.

“Dynamic behaviour of floating bridges exposed to wave excitation”

Knut Andreas Kvåle, 2017:365, ISBN 978-82-326-2800-1 (printed ver.) ISBN 978-82-326-2801-8 (electronic ver.) ISSN 1503-8181.

“Dolomite calcined clay composite cement – hydration and durability”

Alisa Lydia Machner, 2018:39, ISBN 978-82-326-2872-8 (printed ver.) ISBN 978-82-326-2873-5 (electronic ver.) ISSN 1503-8181.

“Modelling of the self-excited forces for bridge decks subjected to random motions: an experimental study”

Bartosz Siedziako, 2018:52, ISBN 978-82-326-2896-4 (printed ver.) ISBN 978-82-326-2897-1 (electronic ver.) ISSN 1503-8181.

“A probabilistic-based methodology for evaluation of timber facade constructions”
Klodian Gradeci, 2018:69, ISBN 978-82-326-2928-2 (printed ver.) ISBN 978-82-326-2929-9 (electronic ver.) ISSN 1503-8181.

“Behaviour and modelling of flow-drill screw connections”
Johan Kolstø Sønstabø, 2018:73, ISBN 978-82-326-2936-7 (printed ver.) ISBN 978-82-326-2937-4 (electronic ver.) ISSN 1503-8181.

“Full-scale investigation of the effects of wind turbulence characteristics on dynamic behavior of long-span cable-supported bridges in complex terrain”
Aksel Fenerci, 2018:100, ISBN 9978-82-326-2990-9 (printed ver.) ISBN 978-82-326-2991-6 (electronic ver.) ISSN 1503-8181.

“Modeling and simulation of the soft palate for improved understanding of the obstructive sleep apnea syndrome”
Hongliang Liu, 2018:101, ISBN 978-82-326-2992-3 (printed ver.) ISBN 978-82-326-2993-0 (electronic ver.) ISSN 1503-8181.

“Long-term extreme response analysis of cable-supported bridges with floating pylons subjected to wind and wave loads”.
Yuwang Xu, 2018:229, ISBN 978-82-326-3248-0 (printed ver.) ISBN 978-82-326-3249-7 (electronic ver.) ISSN 1503-8181.

“Reinforcement corrosion in carbonated fly ash concrete”
Andres Belda Revert, 2018:230, ISBN 978-82-326-3250-3 (printed ver.) ISBN 978-82-326-3251-0 (electronic ver.) ISSN 1503-8181.

“Direct finite element method for nonlinear earthquake analysis of concrete dams including dam-water-foundation rock interaction”
Arnkjell Løkke, 2018:252, ISBN 978-82-326-3294-7 (printed ver.) ISBN 978-82-326-3295-4 (electronic ver.) ISSN 1503-8181.

“Electromechanical characterization of metal-coated polymer spheres for conductive adhesives”
Molly Strimbeck Bazilchuk, 2018:295, ISBN 978-82-326-3380-7 (printed. ver.) ISBN 978-82-326-3381-4 (electrical ver.) ISSN 1503-8181.

“Determining the tensile properties of Arctic materials and modelling their effects on fracture”
Shengwen Tu, 2018:269, ISBN 978-82-326-3328-9 (printed ver.) ISBN 978-82-326-3329-6 (electronic ver.) ISSN 1503-8181.

“Atomistic Insight into Transportation of Nanofluid in Ultra-confined Channel”
Xiao Wang, 2018:334, ISBN978-82-326-3456-9 (printed ver.) ISBN 978-82-326-3457-6 (electronic ver.) ISSN 1503-8181.

“An experimental and numerical study of the mechanical behaviour of short glass-fibre reinforced thermoplastics”

Jens Petter Henrik Holmstrøm, 2019:79, ISBN 978-82-326-3760-7 (printed ver.) ISBN 978-82-326-3761-4 (electronic ver.) ISSN 1503-8181.

“Uncertainty quantification and sensitivity analysis informed modeling of physical systems”

Jacob Sturdy, 2019:115, ISBN 978-82-326-3828-4 (printed ver.) ISBN 978-82-326-3829-1 (electric ver.) ISSN 1503-8181.

“Load model of historic traffic for fatigue life estimation of Norwegian railway bridges”

Gunnstein T. Frøseth, 2019:73, ISBN 978-82-326-3748-5 (printed ver.) ISBN 978-82-326-3749-2 (electronic ver.) ISSN 1503-8181.

“Force identification and response estimation in floating and suspension bridges using measured dynamic response”

Øyvind Wiig Petersen, 2019:88, ISBN 978-82-326-3778-2 (printed ver.) ISBN 978-82-326-3779-9 (electronic ver.) ISSN 1503-8181.

“Consistent crack width calculation methods for reinforced concrete elements subjected to 1D and 2D stress states”

Reignard Tan, 2019:147, ISBN 978-82-326-3892-5 (printed ver.) ISBN 978-82-326-3893-2 (electronic ver.) ISSN 1503-8181.

“Nonlinear static and dynamic isogeometric analysis of slender spatial and beam type structures”

Siv Bente Raknes, 2019:181, ISBN 978-82-326-3958-8 (printed ver.) ISBN 978-82-326-3959-5 (electronic ver.) ISSN 1503-8181.

“Experimental study of concrete-ice abrasion and concrete surface topography modification”

Guzel Shamsutdinova, 2019:182, ISBN 978-82-326-3960-1 (printed ver.) ISBN 978-82-326-3961-8 (electronic ver.) ISSN 1503-8181.

“Wind forces on bridge decks using state-of-the art FSI methods”

Tore Andreas Helgedagsrud, 2019:180, ISBN 978-82-326-3956-4 (printed ver.) ISBN 978-82-326-3957-1 (electronic ver.) ISSN 1503-8181.

“Numerical Study on Ductile-to-Brittle Transition of Steel and its Behavior under Residual Stresses”

Yang Li, 2019:227, ISBN 978-82-326-4050-8 (printed ver.) ISBN 978-82-326-4015-5 (electronic ver.) ISSN 1503-8181.

“Micromechanical modelling of ductile fracture in aluminium alloys”

Bjørn Håkon Frødal, 2019:253, ISBN 978-82-326-4102-4 (printed ver.) ISBN 978-82-326-4103-1 (electronic ver.) ISSN 1503-8181.